Investigation of normal growth faulting in the Columbus Basin, Trinidad, using fault displacement back-stripping

Ulrike A. Freitag

Department of Earth Science and Engineering
Imperial College
London

February 2008

Submitted in accordance with the requirements of the University of London for the degree of Doctor of Philosophy and the Diploma of Imperial College.

The work presented in this thesis is the candidates own. No portion of the work referred to in this thesis has been submitted in support of an application for another degree or qualification of this or any other university or any other institute of learning.

Ulrike A. Freitag

Abstract

The Columbus Basin offshore Trinidad is a thin-skinned detached basin characterised by large-scale, syn-depositional gravitational extensional faulting and rapid creation of accommodation filled by thick sedimentary sequences since the Late Miocene.

The investigation of extensional growth faults using fault displacement back-stripping is based on faults and horizons mapped on a high-quality 3D seismic survey. The study area contains three major block-bounding normal faults, with maximum throws of 1400-2500 m. Smaller fault systems show various evolutionary patterns, including (1) fault linkage after breaching of a relay ramp, and (2) upward splaying into several fault segments from a continuous fault at depth. This suggests that geometric linkage and kinematic linkage are not necessarily simply related.

Most faults have higher throw rates during their early stages that decrease until their deaths. The largest faults have throw rates of up to 2.5-3.5 mm/a, whilst the smaller ones are generally below 1 mm/a. Variations from this general trend are attributed to fault interaction, non-uniform basin extension and the migration of the deltaic depocentre, which governs the location of primary sediment deposition and, therefore, gravitational collapse.

Fault activity was reconstructed for successive time intervals from 2.78 Ma to the present-day. The data show pronounced seaward migration of fault activity for progressively younger horizons which is attributed to the progradation of the shelf-edge delta. Initiation of a major block-bounding fault results in numerous smaller faults in its hanging wall, whose activity rapidly decreases as soon as the next major basinward fault becomes active. The total throw rate across the study area varies over the investigated time span. This may reflect broader regional variations of fault activity that might be controlled by the rate of sediment supply and the location and migration of the centre of gravitational collapse.

A series of vertically persistent, small-scale hanging wall anticlines that are located at kinks in the fault plane and associated with the largest faults in the study area are interpreted as remnants of fault linkage.

In this study, the fault interaction and evolution of several extensional faults in the Columbus Basin were investigated and the throw rates at which these faults moved were determined. Within the study area, the temporal and spatial migration of active faulting in a detached gravitational basin was quantified.

Table of contents

List of Figures

List of Tables

Acknowledgements

I would like to thank all those who supported me, scientifically or morally, during the work on this project.

Most importantly, my supervisors David Sanderson and Lidia Lonergan are thanked for their advice, encouragement, and valuable discussions. Their critical comments and suggestions are much-appreciated and helped to improve the thesis.

This project was made possible by a Janet Watson PhD Scholarship granted by the Department of Earth Science and Engineering at Imperial College London.
BP and BP Trinidad & Tobago are gratefully acknowledged for providing the excellent seismic dataset and additional data as well as financial support. I want to especially thank Tim Bevan for his help and advice.

I would also like to thank my fellow PhD students at the ESE department, past and present, particularly Martin, Kerry, Margaret, Veronica, and Caroline, for their friendship, humour and support throughout our time here together. Dave Parry was a good friend and listened patiently to all the strange stories, problems and achievements that unfolded at university.

Last, but not least, thanks to my parents for their constant emotional support and encouragement during my studies.

Chapter 1

Introduction

1.1 Rationale

Extension within sedimentary basins is accommodated by extensional faults over several scales. Faults that intersect the bedding surface and influence the sediment distribution across the fault whilst being active are called growth faults. Characteristic variations in the thickness of the syn-faulting sediments in the hanging wall and footwall provide information about the timing of fault activity as well as the displacement and propagation history of the fault.

Gravitational faulting is dominant at passive margins with high sediment supply, for example the Gulf of Mexico (e.g. BRUCE, 1973; BUSCH, 1975; SHELTON, 1984; NUNN, 1985; WU et al., 1990; DIEGEL et al., 1995), the West African margin (e.g. DUVAL et al., 1992; LUNDIN, 1992; DAMUTH, 1994; ROUBY & COBBOLD, 1996; VALLE et al., 2001) and the Columbus Basin (LEONARD, 1983; SYDOW et al., 2003; BEVAN, 2007; GIBSON et al., in press). These basins contain very prolific hydrocarbon reservoirs. Deformation is characterised by large-scale, listric extensional faults on the shelf that often detach into a shale or salt succession. The listric faults may be kinematically related to toe thrusts on the slope, the whole system forming in response to mass translation down-slope (BRUCE, 1973; WERNICKE & BURCHFIEL, 1982; GALLOWAY, 1986, 1987).

A few studies have investigated the evolution of tectonic fault populations, and the spatial and temporal distribution of strain within these extensional systems based on seismic data (e.g. MEYER et al., 2002; WALSH et al., 2003b). Reconstruction of the distribution of fault displacement within arrays of sandbox-modelled, gravitational faults (e.g. CHILDS et al., 1993; MOURGUES & COBBOLD, 2006) has also contributed to our understanding of the growth and interaction of gravitational syn-sedimentary faults. The reconstruction of the displacement field for a growth fault system in the Niger Delta (Rouby & Cobbold, 1996) and the restoration of the kinematics and rates of deformation for an evaporate-detached growth fault/raft system on the West African margin (Rouby et al., 2002, 2003) provided important insights into gravitational deformation above mobile substrates. However, the temporal and spatial distribution and evolution of strain within gravitational fault systems is still poorly understood.

This study addresses, on the example of the Columbus Basin, the growth and interaction of individual gravitational extensional faults of different scales (ca. 140 m to 2500 m maximum throws) as well as the evolution of the fault array in a detached basin without a thick mobile substrate. Particular emphasis is placed on the interaction of faults and the resulting throw patterns, establishing the throw rates at which individual faults move as well as cumulative throw rates over time, and the migration of fault activity within the study area.

1.2 Aims and objectives

The aims of the research reported in this thesis are

1) to better understand the geometry and kinematics of extensional growth faulting using fault displacement back-stripping, and
2) to investigate the spatial and temporal distribution of fault (segment) activity, including displacement rate.

This work is mainly based on investigation and analysis of data from the Columbus Basin, offshore Trinidad. This basin was chosen because of the availability of high-quality 3D seismic data, well data and reasonably good biostratigraphic control of marker horizons.

To achieve the research aims, the following specific objectives were defined:

1) detailed mapping of faults and growth sequences on the 3D seismic dataset from the Columbus Basin,
2) determination of throw distribution on the mapped faults,
3) application of fault displacement back-stripping,
4) correction for sediment compaction,
5) calculation of the throw rates at which the faults moved,
6) detailed documentation and investigation of selected case studies,
7) investigation of the survey-wide magnitude of fault activity (fault throw rate) and migration of fault activity with time, and
8) documentation of anticlinal structures related to extensional faulting during fieldwork at Kilve, Somerset, as a comparative study for similar structures seen in the seismic survey associated with fault linkage.

This project investigates the evolution of gravitational, syn-sedimentary extensional faults using a high-quality 3D seismic dataset covering an area of rapidly accumulating sediment. A number of faults and dated marker-horizons, which span an interval of ca. 2.8 Ma duration, enable detailed investigation of fault throw distribution and, after application of fault displacement back-stripping, ultimately fault slip rates to be determined. Resulting from this is the potential to establish the history of throw accumulation on the faults, including throw rates for successive time intervals, to map subtle changes in the fault geometries and throw profiles that may give information about fault interaction and linkage, and to assess the spatial and temporal evolution of the fault array. This will contribute to the understanding of gravitational syn-sedimentary faults and fault arrays compared to rift-related ones.

The novel approach of this study is the use of high-quality seismic data that permits the fault throw data to be determined for several dated horizons. This offers the opportunity to constrain the history of throw accumulation and the distribution of fault activity from quantitative throw data as opposed to qualitative isopach data.

1.3 Resources and methodology

This project was made possible by a studentship granted by the Department of Earth Science and Engineering at Imperial College London and the courtesy of BP and BP Trinidad & Tobago, who generously provided the seismic dataset, well data, and other information (e.g. on horizon ages and porosity-depth trends), that form the basis of the study. The work was carried out with periodic input by BP and BP Trinidad & Tobago during visits to Port of Spain, Trinidad, and Sunbury-on-Thames, UK. The interpretation of the seismic data (fault and horizon network) was carried out using SeisWorks® and GeoProbe® software by Landmark, which is provided to the Department of Earth Science and Engineering at Imperial College London. Badley Geoscience Limited granted access to TrapTester® software, which was used to determine the amount of fault throw accumulated on specific horizons, as well as to investigate variations of fault strike direction and dip angle.

This study of extensional growth fault evolution is based on the principle that growth faults intersect the Earth's surface and, hence, affect the deposition of sediments by creating accommodation on the downthrown hanging wall block. Thus, systematic thickness changes from thinner footwall to thicker hanging wall strata between marker horizons characterise growth faults and can be used to constrain and quantify fault evolution.

Fault displacement back-stripping is a method used to determine the amount of displacement accumulated by syn-sedimentary fault movement during certain time intervals or at certain stratigraphic levels. With this information, detailed studies of the fault evolution can be carried out in order to identify different phases of fault activity. The restoration of throw increments enables quantitative reconstruction of fault movement in relation to mapped variations in fault geometry (e.g. linkage or splaying). Accurate dating of time intervals allows throw rates for each time interval to be determined and interpreted over the duration of activity of the fault.

1.4 Thesis outline

Chapter 2 presents an overview of extensional fault geometries, outlining the terminology and methods used to investigate the throw accumulation on normal faults. The chapter also summarises existing research on normal fault linkage structures and processes, and discusses specific properties of normal growth faults that are the basis of this study.

Chapter 3 introduces the structural setting, depositional environment and basin evolution of the study area, the Columbus Basin offshore Trinidad, with particular emphasis on the extensional fault patterns and the relationship between sediment facies (lithology) and pore fluid pressure in the vicinity of the study area.

Chapter 4 summarises the dataset and methodology used to investigate the normal growth faults in this study. Particular consideration was given to the 3D seismic dataset, depth conversion thereof, and the correlation of well data and mapped horizons. The principles of fault throw analysis and common ways to illustrate the results are discussed, based largely on the methodology applied by TrapTester®, a commercial structural analysis software tool used to analyse the fault throw data. The correction for sediment compaction and its applications are also discussed.

Chapter 5 contains five case studies of individual faults or small fault systems. These are detailed descriptions and interpretations of the fault geometry, throw distribution and throw rate, leading to an evolutionary model of the growth of the fault or fault array. The case studies were chosen on the basis of the size and importance of the fault in accumulating extension in the basin, and to illustrate particularly interesting aspects of fault linkage or splaying present in the study area.

Chapter 6 integrates the throw and throw rate data of the major faults within the seismic survey. The data are presented as a series of maps that show the magnitude of fault activity and its migration in the study area over the past 2.8 Ma. These provide a sub-regional summary of the deformation that links to the case studies in Chapter 5 to provide a more basin-scale insight to the strain distribution and fault activity rate across two ~15 km-sized fault blocks. The novel part of this research is the attempt to quantify the fault activity data in terms of throw rates, which were determined from detailed fault throw measurements at different horizons, as opposed to descriptions of thickness variations of the syn-faulting strata in form of isopach maps.

Chapter 7 describes a series of hanging wall anticlines that have been observed in both the seismic data from the Columbus Basin and in an analogue outcrop in Jurassic rocks in

SW England. The relationship of the hanging wall anticlines to the fault geometry is examined, and their significance and implications for fault linkage models discussed.

Chapter 8 contains conclusions of the results of this study and discusses them in light of previous research. The significance and implications of the findings for existing fault growth models is reviewed.

Chapter 2

Principles of normal faulting

2.1 Characteristics of normal faults

Normal faults are primarily encountered in extensional basin settings (rift basins, passive margins) (e.g. McKenzie, 1978; Wernicke & Burchfiel, 1982; Gibbs, 1984, 1987) but are also found to overprint contractional structures in areas that have undergone late-stage orogenic extension (e.g. Norton, 1986; Platt, 1986). Extensional faults are also a common deformation style in areas affected by salt tectonics and gravity driven tectonics such as the offshore parts of deltas (e.g. Niger Delta, Gulf of Mexico). Normal faults exist over large scale ranges. They can cover cm to 100s km in length and have displacements of a few mm to several km. In this study, normal faults within a sedimentary succession on a continental shelf that formed within an overall transtensional setting are investigated.

2.1.1 Geometry

Normal faults are characterised by relative downward movement of the hanging wall block with respect to the footwall block (Fig. 2.1) as a result of extension of the crust or the sedimentary cover (e.g. Price & Cosgrove, 1990). The line of intersection between a planar stratigraphic bed and the fault surface is called the cut-off line. Footwall and hanging wall cut-off lines are distinguished according to their relative position to the fault (e.g. Suppe, 1985, Peacock et al., 2000). The distance between the footwall and hanging wall cut-off lines of a particular stratigraphic bed offset along the fault plane is termed the separation, the horizontal and vertical components of which are the heave and throw, respectively. For dip-slip movement, the dip-separation is the displacement, and the heave and throw represent the horizontal and vertical components of displacement (Suppe, 1985, Peacock et al., 2000). For known dip angles of the fault, these values can be calculated from each other. The deeper parts of listric normal faults detaching into units of low shear-strength require further consideration due to the change in dip angle.

Normal faulting can affect a volume of sedimentary rocks after deposition or during deposition of these rocks. If faulting occurs during deposition (syn-depositional, growth faulting), accommodation is created on the downthrown hanging wall block, which leads to a characteristic thickening of respective units across the fault (e.g. CHILDS et al., 2003) (see Section 2.2). If the faulting deforms the rocks after deposition (post-depositional), no sedimentary thickness changes occur due to faulting.

A blind normal fault, which does not intersect the Earth's surface when active and is entirely contained within the rock volume that it displaces post-dates deposition of the surrounding sedimentary units and shows uniform primary sedimentary bed thickness across the fault (WATTERSON, 1986; BARNETT et al., 1987). This lack of sedimentary thickness changes associated with faulting makes dating of fault activity of blind faults difficult, it requires detailed information about regional and local basin evolution and/or radiometric dating of fault rocks and mineralization. Relative timing can be derived from cross-cutting relationships of different sets of faults, of associated fault rocks, and of fault-related veins.

Throw distribution on a normal fault surface follows characteristic patterns. Many blind normal faults have an approximately elliptical tip line with systematically decreasing throw from a maximum near the centre to zero at the tip (Fig. 2.2a) (e.g. WATTERSON, 1986; BARNETT et al., 1987; WALSH & WATTERSON, 1987, 1988, 1989; PRICE & COSGROVE, 1990; CHILDS et al., 2003). Fig. 2.2b illustrates the distribution of displacement between the upper and lower tips of a blind normal fault in cross-sectional view (BARNETT et al., 1987; SCHLISCHE, 1995).

Listric normal faults are often large-scale normal faults, which are characterised by decreasing dip angles with depth towards a gently dipping detachment fault and thus a concave-upward geometry (SHELTON, 1984; SUPPE, 1985). In cross-section, listric normal faults show a progressive decrease of fault dip from a typical dip of >60° at the surface, to subhorizontal dips in the detachment layer (Fig. 2.3). The detachment can be located in mechanically incompetent sedimentary rocks such as shales or evaporates, or in a ductile shear zone located between the lower crust and upper mantle. Listric normal faults are found in many extensional setting, including rifts and passive margins (GIBBS, 1984; SHELTON, 1984; GALLOWAY, 1986). Extension along a listric normal fault would lead to a gap between the footwall and a rigid hanging wall (Fig. 2.3b). However, such a gap does not exist in nature due to deformation of the hanging wall block (HAMBLIN, 1965), which leads to the formation of a roll-over anticline (HAMBLIN, 1965; WILLIAMS & VANN, 1987, XIAO & SUPPE, 1992) (Fig. 2.3). The question of how deformation of the hanging wall of a listric fault takes place was a matter of some controversy (HAMBLIN, 1965; WHITE et al., 1986; WILLIAMS & VANN, 1987; DULA, 1991). DULA (1991) compares several methods used to construct the shape of the listric master fault at depth for poorly constrained seismic data knowing the rollover geometry and the fault heave, shear angle or displacement. He

concludes that the inclined shear model (WHITE et al., 1986) (Fig. 2.3d) and the constant-displacement model best approximate the position and shape of the master fault.
An array of simultaneously rotated planar normal faults and intervening rigid fault blocks is referred to as domino faulting (AXEN, 1988; JACKSON et al., 1988; JACKSON & WHITE, 1989; YIELDING, 1990; PRICE & COSGROVE, 1990; ROUBY et al., 1996; PEACOCK et al., 2000; STEWART & ARGENT, 2000). The domino faults can pass into a detachment at depth (PEACOCK et al., 2000; STEWART & ARGENT, 2000). WALSH & WATTERSON (1991) have suggested a soft-domino model, where the block containing several geometrically and kinematically coherent normal faults is not rotated as a whole and a marker horizon has the same elevation at both (fault-perpendicular) ends of the block, which is achieved by reverse drag of the horizon on both sides of each fault. Other variations of displacement on the faults within the block are accommodated by heterogeneous ductile strains.

2.1.2 Fault growth and linkage

Strike linkage

Most faults, as has been demonstrated for dip-slip and strike-slip faults, consist of a number of smaller segments (SEGALL & POLLARD, 1980; PEACOCK & SANDERSON, 1991; TRUDGILL & CARTWRIGHT, 1994; CHILDS et al., 1995; WILLEMSE, 1997). Normal fault segments usually form an en-echelon array along-strike and are either separated by relay ramps or connected by breaching faults. Relay ramps are zones where two individual, synthetic, sub-parallel normal faults overlap in map view (LARSEN, 1988; PEACOCK & SANDERSON, 1991; PEACOCK et al., 2000) and displacement is transferred between them without the faults being physically linked (Fig. 2.4c). These overlap areas generally show steeper lateral throw gradients than other parts of the fault (WALSH & WATTERSON, 1989; PEACOCK & SANDERSON, 1991, 1994; WALSH et al., 2003a) (Fig. 2.4d). If the cumulative throw of both faults at the overlap zone forms a smooth profile, resembling that of a single fault, the faults have been termed geometrically coherent (WALSH & WATTERSON, 1991; CHILDS et al., 1995). However, displacement minima at fault overlap and linkage zones are commonly observed and can be explained with bending, tilting and faulting in the relay structures or by folding and deformation of the wall rocks (PEACOCK & SANDERSON, 1991; WALSH & WATTERSON, 1991; TRUDGILL & CARTWRIGHT, 1994). As extension continues, relay ramps may be breached by the tip of one fault propagating towards the other or by a linking fault, leaving one or two abandoned splays behind, respectively (TRUDGILL & CARTWRIGHT, 1994) (Fig. 2.4). The line of intersection between a "master" fault and a synthetic splay or between two segments of a multi-strand fault is called branch line (WALSH et al., 1999).

Linkage between neighbouring normal faults is distinguished according to the degree of physical linkage between the fault surfaces and the throw distribution along the newly established extended fault plane. "Soft linkage" refers to displacement transfer through ductile

strain between two individual, physically independent faults, whereas "hard linkage" refers to two faults that are physically connected via footwall or hanging wall linkage (propagation of one of the overlapping tips to the second fault) or a breaching fault (WALSH & WATTERSON, 1991; TRUDGILL & CARTWRIGHT, 1994).
TRUDGILL & CARTWRIGHT (1994) and CARTWRIGHT et al. (1996) conclude from a field study in the Canyonlands Grabens in Utah that normal faults do not only grow by radial propagation as described by WALSH & WATTERSON (1987, 1988) but instead by a combination of radial propagation and linkage of precursor segments. The segmentation of faults in the Canyonlands occurs on a scale range of >10 km to tens of meters and TRUDGILL & CARTWRIGHT (1994) argue that any fault segment will consist of a series of successively smaller segments.

Dip linkage

Linkage of normal fault segments not only occurs along fault strike but also in the dip direction (MANSFIELD & CARTWRIGHT, 1996; WALSH et al., 1999; RYKKELID & FOSSEN, 2002). Throw data mapped on high-resolution seismic data of normal growth faults from the Gulf of Mexico display characteristic sub-horizontally aligned throw minima that are interpreted to originate from overlap and eventual linkage of initial fault segments in the dip direction (dip-linkage of MANSFIELD & CARTWRIGHT, 1996). The relay ramps in this case are elongated approximately parallel to fault strike and not parallel to the fault dip as in the case of strike-linkage (PEACOCK & SANDERSON, 1991; MANSFIELD & CARTWRIGHT, 1996; WALSH et al., 1999).

It is concluded from widely available field evidence that segmentation is a fundamental characteristic of normal faults and that linkage between segments therefore plays a crucial role in the growth of faults (SEGALL & POLLARD, 1980; JACKSON & WHITE, 1989; PEACOCK & SANDERSON, 1991; TRUDGILL & CARTWRIGHT, 1994; CARTWRIGHT et al., 1996; WILLEMSE, 1997). CHILDS et al. (1995) argue that the growth of faults is characterised by repetitive cycles of fault overlap, relay formation and breaching, and linkage between neighbouring segments. This has also been shown by MANSFIELD & CARTWRIGHT (2001) in their extensional analogue model. Segmentation of normal faults and strike-slip faults is scale-independent (SEGALL & POLLARD, 1980; PEACOCK & SANDERSON, 1994; MANSFIELD & CARTWRIGHT; 2001), and hence a fundamental feature of faults.

The question of how normal faults grow is currently under debate. Traditionally, a model of systematic simultaneous lateral propagation of the fault and increased accumulation of displacement was proposed (WALSH & WATTERSON, 1988, 1991; COWIE & SCHOLZ, 1992; PEACOCK & SANDERSON, 1996). This means any one fault maintains a constant displacement-length ratio throughout its history. However, WALSH et al. (2002) suggested an alternative model of fault growth where the fault length is rapidly established and subsequent fault interaction retards further lateral propagation. Fault growth is then dominated by accumulation of displacement between essentially constant fault tips, resulting in a progressive increase in the displacement-length ratio over time. Fault evolution following this model has been described by MEYER et al. (2002) and NICOL et al. (2005).

2.2 Growth faulting

Faults that intersect the Earth's surface have the potential to influence the sedimentary record. Extensional faults that are active during sedimentation and influence the distribution and thickness of the deposits are referred to as growth or syn-sedimentary faults (BRUCE, 1973; RIDER, 1978; CHILDS et al., 2003). The strata deposited during fault activity are referred to as syn-faulting. Displacement of the Earth's surface during ongoing sediment deposition create accommodation in the hanging wall block, which leads to characteristic greater thicknesses of equivalent beds in the hanging wall than in the footwall. In cross-section, the displacement on a growth fault progressively increases from young to old horizons (Figs. 2.5a and 2.6, see also Fig. 2.9). Continued movement of a fault accrues initial displacement on the most recently deposited horizon and adds to previously accumulated displacement on all underlying horizons. Thus, the deposition and displacement of any additional strata adds to the total displacement of all horizons, with older horizons accumulating progressively more displacement due to longer involvement in fault activity.
These thickness variations and systematic throw variations allow estimation of the fault throws that occurred subsequent to the deposition of each horizon and, hence, the fault movement history to be determined (CHILDS et al., 1993, 2003). Thus, for well-dated formation boundaries, growth faults can provide information about the timing of fault activity as well as displacement and propagation history of the fault. According to CHILDS et al. (2003), growth faults tend to have distinctive sub-horizontal sub-parallel throw contours in the growth sequence (Fig. 2.5).

In order to determine the timing and amount of fault activity, sedimentation rates must exceed fault displacement rates and the accommodation must be filled to the same base level on the footwall and hanging wall of the fault. Only then will syn-faulting packages be preserved in both the footwall and hanging wall, and the thickening of units across the fault relates directly to the fault activity (CHILDS et al., 2003). However, if fault scarps develop over a longer time and sedimentation does not keep pace with subsidence, the sediment thickness does not relate directly to the fault activity (CHILDS et al., 2003). Similarly, footwall uplift might lead to erosion of the footwall crest during times of low sedimentation and thus the loss of the footwall cut-off geometry and position. CHILDS et al. (2003) describe a fault in the Gulf of Mexico (Fig. 2.5b) that initially existed in the pre-extensional strata as a post-depositional, blind fault and then propagated upwards to intersect the seabed and evolved into a growth fault.

Listric growth faults can accommodate great amounts of displacement by detaching into mechanically weak horizons and show characteristic increase of displacement on successive horizons down the dip of the fault (HAMBLIN, 1965; GALLOWAY, 1987; XIAO & SUPPE, 1992; PEACOCK et al., 2000) (Fig. 2.6, see also Figs. 3.4b-e). The thickening of sediments towards the active normal fault forms characteristic growth "wedges" on the hanging wall that are thickest close to the fault and thin away from it (Fig. 2.6). This has been identified in the US Gulf Coast (BRUCE, 1973; WERNICKE & BURCHFIEL, 1982; GALLOWAY, 1986, 1987) and can be seen in seismic data (e.g. DIEGEL et al., 1995; DAVIES et al., 2000; ROUBY et al., 2003), field studies (e.g. EDWARDS, 1976; WIGNALL & BEST, 2004; NOLL & HALL, 2006) and has been demonstrated by MCCLAY (1990) in analogue models.

Extensional growth faults were first described by BRUCE (1973) as "contemporaneous" faults from seismic data in the Gulf of Mexico that are characterized by fault traces subparallel to the coast, thickening of sediment on the basinward, downthrown side and flattening in cross-section with depth to become bedding-parallel. The formation of these listric normal growth faults was attributed by BRUCE (1973) to gravitational sliding, pore fluid overpressure at shallow depth, the presence of thick shale units that the faults detach into, differential compaction and minimal "deep-seated tectonic effects". GALLOWAY (1986, 1987) attributes the formation of extensional, syn-depositional listric faults near the shelf margin and kinematically related thrust faults at the lower continental slope to gravity gliding within the sedimentary prism of prograding continental margins. Examples can be found in the Gulf of Mexico margin and the Niger Delta, and GALLOWAY (1986, 1987) considers prograding platforms, particularly continental margins, as very likely to be affected by gravity-induced deformation, especially so if sedimentation rates are high.

Field studies of listric growth faults are limited by the often much larger scale of structures observed in the sub-surface compared to available outcrops. Listric growth faults that exhibit thickened sedimentary sequences in their hanging walls are described by RIDER (1978) and WIGNALL & BEST (2004) from the west coast of Ireland. WIGNALL & BEST (2004) have reconstructed the kinematic history of a series of listric growth faults of Carboniferous age along a cross-section of ca. 2 km length. They demonstrate propagation of the fault system, except for one subsidiary fault, in a paleo-landward direction. BHATTACHARYA & DAVIES (2001, 2004) investigated a small-scale outcrop analogue of extensional growth faults in a Cretaceous prograding delta succession in Utah, USA. Within a section of ca. 130 m length, they found complex fault patterns associated with facies changes that demonstrate a complex fault history and no systematic progression of fault development. The growth faults in this example initiated in response to sand deposition in a proximal delta front area and faulting was accommodated by deformation of underlying mobile shales.

2.3 Graphical presentation of throw data

The displacement distribution on a normal fault surface can be illustrated in several ways in order to either visualise them and/or plot them for further investigations:

Strike-projections are constructed by projecting the displacement values at points on a fault surface onto a (vertical) surface parallel to fault strike (e.g. BARNETT et al., 1987; WALSH & WATTERSON, 1991; CHILDS et al., 1993) and contouring of equal displacement values in order to visualise displacement patterns (see sections 2.1.1 and 2.2) and variations thereof (Figs. 2.2 and 2.5). In TrapTester® (Section 4.2), throw contours can be projected directly onto the fault surface.

Diagrams of the depth of the footwall and hanging wall cut-off lines against fault length (CHAPMAN et al., 1978; ALLAN, 1989; horizon separation diagram of CHAPMAN & MENEILLY, 1991) (Figs. 2.7a and 2.7c) show the separation of a horizon between the uplifted footwall and the down-thrown hanging wall sides. If the lateral fault tips are covered, the horizon separation will decrease from an approximately central maximum to zero at the tips.
GIBSON et al. (1989) describe the displacement distribution between the footwall and hanging wall for blind normal faults to be equal according to the elastic dislocation model, but point out that geodetic data for single seismic slip events of dip-slip faults show systematic differences between footwall uplift and hanging wall subsidence (SAVAGE & HASTIE, 1966; STEIN et al., 1988; GIBSON et al., 1989). The amplitude of flexural footwall uplift is generally less pronounced than the hanging wall subsidence according to SCHLISCHE (1995), and a ratio of ca. 10-20% (JACKSON & MCKENZIE, 1983, YIELDING, 1990; GOLDSWORTHY & JACKSON, 2000) is commonly observed.
Un-breached fault overlap zones are characterised by two complementary approximately triangular cut-off geometries that open with steep bedding dips away from the overlapping fault tips towards the respective fault centre (Fig. 2.7c), whereas breached overlap zones exhibit an asymmetric, through-going separation along the major fault and a subsidiary triangular offset of the abandoned splay (CHILDS et al., 1995).

Plots of displacement or throw vs. fault length are most commonly used to characterise the displacement history of a fault. These diagrams provide information on fault length to displacement ratios, lateral and vertical displacement gradients and irregularities in the overall displacement profile (Figs. 2.5, 2.7b&d and 2.8a). The graphs may be approximately semi-elliptical for a single blind normal fault (WALSH & WATTERSON, 1987, 1988, 1989) (Section 2.1), but variations are common, with additional minima indicating a more complex fault history. Irregularities in the overall throw/displacement profile often contain information about fault interaction, for example displacement transfer through soft-linkage or hard-linkage after breaching of a relay (e.g. LARSEN, 1988; PEACOCK & SANDERSON, 1991). If plotted for several horizons displaced by the same fault, throw profiles help to determine if and how propagation and linkage have taken place, and whether the fault was active continuously or discontinuously (MANSFIELD & CARTWRIGHT, 2001; TAYLOR et al., 2004). Additionally, diagrams of fault throw vs. horizon-age (displacement vs. horizon number of CHILDS et al., 1993) for several horizons cut by a fault at one particular location show how the throw accumulated through time (Fig. 2.8b). The throw rate can be directly determined in a throw vs. horizon age diagram as the gradient (slope) of the curve, where the throw rate is determined as Δ throw divided by Δ time for any given time interval (NICOL et al., 1997) (see also Section 2.5). Therefore, steep gradients indicate high throw rates, whereas shallow gradients indicate low throw rates. Where the throw between consecutive horizons is constant, the gradient is 0 and no throw was accumulated during the time interval, i.e. the fault was inactive. Data for several positions along one fault or several faults can be plotted in one throw vs. horizon-age diagram. This allows comparison of the general growth patterns along a fault or between individual faults (e.g. faults growing gently over a long time or growing rapidly and dying quickly), identification of displacement transfer between neighbouring faults while both were active (NICOL et al., 2006), a shift in activity from one fault onto another over a longer time interval or localisation of deformation onto one particular fault after others have died.

2.4 Fault-displacement back-stripping

The analysis of fault throw allows fault activity to be described directly, as opposed to indirect methods such as isopach maps. Fault displacement back-stripping is a powerful method to investigate the distribution and amount of throw that was accumulated along a fault over certain time intervals. Fault throws can be back-stripped sequentially by subtraction of the throw on a horizon from all older horizons to estimate the throw distribution on the fault plane when this particular stratigraphic bed was the unfaulted even surface (CHILDS et al., 1993) (Fig. 2.9). This is similar to flattening or simple structural reconstruction of seismic data, which also removes any post-depositional deformation on a horizon and restores it horizontally to reveal the thickness distribution and topography below the horizon, assuming the depositional surface was (near) horizontal. Alternatively, fault throws can be back-stripped to interval-throws by subtracting the throw between pairs of neighbouring horizons, thus leading to the residual throw which was accumulated in the time intervals between these horizons (Fig. 2.10). With reliable stratigraphic ages for two horizons, throw rates can then be calculated for the intervals bounded by the horizons (see Section 2.5). Interval-throws also give vital information on the throw distribution and lateral throw gradients during each time interval and therefore the successive accumulation of throw on the fault or entire fault system. Fault displacement back-stripping can be applied to both data along the (entire) fault trace in a throw vs. fault length diagram, or at single locations along the fault for throw vs. horizon age data. Chapter 4.3 gives a detailed description of the application of fault displacement back-stripping to the dataset used for this study.

PETERSEN et al. (1992) applied fault displacement back-stripping to reconstruct the throw distribution on a fault surface at several stratigraphic levels. CHILDS et al. (1993) and CHILDS et al. (1995) used the method to show how faults interact and link from soft-linkage to relay-breaching and abandoned hanging wall splays. TAYLOR et al. (2004) determined the amount and distribution of throw at certain stratigraphic levels and reconstructed the growth and propagation of eventually linking fault segments for a set of near-surface faults in New Zealand.

So far, fault displacement back-stripping has mostly been applied to single faults or aligned segments to determine their growth, propagation, and displacement accumulation. WALSH et al. (2003b) used back-stripping to investigate strain localisation between two horizons in order to investigate changes of fault length populations. In this project, the method will be applied to a series of extensional faults in a study area covering several large-scale block-bounding faults and subsidiary faults to determine the evolution and lateral migration of fault activity.

2.5 Throw rate

Throw rate is an important measure of the velocity of throw accumulation. For every time interval between dated horizons, the throw accumulated during this time interval can be determined (Section 2.4), and subsequently the throw rate for each time interval can be calculated by dividing the amount of throw by the duration of the time interval (CHILDS et al., 1993) (equation 4.6). Throw rates are, once they have been calculated, independent of the time interval over which they have been determined and can be compared between different time intervals for a particular fault, or between faults from different basins or tectonic settings.

The displacement rates for the currently active Cape Egmont Fault, New Zealand, were determined on the basis of seismic data to a range of 0.18-2.8 mm/a for the last 3.7 Ma by NICOL et al. (2005). However, these values are not based on decompacted data. TAYLOR et al. (2004) established an average displacement rate of 1.41±0.31 mm/a, also based on seismic data, for a fully linked fault of a total length of about 20 km, consisting of five previously isolated segments. Maximum aggregate displacement rates at linkage zones are as high as 3.4±0.2 and 2.72±0.62 mm/a. Average displacement rates prior to full linkage of the fault system were only 0.47±0.15 mm/a and 0.72±0.23 mm/a for two consecutive time intervals. These results are derived from compaction-corrected displacement data (TAYLOR et al., 2004), and cover fault activity between 1.34 Ma and the Present.

2.6 Figures

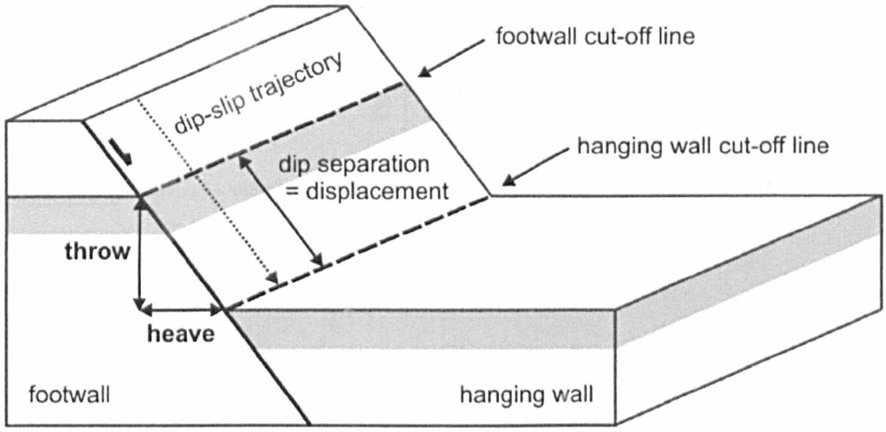

Fig. 2.1: Schematic illustration of the geometry and terminology of a normal fault.

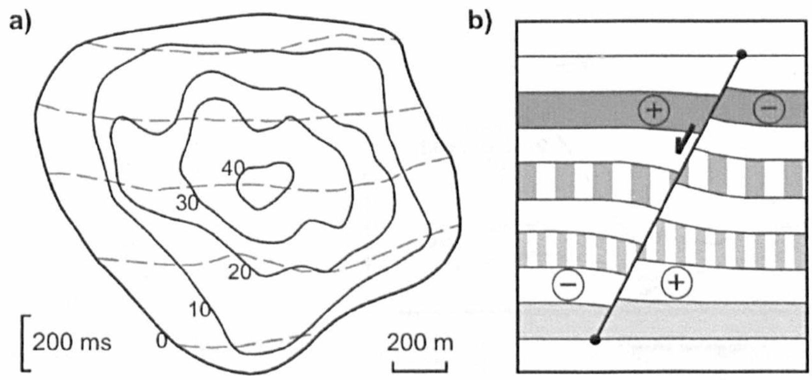

Fig. 2.2: **a)** Throw contours of a blind, post-sedimentary normal fault from the Gulf Coast, USA (dashed lines: horizons) (redrawn after CHILDS et al., 2003) and **b)** cross-section view of displacement distribution and deformation quadrants (+: dilational, -: contractional) along a blind normal fault (redrawn after SCHLISCHE, 1995).

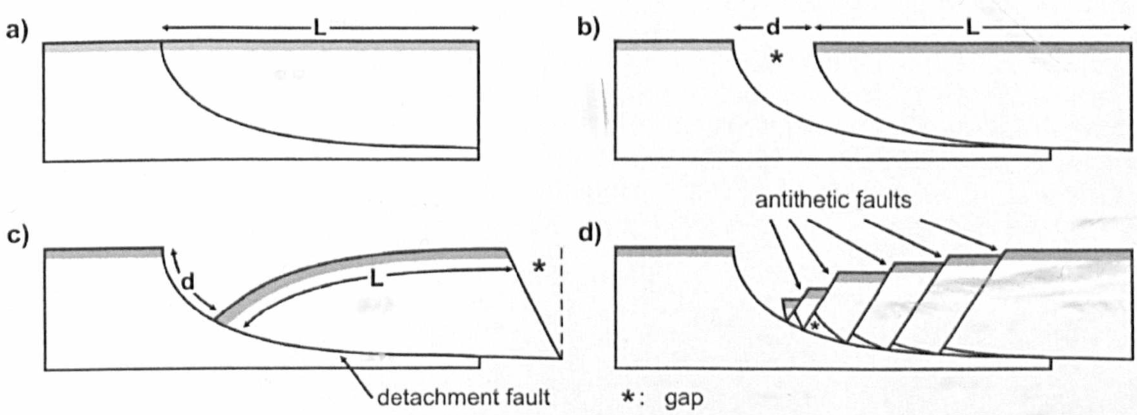

Fig. 2.3: Schematic illustration of the geometry of a listric normal fault and the deformation of its hanging wall due to fault displacement (redrawn after TWISS & MOORES, 1992): **a)** crustal block with future fault trace, **b)** rigid displacement of the HW block of length L by a distance d, which would lead to the opening of a gap, **c)** deformation of the HW by distributed deformation (flexural slip) creates another gap to the right of the HW block, and **d)** antithetic faulting reduces the gaps to misfits along the listric fault plane (inclined shear).

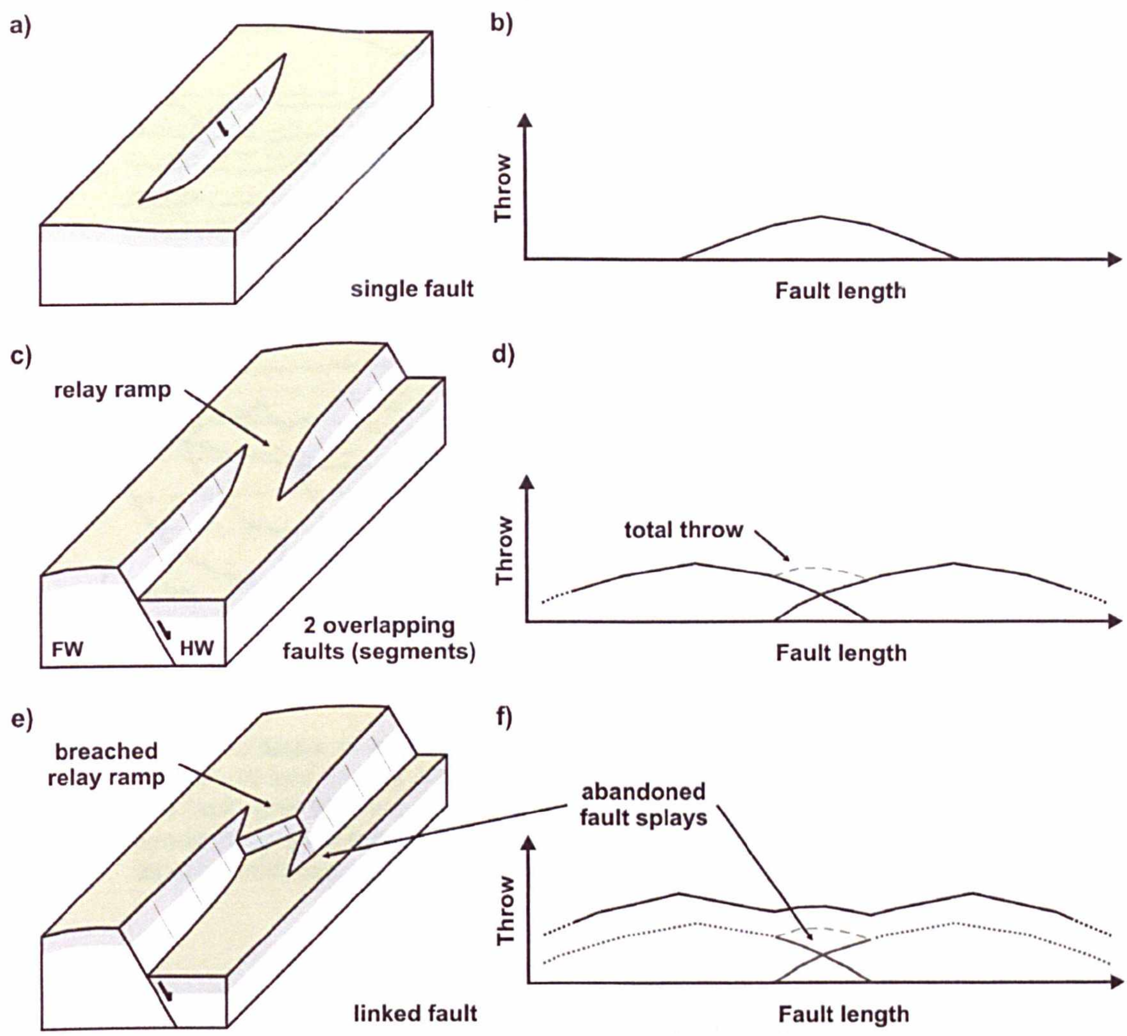

Fig. 2.4: Illustrations of the geometry and respective throw profiles of several stages during the evolution of (post-depositional) fault overlap zones: **a)** and **b)** show a single fault and its throw profile, **c)** and **d)** show two overlapping faults separated by a relay ramp, through which displacement is transferred without actual physical linkage of the faults, in **e)** and **f)** the relay ramp has been breached by a fault that now connects the two initial faults and establishes a through-going fault surface.

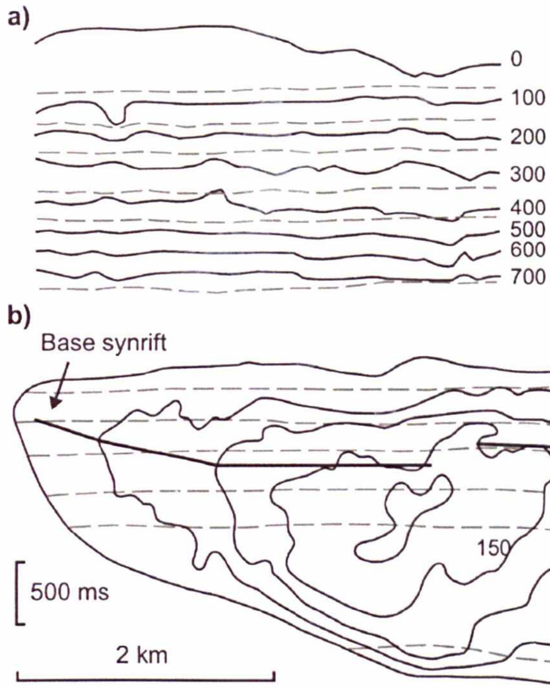

Fig. 2.5: Throw contours of **a)** a portion of the uppermost part of a large-scale (total fault length >10 km) normal growth fault (all horizons are syn-sedimentary with respect to this fault) and **b)** a medium sized fault showing closer throw contour spacing in the syn-faulting sequence from the Gulf Coast, USA (dashed lines: horizons, scale is valid for both examples) (redrawn after CHILDS et al., 2003).

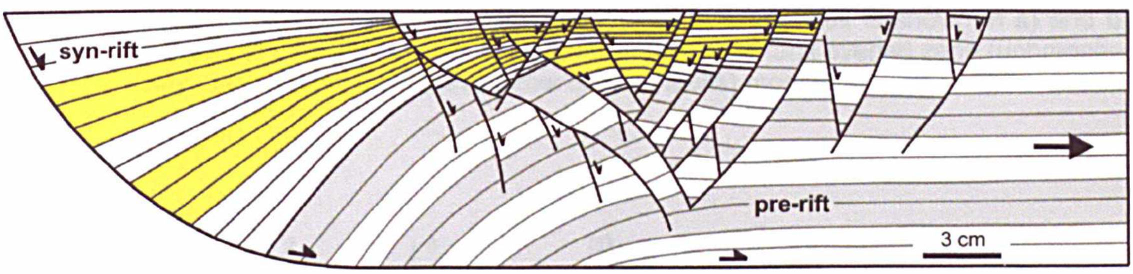

Fig. 2.6: Sandbox model of a simple listric fault (50% extension, arrow pointing to the right indicates extension direction) by McCLAY (1990) (redrawn), illustrating crestal collapse faulting within the rollover anticline and thickening of the syn-rift strata (white and yellow), which overlies the homogeneously thick pre-rift strata (white and grey, top marked by bold line) in the deformed hanging wall.

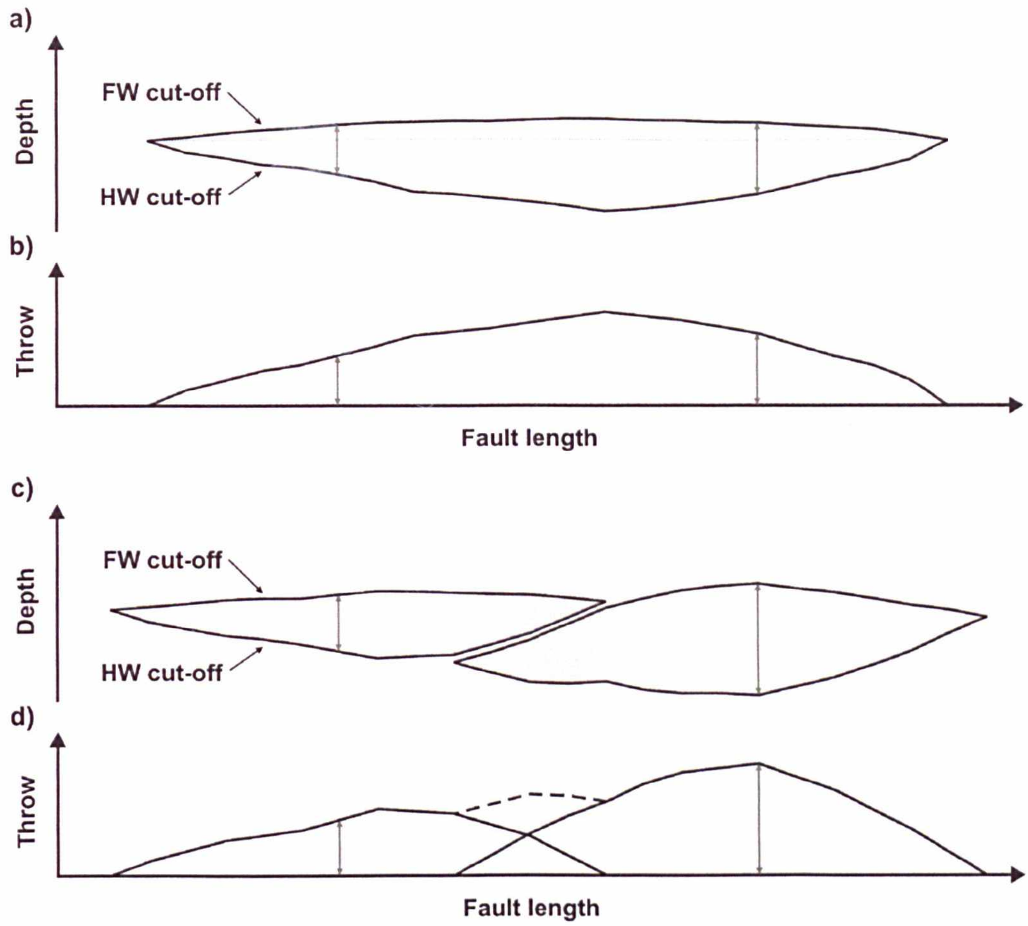

Fig. 2.7: Sketch illustrating the relationship between the footwall and hanging wall cut-offs and the resulting fault throw. An example for a single fault is shown in **a)** and **b)**, whereas **c)** and **d)** show the respective profiles for a fault overlap zone (unbreached relay, dashed line: cumulative throw on both faults) (compare to Fig. 2.4).

Fig. 2.8: **a**) Schematic diagram of fault throw vs. along-strike distance for four horizons intersected by a fault (oldest horizon: blue, youngest horizon: grey). **b**) Fault throw vs. horizon age diagram at the three positions indicated along the fault in a.

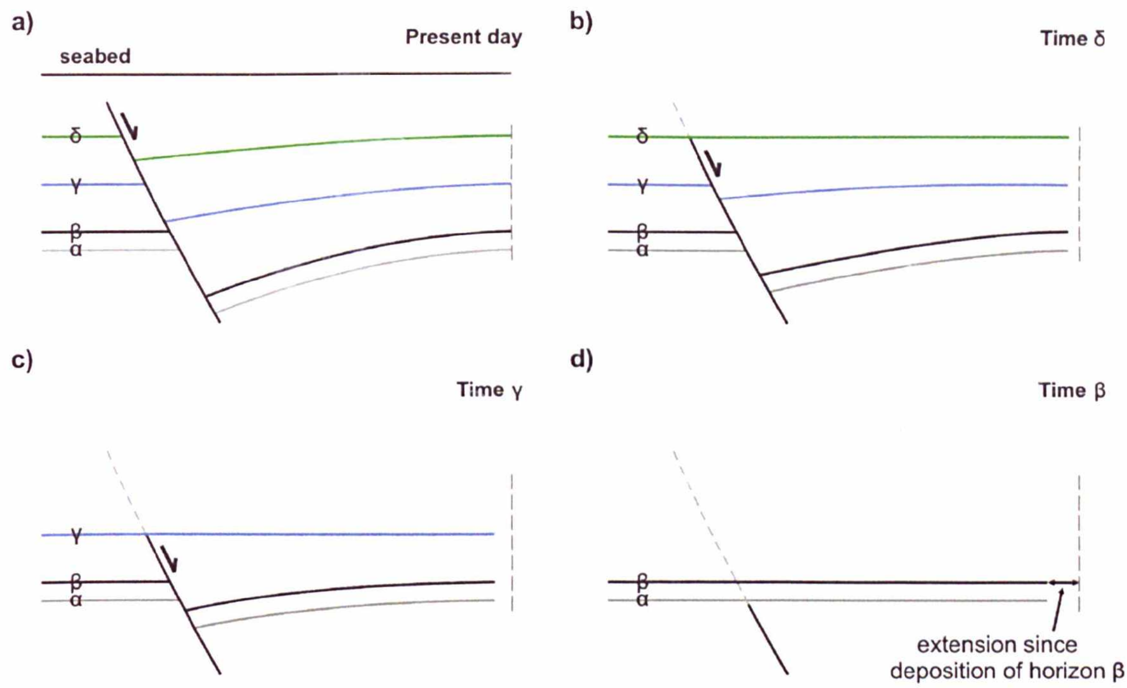

Fig. 2.9: Schematic diagram of the sequential reconstruction of fault throw and geometry on a syn-sedimentary fault. The present-day geometry is outlined in **a)**, where the fault is inactive and does not intersect the seabed. In **b)**, the displacement on horizon δ is removed and the throw distribution reconstructed for the time when horizon δ was the unfaulted (depositional) surface. Further removal of fault displacement shows in **c)** the geometry at time γ, and in **d)** the situation at time β. The interval between horizons α and β is characterised by homogeneous thickness of the strata in the FW and HW and thus this unit was displaced after deposition. The upper tip of the fault was at time β either below horizon α or the fault had not yet nucleated. Note the extension of the cross-section between time β and the present-day.

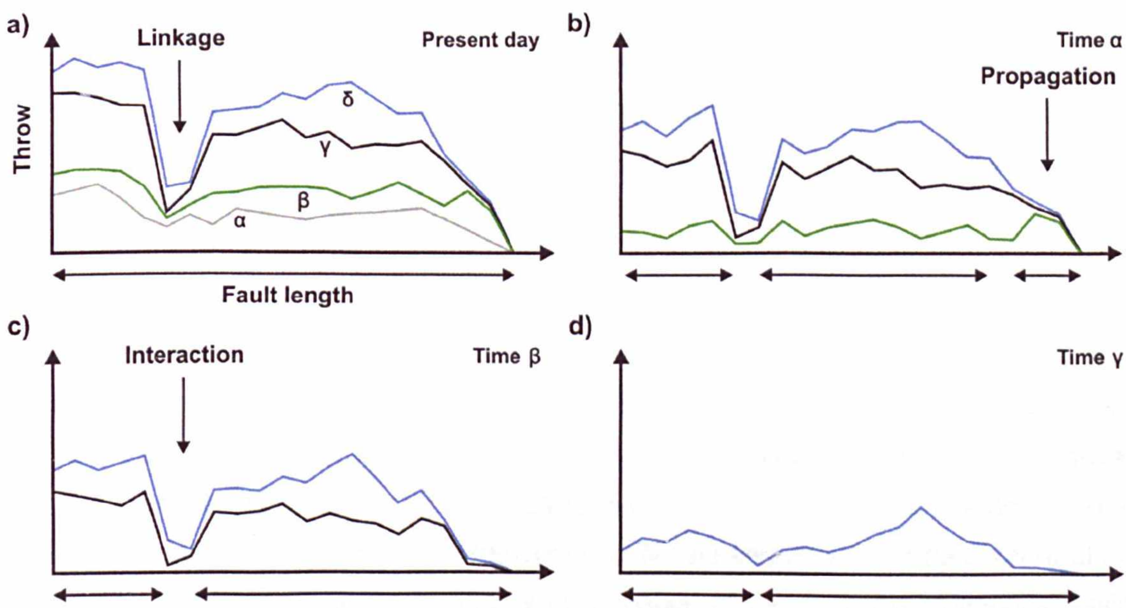

Fig. 2.10: Sequential back-stripping of fault throw along the fault trace, **a**) present-day throw distribution, **b**) fault throw on the youngest horizon (α) was removed, revealing the throw distribution when horizon α was the un-faulted surface, **c**) throw on the next youngest horizon (β) was removed, and **d**) the residual throw of the oldest time interval, when horizon γ was the un-faulted surface and horizon δ was displaced by two initial faults.

Chapter 3

Study area – Columbus Basin, Trinidad

3.1 Tectonic setting

The study area is the Columbus Basin (LEONARD, 1983), which is located SE off shore Trinidad on the South American shelf. The geology and tectonic setting of Trinidad and adjacent areas is complex due to the position at the dextral transform plate margin between the South American and Caribbean plates (Fig. 3.1). Trinidad and the Columbus Basin are situated on the South American Plate, which moves to the west relative to the Caribbean Plate. The southern margin of the Caribbean Plate north of Trinidad is a west-east trending dextral transform system (LEONARD, 1983) that terminates to the east in the north-south trending subduction zone of the South American plate under the Caribbean plate.
The Caribbean plate is largely formed by thicker-than-normal oceanic crust, the Caribbean plateau. The plateau was formed in the Late Cretaceous (ca. 90 Ma) in the vicinity of the present-day Galapagos hotspot in the eastern Pacific (KERR & TARNEY, 2005) (Fig. 3.2). Northeast-ward movement of the Farallon plate caused the plateau to collide with the proto-Caribbean arc and north-western South America (KERR & TARNEY, 2005). Progressive east-ward motion of the Caribbean plate led to its present-day position north of the South American plate (SYKES et al. 1982; KERR & TARNEY, 2005).

The tectonic regime at the Caribbean–South American plate margin has changed several times. From the Jurassic to Cretaceous, South America was located to the south of a broadly E-W trending passive continental margin (ALGAR & PINDELL, 1993). The subsequent advance of the Caribbean plate from the west since Oligocene times led to the development of the Caribbean-South American plate margin (Fig. 3.2), which is characterised by a Late Oligocene to Middle Miocene transpressional fold-and-thrust belt (GIBSON et al., in press). The East Venezuela Basin and its continuation to the east, the Columbus Basin, form the foreland basin to this deformed belt. This foreland basin evolved in a time-transgressive manner with the eastward motion of the Caribbean plate. The foreland basin subsidence in eastern Venezuela and Trinidad began in the Late Oligocene to Early Miocene (GIBSON et al., in press).

A change in relative plate motion at the Caribbean-South American margin from transpression to transtension led to cessation of thrusting in the foreland basins by Middle-Late Miocene times (GIBSON et al., in press). From then on, the plate margin evolved into a transform system with dextral strike-slip motion localized onto a few major fault strands off shore northern Trinidad (North Coast Fault Zone of ALGAR & PINDELL, 1993). Displacement transfer from the strike-slip system at the Caribbean-South American plate boundary southeast-ward to the deformation front of the Barbados accretionary prism during the Plio-Pleistocene enabled the formation of two pull-apart basins: the Gulf of Paria Basin and the Columbus Basin (GIBSON et al., in press) (Fig. 3.3a).

The Columbus Basin is bound to the north by the Darien Ridge, a major structural uplift that marks a change in structural style from thrust-dominated in the north to large-scale extension in the south (LEONARD, 1983; GIBSON et al., 2004). To the west and south of the basin, the Miocene-Pleistocene succession thins onto the shelf of the East Venezuela basin and the Amacuro continental-margin platform, respectively (GIBSON et al., 2004). To the east, the basin continues past the present-day shelf edge into deepwater regions of the continental slope (Fig. 3.3b).

The Miocene-Pleistocene strata of Trinidad and the Columbus Basin are affected by syn- to post-depositional, NW-SE striking extensional faulting, and NE-SW trending contractional folding and local thrusting (GIBSON et al., in press) (Figs. 3.3 and 3.4).

South-directed thrusting dominates the transpressional fold-and-thrust belt onshore Trinidad and continues off-shore east of Trinidad, where the Darien Ridge marks the southern limit of major transpressional tectonics (Fig. 3.3b) The extensional fault system is dominated by a series of large-scale NE-dipping listric normal faults (regional faults). These large-displacement faults (up to several kilometres) detach at depth into a near top-Cretaceous shale unit (GIBSON et al., in press), and are active in a regime of gravitational sliding and creep. Significant thickness variations across these normal faults characterises them as growth faults (Fig. 3.4). The geometry of the normal fault array varies in different parts of the basin (GIBSON et al., in press); in the south of the Columbus Basin (near and south of the Venezuelan border), extension is accommodated by a system of regional listric normal faults with large rollover anticlines in their hanging walls (Fig. 3.4b). Further north, the extensional system is bounded to the NE by large-displacement, SW-dipping (counter-regional) normal faults (Fig. 3.4c). These counter-regional faults reach the seafloor just down-dip of the present-day shelf edge and appear to be intersected and displaced at depth by the NE-dipping faults (Figs. 3.4c, d, e and 3.5) (GIBSON et al., in press; BEVAN, 2007).

A series of sub-parallel, SW-NE-trending anticlines, which formed during the early Pleistocene (SYDOW et al., 2003) and are related to shortening of the shelf domain (GIBSON et al., in press) are present across the basin (Fig. 3.3b). The anticlines are more significant in the NW of the basin with amplitudes generally decreasing from NW to SE. Constructive interference between the extensional roll-over anticlines and the contractional anticlines created closures for major petroleum reservoirs (GIBSON et al., in press).

The study area is located in the southern Trinidadian sector of the basin, ca. 10 km north of the Venezuelan border (Fig. 3.3b). The position of the study area has been chosen in order to minimize the occurrence of compressional tectonics and strike-slip faulting, and to provide a genuine dip-slip faulting province for the investigation of extensional growth faults. The 3D seismic survey covers three regional, large-displacement block-bounding normal faults, the Cassia Fault, the G Fault and the H Fault, and several other synthetic and antithetic faults (Figs. 3.3b, 3.4d, and 4.2). In total ca. 140 faults were mapped.
Seismic data do not allow the sense of movement (e.g. dip-slip or oblique-slip) on a normal fault to be assessed directly. In the Columbus Basin, the elongated nature of the fault blocks make assessment of a possible strike-slip component on the normal faults very difficult. The fault network mapped in the seismic dataset provides, however, evidence for the assumption of dip-slip faulting in the study area. Dip-slip movement is strongly suggested by a number of observations: (1) multiple sets of conjugate faults in cross-section with sub-horizontal lines of intersection and consistent down-dip separation of the strata across faults, (2) dominantly sub-vertical oriented branch lines in fault overlap zones and between faults and subsidiary splays, and (3) fault dips of generally 65-45° with increasingly listric geometries (dip angles below 40°) for large-scale faults at depth.
No independent evidence for strike-slip movement was found. In the upper parts of the seismic survey (above ca. 600 m), a small number of channels could be identified. However, none of them cross-cut any of the major faults. Fault **d** in its uppermost part (ca. 490 m depth) is intersected by a channel that does not show any lateral offset across the fault, which could be attributed to a component of oblique slip on this fault. However, at this level fault **d** has a throw of less than 20 m and any component of oblique slip would be most likely below the seismic resolution and thus probably unrecognisable. Within the dataset, no sign of thrusting or reverse faulting was found.

3.2 Basin evolution

The Columbus Basin formed in the Miocene as a foreland basin overlying a Cretaceous-Early Tertiary passive continental margin, and evolved into a thin-skinned pull-apart basin during Plio-Pleistocene times (GIBSON et al., in press). A detachment near the top of the passive margin strata (near top Cretaceous) structurally decouples this from the late Oligocene-Pleistocene basin fill (GIBSON et al., 2004; BEVAN, 2007). Since Late Miocene times, siliciclastic sediments input from the prograding Orinoco River delta were deposited in the Columbus Basin (GIBSON et al., in press). The progradational sequence consists of interbedded mudstones and poorly consolidated sandstones (WOOD, 2000), which in thickness locally exceeds 9 km (GIBSON & DZOU, 2004).

Large-scale growth faults influence the sediment distribution within the Columbus Basin. SYDOW et al. (2003) describe the reservoirs present in the Southeast Galeota (SEG) Structural Complex, which is located within the study area, as classic prograding delta successions. These deltaic reservoirs were deposited on the outermost shelf to shelf-edge (SYDOW et al., 2003) by so-called shelf-edge deltas. The great thickness (90-150 m) and large number of stacked reservoir intervals are attributed to extremely rapid subsidence of the Columbus Basin growth fault province. Since Middle Miocene times, the NW-SE-trending shelf edge steadily prograded from within on-shore Venezuela to its present-day position 150 km off-shore the modern Orinoco River delta (SYDOW et al., 2003) (Fig. 3.3b).
Figure 3.5 shows a reconstruction of the evolution of extensional faulting across the Columbus Basin since the Pliocene. According to BEVAN (2007), deformation in the Columbus Basin is controlled by early counter-regional and late regional extensional faults. The counter-regional faults form first and their footwall blocks slide basin-ward on the basal detachment. The regional faults take over activity when the rollover into the counter-regional faults causes increasing dips of the HW strata and fault slip becomes blocked. The regional normal growth faults in the Columbus Basin have been activated sequentially from west to east (see thickness changes in Fig. 3.5; GIBSON et al., in press) in close association with the prograding shelf edge (SYDOW et al., 2003). The growth history of each fault starts very rapidly and tapers off as the next seaward growth fault becomes active (SYDOW et al., 2003). The counter-regional faults deform predominantly slope muds, reaching the seafloor down-dip of the shelf-edge at any time. The regional faults appear to be associated with the progradation of sand-dominated shelf systems (BEVAN, 2007). The total extension across the Columbus Basin since Middle Pliocene times was estimated by GIBSON et al. (in press) to about 30 km. More recently, BEVAN (2007) suggested 40-50 km.

In the study area, mud-rich sediments of the outer shelf and slope are overlain by sandy sediments of the prograding delta plain and delta front as shown in Fig. 3.6a. This facies model was generated by BP Trinidad & Tobago using TEMIS 3D basin modelling software and it is based on data from numerous wells. At the level of horizons TP60 and TP80 for example, a SW-NE transition along the paleo-shelf from delta plain to outer shelf and slope can be observed, which corresponds to a change from sand-rich to shale-rich lithologies.
Pore fluids within sedimentary units can either be hydrostatic, in which case the fluids at depth are in correspondence with meteoric water, or over-hydrostatic. Over-hydrostatic pore fluid pressures generally arise as a result of rapid burial of low permeability lithologies, especially shales, because the pore fluids can not be expelled at the same rate as the overburden increases (GILES, 1997). In the Columbus Basin, pore fluid overpressure occurs, but the zone is confined to shale-rich lithologies at depth, usually below 2.5 km in the study area, and shows no correlation with the stratigraphic position of a sedimentary unit, e.g. TP60 and TP80 (Fig. 3.6).

3.3 Figures

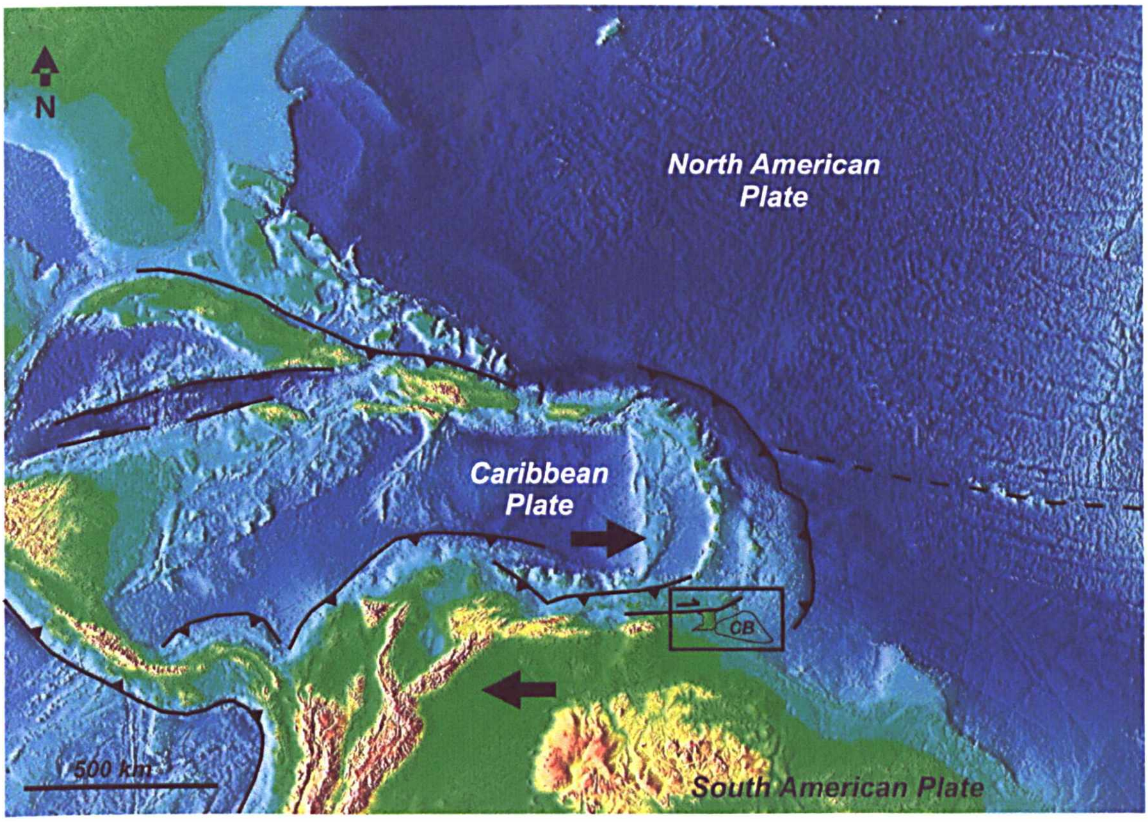

Fig. 3.1: Large-scale tectonic overview of the Caribbean-South American plate margin (after DUERTO & MCCLAY, 2002). The location of the Columbus Basin (CB) is indicated.

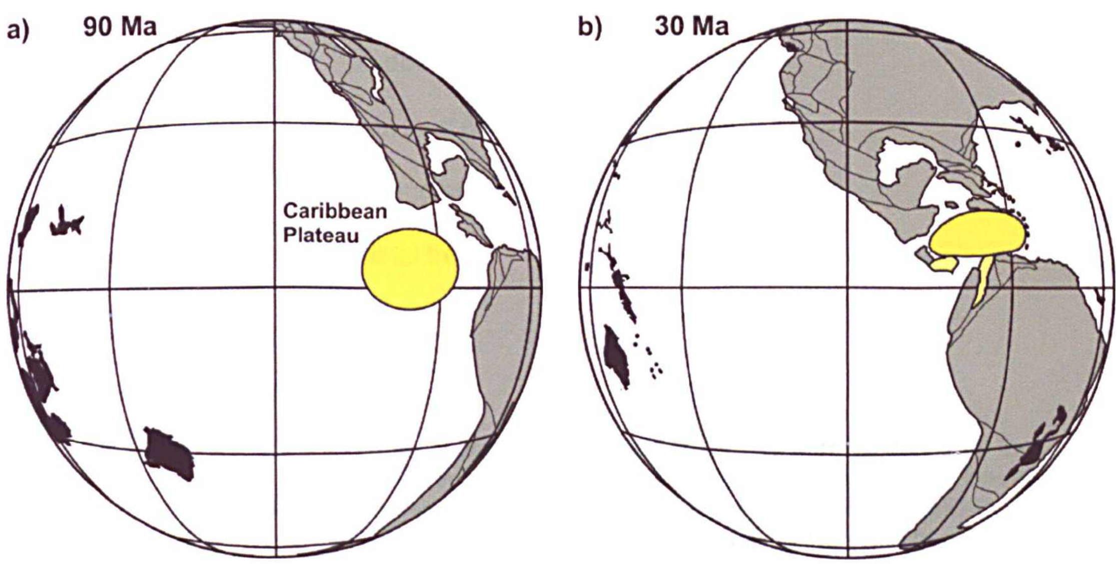

Fig. 3.2: Plate tectonic reconstructions showing the position of the Caribbean Plateau relative to South America at **a)** 90 Ma and **b)** 30 Ma (redrawn after SCHETTINO & SCOTESE, 2000, in KERR & TARNEY, 2005). Other Pacific Cretaceous oceanic plateaus are shown in black.

a)

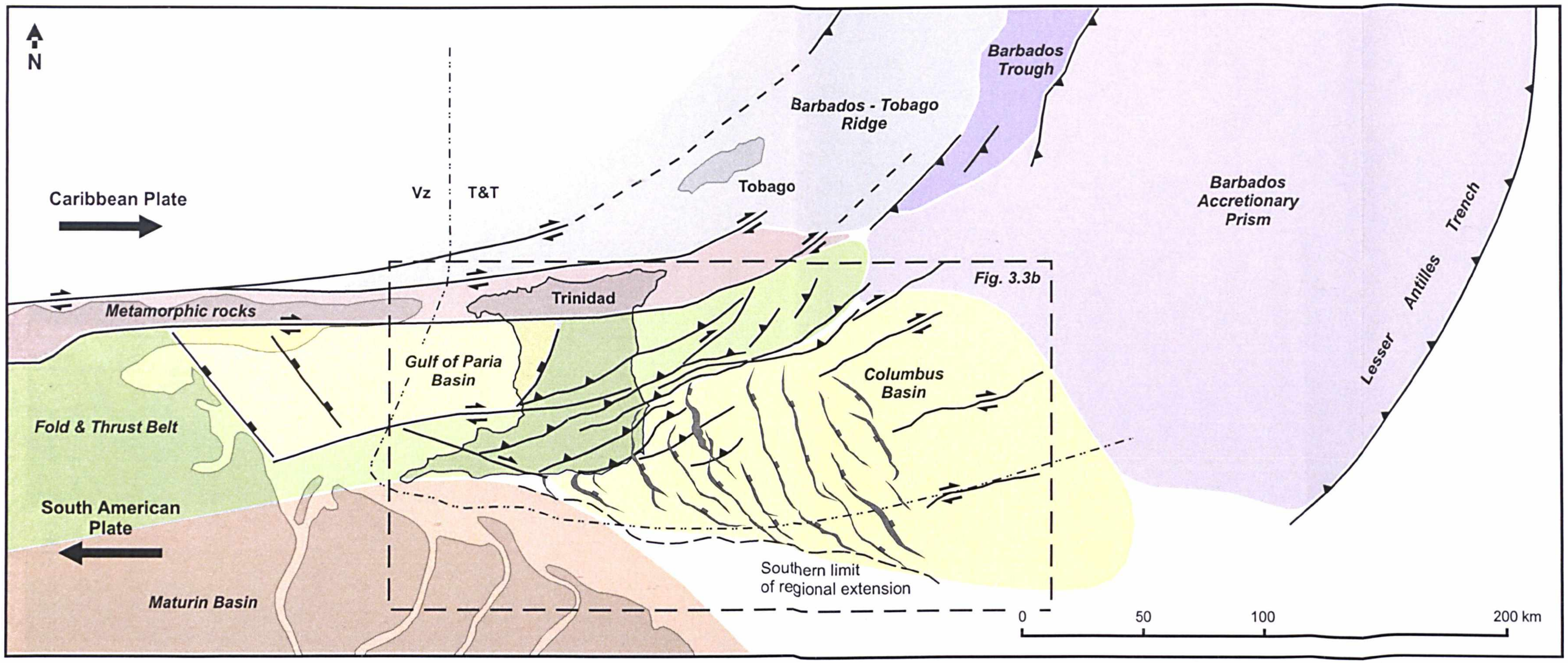

b)

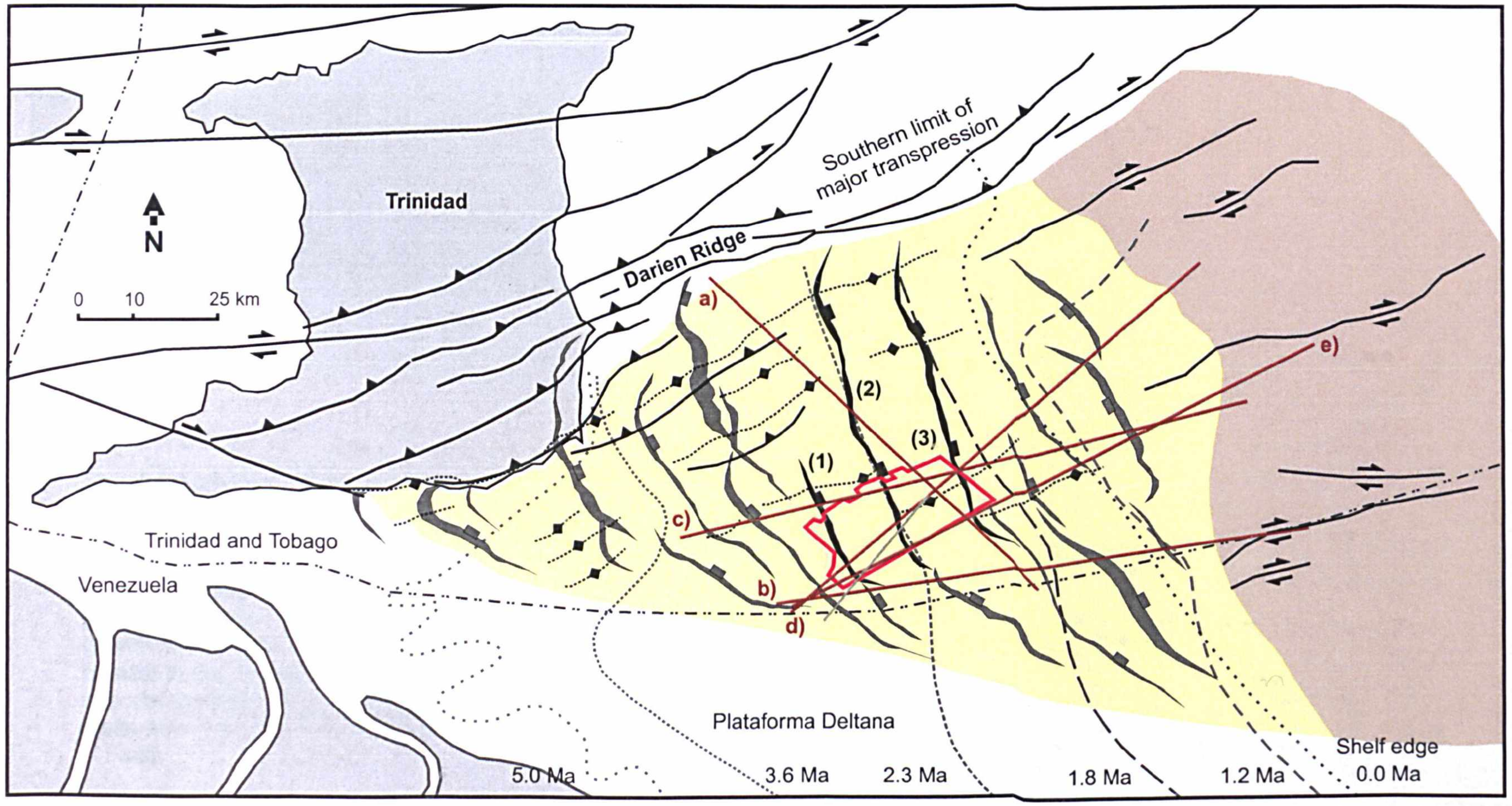

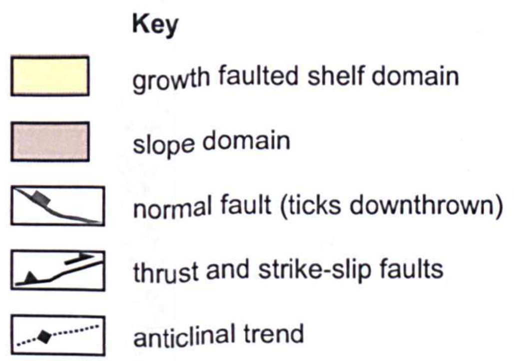

Fig. 3.3: **a)** Map showing Trinidad and the Columbus Basin in the regional context of the transtensional Caribbean - South American plate margin to the north of Trinidad and the subduction zone to the northeast. **b)** Detailed map of the Columbus Basin with the location of the study area (red) and the structural cross-sections (bordeaux, Fig. 3.4), the facies model and pore fluid pressure section (khaki, Fig. 3.6), as well as the migrating position of the shelf edge during the Pliocene and Pleistocene. (1) Cassia Fault, (2) G Fault, and (3) H Fault. Both figures are based on maps by GIBSON et al. (in press), BEVAN (2007), WOOD (2000) and ALGAR & PINDELL (1993).

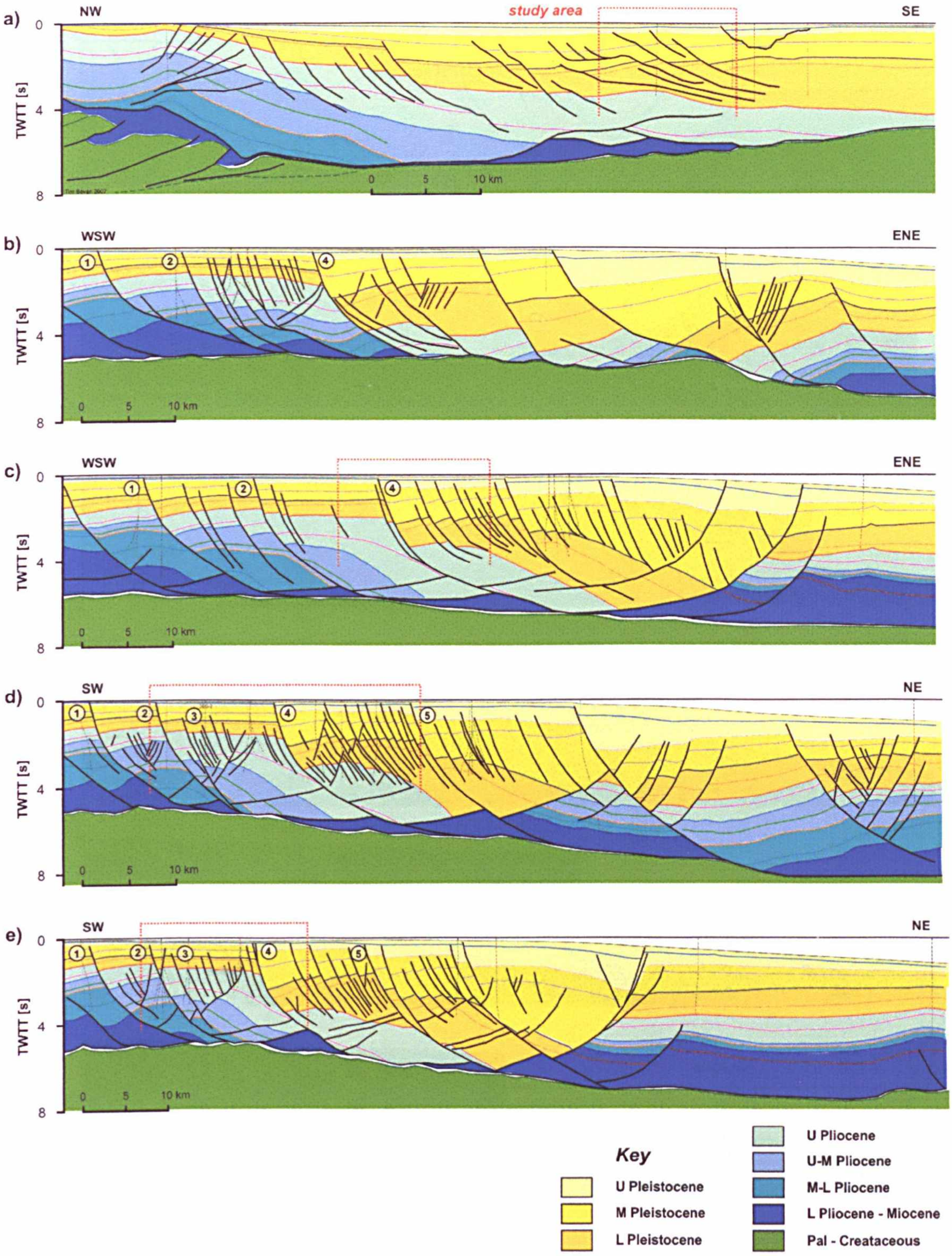

Fig. 3.4: Structural cross-sections across the Columbus Basin by Bevan (2007) as shown in Fig. 3.3, illustrating the variation of deformation style in different parts of the basin: **a)** Strike-section showing the compressional structures in the north of the basin, **b)** section to the south with a series of domino blocks and roll-over into the NE-dipping faults, **c)** section to the north of the study area showing a series of regional (NE-dipping) faults and large-scale counter-regional (SW-dipping) faults bounding the growth strata to the NE, **d)** section across and beyond the study area, and **e)** section parallel to the southeastern border of the study area, for which Fig. 3.5 shows a sequential reconstruction of faulting and the deposition of growth packages. Numbered faults are: (1) Claro Fault, (2) Cassia Fault, (3) Ironhorse Fault, (4) G Fault, and (5) H Fault.

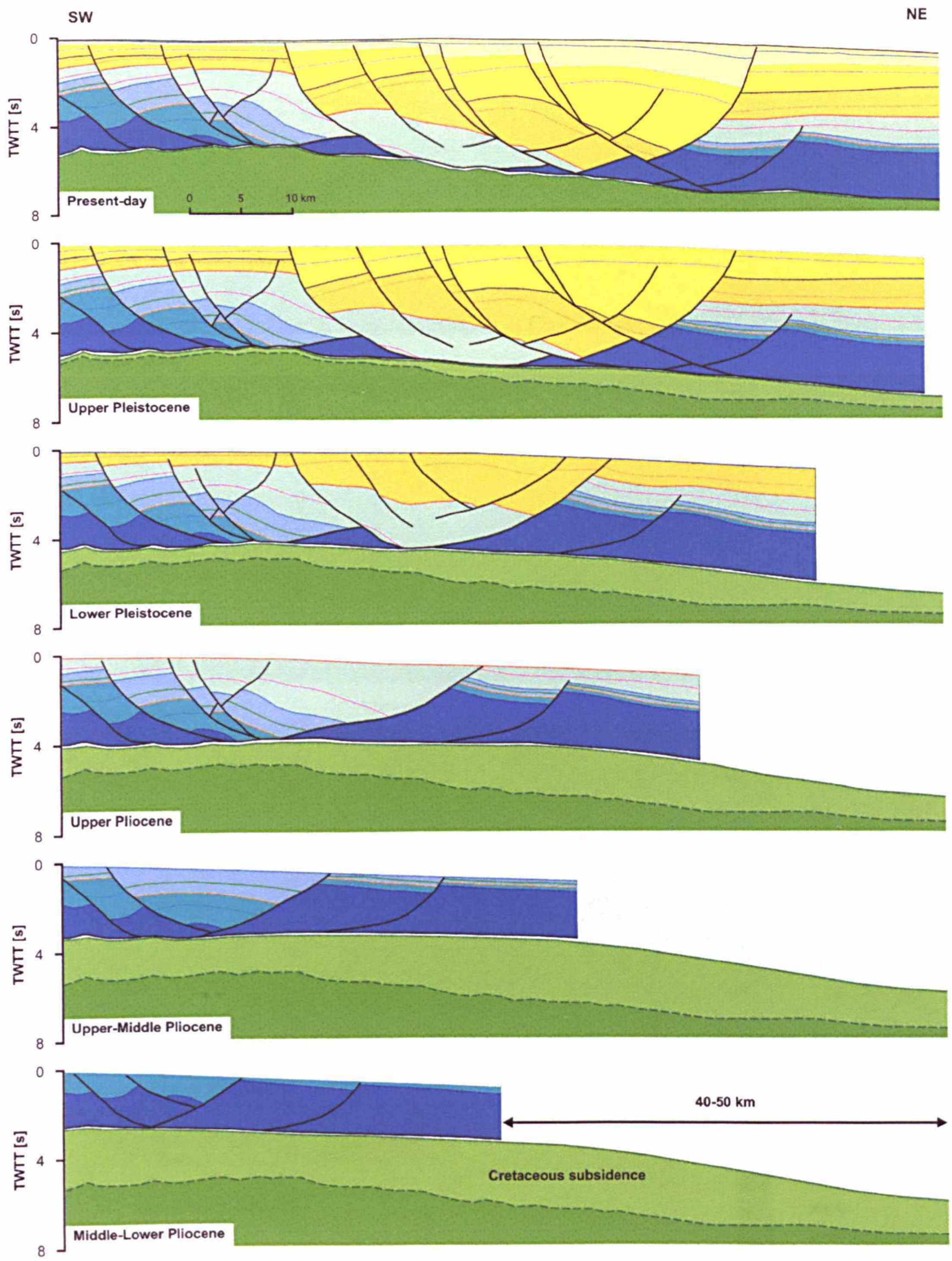

Fig. 3.5: Reconstruction of the evolution of the regional (NE-dipping) and counter-regional (SW-dipping) faults in the Columbus Basin by BEVAN (2007). The cross-section is simplified after section e) in Fig. 3.4. Note the thickness variations associated with fault movement and the total extension since Middle Pliocene times. For legend see Fig. 3.4.

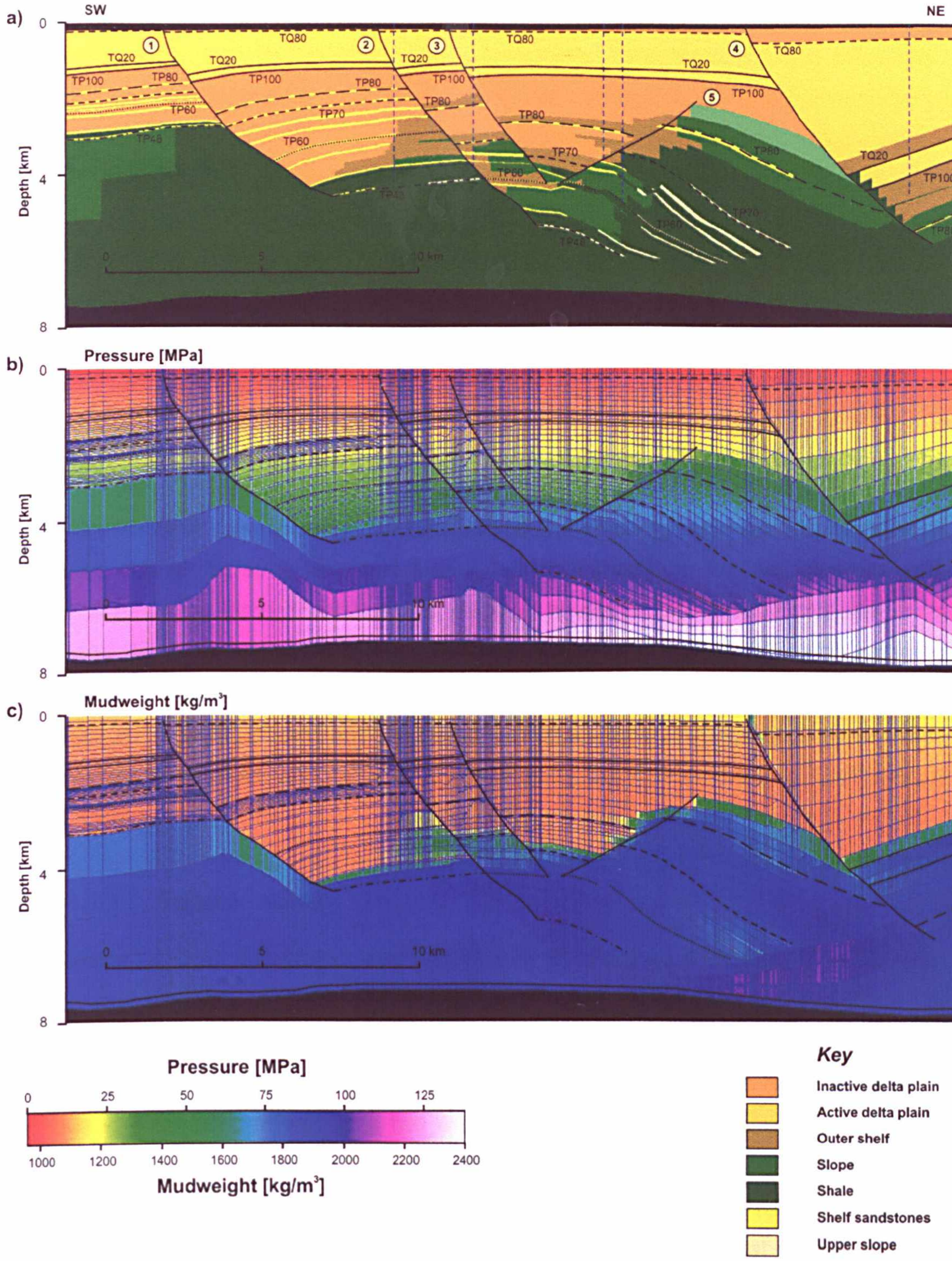

Fig. 3.6: Cross-section covering the study area, illustrating in **a)** the facies distribution in the study area and its vicinity, and in **b)** and **c)** the pore fluid pressure as modelled by BP Trinidad & Tobago with TEMIS 3D basin modelling software. The pore fluid pressure is shown in b) as absolute pressure [MPa], and in c) as the density of the mudweight [km/m^3] (fluid column in wells) that is required to equal the pore fluid pressure at the bottom of wells. Mudweights of around 1000 km/m^3 indicate hydrostatic pore fluid pressures; higher values indicate various degrees of pore fluid overpressure. Note the abrupt and steep increase in pore-fluid pressure in c) from hydrostatic (red-orange) in the more sandy lithologies (delta plain) to highly overpressured (blue) in the mud-rich facies (outer shelf and slope). Numbered faults are: (1) Claro Fault, (2) Cassia Fault, (3) Ironhorse Fault, (4) G Fault, and (5) A4 Fault.

Chapter 4

Methodology

4.1 3D Seismic dataset

Three-dimensional seismic reflection data are vital for sub-surface imaging of geological structures and stratigraphy, and are widely used in exploration for hydrocarbons and in academic basin research. Over the past decade, advanced 3D seismic processing algorithms and rapid innovations in computer-based visualisation and interpretation technology have allowed detailed stratigraphic imaging and the interpretation of complex geological structures such as salt domes and fault systems. These data also enable the interpreter to track horizons and faults and calculate seismic attributes in real time (e.g. CARTWRIGHT & HUUSE, 2005).

4.1.1 Seismic survey

The dataset used for this project was provided by BP Trinidad & Tobago. The 3D seismic survey was acquired in 1998 and reprocessed using "3DDMO-based Pre-Stack Time Migration" (YILMAZ & DOHERTY, 1987) in 2003. The dataset covers an area of ca. 400 km^2 (Fig. 4.1a). The vertical axis of the original survey is in time, with data recorded down to 7 seconds at a sampling rate of 4 ms two way travel time (TWTT). Seismic lines are spaced at 12.5 m, but only every second line is available in the seismic file, increasing the effective line spacing to 25 m. The frequencies of the seismic waves recorded range from 2-75 Hz, with a useable bandwidth of 8-60 Hz, resulting in a maximum horizontal resolution of about 10 m and a minimum bed thickness resolvable of 10 m at depths of 2-4 km (BROWN, 2003). For known seismic velocities of 2.3 km/s at 1.5 km and 3.3 km/s at 3.0 km depth, the sampling interval of 4 ms TWTT limits the vertical resolution to 4.6 m and 6.6 m, respectively.

4.1.2 Seismic interpretation

The interpretation of faults and horizons in the seismic dataset was carried out with SeisWorks® and GeoProbe® software (Fig. 4.2a). An initial horizon grid with data points on every fault block was mapped in SeisWorks®. Alongside the horizon interpretation, faults were generally mapped on every 10th line (spacing 125 m), in areas of very complex geometries such as linkage and splaying also on every line (spacing 25 m). The horizon grid and fault network were then transferred to GeoProbe® to auto-track the remaining horizon surface along the respective reflectors. Settings for this procedure were chosen to stop tracking at the mapped faults, which prevents the interpretation from continuing across the fault. In SeisWorks®, these horizon surfaces were smoothed using a 5x5 cell size moving average algorithm that weights all points equally regardless of their distance from the central point. This smoothing was carried out in order to minimize noise and minor surface irregularities on the horizons before importing the data to TrapTester® for throw extraction (see Section 4.2).

4.1.3 Depth-conversion

Based on a regional three-dimensional seismic velocity model provided by BP Trinidad & Tobago, the entire seismic dataset, as well as all mapped horizons and faults, were depth-converted using TDQ (OpenWorks®) (Fig. 4.2b). The 3D velocity model incorporates data from 106 wells, but it is not calibrated for pore fluid overpressure. Typically, the calibration of the velocity model matches the extent of the checkshot survey or the total depth of the well, below which an extrapolated value was used to calibrate to the base (7 seconds) of the survey (C. ELIGON, 2007, personal communication). As can be seen in Fig. 4.2c, the acoustic velocities increase steadily from about 1.8 km/s at shallow levels to 3.4 km/s at deeper levels. In the hanging wall of the G Fault the higher velocities are generally reached at a deeper level than in its footwall. This might be due to the sediments in the hanging wall being significantly younger and therefore compaction has affected the strata for a shorter duration. On the other hand, the older sediments in the footwall have been subjected to compaction and hence reorganisation of grain packing, reorientation of clay minerals and escape of pore fluids for a longer time. This might have led to increased acoustic velocities of rocks at the same depth in the footwall compared to the hanging wall. Below ca. 4 km depth, local variations with lenses of higher or lower than surrounding velocities occur. Depth-conversion transforms the vertical axis from sampling time to true vertical depth and thus permits visualisation and investigation of the true geometries, dips and thicknesses of geological units, and measurement of throws and thicknesses in meters.

4.1.4 Horizons and well ties

Together with the seismic dataset, 14 wells with ties to biostratigraphically dated marker horizons were provided by BP Trinidad & Tobago. Within the dataset, 16 horizons, all tied to wells, have been mapped and cover a sedimentary sequence between 2.78-0.27 Ma (Table 4.1). Of the 14 wells used, four are located in the footwall of the Cassia Fault, six in the fault block between the Cassia and G faults and four between the G Fault and the H Fault (Fig. 4.1a). The initial horizon grids were correlated in loops between several wells and then expanded to the extent of the survey. Horizon picks in the hanging wall of the G

Fault could neither be traced from the provided wells due to poor quality of the dataset in between the fault and the well locations, nor mapped across the fault due to the very high displacement on it. However, BP Trinidad & Tobago have mapped a number of key horizons regionally around the tips of the G Fault and also correlated them with well data not available to this investigation. Therefore, these essential horizon picks were taken directly from the BP Trinidad & Tobago horizon data base.

Table 4.1: Horizon picks and ages available to this project in the survey area, provided by BP Trinidad & Tobago (horizon ages in bold are reliably biostratigraphically dated, unbold horizons are less reliably dated, and those interpolated between neighbouring horizons are in italics, see below). Horizons TP60 and TP90 have been included for reference but were not mapped in this study.

Horizon	Age (Ma)
TQ80	0.27
TQ68	*0.51*
TQ65	0.56
TQ60	0.82
TQ50	1.10
TQ40	**1.26**
TQ30	1.46
TQ20	**1.59**
TP100	1.71
TP97	*1.78*
TP95	*1.83*
TP90	**1.95**
TP88	*2.07*
TP85	2.30
TP80	**2.46**
TP77	*2.56*
TP70	2.78
TP60	3.45

4.1.5 Horizon ages

Horizon ages are based on calcareous nannoplankton species, which require fully marine conditions. However, the large influx of freshwater from the Orinoco Delta makes survival of the nannoplankton on the shelf difficult, whereas seaward of the progressively migrating shelf edge, conditions will have been good (R.W. Jones, 2007, personal communication). Additionally, the exceptionally high sedimentation rates of siliciclastic sediments in the Columbus Basin (Chapter 3) hinder preservation of the fossils. The biostratigraphical dating was mainly carried out for fully marine sequences beyond the present-day shelf edge and correlated onto the shelf based on lithological considerations. Certain horizons of the Columbus Basin strata are confidently dated within a world-wide framework (e.g. J. Young, unpublished) (Table 4.1). Other horizons are locally dated in the Columbus Basin. In order to establish a reasonable horizon age chart for all horizons considered in this study, the depths of horizon picks in well A were plotted against their ages, which determines the sedimentation rate. Horizon picks from both the BP Trinidad & Tobago database and ones mapped in this study were used. The BP picks only cover the time interval from TP60-TP100 and the younger event TQ40. The additionally mapped horizons complete the stratigraphic section from TQ20 to TQ80. Well A was chosen because it is located in the most landward position within the dataset in the footwall of the Cassia Fault (Fig. 4.1a) and thus thickness variations due to fault-related subsidence should be minimal. However, the fault block containing well A forms the hanging wall to the regional Claro Fault (Fig. 4.1b), which is located to the west of the Cassia Fault outside the study area and was most active during the interval TP50 (3.45 Ma) to TP70 (2.78 Ma) (approximately doubled thickness of the strata in the HW in a time section) and showed continued major activity until ca. TP100. The steep increase of sedimentation rate observed in Fig. 4.3 between ca. 2.5-3.5 Ma is thus attributed to the creation of accommodation space due to activity of the Claro Fault. Well A is located on the distant edge of the hanging wall block of the Claro Fault and there the influence of fault movement, evident through increased thickness of the growth wedge on the hanging wall, after ca. TP80 is minimal compared to the thickness in the Claro footwall. Hence, the influence of fault activity of the Claro Fault (creation of fault-related subsidence) after deposition of TP80 is considered negligible for the plot of horizon age vs. depth at the location of well A.

In order to derive a smooth sedimentation rate curve (J. SYDOW, 2007, personal communication), the available horizons ages were grouped according to their reliability (Figs. 4.3b&c). The ages constrained by recent world-wide correlations (TP80, TP90, TQ20, and TQ40) (J. YOUNG, unpublished) were inserted first and complemented by reliable locally derived dates (TP60, TP70, TQ60, TQ65, and TQ80). Only then, less reliable local dates (TP85, TP100, TQ30) (R.W. JONES, 2007, personal communication) were entered and shifted if necessary. Eventually, the missing dates for horizons not dated in the BP Trinidad & Tobago chart were linearly interpolated between neighbouring horizons.

The resulting graph (Fig. 4.3c) honours all reliable biostratigraphic dates and provides a smooth sedimentation rate curve. Processes other than fault-related subsidence that could influence the available accommodation and, therefore, the sedimentation rate are sea-level changes (glacial eustacy) or climate changes (e.g. increased precipitation in the hinterland and increased influx of sediments into the basin). These are not explicitly incorporated in the best-fit sedimentation-rate curve.

The error bars of the horizon ages vary according to the reliability of the biostratigraphic dating. Horizons TP80, TP90, TQ20, and TQ40 have errors of ±0.05 Ma, whereas all other horizons have errors of ±0.10 Ma. The error bars of the time intervals between horizons are estimated to be ±0.05 Ma.

4.2 TrapTester

TrapTester® is a fault modelling and seal analysis toolkit developed by Badley Geoscience Limited. Beside many other functions, TrapTester® imports seismic interpretations (e.g. horizons and faults) from common software packages and allows creation of fault-fault and horizon-fault intersections within a 3D visualisation environment. The software can be used to build a coherent 3D model of the geometry and interaction of stratigraphic horizons and faults. For this project, TrapTester® was used to calculate, plot and export the throw on several horizons intersected by faults of interest.

The fault displacement data has been sampled in TrapTester® using the "1-D line sampling" technique which uses a regular sampling grid. Displacement data is measured at the points where the sample lines cross the fault polygons (i.e. cut-off lines) and the vertical component of it represents "apparent" throw values (BADLEY GEOSCIENCE LIMITED, 2007). The sampling grid was oriented parallel to the seismic traces, which run nearly perpendicular to the majority of faults in the study area (Fig. 4.1). Thus the difference between "apparent" throw and "actual" throw is negligible. Therefore, for reasons of brevity, "apparent throw" will be referred to as "throw" throughout this document. Use of the "1-D line sampling" grid enables precise positioning of the measured throw values in the study area (i.e. in the seismic survey) and allows comparison of, and further calculations between, the data of neighbouring faults.
To determine the amount of throw on a horizon displaced by a fault, TrapTester® creates a fault surface based on the imported fault interpretation either by triangulating or gridding. For the throw calculation, two distances on either side of the fault surface must be defined on each horizon grid: 1) the trim distance (adjacent to the fault) and 2) the patch width (Fig. 4.4a). The trim distance is the area on each side of the fault within which data will be ignored during calculations due to a lack of confidence in the data quality close to the fault or to minimize the influence of local variations such as normal or reverse drag. The patch width is the area of the horizon grid to which the horizon surface will be fitted and used for throw calculation. The dip of this surface is then projected towards the fault plane. The intersection lines between these projected surfaces and the fault plane mark the position of the footwall and hanging wall cut-off lines. From these footwall and hanging wall cut-off lines the throw is calculated at a user-defined along-strike spacing. These data can be visualised as throw contours on the fault surface as well as throw vs. distance plots within TrapTester® and exported as ASCII files for further calculations.

The throw data exported from TrapTester® for the Trinidad 3D seismic dataset show high frequency undulations of varying wavelengths and amplitudes superimposed onto the general data trend. In order to determine whether these undulations are artefacts of the method TrapTester® applies, which is dependent on the user settings used, or reflect actual structural variations, throw data for different TrapTester® settings (trim distance and patch width) and horizon input data (10x10 lines manually mapped grid, auto-tracked, smoothed auto-tracked) have been compared to manually picked throw data (Fig. 4.5 and Table 4.2). This comparison was carried out for three horizons at different depths (TP80, ca. 3 km, TP100, ca. 1.5 km, and TQ60, ca. 0.5 km, see Fig. 4.2 and Table 4.1) to evaluate the influence of the TrapTester® settings on the throw measurements and to further test whether any variations in the wavelengths and amplitudes of these undulations might be related to the quality and resolution of the seismic data with depth.

Table 4.2: List of the properties of the input horizon data (auto-tracked, smoothed) and TrapTester® settings (trim distance, patch width) compared in Figure 4.5. Each of these graphs was plotted for each of the input horizons (TP80, TP100, and TQ60). "Optimum" lists the preferred horizon properties and TrapTester® settings to achieve accurate throw measurements (see text).

Graph	auto-tracked	smoothed	trim distance [m]	patch width [m]
a (light grey)	–	–	100	300
b (dark grey)	✓	–	100	300
c (yellow)	✓	✓	100	100
d (blue)	✓	✓	100	300
e (light blue)	✓	✓	300	300
f (ruby red)	✓	✓	50	200
optimum	✓	✓	**50-100**	**100-300**

On visual comparison, the TrapTester® curves (Fig. 4.5)

- with the largest trim distance (curve **e**) are over-smoothed for all horizons and do not follow the data trend,
- of all other smoothed auto-tracked input data (curves **c**, **d**, **f**) give a very good correlation with the manually picked throw curve, and
- the manually mapped horizon grid and the auto-tracked horizon (curves **a** and **b**) show generally higher amplitudes of the undulations and lower throw values than the graphs of smoothed, auto-tracked, input data.

The three best-fitting curves (curves **c**, **d**, **f**) and the hand-picked data all detect the same undulations and turning points between upwards and downwards trends in the data and mainly vary in the displayed amplitude of the undulations, which is on the TrapTester® curves rather greater than on the hand-picked data. This suggests that, for this high-quality seismic dataset,

- narrow trim distances of 50 m or 100 m are essential, and
- patch widths should range from 100 m to 300 m, but are less sensitive.

The narrow patch width of 100 m is sufficient to capture the lateral geometry of the horizons for the projected horizon-fault intersection well due to the even initial geometry of the horizons mapped on this high-quality seismic dataset and the additionally applied smoothing.

The generally lower throw measured on the auto-tracked but not smoothed horizon and the horizon grid indicates that the horizon input data should preferably be auto-tracked (include all available data points) and that gentle smoothing has a positive influence on the accuracy of the results.

In order to determine the best fit between the three curves with optimal settings (curves **c**, **d**, **f**) and the manually picked throw data, the root mean square deviation (RMSD) was calculated for each pair of compared curves. The root mean square deviation between the manually picked and TrapTester® derived throw data is smallest for a trim distance of 50 m and a patch width of 200 m (Table 4.3). In addition, the root mean square deviation between each TrapTester® setting and the respective manually picked data is always highest for the deepest horizon (TP80) and lowest for the shallowest one (TQ60) (Table 4.3). This suggests a systematic decrease of vertical resolution within the seismic dataset.

Table 4.3: Comparison of the root mean square deviation (RMSD) between the manually picked throw data along the Ironhorse Fault and the curves with optimal input (smoothed and auto-tracked) and TrapTester® settings (Table 4.2). Note that trim distance and patch width of 50 m and 200 m fit best with the exception of the 100 m and 100 m setting for horizon TP80.

		TP80			**TP100**			**TQ60**	
	(c)	**(d)**	**(f)**	**(c)**	**(d)**	**(f)**	**(c)**	**(d)**	**(f)**
Trim distance [m]	100	100	50	100	100	50	100	100	50
Patch width [m]	100	300	200	100	300	200	100	300	200
RMSD [m]	8.8	12.1	**9.7**	5.1	5.3	**4.2**	3.7	3.8	**3.1**

The throw data extraction in this study was hence carried out using trim distances of 50 m and patch widths of 200 m, which best reflect the real data after comparison with manually determined throw measurements (Table 4.3). Smoothing of 5x5 equally weighed cells was applied to all auto-tracked horizon surfaces prior to importing them into TrapTester® to reduce noise in the TrapTester® reading (Fig. 4.5 and Table 4.3). The throw data were sampled in TrapTester® at a constant sample line spacing of 50 m with the sample lines being parallel to the seismic traces, which themselves are nearly perpendicular to most of the faults in the dataset.

The interpolation of the horizon surface onto the fault plane works well for relatively smooth and undisturbed shallow horizons. However, problems occur at greater depth due to the presence of small faults in either the HW or FW of the fault of interest that cause gaps in the horizon interpretation (Fig. 4.4b). For the applied settings of trim distance and patch width, some patches cross gaps in the horizon or are missing completely for a limited distance. If a patch is interpolated across a gap with the horizon at different heights on each side, anomalous dips may be generated, which result in inaccurate throw determinations. Areas where this problem occurs have been identified and manual throw measurements of the same spacing were incorporated into the TrapTester®-derived data in order to correct for this error.

The good correlation between manually picked and TrapTester®-measured throw data as demonstrated above excludes the algorithm applied by TrapTester® as the source of the high-frequency undulations that are superimposed onto the general throw trend (Fig. 4.5). Possible other reasons for the presence of these undulations are varying drag (normal or reverse) along the strike and dip of the faults, factors associated with the seismic data and processing, or the representation of actual structural variations that could be significant for interpretation of the fault evolution.

4.3 Fault throw analysis and displacement back-stripping

In this study, the fault throw data extracted from the fault and horizon network using TrapTester® (Section 4.2) were imported into MS Excel for further calculations. There, after smoothing (see Section 4.4), the interval-throw between certain horizons was determined by subtracting the throw on the younger bounding horizon from the throw on the older one. Thus, interval-throws for each interval for the detailed investigation of fault evolution (see Chapter 5) and for longer intervals including several horizons (see Chapter 6) were determined. These data can then be investigated similarly to the total throw data (e.g. by identifying throw minima and fault length to throw ratio). These interval-throws must be decompacted before they can be considered as accurate representations of the initial throw accumulated by the fault in the geological past (see Section 4.5).

Problems with the throw data occur where the graphs for different horizons overlap in a throw vs. distance plot (Fig. 4.6). This contradicts the well-established process of gradual throw accumulation on older horizons during displacement of subsequently deposited younger horizons on syn-sedimentary faults, thus resulting in higher throws on older horizons and progressively lower throws on younger horizons. This principle is utilised in reverse for fault displacement back-stripping, and the contrary cannot be explained by conventional fault behaviour. Zones of overlapping throw graphs, where younger horizons display more throw than older ones, result in negative back-stripped throws for the respective time interval.

The problem is largely, but not entirely, resolved by depth-conversion of the seismic data. Possible other reasons for the occurrence of throw overlap, after exclusion of erroneous horizon data, are local variations of drag, throw values at the resolution limit, throw variations due to fault linkage, variations in the dip of the fault and differential compaction across the fault. For intervals of little or no fault activity, the throw on neighbouring horizons along a large fault (without influence of fault tips) should be identical due to post-depositional intersection of the strata. However, topography on the horizon surfaces or decreasing seismic resolution (e.g. at greater depths) might cause overlaps. Variations in the type of drag, normal or reverse, in the dip direction of the fault in both the footwall and hanging wall might under- and overestimate the throw on certain horizons, leading to overlap when the throw on a younger horizon is over estimated and the throws are similar initially. Differential compaction of an individual unit on the footwall and hanging wall of a fault might occur if the lithology varies significantly across the fault (i.e. from sandy in the footwall to shaly in the hanging wall). Higher compaction of the shaly unit in the hanging wall due to greater burial depth and lithology (see Section 4.5) can lead to over-estimation of the throw on the younger interval boundary. If the throw value on the younger boundary exceeds the amount of throw on the older interval boundary the two graphs will overlap. Relay zones are often characterised by throw minima due to deformation of the wall rocks, rotation and sub-seismic faulting. If the through-going fault after linkage of the initial segments shows increased slip rates and accumulation of throw near the centre of the newly created larger fault, the graphs of the pre-linkage and post-linkage horizons might overlap. Decreasing dip angles of faults (e.g. shallowing of listric faults at depth) result in decreasing throw values for progressively deeper horizons even for constant displacement on these horizons. This is due to the definition of throw as the vertical component of displacement and a simple trigonometric relationship between the dip-separation, the throw and the dip of the fault.

4.4 Smoothing

The throw data calculated in TrapTester® (Fig. 4.7) was subsequently analysed with Microsoft® Excel in order to back-strip the fault displacement and to determine the throw rates along the faults. Where the TrapTester®-derived fault throw curves did not drop to zero throw at the lateral tips of the faults or at the edges of the seismic dataset, they were manually extended to zero using the measured throw gradient close to the tips.

On throw graphs two orders of features can be observed. Firstly, a 1st-order feature represents the general trend of fault throw along a fault, with a central maximum and decreasing throw towards the fault tips (Section 2.1) which, for the example in Fig. 4.7b, is more box-shaped for the older horizons and more semi-elliptical for the younger horizons. Secondly, the 2nd-order feature is formed by high-frequency undulations (wavelengths of <1 km and varying amplitudes) that are superimposed onto the general trend. Within the objectives of this project, the 1st-order trend of the data is used to determine the broad-scale throw and throw rate on the faults that accommodate most strain (i.e. for basin-wide comparison (Chapter 6)). The 2nd-order throw undulations represent small-scale throw variations and these are used for a more detailed study of fault growth (i.e. fault linkage (Chapter 7)).

Hence, smoothing of the throw data is required in order to determine the 1st-order throw trend, before the displacement can be back-striped and the throw rates are determined.

Moving-average-trends were initially considered for smoothing, but this method loses data points at either end of the fault trace. Instead, polynomial curve-fitting was utilised. These were chosen because they reflect, at higher polynomial orders, the general trend of the curves very well and smooth small-scale noise to a large degree without losing data points at the end of the fault throw graphs.

Several polynomial trends were fitted to the throw data (Figs. 4.8) and compared to the original data. The root mean square deviation (RMSD) was used as a measure of fit between the data and the fitted curves (Figs. 4.9 and 4.10). The 4th order polynomial fit oversimplifies the data – it reproduces the overall semi-elliptical shape of the throw-distance graph but loses much of the subtle detail that might be important to reconstruct fault evolution (Fig. 4.8a). The 6th order polynomial fit represents the original data better but still lacks the detail necessary for high-resolution fault investigation (Fig. 4.8b). The 8th and 10th order polynomials reproduce the shape of the profiles well and smooth the high-frequency irregularities (Figs. 4.8c&d).

The root mean square deviation was determined between the original throw data and all four polynomial trends. The comparison of the 4th, 6th, 8th and 10th order polynomials reveals a systematic decrease of the RMSD with increasing order (Fig. 4.9) and therefore an increasing similarity to the shape of the data, especially for the older horizons considered (TP80-TP100). For the younger horizons (TQ20-TQ80), the RMSDs are generally lower and the higher polynomials yield less reduction in the RMSD. This is more clearly seen when the RMSD is plotted against horizon age (Fig. 4.10), where low order polynomials produce good fits for horizons younger than about 1.5 Ma and higher-order polynomials are required to fit the older horizons. For of the throw data analysis, the 8th order polynomial was chosen as a reasonable fit to the data.

4.5 Decompaction

With increasing burial depth and weight of overburden, sedimentary rocks are subject to thickness reduction due to compaction (Magara, 1980; Sclater & Christie, 1980). The present-day throw data, as determined from horizons and faults mapped on seismic data, are measured between compacted sedimentary units. Because the faults investigated in this study are growth faults, the accumulation of initial throw during each time interval took place close to the seabed (depositional surface). Therefore, the determination of the initial throw and throw rates during any time interval requires decompaction of the throw data from the respective present-day values at various depths to near-surface values.

Compaction is not simply equivalent to the reduction of pore volume but covers all processes that result in volumetric strain applied to the rock. Three groups of processes contribute to compaction and loss of porosity (GILES, 1997):

- mechanical compaction – generally caused by denser packing (rearrangement and compression) of grains and escape of pore fluid
- physico-chemical compaction – removal of grain material, e.g. by pressure solution
- cementation – reduction of the pore space by mineral precipitation, can stabilise the grain framework and thus prevent substantial mechanical compaction

Statistical relationships have been established between porosity loss and burial depth or effective vertical stress for different lithologies (sandstone, shale). These generally show decreasing porosity with increasing depth (MAGARA, 1980). A modification of this general trend is secondary porosity, which can be caused by solution of grains or cement, fracture porosity, or retained higher porosities in over-pressured units where an over-hydrostatic pore fluid pressure can counteract mechanical compaction. Depositional porosities of sandstone amount to 40-50%, while depositional porosities of shales may be as high as 75-80% (GILES, 1997). These values decrease rapidly in the first kilometre of burial, more so in shale than in sandstone, and continue to decrease but at lower rates with increasing depth (MAGARA, 1980). This relationship of decreasing porosity with depth is often described as an exponential function with the following equation

$$\varphi_z = \varphi_0 e^{-cz} \tag{4.1}$$

where φ_z is the porosity at depth, φ_0 the initial porosity at the time of deposition, z the depth of a horizon or unit, and c a constant. Porosity loss is a complex, largely irreversible process that is influenced by a variety of factors. In sandstones it is a function of sorting, clay content, depositional facies and lithology of components. In shales it is a function of clay mineral rearrangement and pore fluid expulsion, which is dependent on the (progressively decreasing) permeability (GILES, 1997). Since most of the processes that contribute to compaction during burial are not easily quantified, a simple porosity-depth function is used for decompaction in this study.

BP Trinidad & Tobago provided a number of porosity-depth curves for the study area: (1) individual lithologies (sandstone, shale), (2) generalised trends for different settings on the shelf (inner and outer shelf), which are based on well and log data from the Columbus Basin, and (3) output data for two wells of their basin modelling software (Temis 3D), which additionally take pore fluid pressures, bulk densities and other information into account. The modelled curves for wells B and C (Fig. 4.1a) were compared to the large range of trends for sandstone and shale as compiled by GILES (1997). The local porosity-depth data for the study area are rather steep compared to the overall variations in data for sandstones and shales (Fig. 4.11) and reflect rather sandy lithologies, which is in agreement with the facies model for the study area (Fig. 3.6a). GILES (1997) points out that porosity loss curves are best based on local data due to the wide variety of available "standard" curves, therefore the data from the Columbus Basin were given priority over curves, such as those by SCLATER & CHRISTIE (1980) which are based on North Sea data.

Two porosity-depth curves, one for the fault block between the Cassia and the G faults (well B) and one for the fault block between the G and the H faults (well C), were provided by BP Trinidad & Tobago. Well B and the surrounding area are covered by a dense cell grid in the basin model, which allows high-resolution input data to be taken into account and similarly high-resolution output data to be gained. Well C is located in an area of the basin model where large grid cells dominate, which causes the low vertical resolution of the curve with significant intervals of constant porosity with depth and in general less reliable results (A. HOSPEDALES, 2007, personal communication) (Fig. 4.11).

Both graphs show disturbances in the interval between ca. 1-2 km, characterised by a sudden loss of porosities of ca. 5% (at ca. 1300 m), followed by a small increase and another sudden loss of ca. 5% (at ca. 2000 m). Due to the large displacement on the G Fault separating the two wells, this interval in the porosity-depth graph does not represent the same stratigraphic units in both wells (well B: ca. TQ30-TP95, well C: ca. TQ65-TQ40). The gamma ray logs of both wells, which allow a qualitative distinction between lithologies naturally emitting different amounts of gamma rays (SCHLUMBERGER OILFIELD GLOSSARY) (in general: low: sandstone, high: shale), show much lower thicknesses of interbedded lithology (ca. 30-100 m) than the interval of the anomalous porosity graphs (ca. 200-400 m). Therefore, the presence of a thick, laterally continuous, over-compacted shale unit, overlying and sealing an under-compacted, possibly over-pressured sandstone in this interval, is considered unlikely. Hence, the trendline honouring all data points along the profile was used for decompaction, without discrimination between different trends for certain depth intervals.

The two porosity-depth curves are very similar regarding the general trend and degree of porosity loss and are therefore considered to be representative for the porosity-depth trend for this part of the Columbus Basin. The trendline to the graph for well B was chosen for decompaction of all throw data because of the higher resolution of the underlying data. Based on equation 4.1, the initial surface porosity φ_0 and the constant c were determined to be 0.455 and 0.000263, respectively.

Because of the nature of the faults investigated here (i.e. extensional growth faults) each interval-throw increment can be directly related to the thickness variation between the footwall and hanging wall for this particular time interval (Fig. 4.12) and hence the throw increment for this time interval. Therefore, the residual throw for any time interval can be considered to be a column of sedimentary rock that has been subject to compaction since its deposition at the seabed. The present-day porosity of the rocks for each time interval was obtained by calculating the average depths between the hanging wall cut-offs of the interval-bounding horizons and applying the porosity equation to these values. Then, the present-day interval-throw was expanded from present-day porosity to near-surface (45.5%) porosity by a decompaction factor D_z, defined as

$$D_z = \frac{(1-\varphi_z)}{(1-\varphi_0)} \tag{4.2}$$

This relationship is derived from

$$t_0 = 1 = \varphi_0 + s \quad \text{from which follows} \quad \varphi_0 = 1 - s \qquad \text{(4.3 and 4.4)}$$

$$\text{and} \quad \varphi_z = \frac{(t_z - s)}{t_z} \tag{4.5}$$

where φ_0 is the initial porosity, s the solid material of the sediment unit, t_0 the initial thickness of the interval, and φ_z and t_z are the compacted porosity and interval thickness at depth, respectively.

If the mid-interval depth graphs dip with more than 3° along strike, the present-day porosity was determined for the minimum and maximum depths along the fault and linearly interpolated in between. Increments of higher expansion factors were then added to the minimum expansion factor for every data point during the calculation towards the deeper buried and therefore more compacted side of the fault. If the mid-interval depth graphs dip with less than 3°, an average value of the mid-interval depth was calculated along the fault length and used to determine the present-day porosity and the decompaction factor.

Decompaction is essential for accurate determination of the fault throw rate. If the interval-throw between horizons is not corrected for sediment compaction, the amount of throw actually accumulated during each time interval will be underestimated systematically, more so the deeper the location of the horizon interval. The maximum decompaction factor applied to interval-throw data during this study is 1.45 for an interval that is now buried at about 3 km depth in the hanging wall of the Cassia Fault. According to TAYLOR et al. (2007), the loss of displacement on growth faults due to compaction is generally <20%, or even <15% in mixed sand-shale sequences, such that general displacement patterns and fault growth histories can be identified without decompaction. However, decompation of displacement data is beneficial for deeply buried growth sequences.

Above-hydrostatic pore pressure can affect the porosity evolution at significant burial depths, although its exact effects are difficult to constrain. The Columbus Basin contains units of over-pressured sedimentary rocks. However, the above-hydrostatic pore pressures occur most commonly in low-permeable high-shale units of outer shelf, slope and basin facies (compare Figs. 3.6a&c). Furthermore, the over-pressured units are located well below TP80 in the SW of the dataset, where many of the investigated faults are located (Fig. 3.6b&c). In the immediate footwall of the G Fault, the overpressure is encountered as shallow as stratigraphic level TP90 (not mapped in this study) but is still below the depth where horizons and faults are mapped and, therefore, where fault throw data were determined in this area. In the hanging wall of the G Fault, the overpressure occurs at about the same depth (ca. 3 km) but the greatly increased thickness of the stratigraphic units there, the associated deeper burial depths, and the transition into more shale-rich facies of the younger strata to the NE (Fig. 3.6a), cause horizons TP100 and TQ20 to lie within the over-pressured succession. This is probably reflected by the prominent excursion of the porosity-depth graph of well C, which is located to the NE of the cross-section shown in Fig. 3.6 towards higher porosities (>5%) in the interval of ca. 3200-3500 m.

4.6 Throw rate

Fault throw rate describes the speed at which a fault moves. It can be calculated as an average over the total throw accumulated during a fault's life, or successively for individual intervals between dated horizons, using

$$throw\ rate = \frac{throw}{time} = y = \frac{x_1}{x_2}. \qquad (4.6)$$

Determining the throw rate for a number of intervals increases the resolution of the information compared to an average value, and might indicate phases of increased or reduced fault activity.

4.6.1 Errors related to fault throw rate calculations

The error of the throw rate depends on the errors of the throw data and the interval durations. The uncertainties in the horizon depths and associated throw data are due to uncertainties in a number of contributing factors including the seismic resolution (Section 4.1.1), the interval velocities used for depth-conversion of the seismic survey and the horizon and fault interpretation (Section 4.1.3), the method used by TrapTester® to extrapolate the horizons towards the fault surfaces to create the fault cut-offs (Section 4.2), and the corrections for sediment compaction. The resulting error of the interval-throw values is estimated to be 15 m. More detailed assessments of uncertainties related to seismic data are given by BROWN (2003) and THORE et al. (2002). The error of the interval durations is considered to be 0.1 Ma (±0.05 Ma) (Section 4.1.5).

The systematic error of a parameter that is a function of several independent, erroneous values is calculated using a TAYLOR series (GERTHSEN & VOGEL, 1997):

$$\Delta y = \sum_{i=1}^{m} \left| \frac{\partial y}{\partial x_i} \right| * \Delta x_i \tag{4.7}$$

Where, in this case, Δy is the error of the throw rate and x_i and Δx_i are the throw and interval duration (time) and their errors, respectively ($m = 2$). Integrating equation 4.6 into equation 4.7 and substituting x_1 by throw and x_2 by time lead to

$$\Delta y = \left| \frac{\partial y}{\partial x_1} \right| * \Delta x_1 + \left| \frac{\partial y}{\partial x_2} \right| * \Delta x_2 \tag{4.8}$$

$$\Delta y = \left| \frac{1}{x_2} \right| * \Delta x_1 + \left| -\frac{x_1}{x_2^2} \right| * \Delta x_2 \tag{4.9}$$

$$\Delta y = \frac{\Delta x_1}{x_2} + \frac{x_1 * \Delta x_2}{x_2^2} \tag{4.10}$$

$$\Delta\, throw\, rate = \frac{\Delta\, throw}{time} + \frac{throw * \Delta\, time}{time^2} \tag{4.11}$$

The error of the throw rate is, according to equation 4.11, dependent on both the interval duration and the interval throw. If the interval duration is smaller than or the same as the time error (0.1 Ma), the error on the throw rate can, even for large throw values (e.g. Cassia Fault, Fig. 4.13), be larger than the actual value. For small interval durations (e.g. fault system **d**), the error of the throw rate can become significantly higher then the value itself, leading to high uncertainties. However, from moderately well-defined throw rates at the high-throw central parts of the fault trace, throw rates can only decrease towards the fault tips because the throw accumulated there over the same time interval decreases to zero. Additionally, the ratio of the hanging wall to footwall thickness of a unit across the fault (growth index), which is a measure of the accommodation created by fault movement, can be determined as a time-independent parameter to assess fault activity. The throw rate error becomes progressively smaller for increasing interval durations and interval-throws.

The interval durations for which throw rates are determined in this study vary due to the horizon ages for the interval-bounding horizons. For the example of the Cassia Fault, the errors of the throw rates on the fault are shown in Fig. 4.13 for different horizon intervals (larger basin-scale intervals and shorter intervals between neighbouring horizons) at one particular location.

4.7 Figures

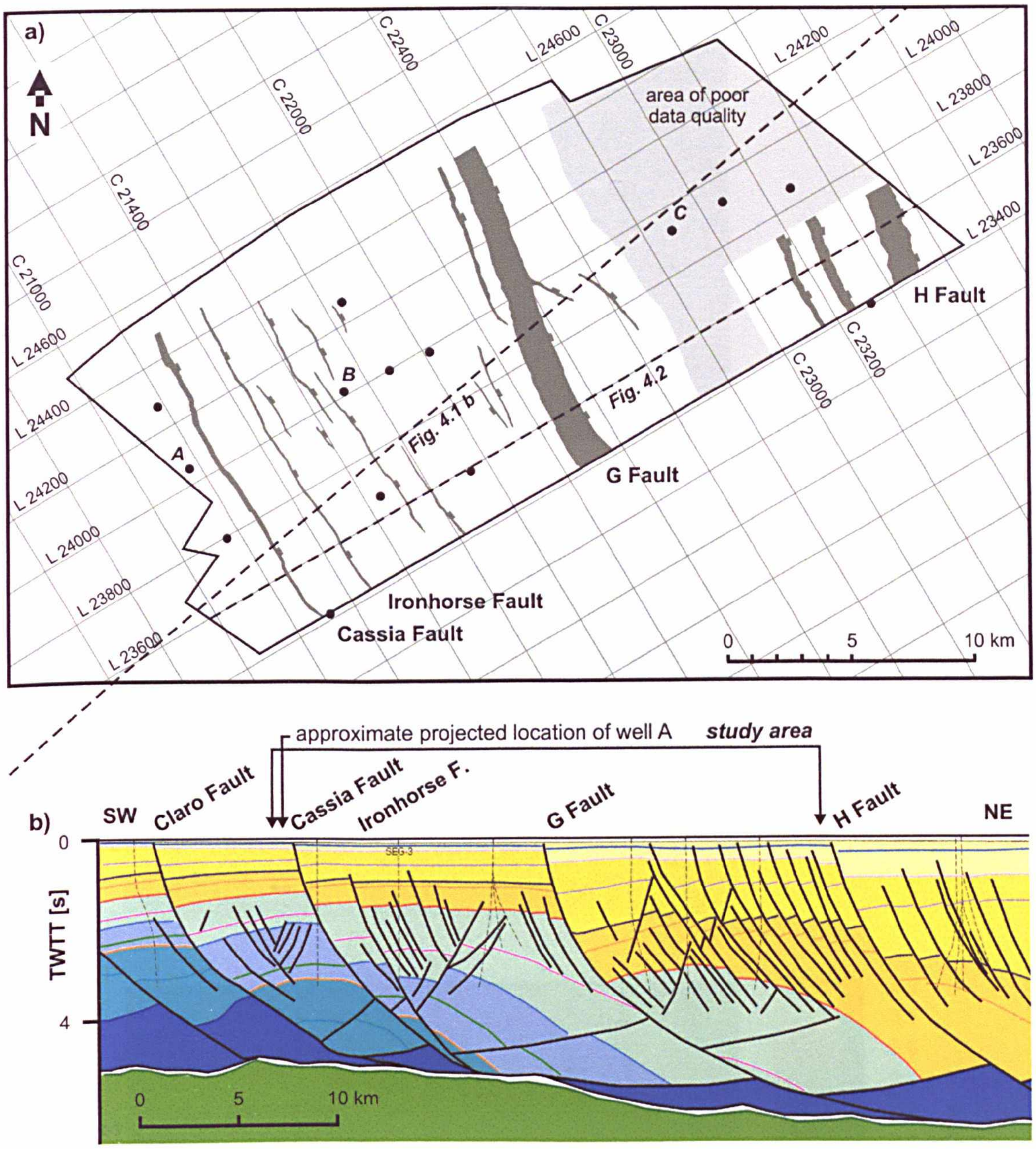

Fig. 4.1: **a)** Base map of the study area with survey outline, locations of wells used in this study (filled black circles, wells A, B, and C are referred to in the text), and the fault heaves at horizon TQ40 (the Cassia, Ironhorse, G, and H faults are annotated). **b)** Blow-up of part of the cross-section in Fig. 3.4d with indication of the locations of the Claro Fault and well A.

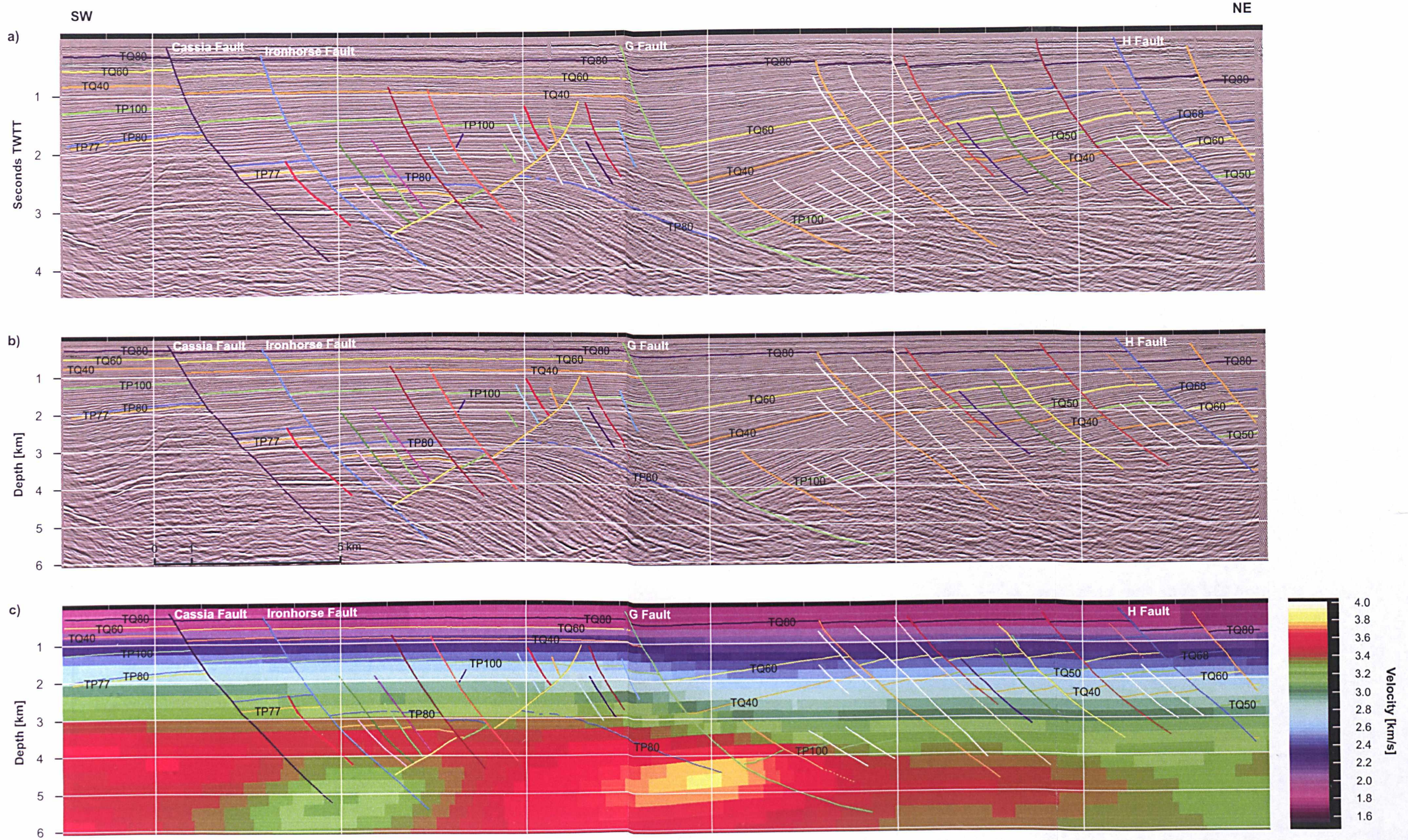

Fig. 4.2: Illustration of seismic line 23600 (for position see Fig. 4.1) in **a)** in two way travel time (TWTT, vertical axis), **b)** in true depth after depth-conversion and **c)** the velocity distribution along this cross-section in the three-dimensional velocity model, which was used for depth-conversion. Faults and selected horizons are shown and labeled for orientation. Note the change in fault geometry and distances between neighbouring horizons (they become closer at shallow levels and are streched at depth) before and after depth-conversion.

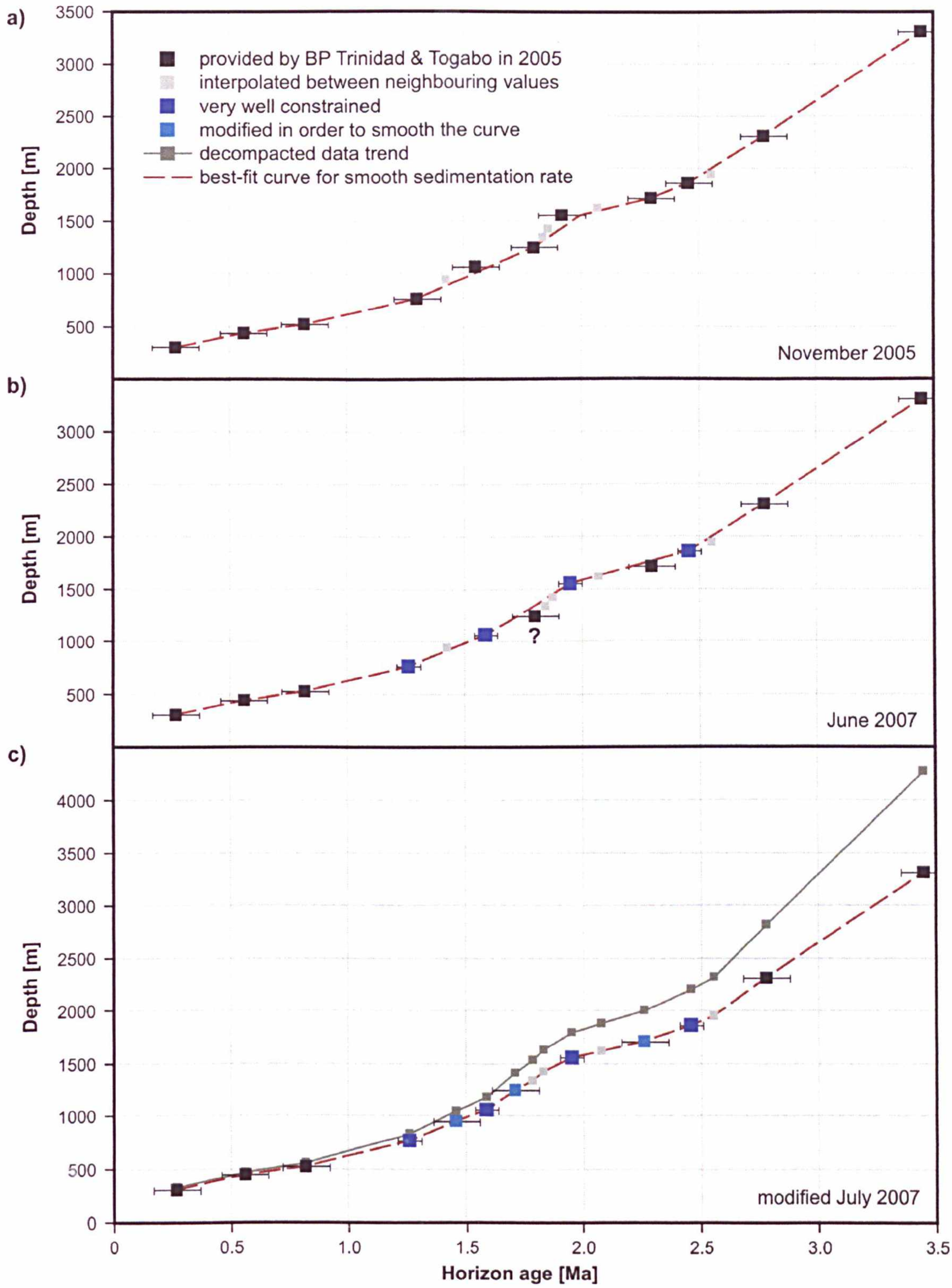

Fig. 4.3: Series of horizon age vs. depth diagrams for the horizons encountered in well A (see Fig. 4.1), illustrating the approach to determine best-fit horizon ages for the investigated strata: **a)** the initial horizon ages received from BP Trinidad & Tobago, **b)** updated horizon ages for certain fossils based on recent research, and **c)** the final modified ages. In c) the present-day (compacted) and decompacted (gray) depths for the respective horizons are shown. The decompacted horizon age vs. depth graph represents the initial sedimentation rate at the time of deposition. It is based on the considerations and the porosity-depth trend described in Section 4.5. Error bars displayed for the horizon ages are ±0.05 Ma for the well constrained ages and ±0.1 Ma for all other ages. Well constrained ages are based on J YOUNG (unpublished), and RW JONES (2007), personal communication, (?) in b) indicates an unreliable biostratigraphic age.

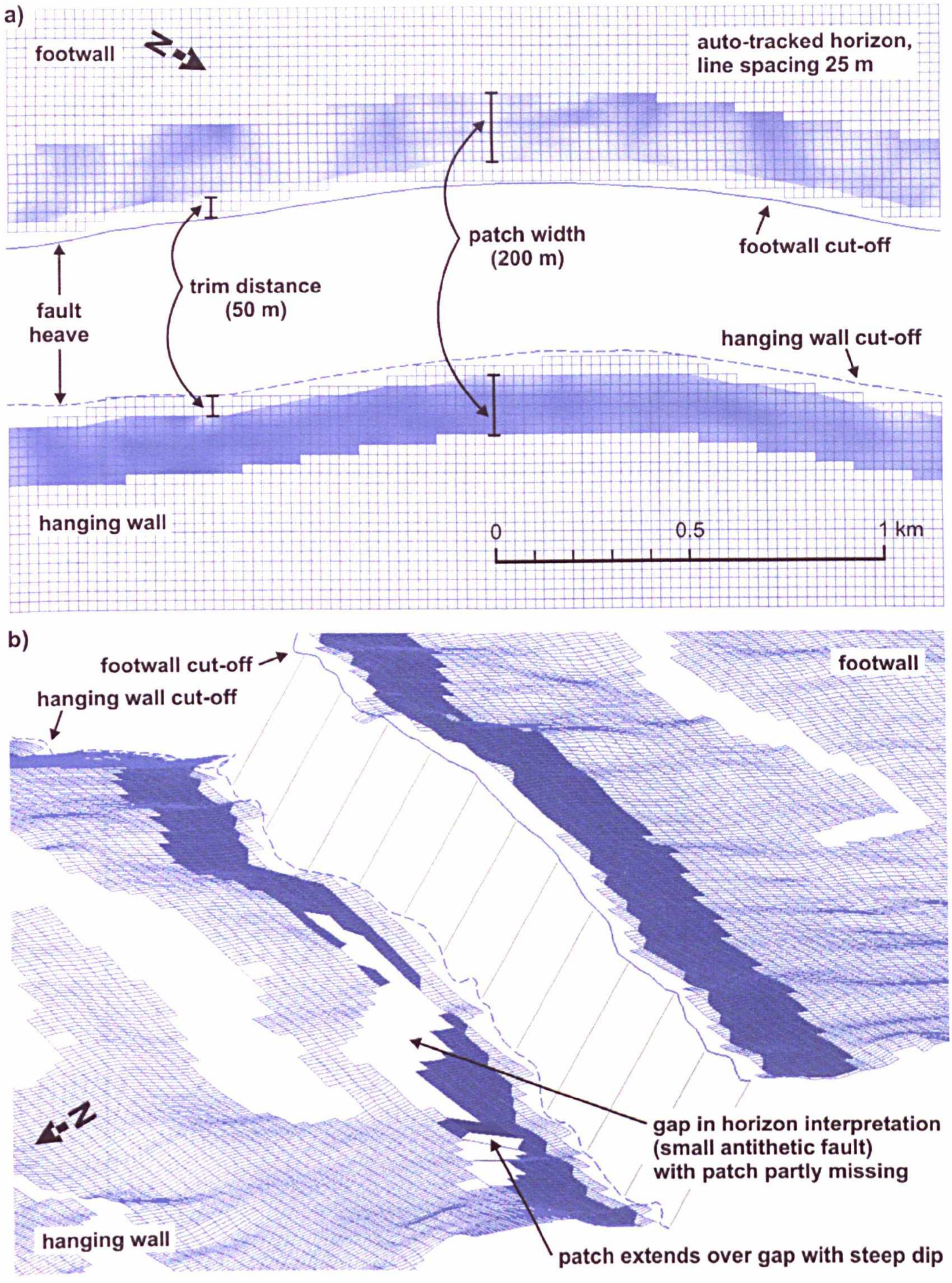

Fig. 4.4: Sections of horizon TP80 (displaced by the Ironhorse Fault) showing **a)** the trim distance and patch width on either side of the fault generated by TrapTester® in map view, and **b)** the problems that can arise from discontinuous and stepping horizon interpretation due to the presence of small faults within the patch area in an oblique view. The footwall and hanging wall cut-off lines are determined by TrapTester® as horizon-fault-intersection lines by projecting the geometry of the patch onto the fault surface, the throw is then calculated as difference between the respective depths of the cut-offs at each sampling location. The undisturbed horizon in a) is located at the southern end of the fault, whereas at the northern end (b) small faults are present in close proximity to the Ironhorse Fault.

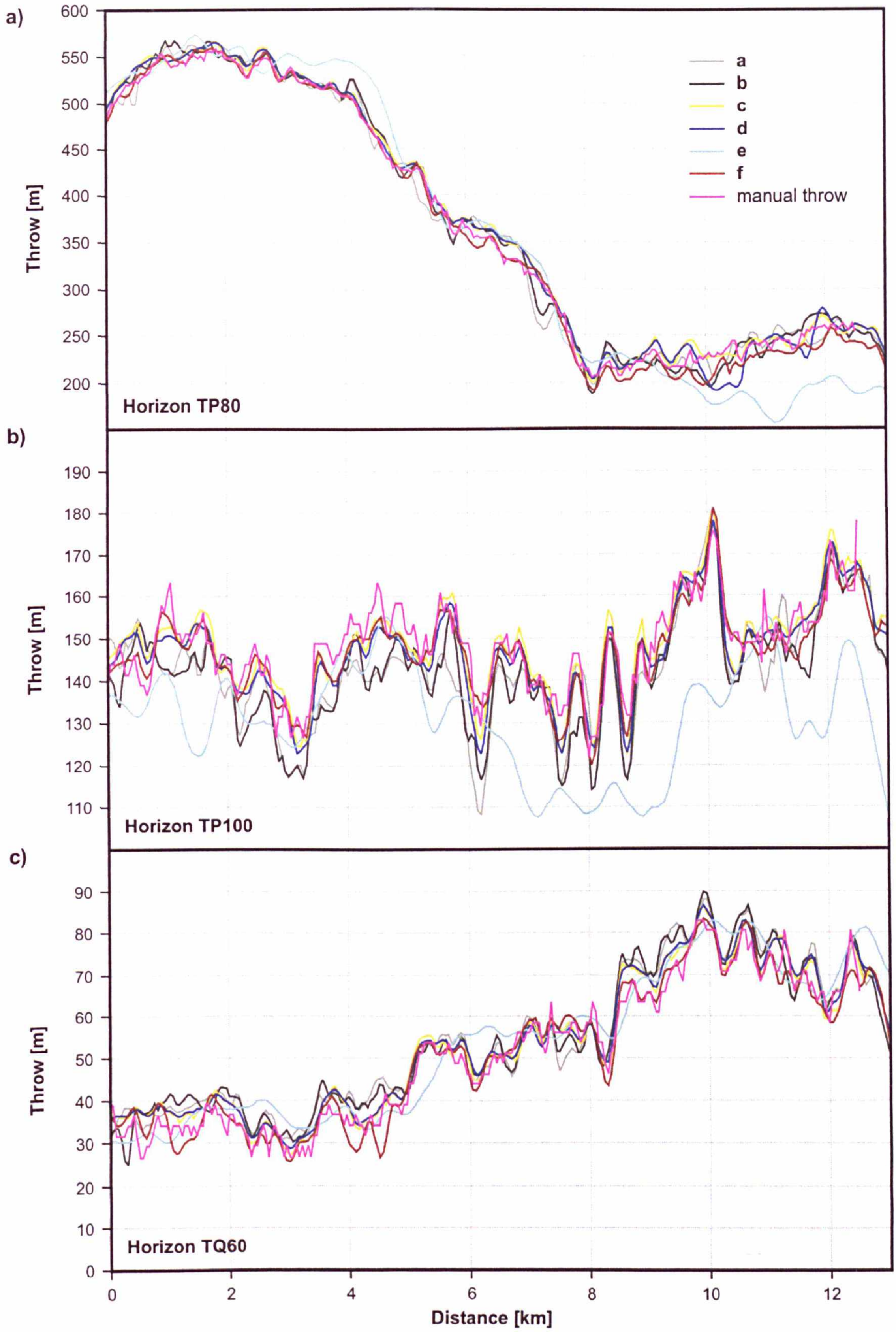

Fig. 4.5: Comparison of throw data measured with different horizon input settings and TrapTester® settings (Table 4.2) and manually picked data for horizons **a)** TP80, **b)** TP100, and **c)** TQ60 displaced by the Ironhorse Fault.

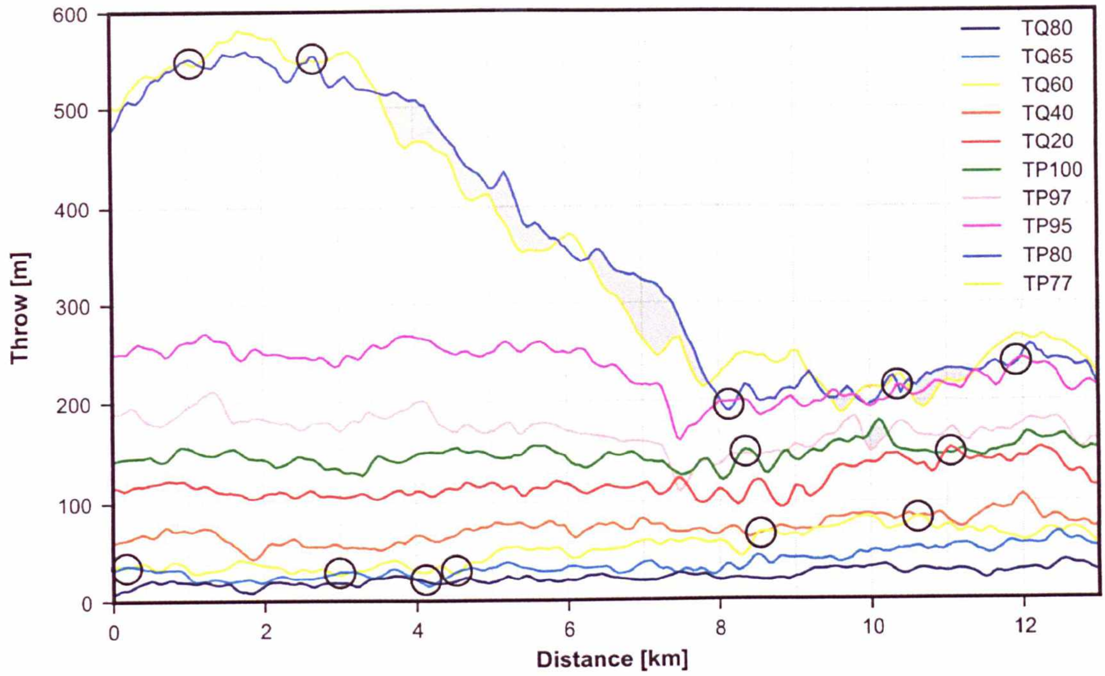

Fig. 4.6: Diagram of fault throw vs. distance for ten horizons intersected by the Ironhorse Fault. Note the overlap zones (shaded and circled), where younger horizons locally have higher throw than older horizons, which can not be explained by conventional fault behaviour.

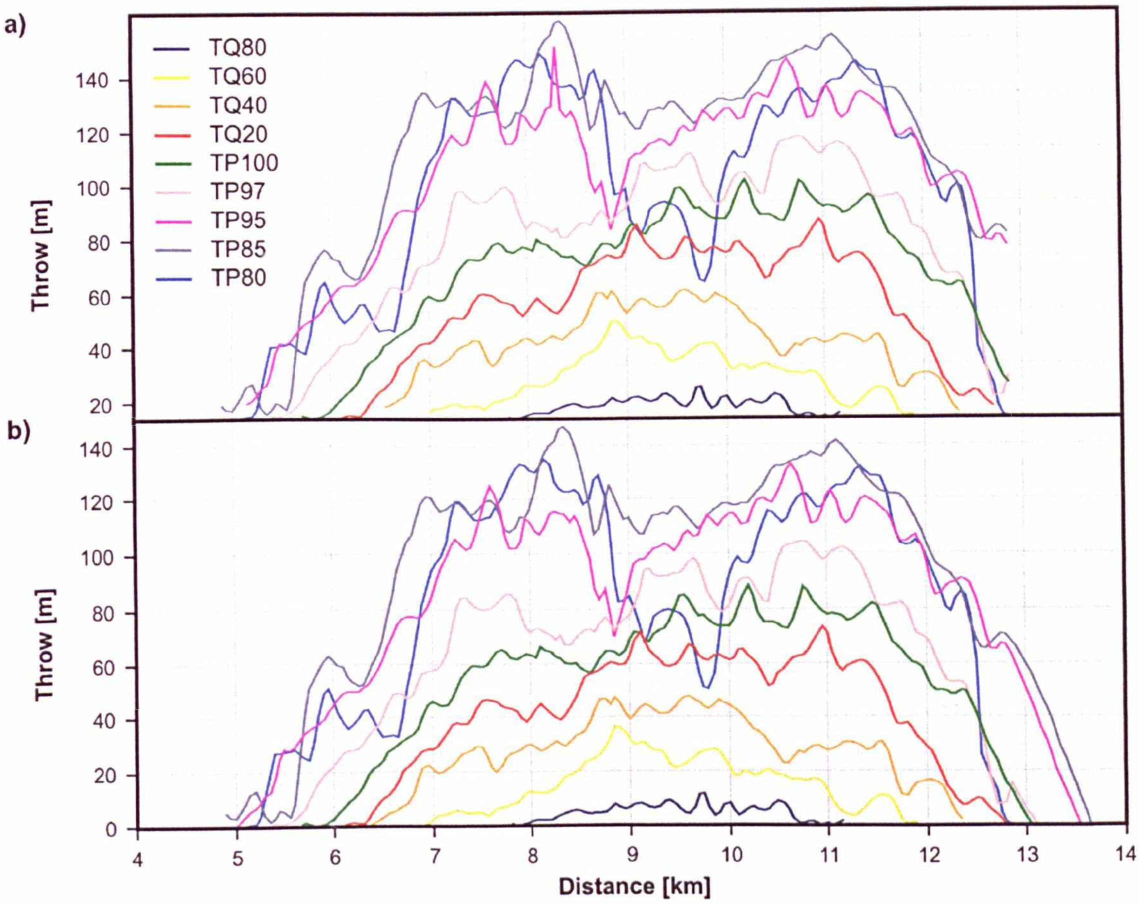

Fig. 4.7: **a)** Present-day throw as exported from TrapTester® for fault system **d** (cumulative throw of all fault segments and splays). **b)** Original data with fault tips manually extended to zero at the end of the dataset (north of 12.85 km) as well as within the dataset (tips of splays) using the throw gradient adjacent to the missing data points.

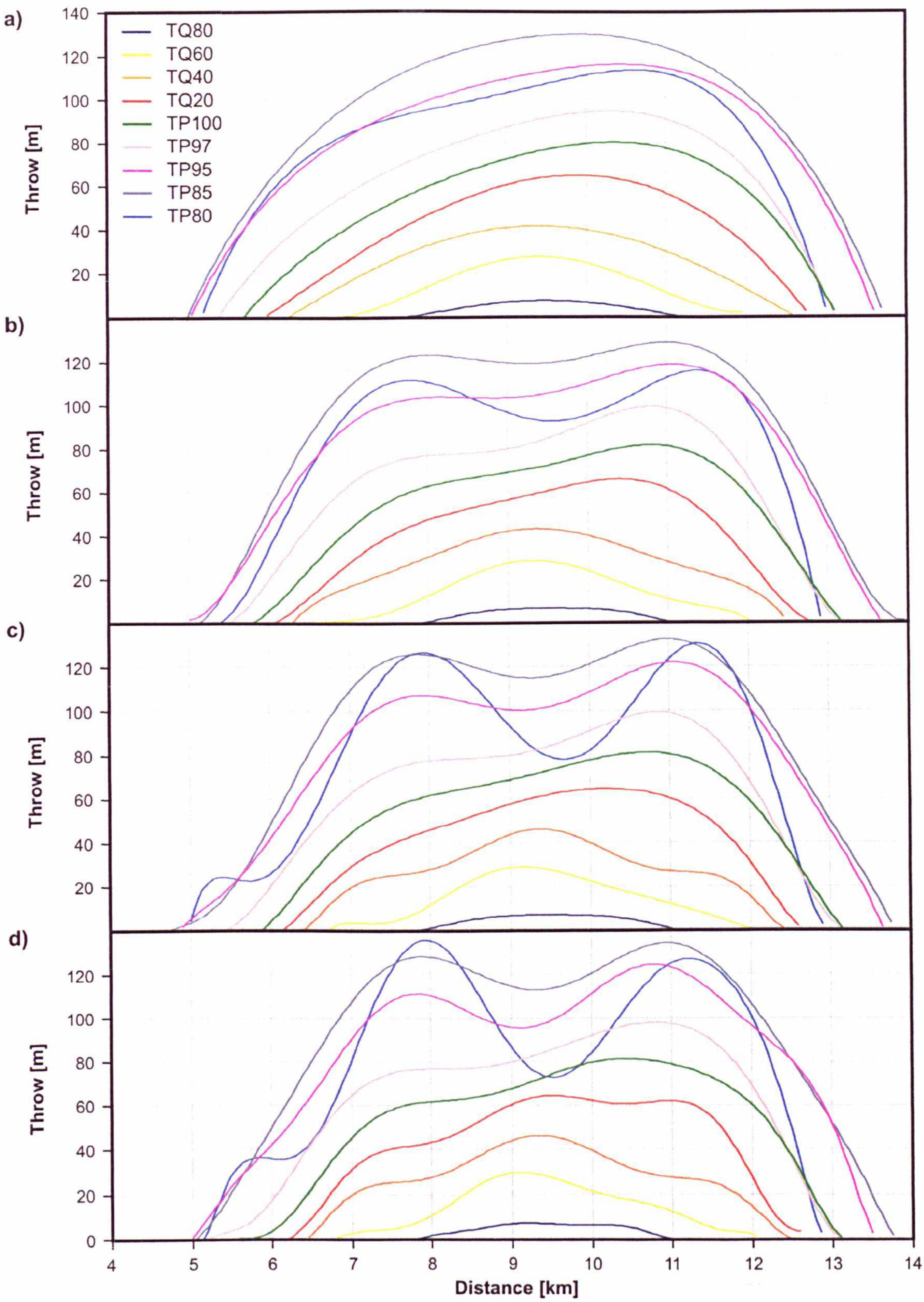

Fig. 4.8: **a)** 4th order polynomial trend, **b)** 6th order polynomial trend, **c)** 8th order polynomial trend, and **d)** 10th order polynomial trend fitted to the original data (Fig. 4.7).

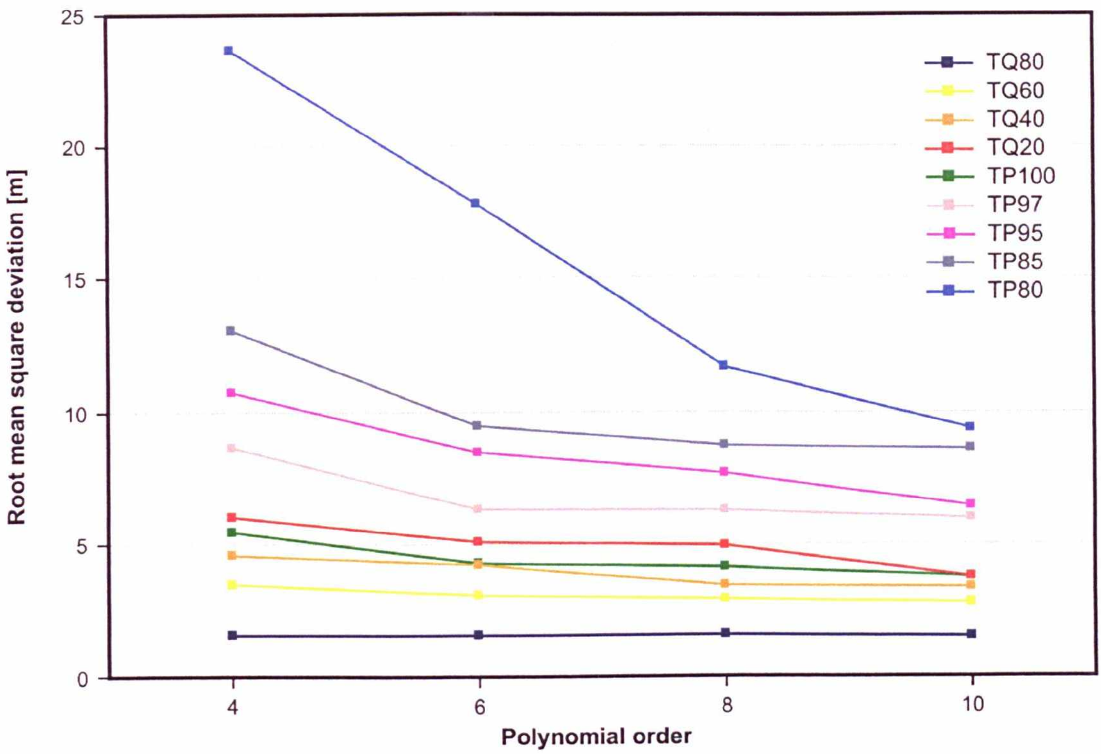

Fig. 4.9: Root mean square deviation between the fitted polynomial trends and the original TrapTester® data vs. the order of the polynomial trend. Note the decreasing RMSD towards higher polynomial orders, which is most obvious for the older horizons.

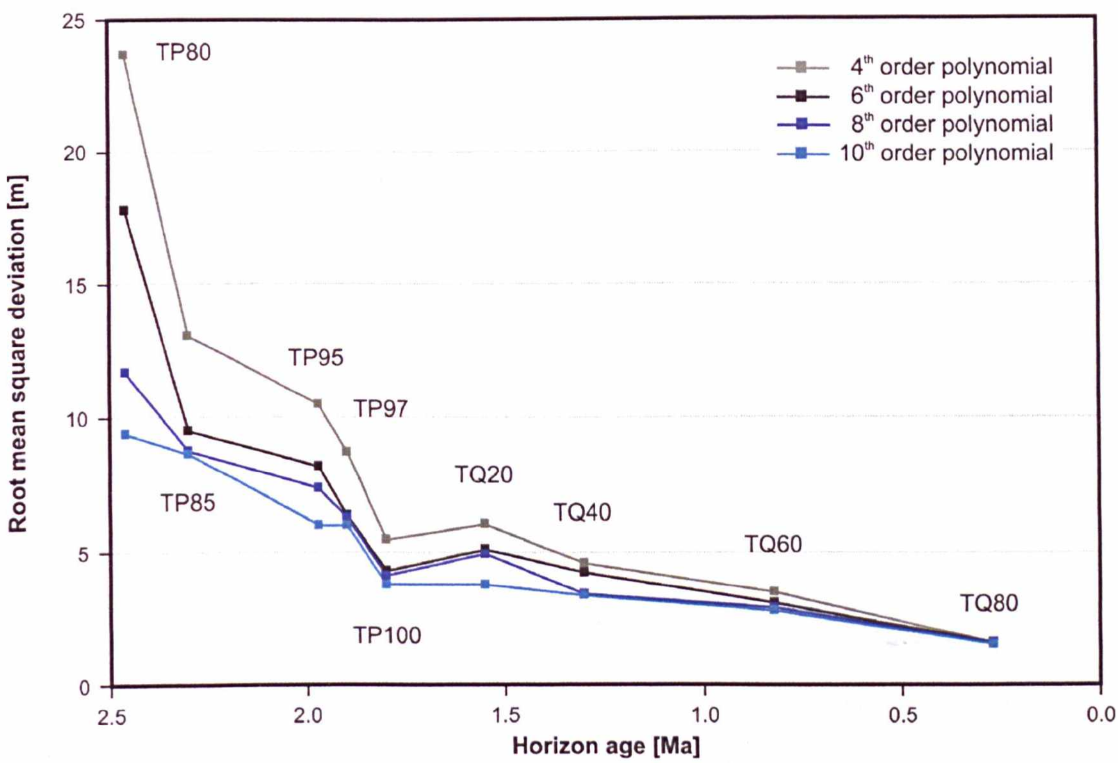

Fig. 4.10: Root mean square deviation between the polynomial trends and the original TrapTester® data plotted for 4th, 6th, 8th, and 10th order polynomial graphs vs. horizon age of the respective horizons. Note the steady overall decrease of RMSD and the decreasing range of RMSD for any one horizon towards younger horizons.

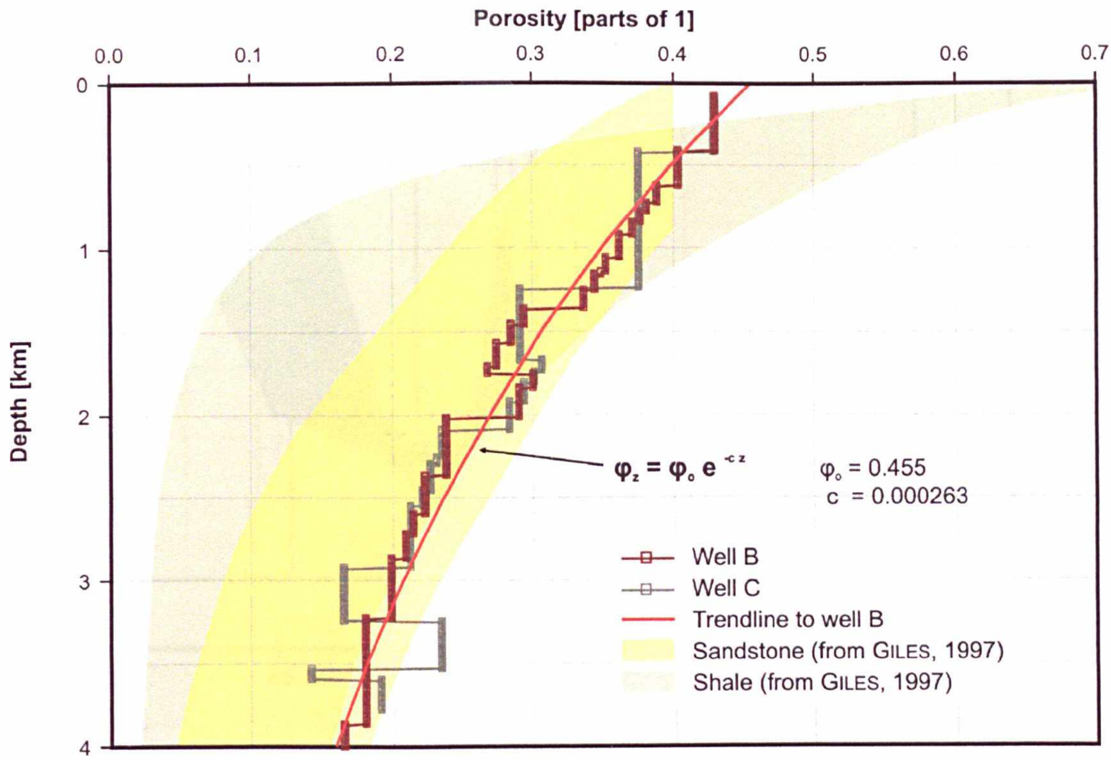

Fig. 4.11: Porosity-depth curves for wells B and C as determined by the basin model (Temis 3D) for the Columbus Basin, provided by BP Trinidad & Tobago. The two curves display very similar porosity-depth relationships, and the trendline to the curve of well B was chosen for decompaction of the interval-throw data. Overlain are the wide ranges of porosity-depth trends for sandstone and shale as compiled by GILES (1997).

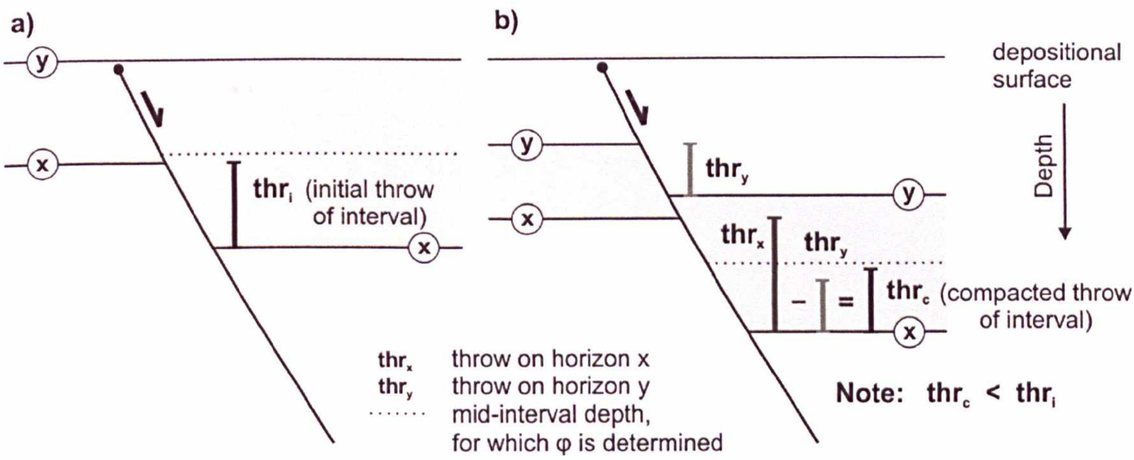

Fig. 4.12: Sketch illustrating in **a)** the initial fault throw (thr_i) for the horizon interval x-y and in **b)** the reduced interval-throw (thr_c) after further fault movement, sediment deposition and resulting compaction of the interval x-y (not to scale). Note that $thr_c < thr_i$ due to sediment compaction. For each interval, the present-day porosity (φ) is related to the respective present-day mid-interval depth in the HW and used for decompaction of the interval-throw data to near-surface porosity values.

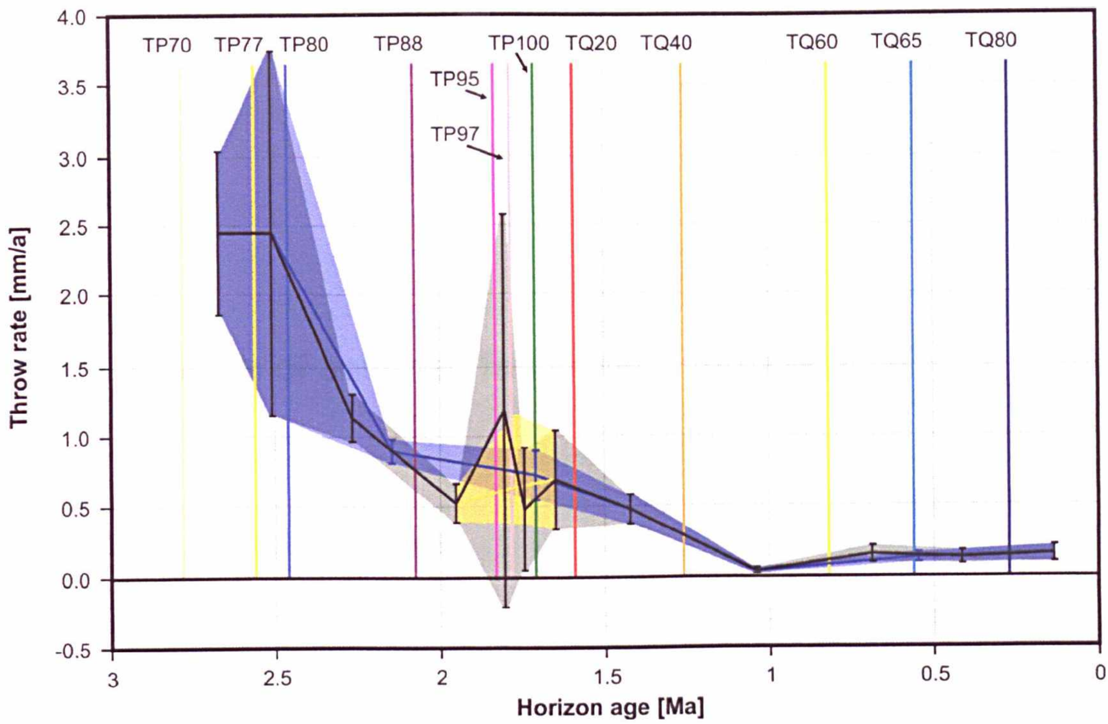

Fig. 4.13: Diagram of throw rate vs. horizon age at position 2 km along strike of the Cassia Fault, illustrating the amount of throw rate and its associated error for different interval durations that the throw rate is determined for. The area shaded in grey shows the throw rate for every available time interval, whereas the blue area is based on larger intervals (TP80-TP95 and TP95-TQ20), and the yellow graphs show the resulting throw data for interval TP95-TP100. The varying rates and error bars are superimposed to enable comparison of the results.

Chapter 5

Case studies of selected faults and fault systems

5.1 Aim and motivation

The high-quality 3D seismic dataset available for this study allows a very detailed investigation of fault geometries and, based on a closely spaced horizon network, fault evolution in the extensional Columbus Basin. In this chapter, a number of case studies of selected faults and small fault systems (Fig. 5.1) are presented that illustrate various aspects of the geometric and kinematic evolution of extensional growth faults. The case studies include two examples of medium (up to 250 m maximum throw) fault systems that show linkage and splaying, and three examples of sections of large (in excess of 600 m maximum throw), regional faults.

Each of the following sections (5.3, 5.4, and 5.6-5.8) presents one case study. These

1. outline the present-day fault geometry and throw distribution,
2. describe the resulting incremental throws and throw rates after smoothing, back-stripping and correction for sediment compaction, and
3. allow an interpretation and discussion of the fault evolution.

5.2 Methodology

The analysis of fault evolution is based on detailed mapping of the fault geometry and stratigraphic horizons imaged on the 3D seismic dataset. The present-day fault throw distribution was determined using TrapTester® and was used as input for subsequent calculation of fault displacements through time. Corrections for sediment compaction enable the determination of the initial throw rates for distinct time intervals during the evolution of the faults (see Chapter 4).

In all diagrams of horizon throw, interval-throw, throw rate, dip-separation and cut-offs vs distance along fault strike, the distance is plotted from southeast (left, 0 km) to northwest (right). Data displayed for an interval (interval-throw and throw rate) are always shown in the colour of the younger, interval-bounding horizon.

If the throw graphs indicate the presence of two or more separate fault strands during early stages of fault evolution, i.e. fault system **d**, these data were smoothed individually for each graph in order to accurately represent the geometries. Throw profiles that display a single throw maximum near the centre of the fault were smoothed as an entity. These are typical of the younger horizons, but may consist of faults with initial segments and a later breaching fault.

If the lateral and upper tips of a fault are present within the dataset, the fault traces are shorter on successively younger horizons. In these cases in order to both back-strip and then compare the throw profiles, the throw profile of each horizon was normalised to the length of the next older horizon, keeping the fault throw vs. length ratio constant (Fig. 5.2). By normalising the throw on a younger horizon to the next older one, the expected throw distribution on the younger horizon for a constant fault length (without shortening of the trace towards the upper tip) is calculated. This allows comparison of the throw profiles, and the residual interval-throw between two successive horizons obtained by this procedure reflects the amount of throw that accumulated during the respective time interval.

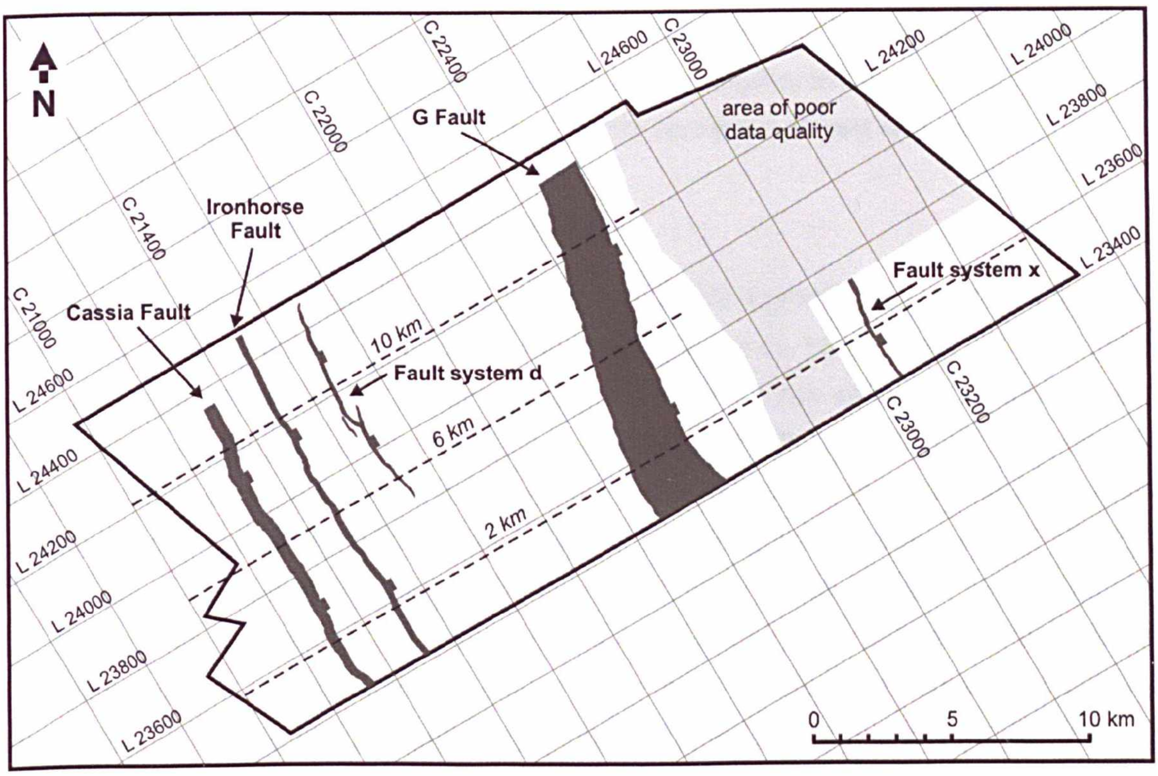

Fig. 5.1: Map of the survey area showing the faults and fault systems discussed in this chapter. Fault heaves are shown on horizon TP95, apart for the G Fault (TP100) and fault system **x** (TQ60).

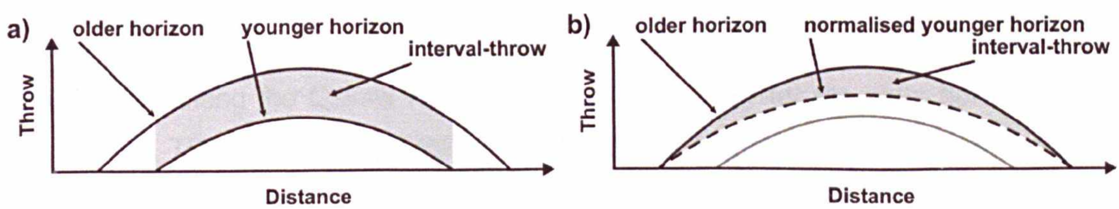

Fig. 5.2: Illustration of the method to normalise throw graphs of younger horizons to those of older ones in case of retreating tip lines.

5.3 Cassia Fault

The Cassia Fault is the westernmost fault investigated in this study and a major block-bounding fault in the Columbus Basin (Figs. 3.3 and 5.1). Because of insufficient imaging of the seismic data at the northern margin of the dataset, not all horizons could be mapped in the vicinity of the fault and therefore the data discussed in the diagrams below is only considered along a strike-length of 11.6 km.

5.3.1 Geometry

The Cassia Fault is a major fault in the Columbus Basin with a total length of more than 25 km. The central part of the fault trace is covered by the seismic survey over a length of ca. 12 km; both lateral tips are located outside of the study area. The fault can be confidently mapped to depths of ca. 5 km (Fig. 5.3a). The fault trace shows minor irregularities (small bends in map view) but there were no splays mapped in either its hanging wall or footwall (see Fig. 5.7). The Cassia fault shows one of the widest ranges of horizons offset by one particular fault that can be mapped with the information available to this study, providing throw data for both the oldest horizon, TP70, and the youngest one, TQ80.

5.3.2 Present-day throw distribution

Throw on the Cassia Fault increases characteristically for a growth fault towards depth (i.e. the oldest horizons) and reaches maximum throw values of ca. 1600 m on TP70 (Figs. 5.3b and 5.4a). The throw on the oldest horizon, TP70, decreases anomalously towards the north, where it drops below the throw values on TP77 and TP80 (Fig. 5.4a). This is caused by the rapid increase in thickness of the interval TP70-TP77 in the footwall from about 6 km along-strike to the north, which is not seen on the hanging wall, where the TP70-TP77 thickness remains constant along strike. It leads to deeper burial of the TP77 footwall cut-off than for the younger horizons and, thus, a relative convergence between the footwall and hanging wall cut-offs, which results in lower throw values. The consideration of the throw data of TP70 is vital to determine fault activity of the oldest available horizon interval, TP70-TP77. Therefore, the throw data on TP70 in the south, between 0-6 km, were included in the investigation of fault evolution, and the throw data in the north were omitted. The throw data for all other horizons display a plateau with highest throw values in the north (Fig. 5.4a) and a steady decrease towards the south.

Alternating throw maxima and minima that correlate well between neighbouring horizons are observed along the Cassia Fault (Fig. 5.4a), especially for the older horizons (TP70, TP77, TP80, TP88, TP95, and TP97). These maxima and minima have amplitudes of ca. 100 m and wavelengths of 0.5-1.5 km.

The throw graphs of horizons TP100 and TQ20 converge to the north and partly overlap, so that TQ20 has higher throw than TP100. This also applies to the smoothed throw graphs and results in negative interval-throws for these areas of overlap. Similarly, the throw graphs of TQ40 and TQ60 converge to the south but do not overlap so that the interval-throw remains positive.

5.3.3 Interval-throw and back-stripping

The interval-throws for a number of horizons show nearly uniform distribution along strike (TP70-TP77, TP77-TP80, TQ20-TQ40, TQ60-TQ65, TQ65-TQ80) and inclined patterns with larger interval-throws in the north for others (TP80-TP88, TP88-TP95, TQ40-TQ60) (Fig. 5.4b). Only interval TP100-TQ20 shows larger throw accumulations in the south. Interval-throws become negative (omitted from diagrams) and very small (<50 m) for intervals TP100-TQ20 and TQ40-TQ60, respectively. This produces very low throw rates (<0.05 mm/a) for interval TP100-TQ20 between 7-12 km and for interval TQ40-TQ60 between 0-4 km. This indicates very much reduced activity of parts of the fault during these intervals.

Throw rates for the oldest two intervals are very similar at high values of 2-3 mm/a all along the fault, and after deposition of horizon TP80 the throw rates decrease and differences between the southern and northern parts of the fault are established (Fig. 5.5a). Fig. 5.5b illustrates the higher fault activity in the north (10 km) during intervals TP80-TP88, TP88-TP95, and TP95-TP100 compared to the south (2 km), and the very low activity during TP100-TQ20 and TQ40-TQ60 of parts of the fault (see above).

The growth indices for three locations along the Cassia Fault are all above 1.0 and therefore confirm the syn-sedimentary character of this fault (Fig. 5.5c). The highest values reached are between 2.5-3.5, which indicates two to three times higher thickness of the hanging wall strata than the footwall strata for these time intervals and, therefore, very rapid fault movement and creation of accommodation. The throw rates and throw indices correlate very well and decrease gradually towards more recent times, only interrupted by the anomalously low activity described above, from high values during the oldest intervals to low values during the younger intervals.

The oldest mapped horizon, TP70, has the highest throw, at least in the southern part of the fault, and except for the anomalous throw values on TP70 in the northern part of the fault, no decreasing throws towards a lower tip line have been mapped. Therefore the fault was active throughout the studied time intervals and the onset of fault activity of the Cassia Fault must have occurred prior to 2.78 Ma but can not be constrained precisely in this study due to a lack of data for older horizons.

Most parts of the fault were active continuously since 2.78 Ma, apart from the northern half during interval TP100-TQ20 and the southern half during interval TQ40-TQ60.

Possible reasons for these temporal cessations of fault activity could be lateral migration of the main delta away from the study area, with associated reduced sediment deposition and

hence reduced tendency of gravitational failure and fault movement or interaction with neighbouring faults where major movement is transferred through soft-linkage.
The pronounced and well-correlated undulations of especially the older throw graphs (TP70-TP97) suggest a sequence of initial segments that eventually linked to form the through-going Cassia Fault. The fact that the fault moved uniformly and at high throw rates during interval TP70-TP77 (in the south) and that no abandoned splays were found at this level suggests that any linkage must have occurred prior to deposition of horizon TP70. The undulations would then be introduced as minima by reduced slip tendency at the positions of former breaching faults and maxima at the positions of former segment centres, where the slip tendency is not reduced.

5.3.4 Conclusion

The Cassia Fault is one of the largest faults in the study area and has accumulated throws of up to 1600 m on the oldest horizon, TP70. The throw graphs of all horizons, except for TP70, are characterised by a plateau of high throws in the north and decreasing values to about half or less to the south. The throw rates are highest for the two oldest time intervals (prior to 2.46 Ma) at ca. 2.5 mm/a, and then generally decrease gradually to values of below 0.3 mm/a for the most recent intervals (since 1.26 Ma). The initiation of movement on the Cassia Fault can be constrained to prior of the deposition of horizon TP70, but due to a lack of older horizons available to this study not more precisely.
The fault's evolution is characterised by rapid fault movement during the early stages and continuously decreasing activity until the death of the fault. Exceptions to this general trend over the studied period are the almost identical present-day throws of successive horizons (TP100/TQ20 and TQ40/TQ60) on different parts of the fault. In these locations, very low or even negative interval-throws and resulting throw rates for intervals TQ40-TQ60 and TP100-TQ20 indicate very little or no fault activity during the respective intervals. These phases of greatly reduced fault activity are, however, limited to certain parts of the fault, so that the fault never ceased to be active along its entire trace at once.
Undulations of the throw graphs that correlate very well in amplitude and wavelength between mainly the older horizons suggest formation of the Cassia Fault through linkage of a number of initial fault segments, although no splays could be mapped. The undulations might form as throw maxima at the positions of former segment centres, and minima at the position of former overlap zones and breaching faults.

5.3.5 Figures

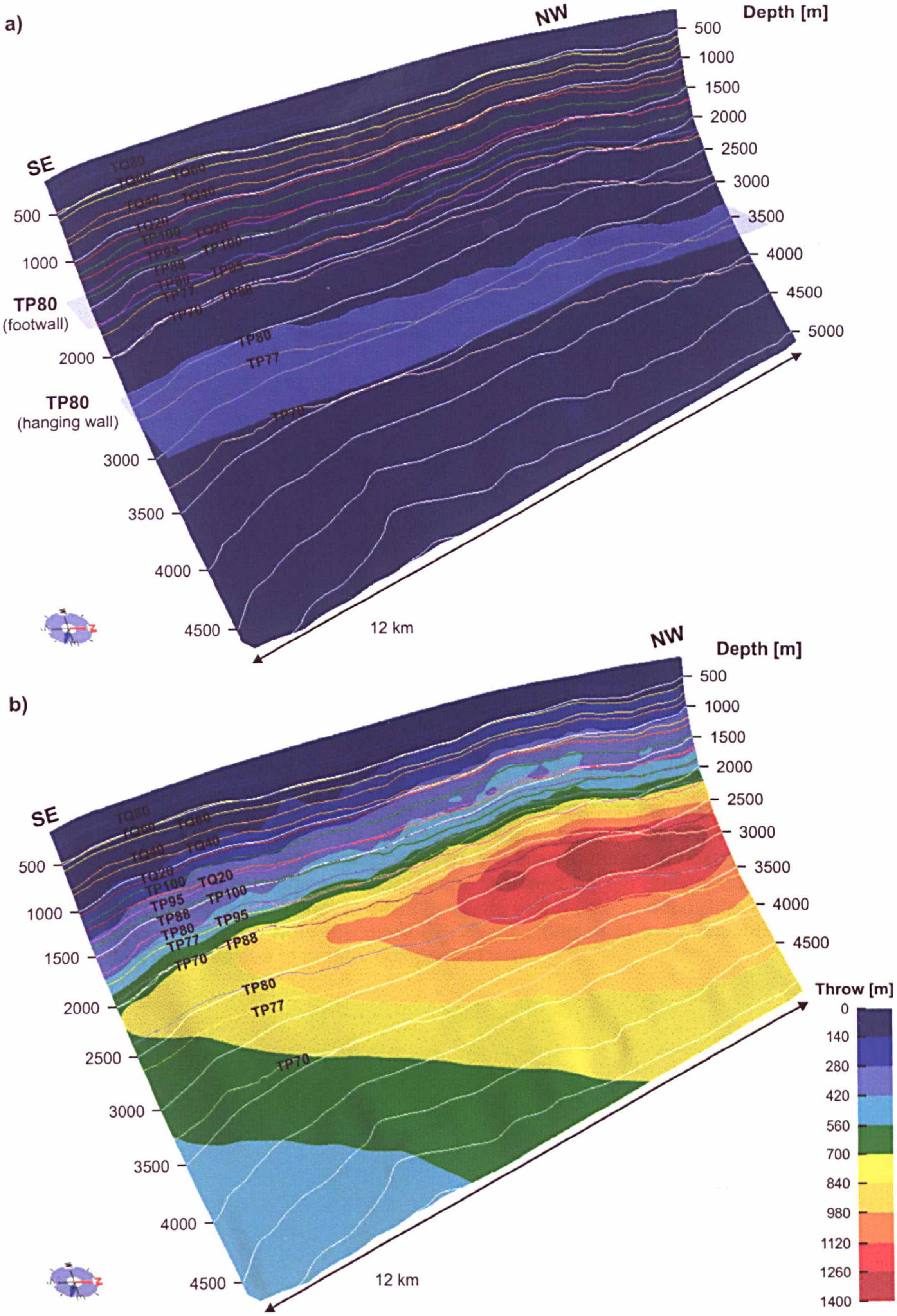

Fig. 5.3: 3D view of the Cassia Fault, illustrating in **a)** the general geometry and in **b)** the throw distribution with indication of the horizon cut-off lines, where those of TP97 and TQ65 were omitted for clarity. Annotation of the cut-off lines is FW on the left and HW on the right. Note the sub-horizontal orientation of the throw contours in the upper half of the fault, which are an indicator of syn-sedimentary fault movement.

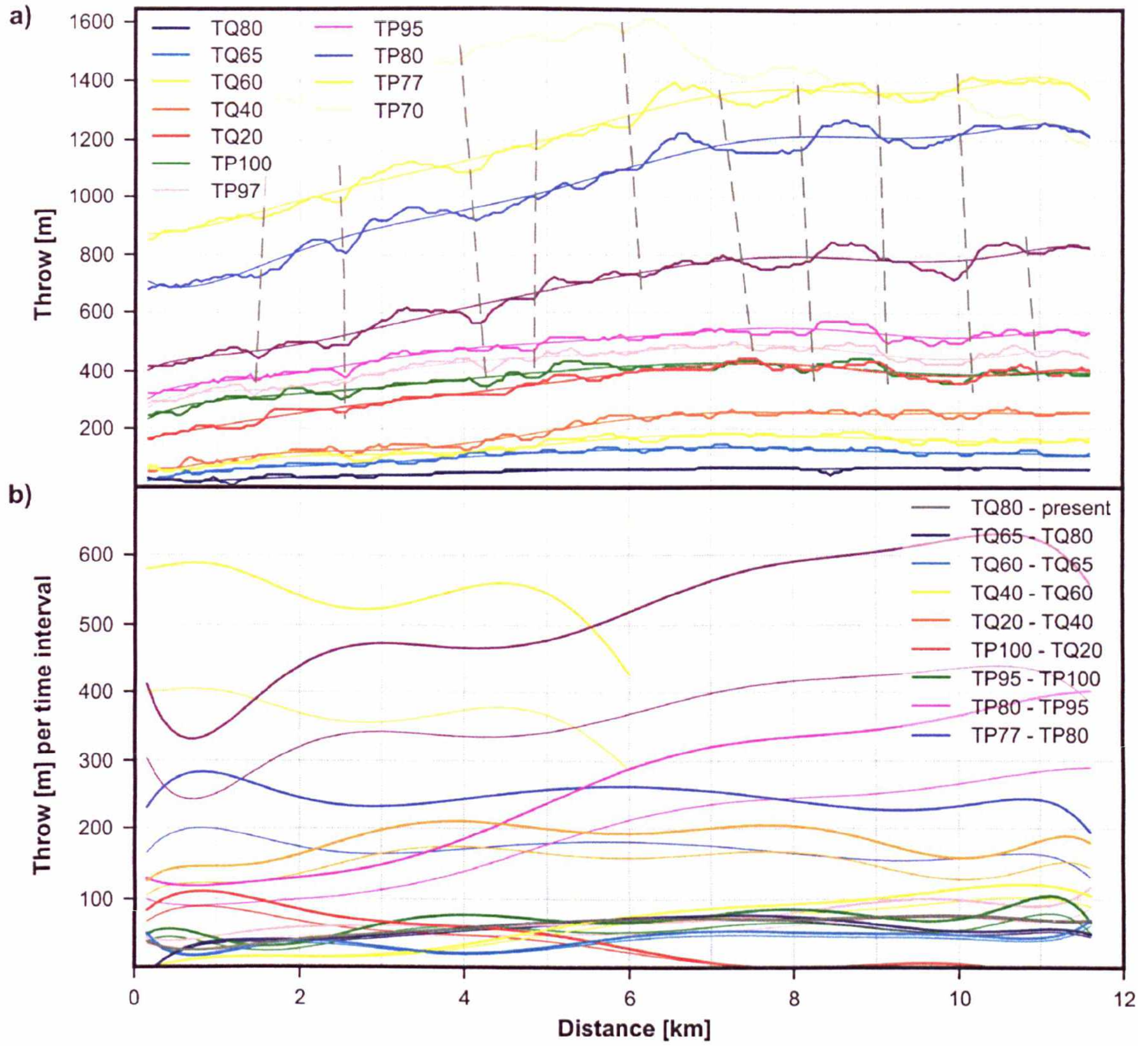

Fig. 5.4: **a)** The original throw data for all horizons and overlain the smoothed throw for the Cassia Fault. Dashed lines indicate correlation between persistent throw minima or maxima on successive horizons. In **b)**, the interval-throws for each interval between the mapped horizons are shown as determined for the present-day (thin line) and decompacted (bold line) to initial amounts at the time of deposition of the upper interval boundary. Note the more significant increase of the interval-throw for older time intervals due to greater compaction there.

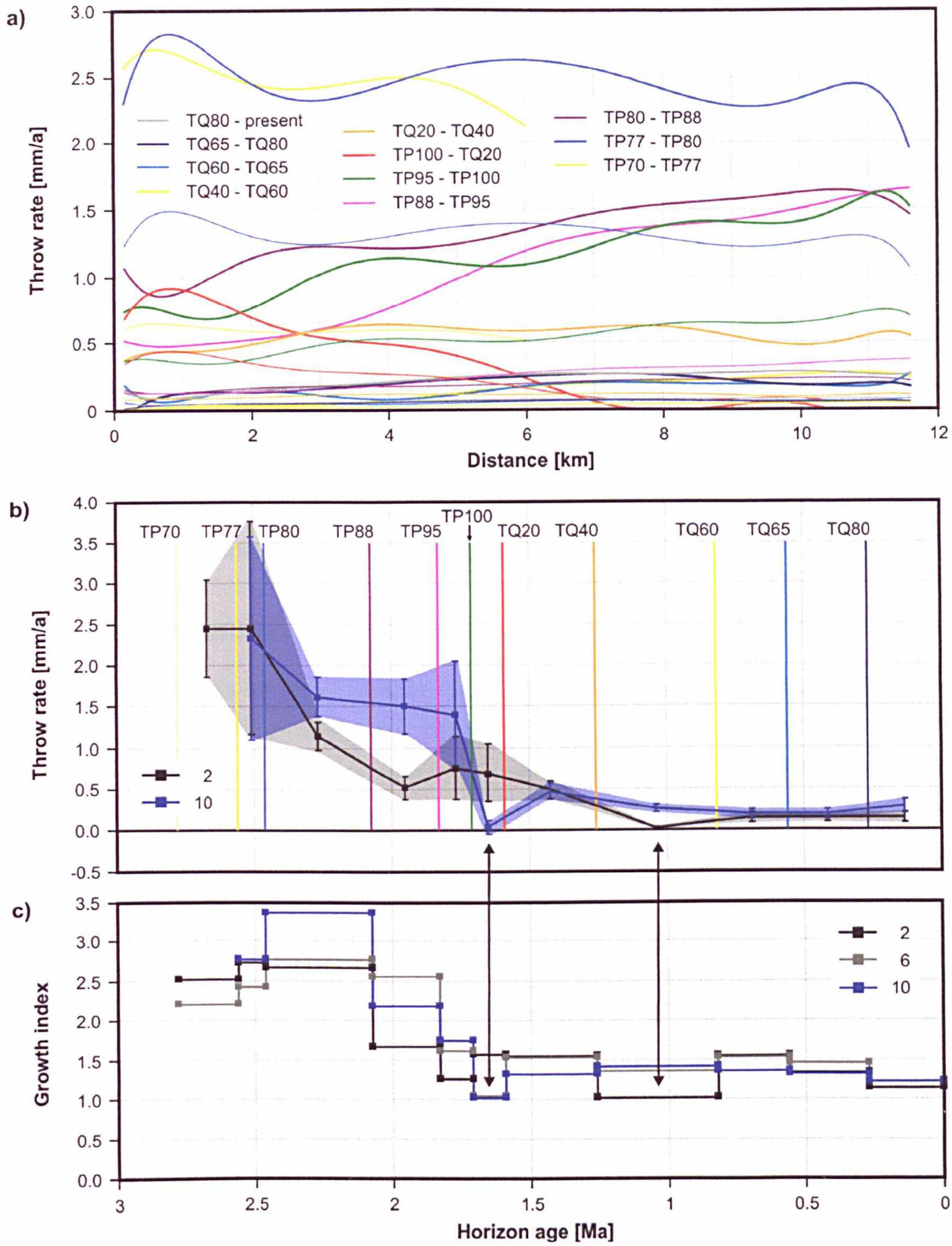

Fig. 5.5: **a)** Throw rate for all intervals (bold) and the associated errors (thin lines) for the Cassia Fault. In **b)**, the throw rates and their errors (shaded) are shown for two locations on the fault, 2 km and 10 km. In **c)**, the growth indices for three locations on the fault are presented, 2 km, 6 km, and 10 km. Note the very good correlation between low throw rates in b) and growth indices close to 1.0 in c).

5.4 Ironhorse Fault

The Ironhorse Fault is a medium-sized fault in the Columbus Basin and extends beyond the boundaries of the study area. The fault is located in the hanging wall of the major Cassia Fault and runs at a distance of ca. 2.5 km sub-parallel to it (Figs. 4.2 and 5.1). As for the Cassia Fault, the full range of mapped horizons is displaced by the Ironhorse Fault, providing data on fault throw over a long time interval (2.78 Ma to the present-day).

5.4.1 Geometry

The Ironhorse Fault extends across the entire width of the study area of 13 km. Both lateral tips are located outside of the study area. The Ironhorse Fault is a medium-sized fault within the study area, the fifth biggest, and can be confidently mapped to depths of about 4.5 km (Figs. 5.6a and 5.7). The fault trace shows small undulations in map view but only one very small splay was mapped in the hanging wall of the fault.

5.4.2 Present-day throw distribution

The maximum throws on the Ironhorse Fault are jointly accrued on horizons TP77 and TP80. The throw profile on the oldest mapped horizon, TP70, is sub-parallel to those of TP77 and TP80, but ca. 100 m less throw was accumulated (Fig. 5.8a). The throw graphs of horizons TP77 and TP80 overlap repeatedly where the throw on TP80 is ca. 50 m higher than on TP77. This is pronounced along the central part of the fault between ca. 3.5-8 km. For each of the three oldest horizons the throws are more than twice as high in the south than in the north. For all other horizons, TP95-TQ80, the throws are fairly constant along the fault trace (Figs. 5.6b and 5.8a). Similar to the along-strike throw variations observed for the Cassia Fault, the throw graphs of horizons TQ40-TQ60 and TQ65-TQ80 converge at about 9-10 km and 1-4 km, respectively.

The throw distribution along the Ironhorse Fault is noisy, with many high-frequency undulations (10-40 m amplitude) present on most throw profiles. However, few of these undulations persist on more than two neighbouring horizons. In the case of the pronounced minima (ca. 40 m less throw than adjacent areas) on horizons TP95 and TP97 at ca. 7.5 km along-strike, these can be associated with a small splay fault (ca. 700 m vertical and 300 m lateral extent) mapped in the hanging wall of the Ironhorse Fault. This fault shows maximum throws of up to 30 m on TP97.

5.4.3 Interval-throw and back-stripping

Fault displacement back-stripping reveals interval-throws of up to 400 m for interval TP80-TP95 in the south, most other interval-throws are much lower, generally below 100 m, and are mainly uniform along the fault trace (Fig. 5.8b).

The interval-throw for TP70-TP77, the oldest interval, is negative for the entire trace length and was not included in Fig. 5.8b and the throw rate calculations. The fact that the throw graph for horizon TP70 is persistently below and fairly parallel to those of TP77 and TP80 (Fig. 5.8a) indicates post-sedimentary displacement of the interval TP70-TP77. For interval TP77-TP80, three isolated throw accumulations (0-3.5 km, 7.5-10 km, and 11.5-13 km) have been determined, which may represent initial fault segments. However, these interval-throws are low at decompacted values of 22-33 m and are thus less reliable. In addition, no additional indicators of former segment boundaries or segment linkage (i.e. persistent throw anomalies, splays) have been found. During interval TP80-TP95, a large amount of throw accumulated in the southern half of the fault trace, but only minor throw (25 m or less) was accumulated in the north. This indicates that initiation of major fault activity on the Ironhorse Fault, after deposition of horizon TP80, was restricted to the southern half of the study area. This initial fault might have its centre at about 2 km along strike (where the highest interval-throws occur), or it could be the northern end of a fault propagating into the study area from the south. A small fault segment in the north seems to have been active during TP80-TP95 and to have initiated during TP77-TP80, and suggests the presence of a small fault to the north (11-13 km), separated from the main fault by a displacement-low at about 10-11 km. The Ironhorse Fault became active along its entire length (within the study area) during interval TP95-TP100, and remained active almost until the present. Similar to the Cassia Fault, converging throw graphs are observed for individual intervals, each time restricted to either the northern or southern half of the fault, where interval-throws decrease to minimal values and the fault seems to have locally ceased to be active. These examples are intervals TP100-TQ20 in the north (Figs. 5.8 and 5.9a) and TQ65-TQ80 in the south.

The throw rates on the Ironhorse Fault reach a maximum of ca. 1.2 mm/a for interval TP95-TP100. All other values are below 0.7 mm/a for TP77-TP80, TP80-TP95 and TP100-TQ20, and even below 0.2 mm/a for all intervals between TQ20 and the present (Fig. 5.9a). Fig. 5.9b illustrates the variations of the throw rate for two locations on the fault.

The growth indices presented in Fig. 5.9c correlate well for the low throw rates during interval TP80-TP95 in the north, and the generally high throw rates during interval TP95-TP100. The values for interval TP70-TP77 are below 1.0, indicating post-sedimentary displacement of this interval. The growth index should yield values of 1.0 for uniform thicknesses on either side of a fault. The lower values determined here are likely to be the result of differential compaction between the footwall and hanging wall block.

5.4.4 Conclusion

The Ironhorse Fault is a major fault within the study area and has a maximum throw of just less than 600 m on horizon TP77. The throw on the next younger horizon TP80 is very similar to that of TP77, whereas the throw on TP70, the oldest horizon, is lower than on TP77 and TP80. This throw distribution indicates post-sedimentary displacement of horizon

TP70 and the interval TP70-TP77. The fault might have initiated as three isolated small faults during interval TP77-TP80, but certainly propagated from the south (outside the study area) to the north, to about 10 km along strike distance during interval TP80-TP95. From then on, the fault was almost continuously active until after the deposition of horizon TQ80. Fault activity of the Ironhorse Fault ceased before the present-day. Throw rates reached a maximum of up to 1.2 mm/a during interval TP95-TP100 and then decreased rapidly to values of ca. 0.4 mm/a and even below 0.2 mm/a for the youngest intervals. Growth indices greater than 1.0 for all but the oldest interval show that the fault was active as a syn-sedimentary fault and correlate well with variations in throw rate along strike.

5.4.5 Figures

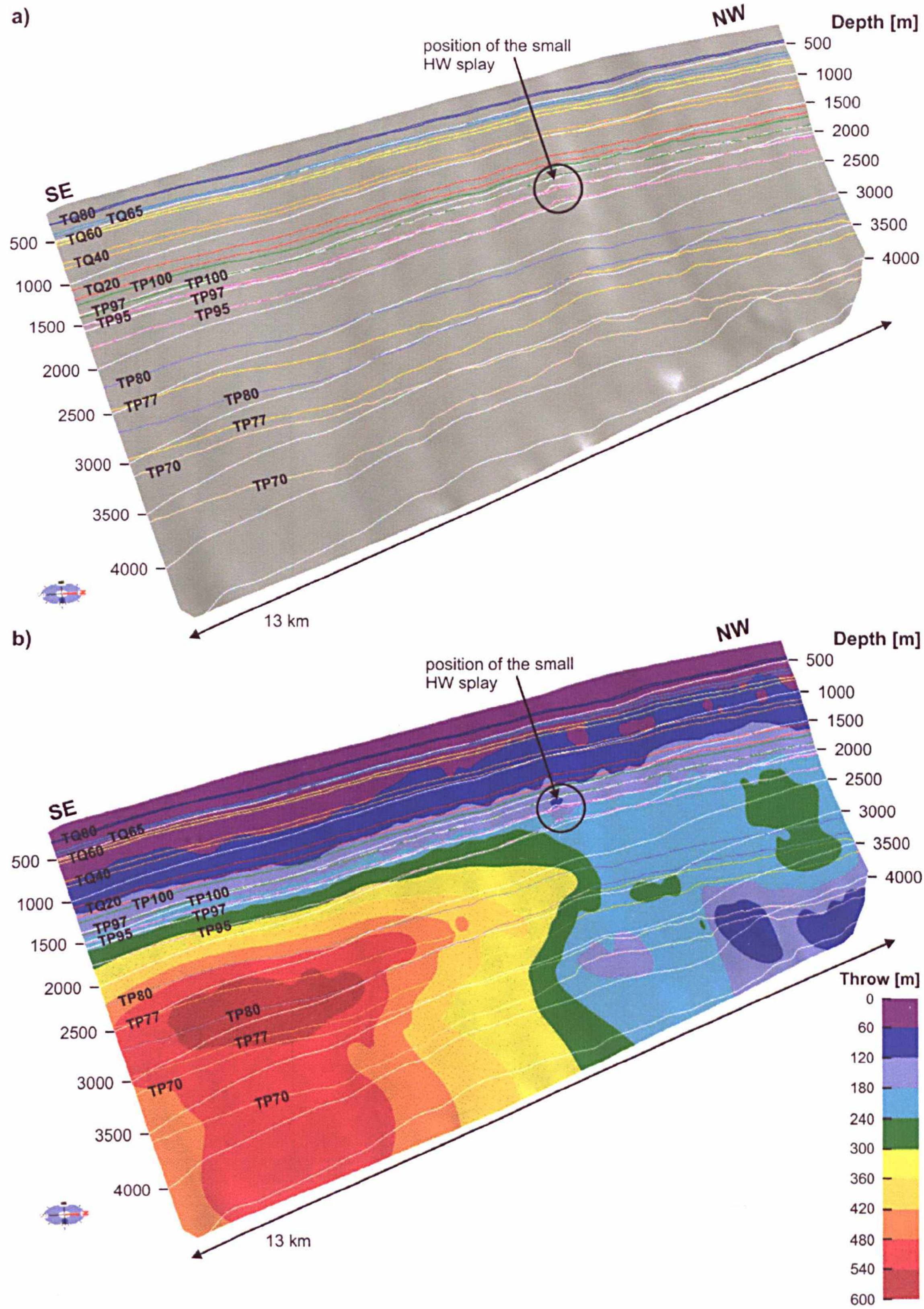

Fig. 5.6: 3D view of the Ironhorse Fault, illustrating in **a)** the general geometry and in **b)** the throw distribution with indication of the horizon cut-off lines, annotation of the cut-off lines is footwall on the left and hanging wall on the right. Note the sub-horizontal orientation of the throw contours for throws of 180 m and less along the entire fault length and for throws of less than 360 m in the southern part, which are an indicator of syn-sedimentary fault movement.

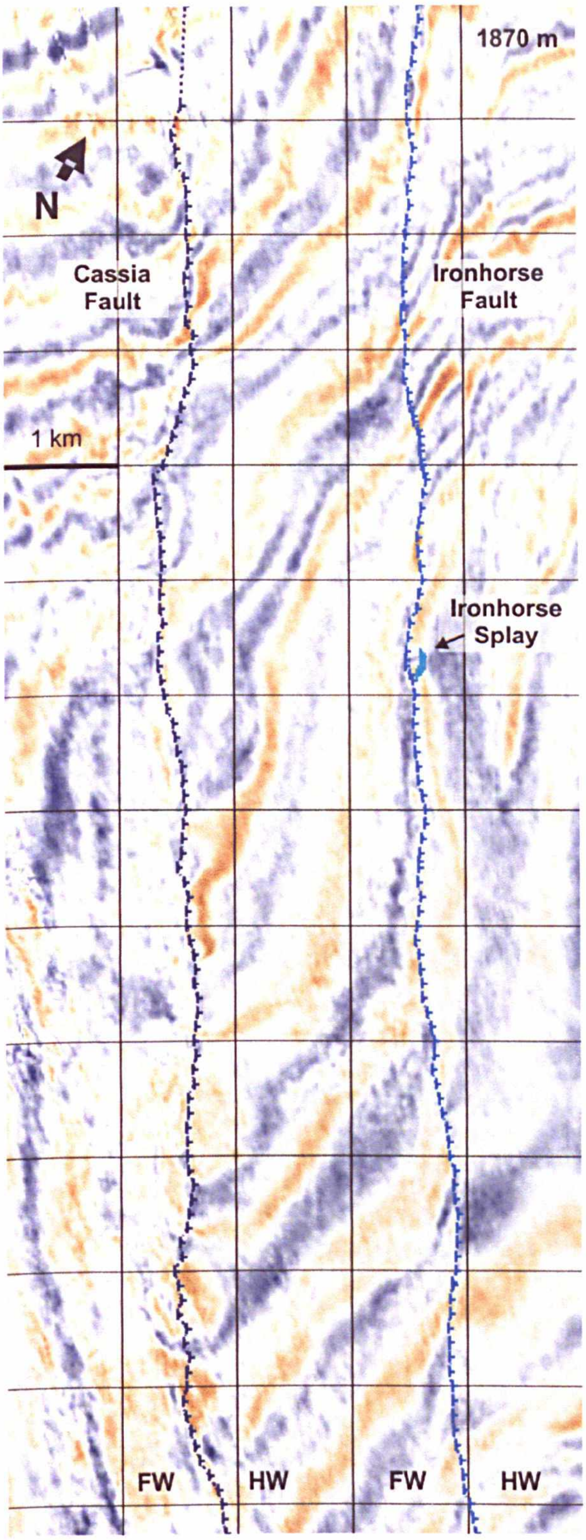

Fig. 5.7: Depth slice at 1870 m, showing the fault traces of both the Cassia and Ironhorse faults. Note the small synthetic hanging wall splay of the Ironhorse Fault and the absence of any splays of the Cassia Fault.

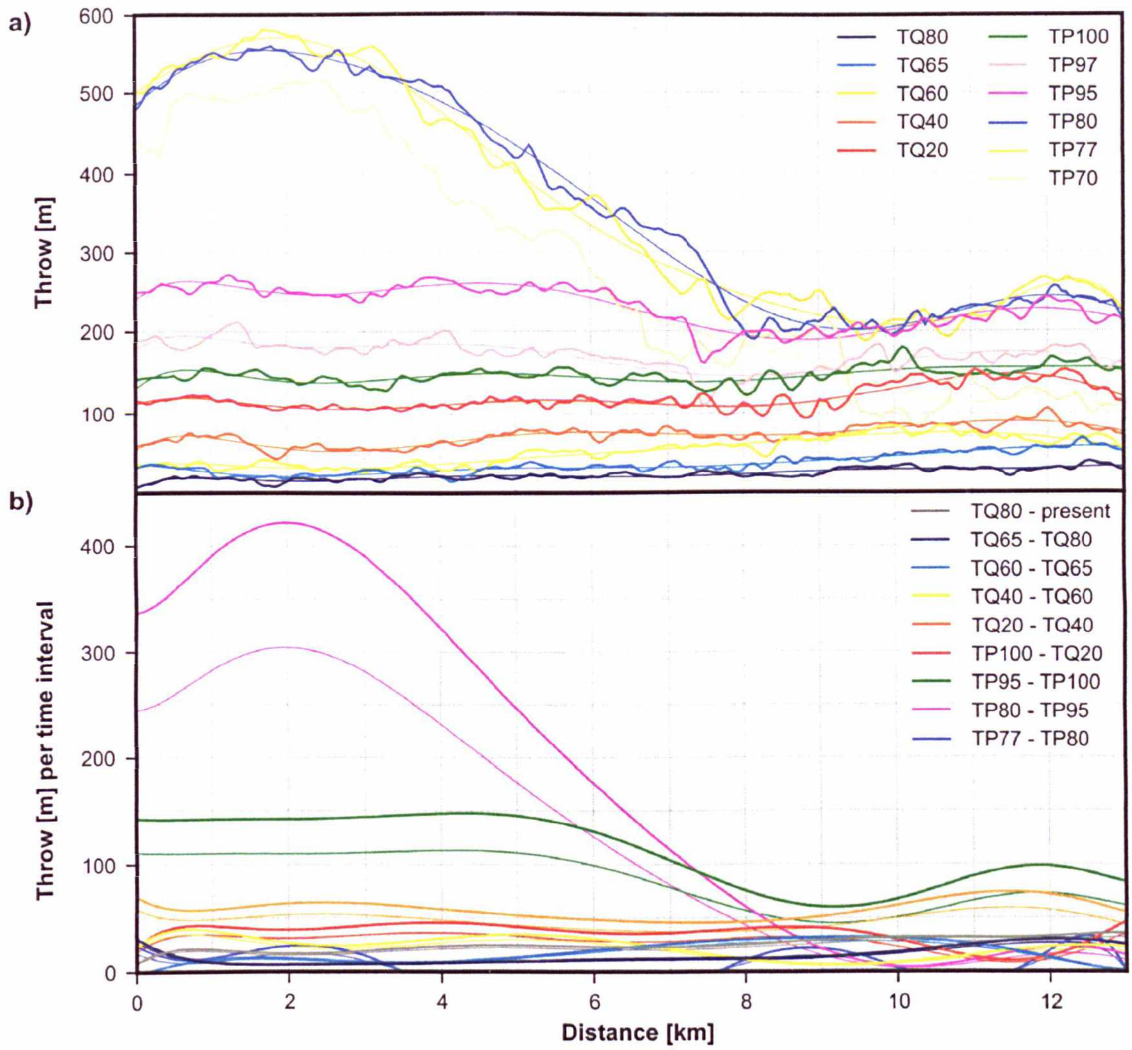

Fig. 5.8: **a)** The original throw data for all horizons and the smoothed throw for the Ironhorse Fault. Note the significantly higher throw on the oldest horizons (TP70, TP77 and TP80) in the south than in the north, and that the throw on TP70 is consistently lower than on TP77. In **b)**, the interval-throws for each interval between the mapped horizons are shown as determined for the present-day (thin line) and decompacted (bold line) to initial amounts at the time of deposition of the upper interval boundary.

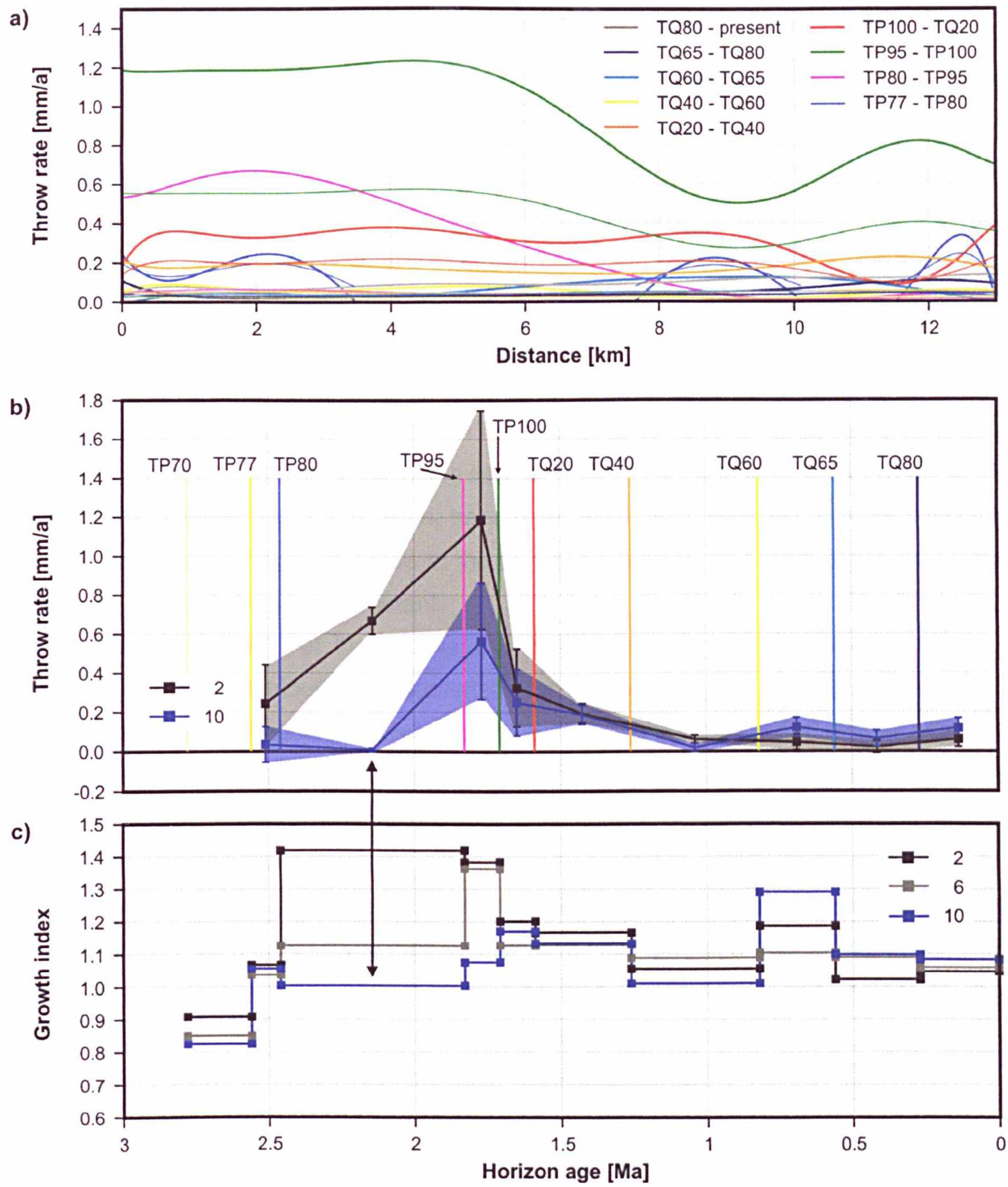

Fig. 5.9: **a)** Throw rate for all intervals (bold) and the associated errors (thin lines) for the Ironhorse Fault. In **b)**, the throw rates and their errors (shaded) are shown for two locations on the fault, 2 km and 10 km. In **c)**, the growth indices for three locations on the fault are presented, 2 km, 6 km, and 10 km. Note the good correlation between low throw rates in b) and growth indices close to 1.0 in c) and the growth indices below 1.0 for the oldest interval TP70-TP77 that was displaced after deposition.

5.5 Interaction between the Cassia and Ironhorse faults

The Cassia and Ironhorse faults are oriented parallel to each other and are only 2.5 km apart, hence soft-linked fault interaction is likely to have occurred.

The Cassia Fault shows an increase in throw from about 850 m in the south to about 1400 m in the north for horizon TP77, with similar variations for horizon TP80, and to a lesser degree TP95 (Fig. 5.10a). On the other hand, the Ironhorse Fault has a throw of ~550 m in the south, decreasing to ~200 m in the north (Fig. 5.10b). The sum of the throws for the two faults is more nearly horizontal for horizons TP77, TP80 and TP95 (Fig. 5.10a).

During interval TP77-TP80, the Cassia Fault moved uniformly along the entire fault trace, whilst there was little if any growth on the Ironhorse Fault. The Ironhorse Fault initiated in the southern part of the study area during interval TP80-TP95 with little, if any, throw to the north of 8 km. Displacement was, thus, transferred from the Cassia Fault to the Ironhorse Fault, and the Cassia Fault grew less in the south of the study area so that the total throw on both faults remained nearly constant.

The summed throw data of the Cassia and Ironhorse faults are nearly horizontal and resemble the throw distribution characteristic for the central parts of large-scale growth faults, whereas the individual graphs for each fault are more irregular and display opposing trends of increasing throw values along-strike. Thus, the Cassia and Ironhorse faults although physically separate on independent fault planes acted, certainly during interval TP80-TP95, as one large-scale fault.

The throw rates for the aggregate throw on the Cassia and Ironhorse faults exhibits a much smoother trend than the individual graphs (compare Figs. 5.5b and 5.9b to Fig. 5.10c), with an early maximum rate during interval TP77-TP80 and almost steadily decreasing values to the present day. Additionally, the pronounced differences between the graphs at 2 km and 10 km, seen in both Fig. 5.5b and Fig. 5.9b, have disappeared.

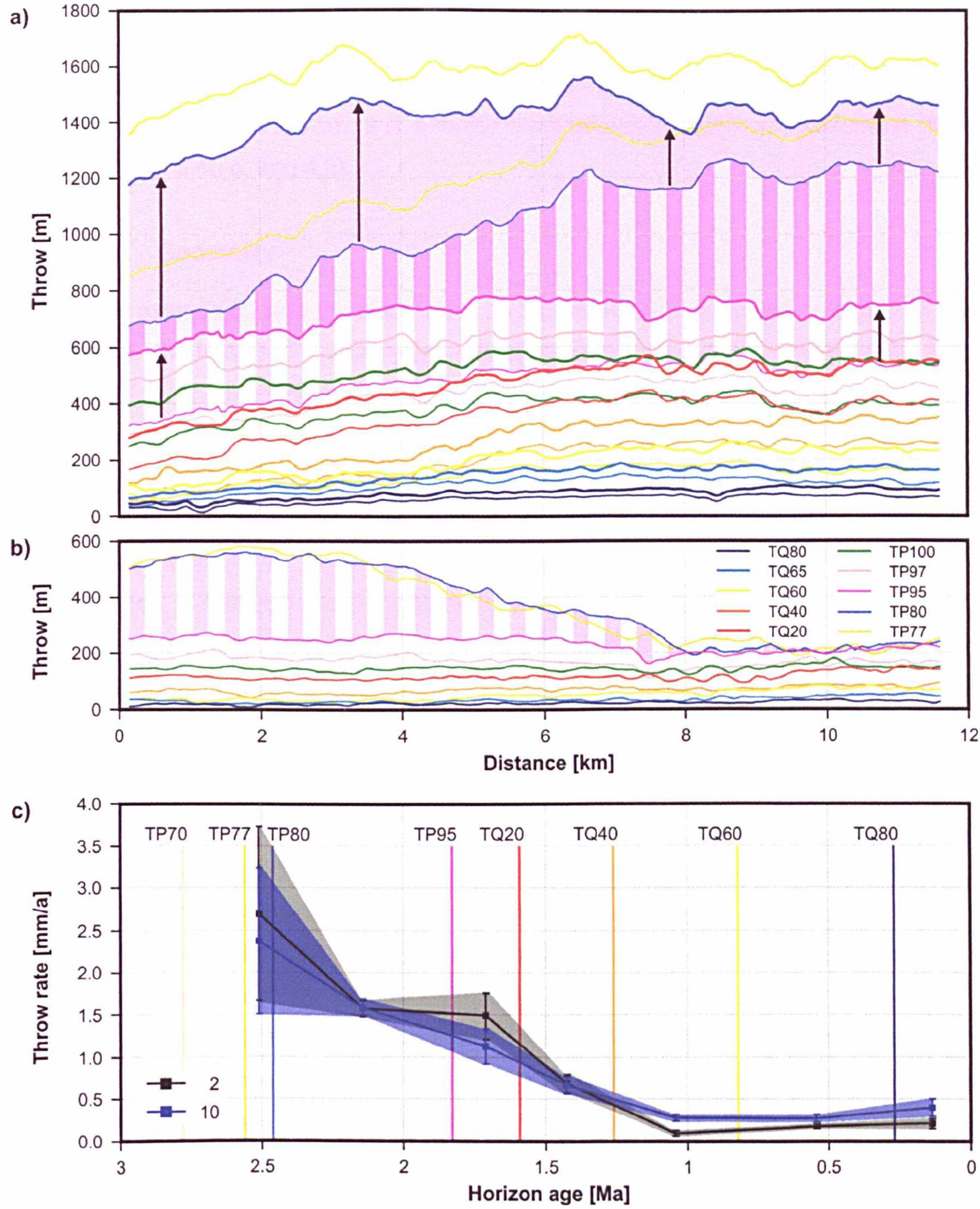

Fig. 5.10: **a)** The throw graphs for the Cassia Fault (thin lines) and the sum between the Cassia and Ironhorse faults (bold). Note the near-horizontal orientation of the new graphs for horizons TP77, TP80, and less pronounced, TP95. The intervalTP80-TP95 is shaded pink for the summed throw and pink and white for the individual faults. In **b)**, the throw graphs for the Ironhorse Fault are shown in the same scale. In **c)**, the throw rates of the aggregate throws on both faults are shown at two locations along strike (compare to Figs. 5.5b and 5.9b).

5.6 G Fault

The G Fault is the largest fault in the study area, with a total length of ~50 km and with a maximum throw of up to 2.5 km. It is a major block-bounding fault in the Columbus Basin (Figs. 5.1, 3.3b, 3.4b-e, and 4.2).

5.6.1 Geometry

The G Fault extends outside the study area, so both fault tips are located outside of it. The fault trends to the NNW in the study area, slightly oblique to the general trend of most other faults (Fig. 5.1). The fault trace is mainly straight with only minor irregularities and is slightly convex towards the hanging wall. The fault can be confidently mapped to depths of ca. 5 km in the available dataset (Fig. 5.11a) and extends further to reach the basal detachment of the Columbus Basin (Figs. 3.4b-e). The strata in the footwall of the G Fault are gently inclined to the north, whereas in the hanging wall they form an anticline whose crest is located at ca. 6-7 km along strike (see horizon TQ40 in Fig. 5.11a).

The oldest horizon that could be mapped in the footwall and hanging wall of the G Fault with available age information is TP100. This limits the reconstruction of the fault evolution to times younger than 1.71 Ma.

5.6.2 Present-day throw distribution

The throw distribution on the G Fault shows sub-parallel throw contours in the upper part of the fault (Fig. 5.11b) and sub-parallel throw graphs in the throw vs. distance diagram (Fig. 5.12a), with a maximum in the south and decreasing throws to the north. Maximum throws of ca. 2500 m are accrued on horizon TP100 in the south. The next younger horizon, TQ20, has in the north ca. 100 m more throw than TP100, whereas in the south it has ca. 100 m less throw. The following horizon, TQ30, has consistently less throw than TQ20, but also slightly more throw than TP100 in the north. All other horizons have progressively less throw the younger they are (Fig. 5.12a).

The anomalous overlap of the throw graphs of horizons TP100, TQ20, and TQ30 might be the result of differential compaction of the footwall and hanging wall strata or the decreasing fault dip with depth, from ca. 50° at horizon TQ30 to ca. 45° at TP100; this accounts for about 8% of the reduction of throw for constant dip displacement. Differential compaction, although potentially significant at differences in burial depth between the footwall (around 2 km) and hanging wall (around 4 km) of TP100 of 1.5-2.5 km (i.e. the amount of throw accumulated) is considered less important, because interval TP100-TQ20 in the hanging wall of the G Fault is affected by over-hydrostatic pore fluid pressures (Fig. 3.6c). This may counteract mechanical compaction and thus might limit the effects of differential compaction for this interval. The effect of decreasing fault dip with depth is discussed in Section 5.6.4.

5.6.3 Interval-throw and back-stripping

The interval-throws for all intervals but the oldest are more or less uniform along strike, slightly decreasing to the north at values of up to 700-800 m for intervals TQ30-TQ40, TQ40-TQ60, TQ60-TQ65, and TQ65-TQ80. Only for intervals TP100-TQ20, TQ20-TQ30, and TQ80-present are values significantly lower (Fig. 5.12b).

During interval TP100-TQ20, throw only accumulated in the southern part of the study area with interval-throws decreasing to zero at about 4 km along strike. This, together with the fairly uniform interval-throw for interval TQ20-TQ30 along the fault trace, suggests formation of an initial fault in the south of the study area during TP100-TQ20, possibly propagating north from a pre-existing fault outside of the study area. Further northward propagation occurred during interval TQ20-TQ30, when the fault traversed the entire study area. From then on, the fault moved at rather similar amounts along strike until the youngest interval. The limitation of throw data for horizons TP100 (1.71 Ma) and younger restricts the determination of the faults earliest initiation in the study area. In the southern part of the study area, the fault was at least active from interval TP100-T20 onward, but might have initiated earlier. In the northern part, the available throw data enables the onset of fault movement to be constrained more precisely to interval TQ20-TQ30.

The throw rates for the G Fault decrease marginally to the north and are as high as 3.5 mm/a for interval TQ30-TQ40 (Fig. 5.13a). The associated errors are mostly significantly lower than the throw rates because of the large interval-throws. The diagram of throw rates with time (Fig. 5.13b) shows low rates for the two oldest intervals, followed by a first maximum during interval TQ30-TQ40. A local minimum during TQ40-TQ60 is followed by a second maximum during TQ60-TQ65 and TQ65-TQ80, and very low values between TQ80 and the present-day. The maximum during intervals TQ60-TQ65 and TQ65-TQ80 interrupts the commonly observed pattern of more or less steadily decreasing throw rates from an early maximum towards the death of the fault (see sections 5.3 and 5.4, see also section 5.7). Fig. 5.13b illustrates the decreasing throw rates to the north with values and error range for the data at 10 km being consistently below those at 2 km, except for interval TQ20-TQ30 where the values are very similar.

The growth indices for three sections along the G Fault are greater than 1.0 indicating synsedimentary faulting, except for the values for 6 km and 10 km for interval TP100-TQ20. These two values correspond well to the evolution of the fault, which had not yet propagated to these positions at this time, and thus indicate post-sedimentary displacement of this interval. The occurrence of values below 1.0 is most likely due to differential compaction of the strata. The fact that these two values (0.95 and 0.96, respectively) are not even lower (0.8-0.9 for interval TP70-TP77 at the Ironhorse Fault, Fig. 5.9), might be due to the presence of pore fluid overpressure in the hanging wall of the G Fault but not those of the

Cassia and Ironhorse faults (Fig. 3.6), which can counteract mechanical compaction and therefore limit the effects of differential compaction.

For the intervals between horizon TQ20 and the present, the growth indices correspond very well to the throw rates. Local maxima of throw rates during interval TQ30-TQ40 and from TQ60 until TQ80 are mirrored by the highest growth indices, whereas for local minima of throw rates during intervals TQ40-TQ60 and TQ80-present, the growth indices show distinctly lower values.

5.6.4 Present-day displacement distribution

The decreasing dip angle of the G Fault with increasing depth (Fig. 5.14) would result in decreasing throw values for constant displacement on the fault due to the trigonometric relationship between these terms (Fig. 2.1). Evaluation of this requires more careful comparison of Figs. 5.15 (dip separation) and Fig. 5.12 (throw).

The throw of horizons TP100 and TQ20 are virtually the same (Fig. 5.12a) with many overlaps; TQ30 has similar throws to TQ20, but generally about 100 m less, especially in the south. All show an overall decrease in throw to the north. The dip-separation graphs of all horizons (Fig. 5.15a) show a similar overall decrease to the north as the throw graphs. However, the dip-separation of TP100 is consistently greater than that of TQ20, which is in turn greater than that of TQ30. Close inspection of the dip separation of TP100 and TQ20 shows two locations at distances of ~5.5 km and ~12 km where the two horizons have the same dip separation. Between 0-4 km and 6-12 km there is a fairly clear difference in separation of ~200 m (Fig. 5.15b).

This modifies the interpretation of the initiation and earliest evolution of the G Fault. The G Fault may have initiated as two separate faults segments during interval TP100-TQ20. These subsequently linked during interval TQ20-TQ30, to extend over most of the study area and then grew more uniformly along strike.

5.6.5 Conclusion

The G Fault is the largest fault in the study area, accumulating maximum throws of ca. 2.5 km. It forms a major block-bounding fault in the Columbus Basin, reaching its basal detachment. At a total length of ca. 50 km, only a part of the G Fault is covered by the 3D seismic survey used for this study. The throw distribution on the G Fault is characterised by sub-parallel throw graphs for most horizons and decreasing throws by 30-50% from south to north across the study area (Fig. 5.12a). The throw graphs of horizons TP100 and TQ20 overlap from about 4.5 km along strike to the north anomalously with higher throw on the younger horizon TQ20 than on TP100, resulting in positive interval-throws in the south and negative ones for the distance of the anomalous overlap. Possible reasons for these apparently lower throw values on horizon TP100 than on TQ20 are the decreasing dip of the fault with increasing depth and differential compaction between the footwall and hanging wall strata.

The decreasing dip angle of the G Fault between the cut-off lines of horizon TP100 and TQ20 is, however, considered crucial since decreasing dip angles result in decreasing throws for equal displacements. Therefore, the throw data determined for the G Fault was compared to the displacement data for the same horizons (Figs. 5.12a and 5.15a). The displacement patterns are, apart from consistently higher values, very similar to the throw patterns for all horizons, except for the relationship between TP100 and TQ20. Importantly, the displacement on TP100 is higher than that on TQ20 over most of the trace length, interrupted by a minimum at about 5-6 km strike distance, which is more distinct in the original than in the smoothed data. The interval-displacement thus suggests the presence of two individual faults or at least two locations of increased displacement accumulation separated by a minimum.

Hence, whereas the interpretation of the throw data suggests the initiation of the G Fault by formation of a small fault in the south of the study area during interval TP100-TQ20, it might have propagated there from further south, and subsequent northward propagation during interval TQ20-TQ30 displacing strata across the entire study area, the displacement data favours the development of two initial faults, which cover together most of the strike distance across the study area and are separated by a distinct displacement low or even unfaulted area at about 5-6 km during interval TP100-TQ20, and linkage and subsequent uniform growth during interval TQ20-TQ30. These varying interpretations of the initial size and location of the G Fault underline the importance of integration of different datasets in order to best constrain a faults evolution.

The throw rates determined for the G Fault are up to 3.5 mm/a during interval TQ30-TQ40. These are the highest measured in the study area. The trend of the throw rate observed for the G Fault is confirmed by the age-independent growth indices, which correlate very well with the succession of maxima and minima observed. With very high throw rates during the younger half of its activity, the G Fault displays a very different trend compared to that of the Cassia and Ironhorse faults, both of which have highest throw rates during earlier stages of their evolution and more-or-less steadily decreasing rates during their later stages (compare Figs. 5.5b, 5.9b, 5.10c, and 5.13b).

5.6.6 Figures

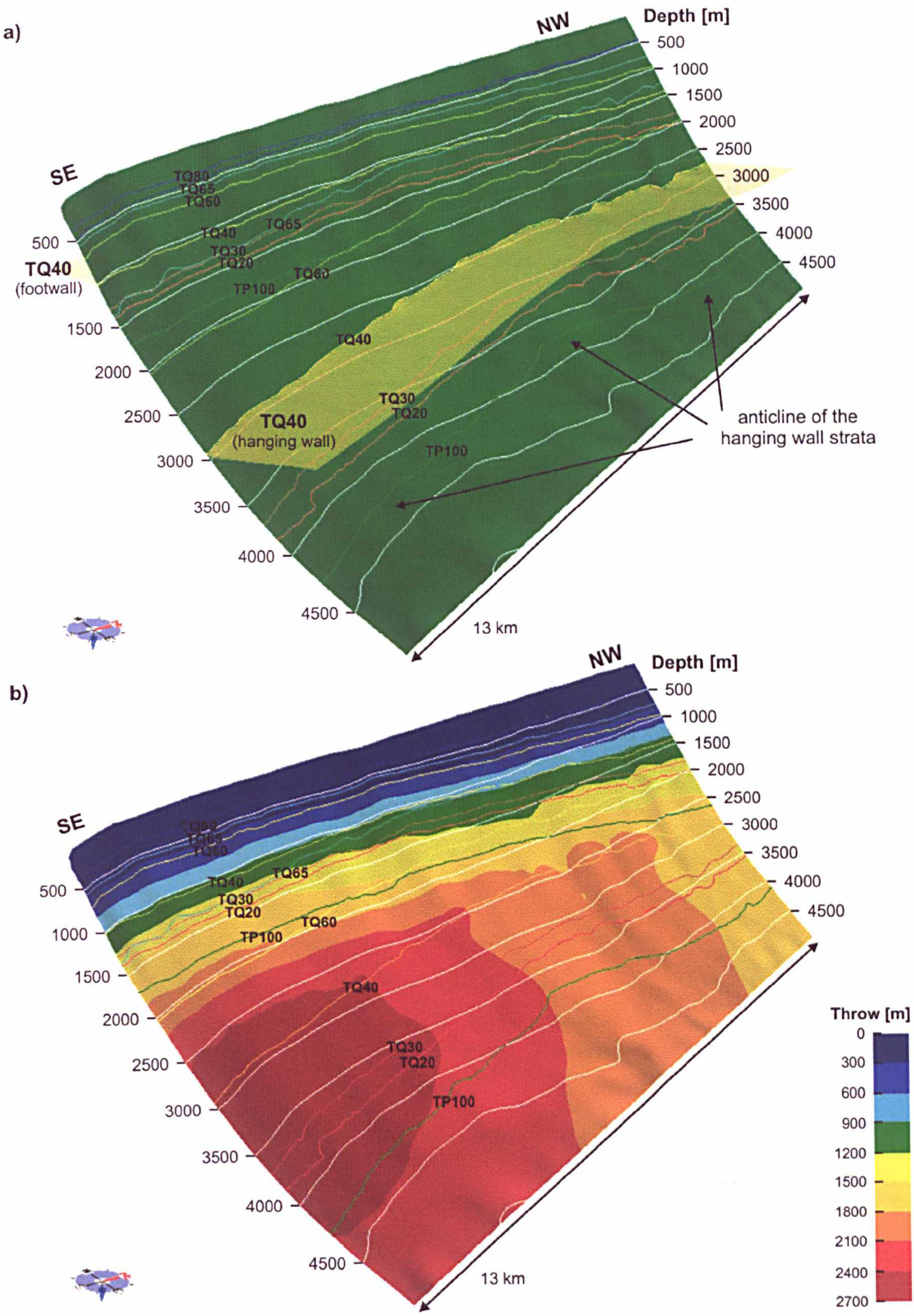

Fig. 5.11: 3D view of the fault, illustrating in **a)** the general geometry and in **b)** the throw distribution with indication of the horizon cut-off lines. Cut-off lines are annotated for the FW on the left and the HW on the right. Note the broad anticline in the HW of the G Fault and the sub-horizontal orientation of the throw contours in the upper half of the fault, which are an indicator of syn-sedimentary fault movement.

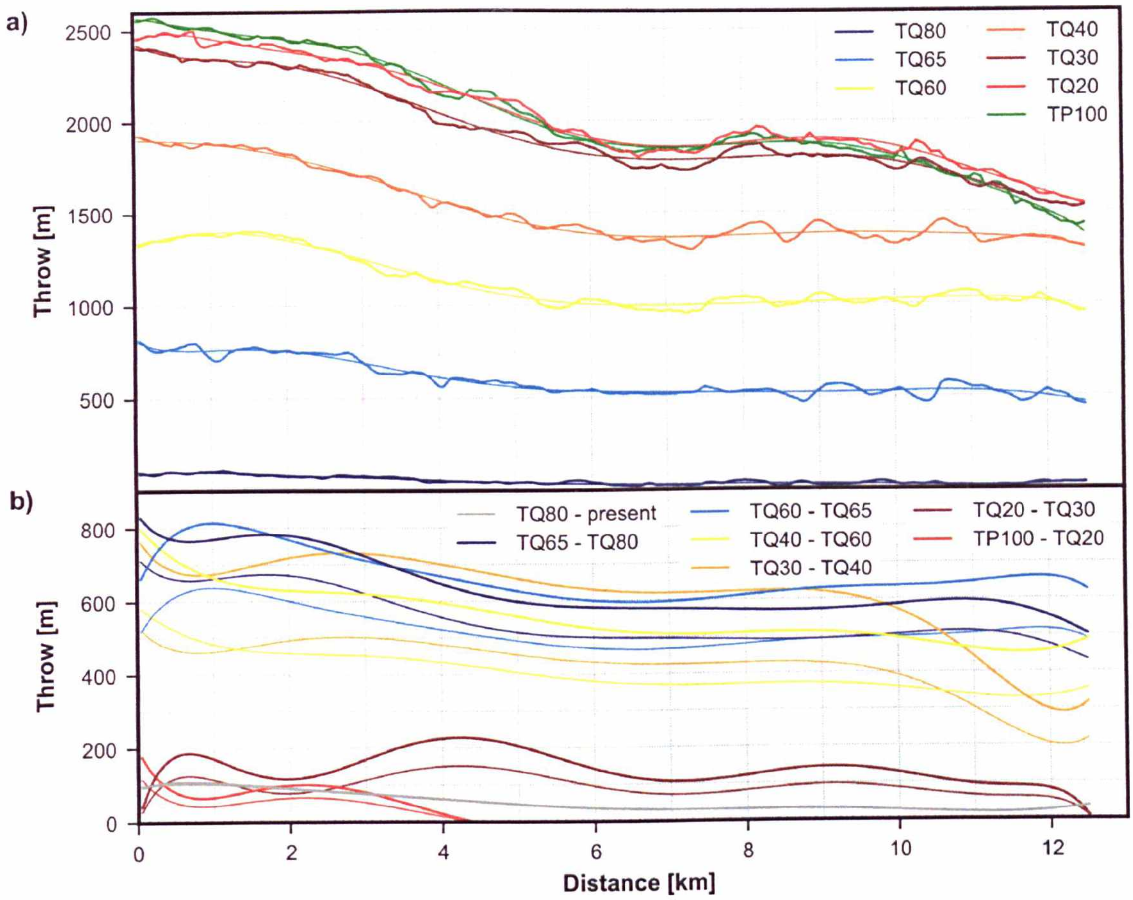

Fig. 5.12: **a)** The original throw data for all horizons and the smoothed throws for the G Fault. Note the sub-parallel throw graphs for all horizons, and the decreasing throw values to the north. In **b)**, the interval-throws are shown for each interval as determined for the present-day (thin line), and decompacted (bold line) to initial amounts at the time of deposition of the upper interval boundary.

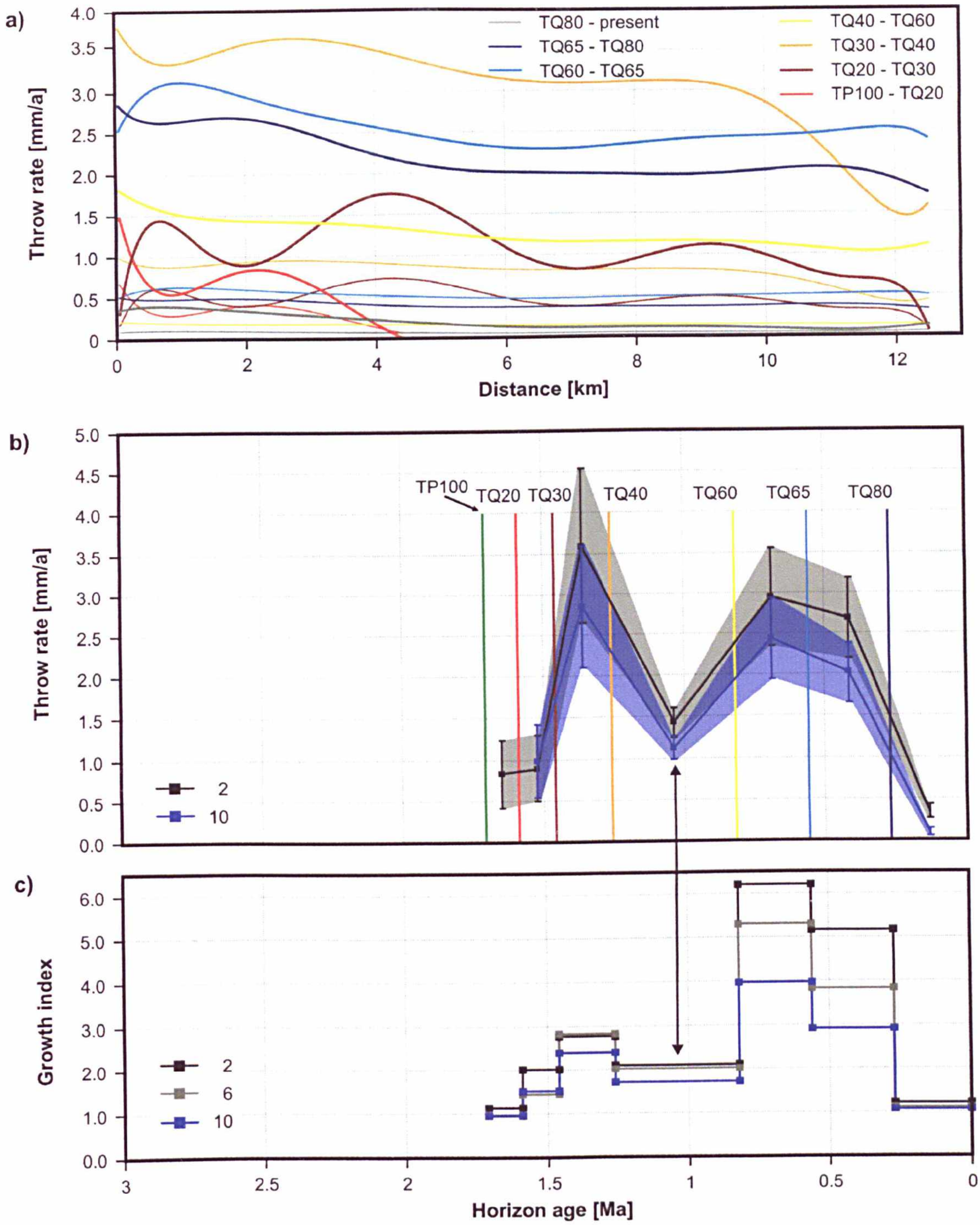

Fig. 5.13: **a)** Throw rates for all intervals (bold) and the associated errors (thin lines) for the G Fault. In **b)**, the throw rates and their errors (shaded) are shown for two locations on the fault, 2 km and 10 km. In **c)**, the growth indices for three locations on the fault are presented, 2 km, 6 km, and 10 km. Note the good correlation between low throw rates in b) and growth indices close to 1.0 in c) and the growth indices below 1.0 for the oldest interval TP70-TP77 that was displaced after deposition.

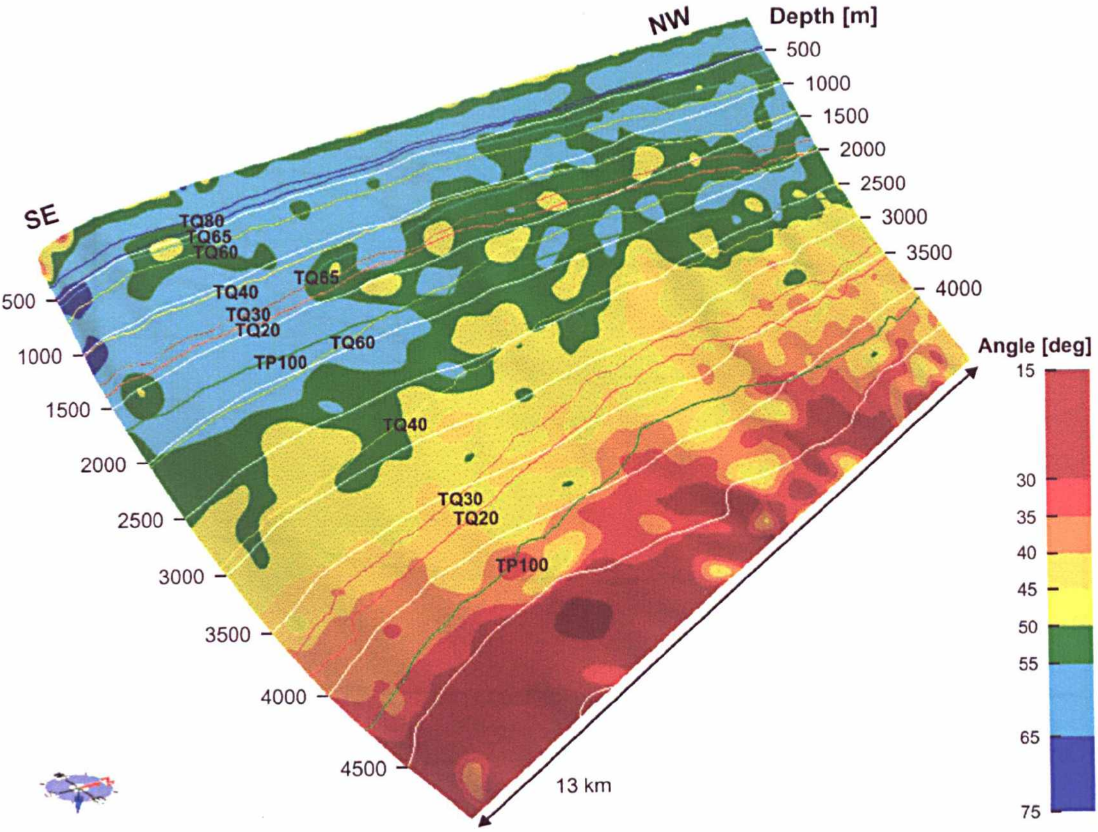

Fig. 5.14: 3D view of the G Fault, illustrating the fault surface dip with indication of the horizon cut-off lines and depth.

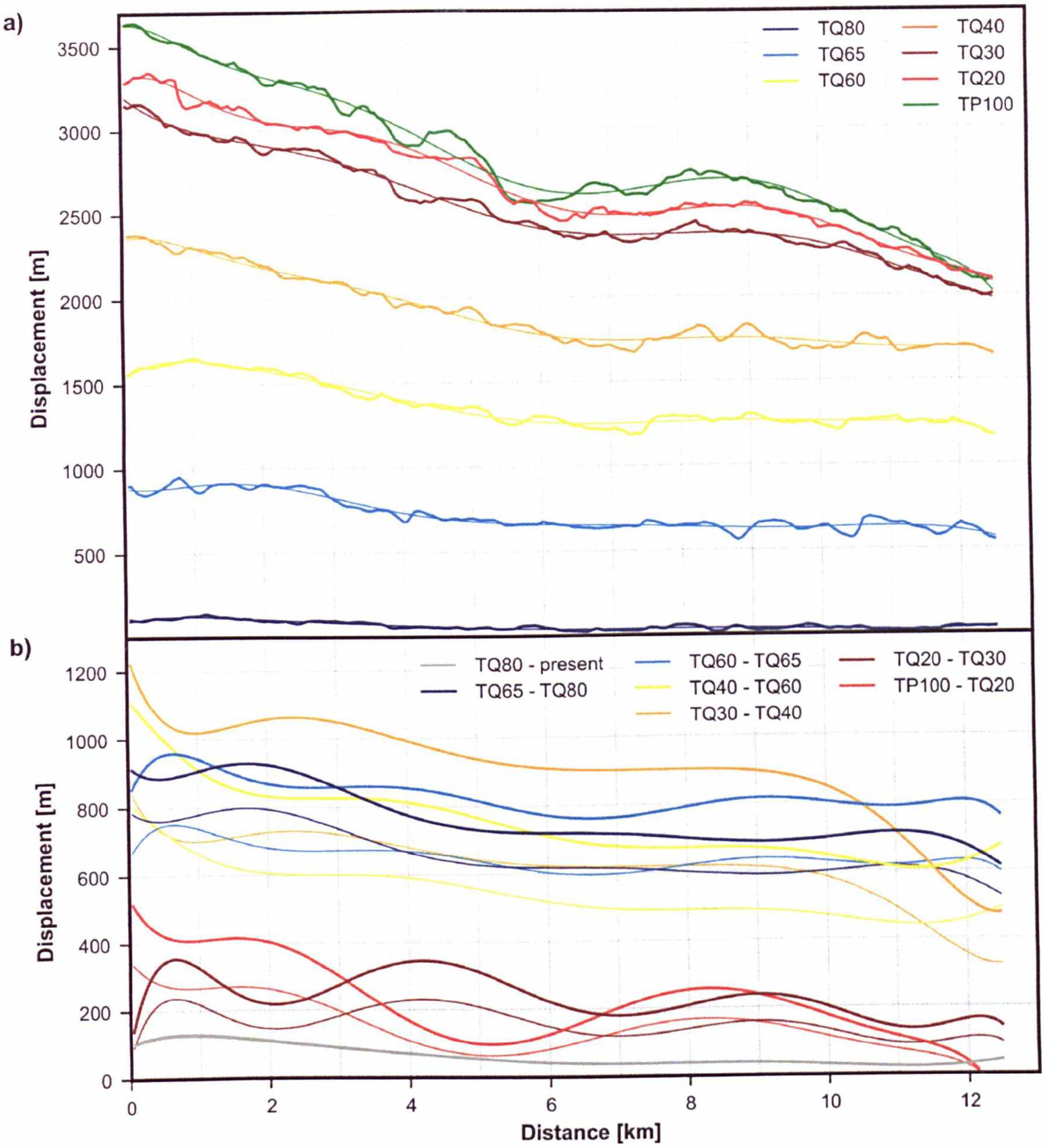

Fig. 5.15: **a)** The original and smoothed displacement data for all horizons for the G Fault (compare to Fig. 5.12). Note the great similarity of the patterns of displacement data and throw data for horizons TQ30-TQ80. In **b)**, the interval-displacements are shown for each interval as determined for the present-day (thin line), and decompacted (bold line) to initial amounts at the time of deposition of the upper interval boundary.

5.7 Fault system d

Fault system **d** is located in the west of the study area and provides an excellent example of a system of initially unconnected overlapping faults that subsequently linked to form a larger, through-going fault.

5.7.1 Geometry

The strike length of the entire fault system **d** is about 8.5 km. The maximum mappable vertical extent of the fault surface at the centre of the fault is about 3 km. The northern lateral tip of the fault is located outside the seismic survey for horizons TP85-TP100. There, the throw data were manually extended to zero throw using the respective throw gradient of each horizon adjacent to the missing data points.

At depth (e.g. 2740 m in Figs. 5.16 and 5.17a), the fault system consists of two overlapping faults, separated by a relay ramp. The faults are sub-parallel and are about 500 m apart. They both dip and down-throw to the NE. At shallower depths (e.g. at 2130 m in Fig. 5.17b), the breaching fault is present, connecting the main fault segments at an angle of ca. 45°. Shallower still (e.g. at 1520 m in Fig. 5.17c), the eastern splay has disappeared and the western splay has become shorter and isolated from the fault plane. Towards the upper tip of the fault (e.g. 1220 m and 610 m in Fig. 5.17d & e), the fault consists entirely of the main segments and the breaching fault, and the trace becomes progressively smoother.

Thus, in the central part, fault system **d** consists of five distinct fault segments: two main segments to the north and south (d-s and d-n), two abandoned splays to the east and west (d-e and d-w) and a breaching fault (d-b) (Figs. 5.16 and 5.17). The main fault segments are parallel and synthetic, and are each extended by one of the splays towards a fault overlap zone. The splays can be mapped to similar depths as the major segments but stop at about two thirds of the present-day vertical height of the fault plane. The contact between the splays and the major segments are vertical branch lines at positions 8.3 km and 8.8 km along strike. The breaching fault connects the main segments obliquely between the same branch lines but does not reach as deep as the other fault segments. It can be mapped about two thirds down from the upper tip of the present-day fault plane and is one of the few faults in the dataset where the lower fault tip can be confidently mapped.

5.7.2 Present-day throw distribution

The present-day throw graphs (Figs. 5.18 and 5.19) define two individual, single-fault profiles for the older horizons (TP80, TP85, TP88, TP95, and TP97), that overlap for ca. 1 km along strike. Each fault has separate throw maxima of ca. 140 m and is between 3.5 km and 5.5 km long at the level of horizon TP88. The throw graphs of horizons TP80 and TP85 are irregular and show for the most part less throw than the younger horizon TP88 (except TP85 at ca. 11 km), which indicates post-sedimentary displacement of these horizons (Fig.

5.19). Hence, horizons TP80 and TP85 were not considered in the reconstruction of the fault evolution.

For the younger horizons (TP100-TQ80), the throw graphs resemble those of single faults, having only one, approximately central throw maximum each. They exhibit progressively decreasing fault trace lengths and throw maxima towards the youngest horizon as a result of tip line retreat and the eventual death of the fault.

The throw profiles of the breaching fault show a general trend of decreasing throw from north to south along the fault (Figs. 5.18a and 5.20). The highest throws on the breaching fault are present on horizon TP97 in the north with ca. 75 m and on horizon TP100 in the south with ca. 55 m. Lower throw values are observed for both older and younger horizons.

5.7.3 Interval-throw and back-stripping

The back-stripped throw data for all horizon intervals show significant along-strike variations of throw accumulation over time (Fig. 5.21b), and the interval-throws are small (less than 40 m) even after decompaction. The only higher interval-throw of ca. 60 m for TP95-TP97 on the d-e splay (* in Fig. 5.21b) reflects the sudden decrease in throw between these two horizons due to progressive abandonment of this splay rather than continuous growth of the fault.

Initially, this fault system consisted of only two individual faults during the oldest interval investigated here, TP88-TP95. In the following interval, TP95-TP97, two individual faults were still present: overlapping to form a relay ramp and probably propagating laterally to the present-day trace lengths of the main segments.

Full linkage was achieved at about the time of deposition of horizon TP100, which is indicated by the deaths of the abandoned splays: TP97 is the youngest horizon displaced by splay d-e (less than 20 m throw) and TP100 is the youngest horizon displaced by splay d-w (ca. 6 m of throw). Afterwards, the fault moved along the newly established fault trace consisting of the southern segment, the breaching fault and the northern segment. This is also indicated by the throw profiles of the breaching fault, where for horizons TP100 and younger, the throw data on the breaching fault and the main segments form a smooth continuous transition in contrast to the situation on horizons TP88-TP97, where large steps exist between the throw on the breaching fault and the neighbouring fault segments (Fig. 5.20a). The breaching fault has its throw maximum on horizon TP97 in the NW and on TP100 in the SE (Fig. 5.20b). This indicates propagation of the breaching fault from the NW, the northern main segment, towards the SE, the southern main segment over two time intervals: during TP95-TP97 the propagation of the breaching fault begins and it intersects the seabed, and during TP97-TP100 linkage to the southern main segment is completed.

The high throw on the breaching fault on horizon TP88 in the NW indicates an earlier stage of initiation of the breaching fault before it propagated to connect the main segments. The breaching fault most likely originated as a blind splay of the northern main segment and was later reactivated and intersected the seabed prior to deposition of TP97 (see also Fig. 5.24).

The interval-throw distribution seen in Fig. 5.21 shows distinct maxima of fault throw accumulation on either side of the breaching fault even after linkage took place. This is particularly the case for intervals TP100-TQ20, immediately after linkage was completed, and TQ40-TQ60.

Interval-throw minima at the breaching fault indicate that it acts, at least partly, as an obstruction to throw accumulation through reduced slip tendency and probably as well as a barrier to rupture propagation, which would limit some rupture events to one side of the breaching fault and thus favour asymmetric accumulation of throw on either side of the breaching fault. Thus, throw maxima on either side of the breaching fault indicate preservation of individual behaviour of both initial segments even after fault linkage took place. Only towards the upper tip of the fault, intervals TQ60-TQ80 and TQ80-present, a single maximum develops, resembling the throw profile on a single fault.

This fault behaviour displays a delay between the time when geometric linkage (i.e. a physical connection between the fault planes) is established and the achievement of kinematic linkage (i.e. movement of the newly established fault as an entity). The presence of individual throw maxima after geometric linkage suggests that geometric and kinematic linkage are not necessarily simultaneous but that kinematic linkage can occur some time after geometric linkage was reached.

Throw rates determined for fault system **d** are low at values generally below 0.15 mm/a and a maximum of less than 0.4 mm/a (Fig. 5.22a). The throw rates are associated with large errors (90-250%) that are higher towards the fault/interval tips, due to the small initial interval-throw values and short interval durations for some intervals (see Section 4.6). Nevertheless, a decrease of throw rates over most of the faults lifetime can be shown (Fig. 5.22b). The throw rate for the oldest time interval is below 0.1 mm/a, followed by a steep increase for interval TP95-TP100 to values of around 0.25 mm/a and a steep decrease during interval TP100-TQ20 to values again below 0.1 mm/a. For all younger time intervals and towards the death of the fault during interval TQ80-present, the throw rates are consistently low.

Despite the large errors, the high throw rates during interval TP95-TP100 are supported by the independent measure of the growth index (Fig. 5.23b). This shows a maximum with values over 1.1, i.e. higher thickness of the hanging wall than the footwall strata, for the central parts of the southern and northern segments for this interval and hence confirms greatest fault displacement during interval TP95-TP100.

5.7.4 Growth indices

With ca. 140 m maximum throw, fault system **d** is a smaller example of the well-imaged faults in the study area. The question arises, whether the fault is a growth fault or a blind fault. The relatively low throw creates only minimal thickness variations between the footwall and hanging wall intervals. Growth indices can be used to determine and compare thickness variations across faults and are defined in several ways. The simple ratio of the (vertical) thicknesses (hanging wall thickness / footwall thickness) is used here. A possible alternative was suggested by CHILDS et al. (2003) as (hanging wall thickness – footwall thickness / footwall thickness), which expresses the relative ratio of throw rate and footwall sedimentation rate. CHILDS et al. (2003) conclude that growth indices below 0.1, which denote more than 10 times higher sedimentation rates than throw rates, are typical for post-sedimentary faults. However, they have also shown that growth indices in the upper part of a syn-sedimentary fault (ca. 7 km trace length and 200 m maximum throw) can be as low as 0.01 towards the lateral tips. The value of <0.1 in the growth index of CHILDS et al. (2003), as a possible threshold to distinguish post-sedimentary from syn-sedimentary faults, corresponds to <1.1 for the thickness ratio used here.

The growth indices on six sections on faults system **d** (two sections each for the southern segment, northern segment and the breaching fault) are shown in Fig. 5.23b. For horizon intervals younger than 1.71 Ma (horizon TP100) all growth indices are above 1.0, indicating hanging wall thicknesses greater than FW thicknesses but only reach values of 1.1 or greater for a few intervals on the southern and northern fault segments. During the interval 1.83-1.71 Ma (TP95-TP100), the values for the main fault segments are greater than 1.0 and indicate syn-faulting accumulation of sediments on the hanging wall; only for the breaching fault do the data suggests post-sedimentary faulting. During the oldest time interval, all data points apart from one for the breaching fault (see below) are below 1.0, suggesting post-sedimentary displacement on the units. These values might, however, be due to differential compaction between the footwall and hanging wall, masking subtle thickness changes.

The throw rates for fault system **d** are much lower than the sedimentation rate determined for well A (see Section 4.1.5). Well A is located in the footwall of the Cassia Fault, and this footwall sedimentation rate for the most landward position in the study area can be considered equal to or a minimum for all other locations in the study area. The much higher sedimentation rates than throw rates might mask the increased sediment thickness in the hanging wall due to fault movement substantially, and thus make it difficult to identify fault system **d** as syn-sedimentary. However, the asymmetric throw vs. depth graphs for all parts of fault system **d** (Fig. 5.23a), showing lower vertical throw gradients above the respective throw maxima and higher throw gradient below them due to the accommodation of post-sedimentary displacement on the oldest two horizons, TP80 and TP85, suggest the syn-sedimentary nature of this fault system.

5.7.5 Conclusion

Fault system **d** provides an example of a fault system that evolved from two initially separate faults, with an overlapping region forming a relay ramp. As the fault developed, the linking region produced a fault system with five fault segments: two main segments to the south and north, linked by a breaching fault, leaving two splays behind that are co-planar with the main faults and were previously part of the main segments. These splays were subsequently abandoned and are not seen in the upper parts of the fault, where a single, non-linear, fault trace developed.

The reconstruction of interval-throws reveals the lateral propagation of two initially independent segments, and the timing and direction of growth of the breaching fault, which links them.

The timing of fault linkage is also constrained by both the vertical extent of the abandoned splays and the throw distribution on the breaching fault itself. Linkage took place over the intervals between horizons TP97 and TQ20. The splay in continuation of the southern main segment (d-e), ceased to be active before deposition of TP100: it displaces TP97 by less than 20 m. The splay in continuation of the northern main segment (d-w) was active until after the deposition of TP100, displacing it by less than 6 m. Abandonment of the splays suggests the availability of an alternative plane of movement, the breaching fault, which accommodates displacement on the now continuous fault plane.

The breaching fault initiated during interval TP88-95, prior to its main phase of propagation, as a blind synthetic hanging wall splay of the northern main segment and was later reactivated as a syn-sedimentary fault (Fig. 5.24). The breaching fault propagated from the northern main segment towards the southern main segment over the intervals TP95-TP97 and TP97-TP100, which is evident from the maximum throw on the breaching fault in the northwest on horizon TP97 and in the southeast on TP100 (Fig. 5.20).

The interval-throws accumulated after deposition of horizon TP100, particularly during TP100-TQ20 and TQ40-TQ60, show distinct throw maxima at either side of the breaching fault and minima at/near the position of the breaching fault (Fig. 5.21c&d). Interval-throw maxima on either side on the breaching fault, after geometric linkage was achieved at about the time of deposition of TP100, indicate that geometric linkage, the physical connection of the main segments via a breaching fault, and kinematic linkage, movement along the newly established fault plane and the existing main segments as an entity, are decoupled in this fault system. Only towards the upper tip of the fault does a single interval-throw maximum develop (Fig. 5.21), which resembles the throw profile on a single fault (WALSH & WATTERSON, 1989; CHILDS et al., 2003). Geometric linkage therefore predates kinematic linkage, when the fault has a continuous throw profile with a single maximum.

5.7.6 Figures

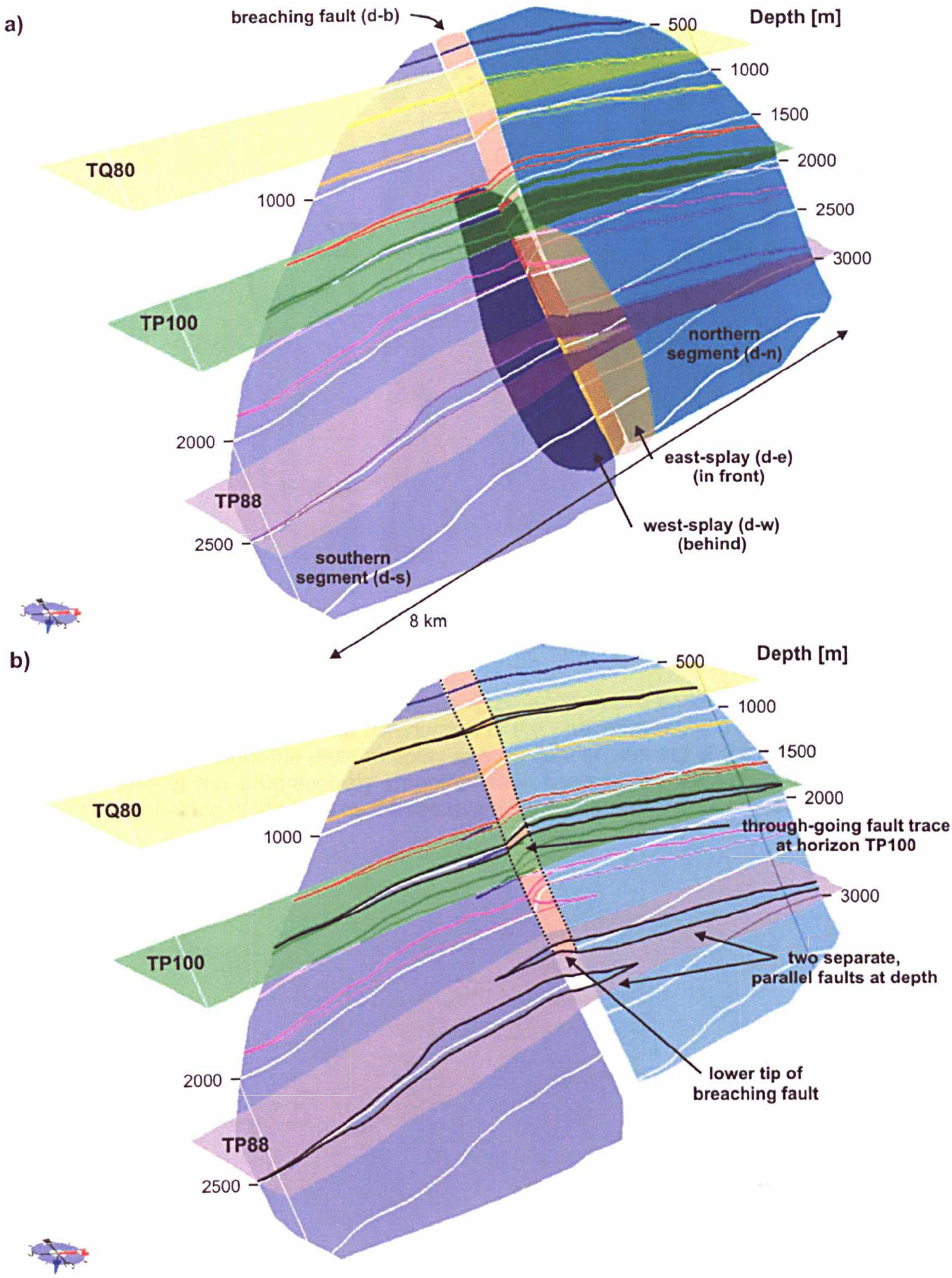

Fig. 5.16: 3D views of the fault system. In **a)** all five fault segments are shown, whereas in **b)** only the southern and northern segments and the breaching fault are shown. Note the cut-off lines of the different horizons illustrating the change in geometry from two overlapping faults at depth to a continuous fault trace at shallow levels. View from the hanging wall onto the fault surface.

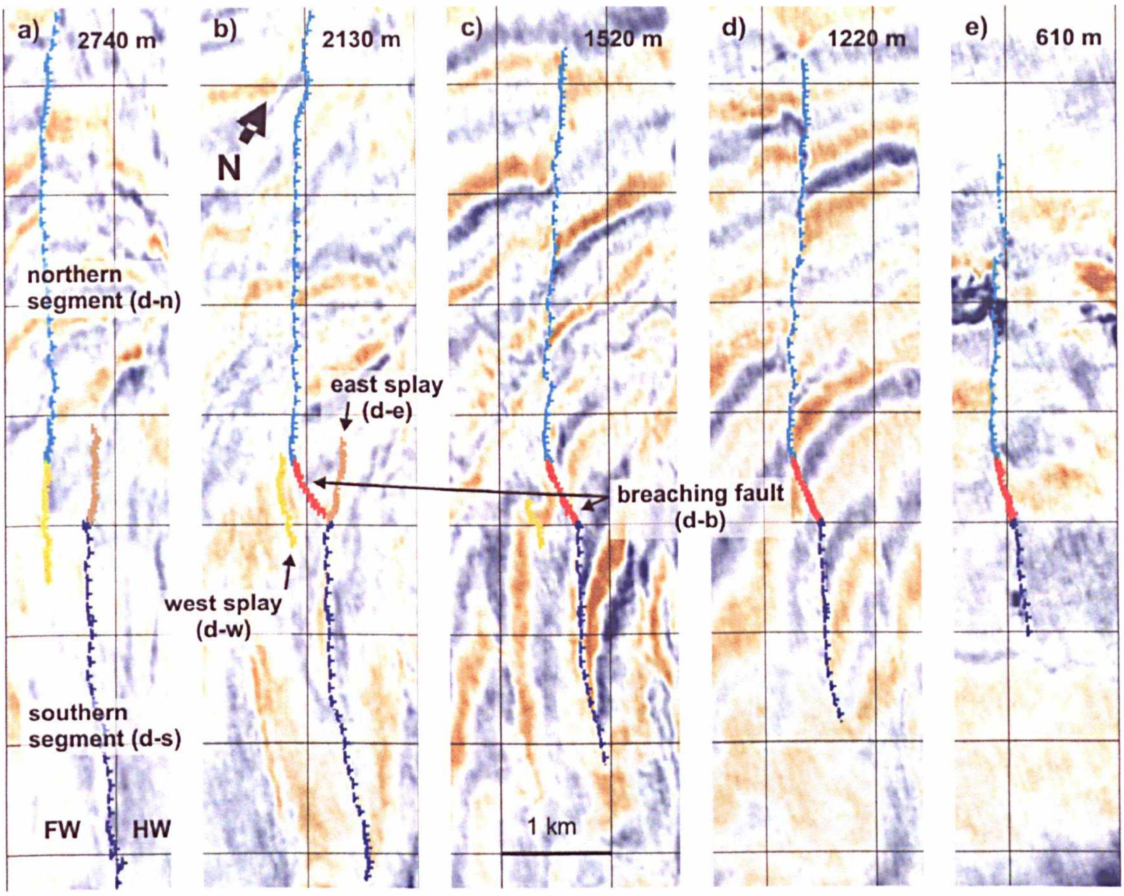

Fig. 5.17: Depth slices at five different levels showing in **a)** two parallel, synthetic, overlapping faults at depth, in **b)** the introduction of the oblique breaching fault, and in **c)** the disappearance of the eastern splay and gradual shortening of the western splay. In **d)** and **e)** the progressively smoother fault trace of the through-going fault and the shortening of the total fault trace due to tip-line retreat are illustrated.

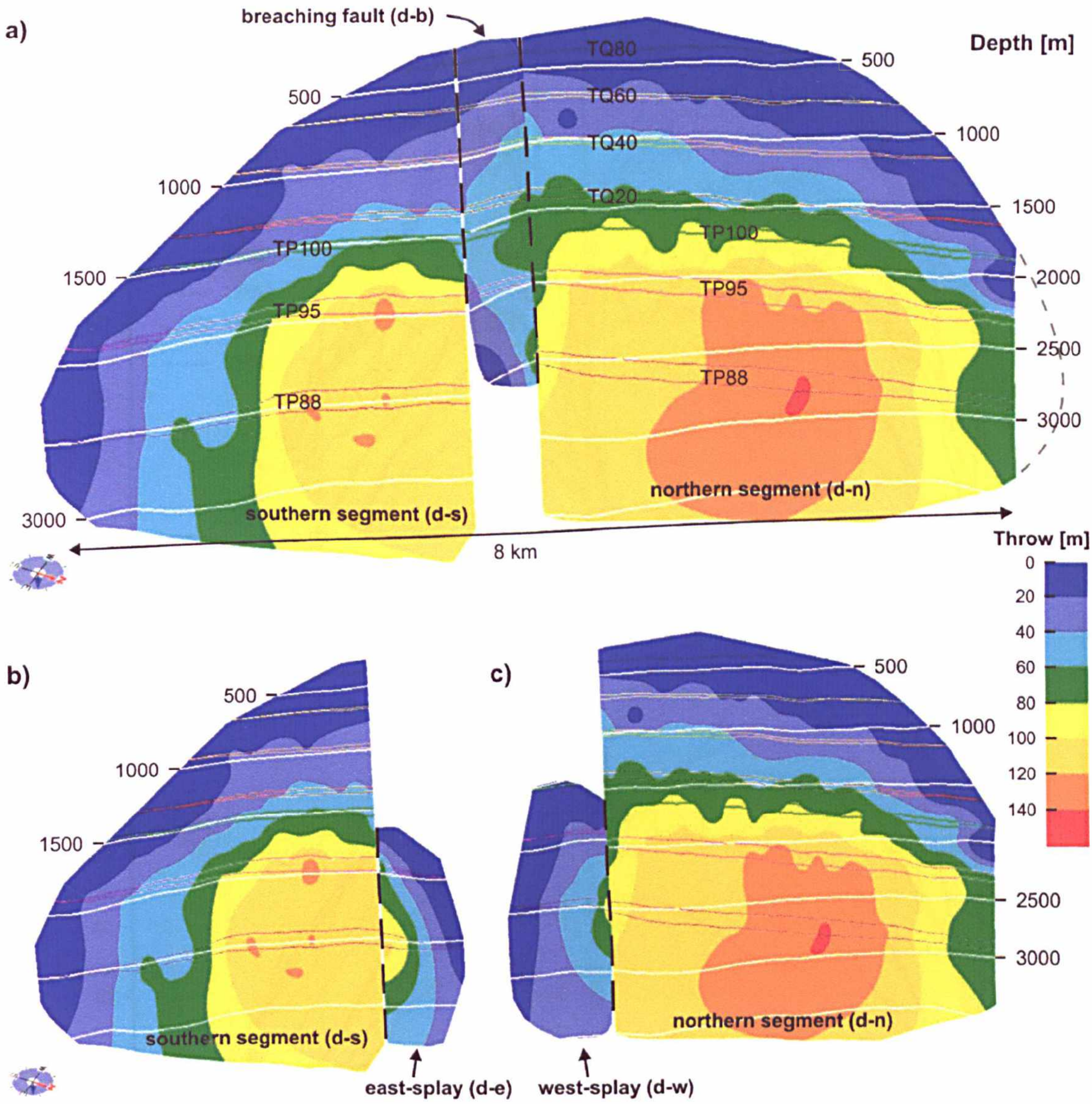

Fig. 5.18: Throw contoured on the fault surface for **a)** the southern and northern segments and the breaching fault, and in **b)** for the southern and northern segments and their respective abandoned splays. View from the hanging wall onto the fault surface, branch lines are dashed. Note the near-horizontal orientation of the throw contours of 60 m and 100 m, indicating syn-sedimentary fault movement (CHILDS et al., 2003). Note the horizon cut-off lines from which the throw data is calculated (note that those for horizons TP80, TP85, and TP97 were omitted).

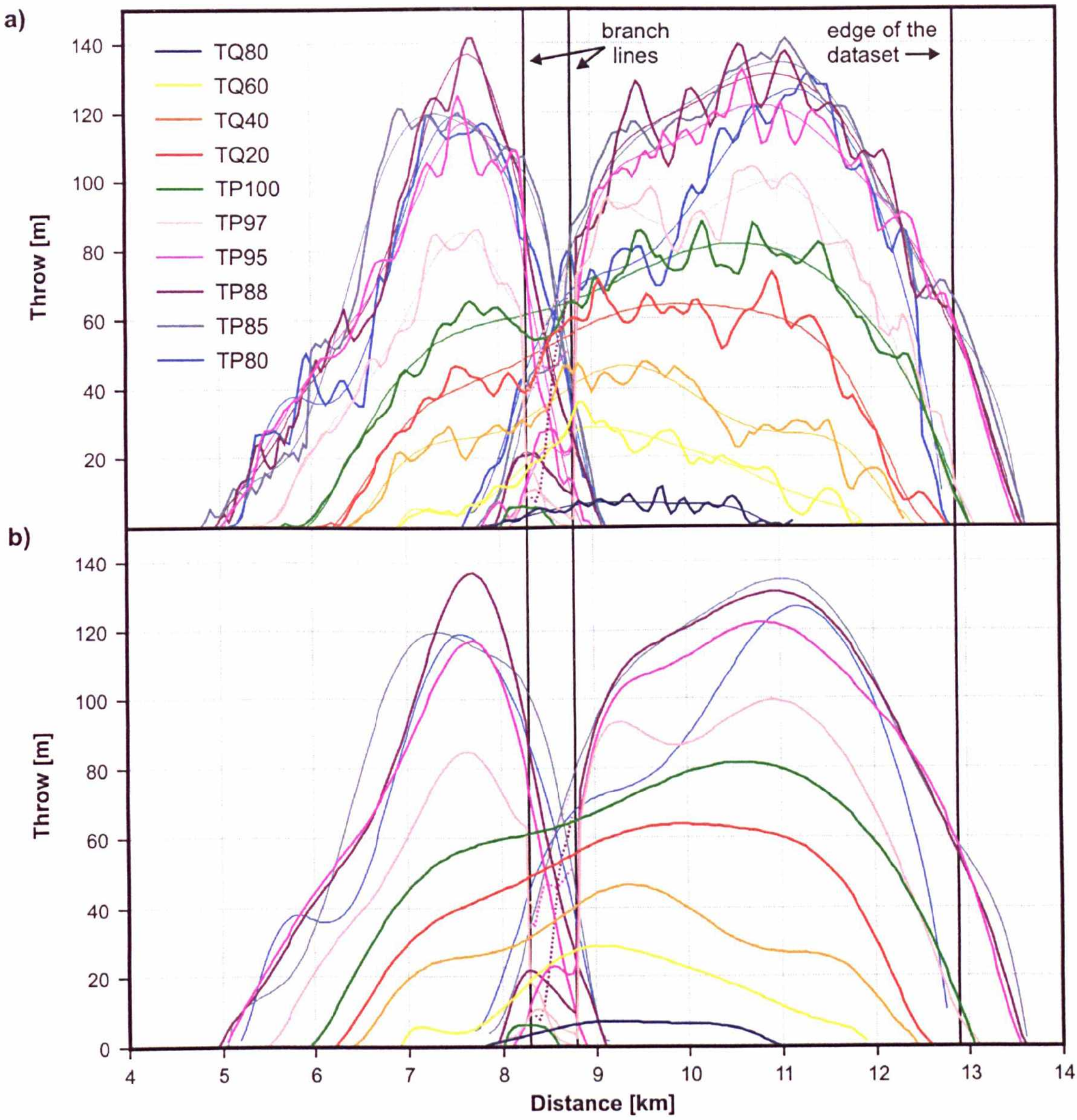

Fig. 5.19: **a)** Fault throw profiles of fault system **d** showing the two distinct maxima for the individual fault segments of older horizons (TP80-TP97) and continuous, single-maximum throw graphs for the younger horizons (TP100-TQ80). **b)** Smoothed graphs of the respective throw data. Note the branch lines, between which the breaching fault connects the main fault segments d-s and d-n and which also form the boundary between the main segments and the eventually abandoned splays d-e and d-w. The throw accumulated on the breaching fault on the old horizons TP88, TP95 and TP97 is shown as dotted lines. Throw data at the northern fault tip (beyond 12.9 km) was extrapolated manually using the respective gradient on the relevant horizons, TP85-TP100.

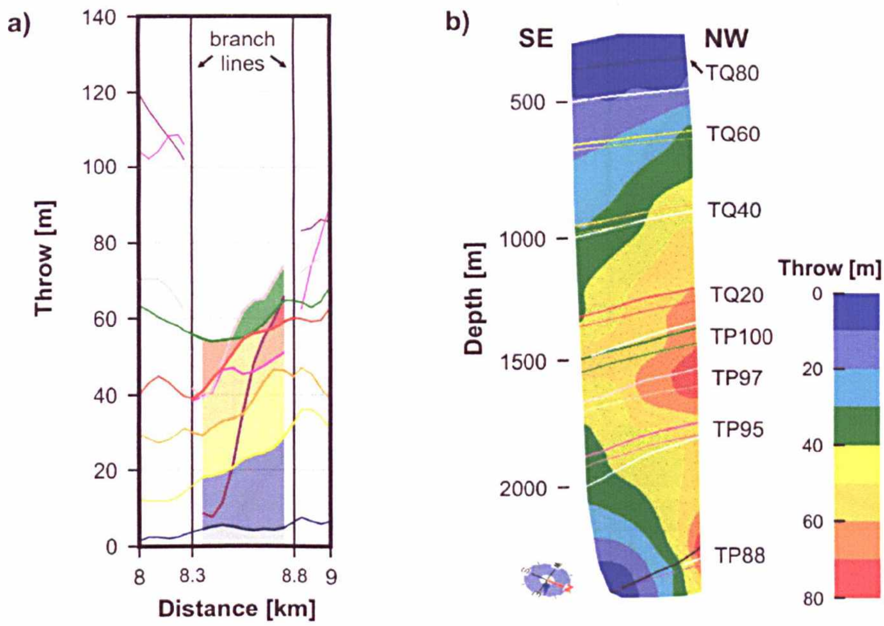

Fig. 5.20: **a)** Throw graphs on the breaching fault and on the adjacent southern and northern segments with shading of the respective interval-throws, and **b)** throw contours projected onto the fault plane illustrating the throw maxima at horizons TP97 and TP88.

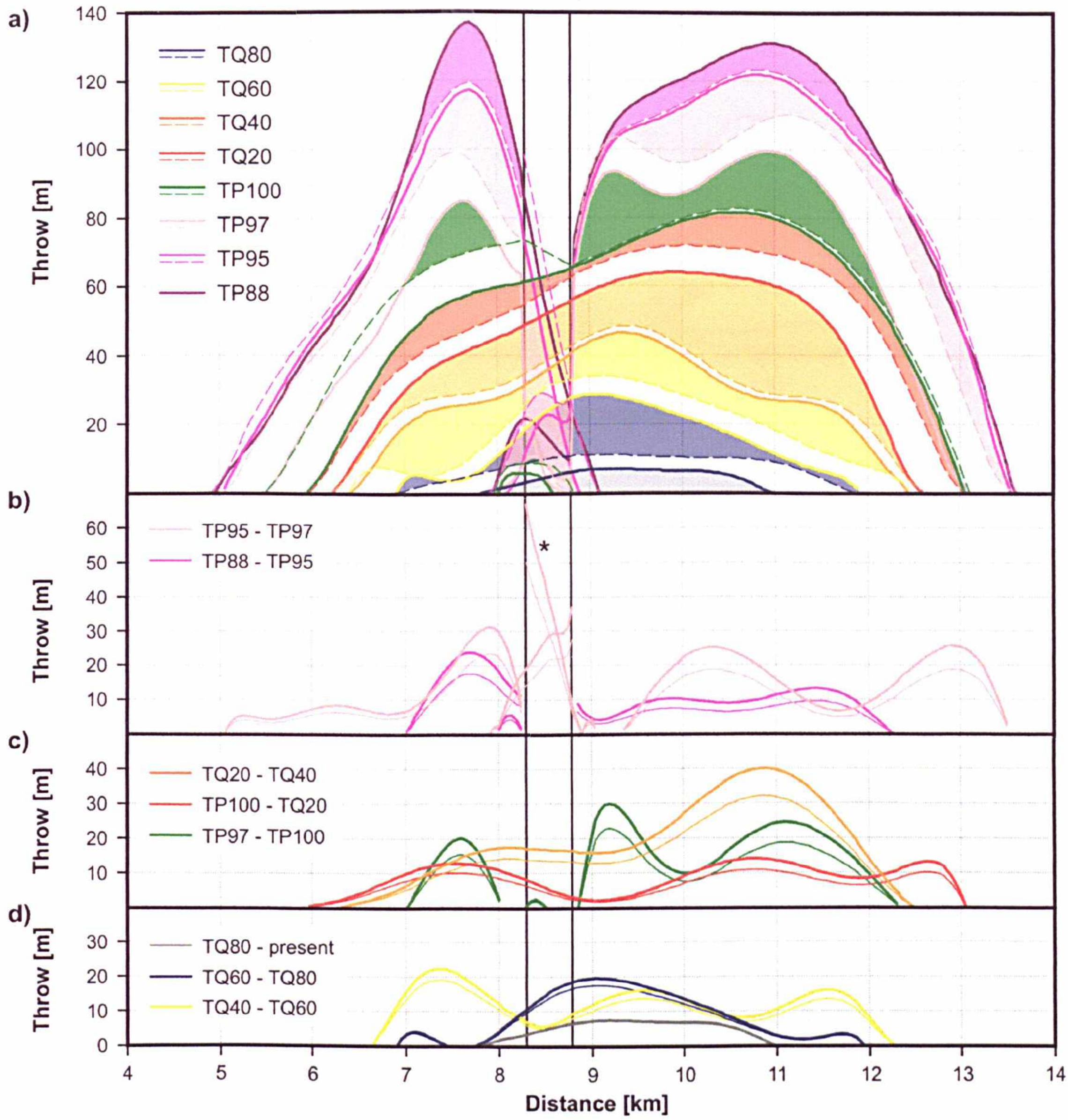

Fig. 5.21: **a)** Diagram of the smoothed present-day throw data (bold) and the graphs of each horizon trace extended to the next older horizon (dashed). The resulting interval throws are highlighted in the colour of the younger interval bounding horizon (see Fig. 5.2). **b)**, **c)**, and **d)** show the interval throws for successive intervals, which were decompacted (bold) from the present-day measurements (thin lines) in order to represent initial values immediately after deposition of each horizon interval.

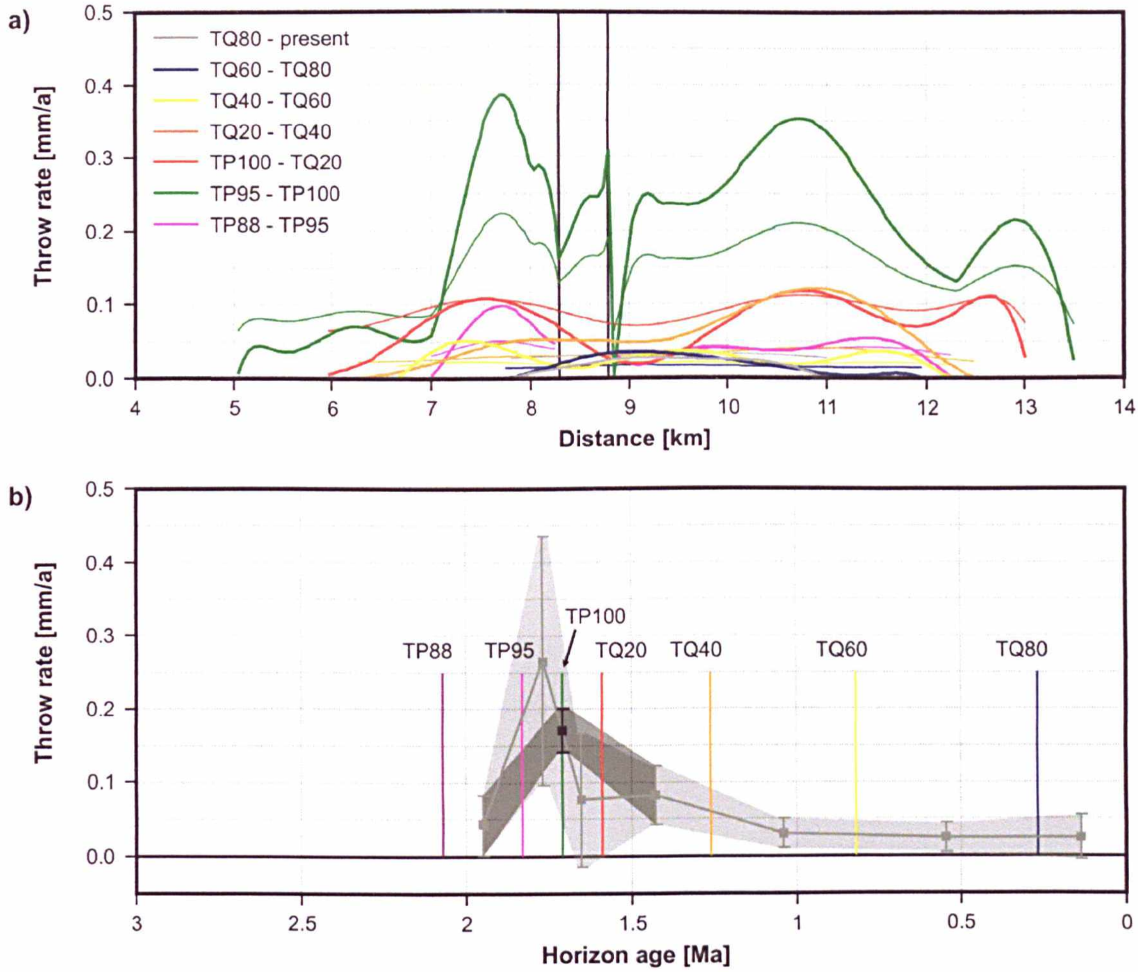

Fig. 5.22: **a)** Throw rates (bold) and associated total errors (thin lines) for fault system **d** for a number of time intervals. The large errors are due to the small interval throws accumulated on the fault and the short durations of some time intervals. **b)** Throw rate vs. horizon age plot for a cross-section at 10 km. The grey graph and error bars represent values for the intervals shown in a), whereas the black data point and error bars were calculated for the longer interval TP95-TQ20 in order the show the influence of the interval duration on the throw rate results. Note that the throw rate for the longer time interval still represents a maximum compared to all other time intervals and thus points to higher fault activity during this period despite the large errors on the data for interval TP95-TP100.

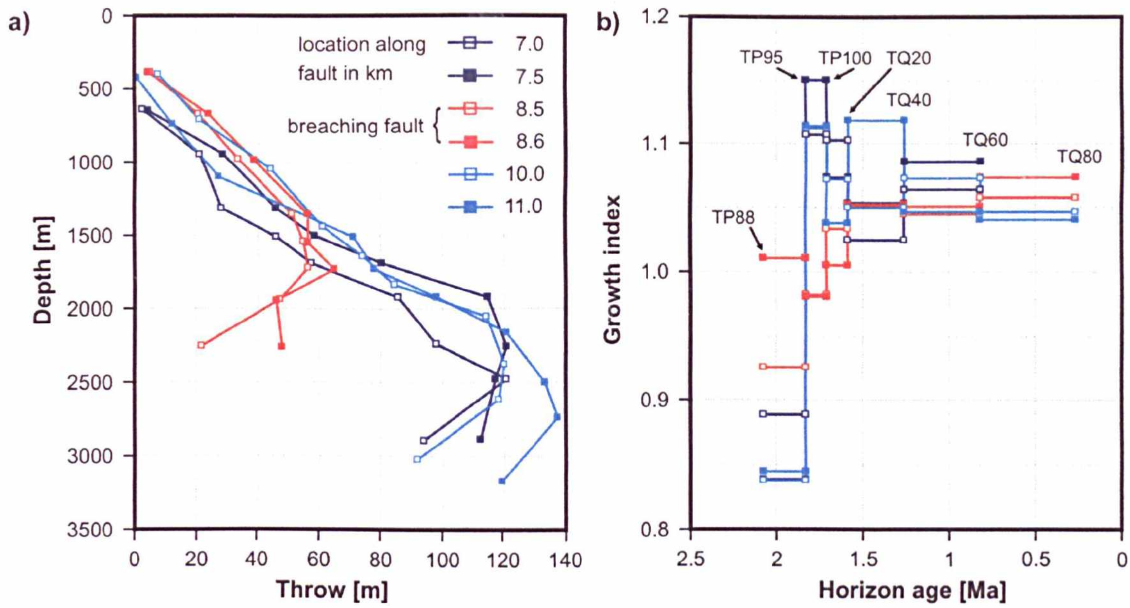

Fig. 5.23: **a)** Throw vs. depth graphs for six sections on fault system **d**, and **b)** the growth indices (HW thickness / FW thickness) for the same sections along the fault. Compare the growth indices to the throw rates in Fig. 5.22.

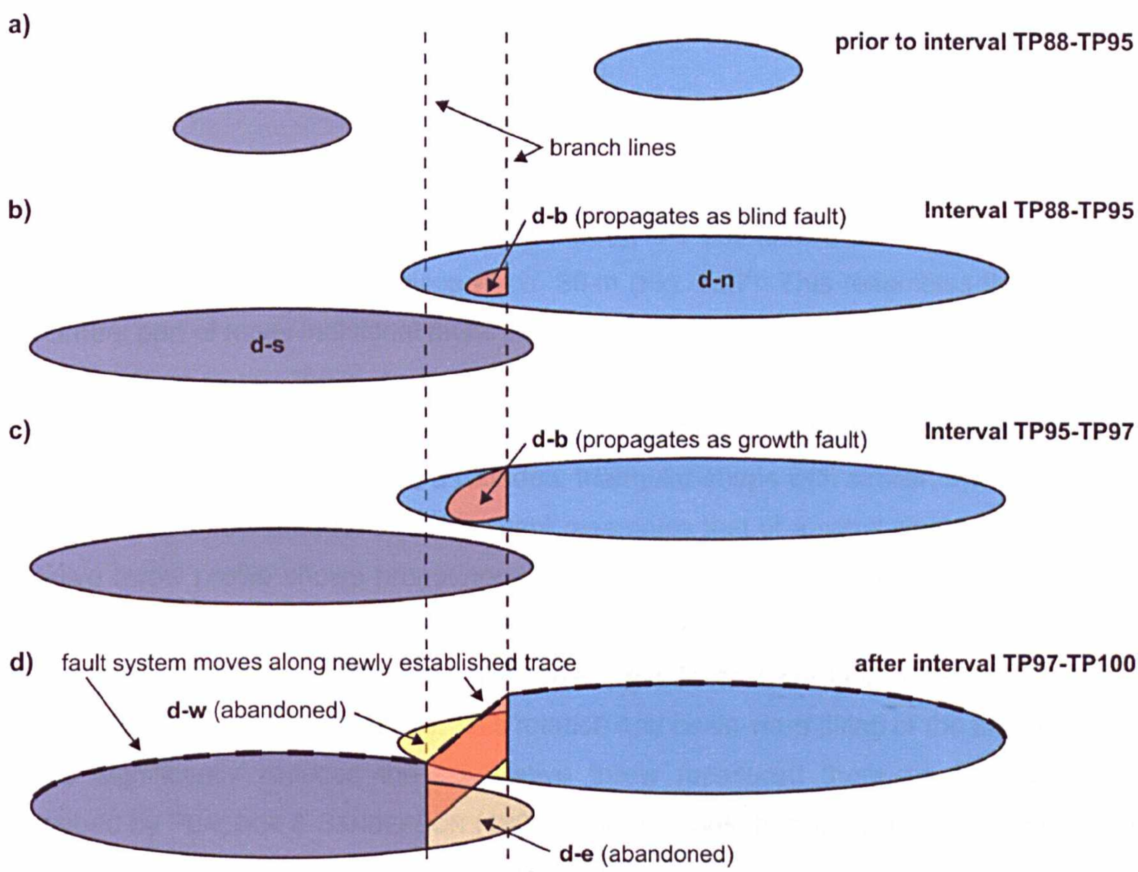

Fig. 5.24: Series of sketches illustrating the evolution of fault system **d** (not to scale). **a)** Two individual faults, **b)** the faults propagated laterally to overlap and a blind splay grows off fault d-n, **c)** the splay intersects the seabed and propagates further towards fault d-s as a syn-sedimentary fault, **d)** the breaching fault (d-b) has hard-linked the previously unconnected faults, the former overlapping tips are abandoned and the fault moves along the newly established fault plane.

5.8 Fault system x

Fault system **x** is located in the east of the study area (Fig. 5.1) and forms a system of seven short splay faults that merge downward into a single through-going fault. It is one of three examples of this fault geometry identified in the study area, all of which evolve into right-stepping en echelon arrays. Fault system **x** was selected for detailed investigation because it consists of seven splays, more than the three and five splays in the other examples, and the fault surface and hence the throw data is not disturbed by subsidiary antithetic faults.

5.8.1 Geometry

The fault system can be mapped over a distance of 4 km along-strike. The lateral tips could not be mapped as the southern tip is outside the study area and the northern tip is located in an area of low quality of the seismic data. At depth, i.e. below ca. 1300 m, the fault trace is laterally continuous but towards the upper tip, the fault surface branches and separates into seven splays, which rotate anti-clockwise with respect to the fault trace at depth and form an en echelon fault array in map view (Figs. 5.25 and 5.26). The individual splays reach lengths of 0.4 km to more than 1 km and overlap with the neighbouring splays for about 0.3 km on either side (Figs. 5.26 and 5.27).

5.8.2 Present-day throw distribution

For the older horizons (TQ40, TQ50, and TQ60), the cumulative throw profiles increase from north to south, with undulations of ca. 30 m (Fig. 5.27). This resembles the profile of the central part of many individual faults in the region. The total throw increases to the north from ca. 100 m to ca. 250 m on the oldest mapped horizon, TQ40. At horizon TQ68, the fault is intensely segmented due to rotation and branching. The throw profiles of each individual segment in Fig. 5.27b have a rounded, triangular shape with similar, symmetrical tip-gradients. The throw data for each segment resembles that of a small single fault. The cumulative throw profile shows pronounced minima (*) at segment overlap zones. At these fault overlap zones, pronounced basin-ward tilting of the strata in the relay ramps was observed (Figs. 5.28b&c) compared to the general gentle land-ward dip of the strata outside fault overlap zones (Figs. 5.28a&d). This rotation and basin-ward tilting of the strata at relay ramps significantly reduces the cumulative throw measured there on both faults as described by PEACOCK & SANDERSON (1991). The youngest horizon TQ80 is only displaced by two of the seven fault segments (splays x3 and x8).

In Fig. 5.29a, the cut-off graphs for all seven splays are shown and a general footwall and hanging wall trace trend can be identified (gray). Between the highest local FW cut-offs and the deepest local HW cut-offs at overlap zones, the total throw across the relay ramp was determined. This was plotted in Fig. 5.29b, together with the individual throw profiles of each splay and the sum of throw at the overlap zone (gray). The total throw (black) is significantly higher than the sum of throws and is in the order of the local throw maxima of the medium sized splays (splays x3, x4, x5, and x7). Showing the individual, summed, and total throws in the same diagram allows assessment of the ratio of the summed throw to the total throw. The sum of the throw on overlapping fault segments underestimates the total throw for this example by 30-50%, locally even more. This difference may be accommodated by wall-rock deformation and rotation of the strata in the relay ramp (PEACOCK & SANDERSON, 1991). This is in accordance with WALSH et al. (2003a), who suggest that throw profiles resemble that of a single, through-going fault once continuous deformation and rotation are incorporated.

Good correlation is observed between the throw maxima and minima on horizon TQ60 and the throw maxima and segment boundaries on horizon TQ68. This suggests that the fault is affected by segmentation at the level of horizon TQ60, which is shown by overlapping throw graphs for horizon TQ60 at several segment boundaries in Fig. 5.27 and the intersection of splays x7 and x8 below TQ60 in Fig. 5.28c.

5.8.3 Interval-throw and back-stripping

Back-stripping to interval-throws reveals fairly uniform distribution along the fault trace, apart for the oldest and youngest intervals (TQ40-TQ50 and TQ80-present) (Fig. 5.30b). The resulting throw rates are generally low at values below 0.3 mm/a, only for interval TQ40-TQ50 are values of up to 0.7 mm/a reached (Fig. 5.31a). The throw rates for the interval between TQ80 and the present day are very low (≤0.1 mm/a) if calculated over the entire interval between TQ80 and the present day. This underestimates the actual value as the fault terminates just above horizon TQ80 and was only active for a short time after the deposition of TQ80. Interval TQ50-TQ60 shows lower throw rates than the intervals both above and below it (Figs. 5.30a&b). Although this may be attributed to errors in the dating, it may also represent a real reduction in throw rate as it is supported by the growth indices determined for the respective intervals (Fig. 5.31c). The throw rates have a maximum during the oldest interval, followed by a relatively steep decrease and then an increase over intervals TQ60-TQ68 and TQ68-TQ80. The growth indices at locations 1.0 km and 3.5 km illustrate the drop to very low throw rates during interval TQ80-present by corresponding low values.

The bifurcation of the fault plane into numerous splays occurred mainly between horizons TQ60-TQ68. The throw rates for interval TQ68-TQ80 are of similar magnitudes to the other intervals (Fig. 5.31) and therefore it seems that the development of the splays has not reduced the rate at which the fault moved. The growth indices determined at a few locations along fault system **x** are consistently greater than 1.0 and hence demonstrate syn-sedimentary fault activity throughout its evolution, including during the segmentation into en echelon splays.

5.8.4 Conclusion and discussion

Fault system **x** exhibits a progressive decrease of geometric linkage from a previously laterally continuous fault trace through upward splaying and branching of the fault surface into seven en echelon segments.

At horizon TQ68, the throw graphs for each of the seven splays show patterns characteristic of single faults: a single central throw maximum and symmetrically decreasing throw to the tips (Fig. 5.27). The summed throw between neighbouring splays exhibits distinct minima at each overlap zone, but this is caused by rotation of the strata from the gentle, regional land-ward (SW) dip outside of fault overlap zones to steep sea-ward (NE) dip within the relay ramps (Fig. 5.28).

In contrast, the total throw across the fault, determined between the footwall and hanging wall cut-off envelopes is in the order of the maximum throws for the inner splays (x3, x4, x5, x7) and thus shows no minima at overlap zones (Fig. 5.29). The determination of the total throw between the footwall and hanging wall cut-off envelopes captures the total offset of the horizon across the fault zone (overlapping splays) and is not affected by the deformation within the relay ramp (tilting and likely sub-seismic faulting).

Although the fault is separated into seven splays at horizon TQ68, it nevertheless remains fully kinematically linked (see Fig. 5.29), and the throw distribution at the level of the splaying resembles that of the single, through-going fault. This observation is in agreement with ideas of WALSH et al. (2003a) according to which the loss of geometrical coherence (i.e. the development of splays) does not lead to any loss of kinematic coherence.

The good correlation of the throw graphs of horizons TQ60 and TQ68 in Fig. 5.27 can be explained by segmentation of the fault plane at these levels and the associated throw variations along a series of overlapping segments (throw maxima at segment centres and minima at zones of overlapping segment tips). Because is fault system is kinematically coherent and moves like a single fault (see Fig. 5.29), the throw graphs for horizons TQ60 and TQ68 in Fig. 5.27 do not reflect the actual throw distribution across the fault, which is much smoother and not characterised by a series of maxima and minima for horizon TQ68 (Fig. 5.29). At horizon TQ50 the fault is not affected by segmentation and hence the throw graph will not show variations related to fault segment boundaries.

The throw rates along fault system **x** are characterised by the highest values for the oldest documented interval (TQ40-TQ50), a subsequent decrease during TQ50-TQ60 and increasing values during both TQ60-TQ68 and TQ68-TQ80. This trend is supported by growth indices, which are independent of horizon ages and thus are not affected by the large errors associated with the throw rate data (Fig. 5.31).

The transition of the continuous fault at depth into the segmented array at shallower levels can not be explained by growth of the fault at the free surface. Two possible explanations are (1) subsequent overprinting of an existing continuous fault by the segmented array or (2) periodic growth of the fault by upward propagation into sediments deposited above the fault tip in the meantime (Fig. 5.32). In the second model, the fault slips intermittently allowing sediment to accumulate above the upper fault tip during one or more periods of quiescence. Upward propagation of the temporarily buried fault into the overlying sediment volume enables out-of-plane rotation and segmentation of the fault surface into an en-echelon array. The renewed slip of the fault creates accommodation in the hanging wall, which is filled subsequently by the deposition of syn-faulting strata, creating the observed thickness variations across the fault.

Multiple periods of quiescence may occur (only one is illustrated in Fig. 5.32), however their durations are short compared to the horizon intervals because thicker hanging wall than footwall successions for all intervals are evident from the progressively decreasing throw values for younger horizons (Fig. 5.27) and growth indices greater than 1.0 (Fig. 5.31c). Higher frequency mapping of horizon intervals would be required in order to determine the number of uniform-thickness intervals that represent periods of fault quiescence.

Fault segmentation as reported here can be caused by host rock heterogeneities, non-uniform stress fields, or stress field reorientation (WALSH et al., 2003a). These possibilities are considered with respect to the tectonic setting of the study area, the local lithologies, and the available data.

The three examples of upwards-splaying observed in the dataset occur at different horizon levels and therefore different ages, given the faults are growth faults, and are not clustered together but are located 4-16 km apart. For this reason, host rock heterogeneities are considered unlikely as a cause because all the examples are contained in a thick, young sedimentary succession (at least 7 km thickness, Miocene to present, interbedded sandstones and shales) (Fig. 3.6, see also Fig. 3.4) without any obvious relationship to major changes in rock properties, e.g. like between sediments and crystalline basement rocks. Therefore, fault reorientation and splaying above a lithological boundary as described by COSGROVE & AMEEN (2000) does not apply in this case.

A non-uniform stress field or stress field reorientation (rotation of the horizontal principal stress or introduction of a strike-slip component to the extensional deformation) are possible causes but their presence is difficult to assess in a seismic dataset due to the lack of fault slip indicators. However, upward-splaying has only been found in three examples out of ca. 140 mapped faults in the 400 km^2 study area, and these three faults have maximum throws of less than 250 m. It therefore seems unlikely that the upwards splaying is due to significant regional stress field reorientation because such changes would be expected to have affected more faults including the large ones. Nonetheless, all three examples show anti-clockwise rotation of the horizontal stresses to a more north-south orientation of the minimal stress, which would be consistent with a sinistral strike-slip component to the extension.

5.8.5 Figures

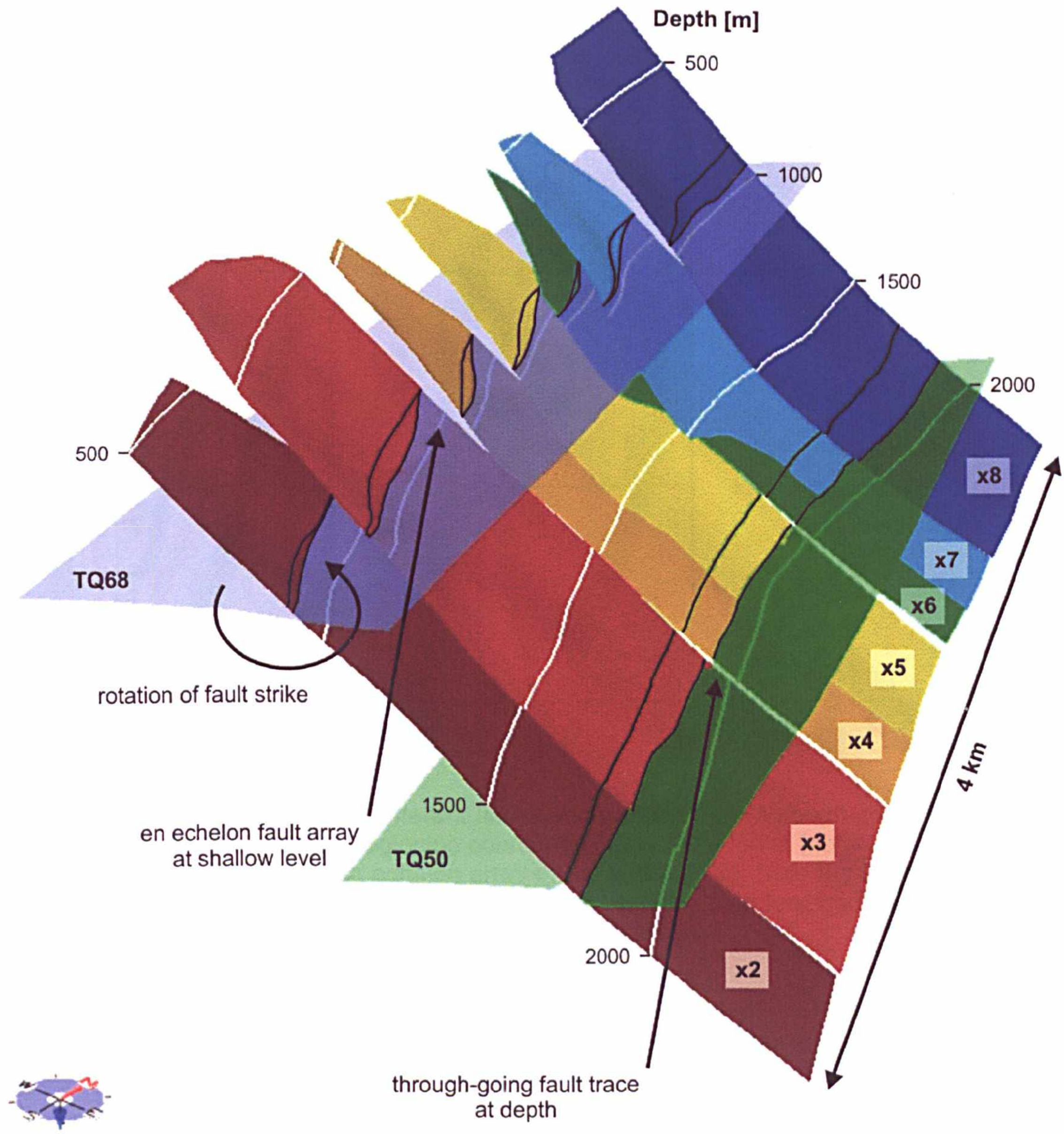

Fig. 5.25: 3D view of the fault system illustrating the change in geometry from a continuous fault surface at depth to seven splays at shallow levels that form an en echelon fault array. Black lines indicate the cut-off geometries and show lenticular shapes with near-central maxima for the splays at horizon TQ68, which are characteristic for single faults.

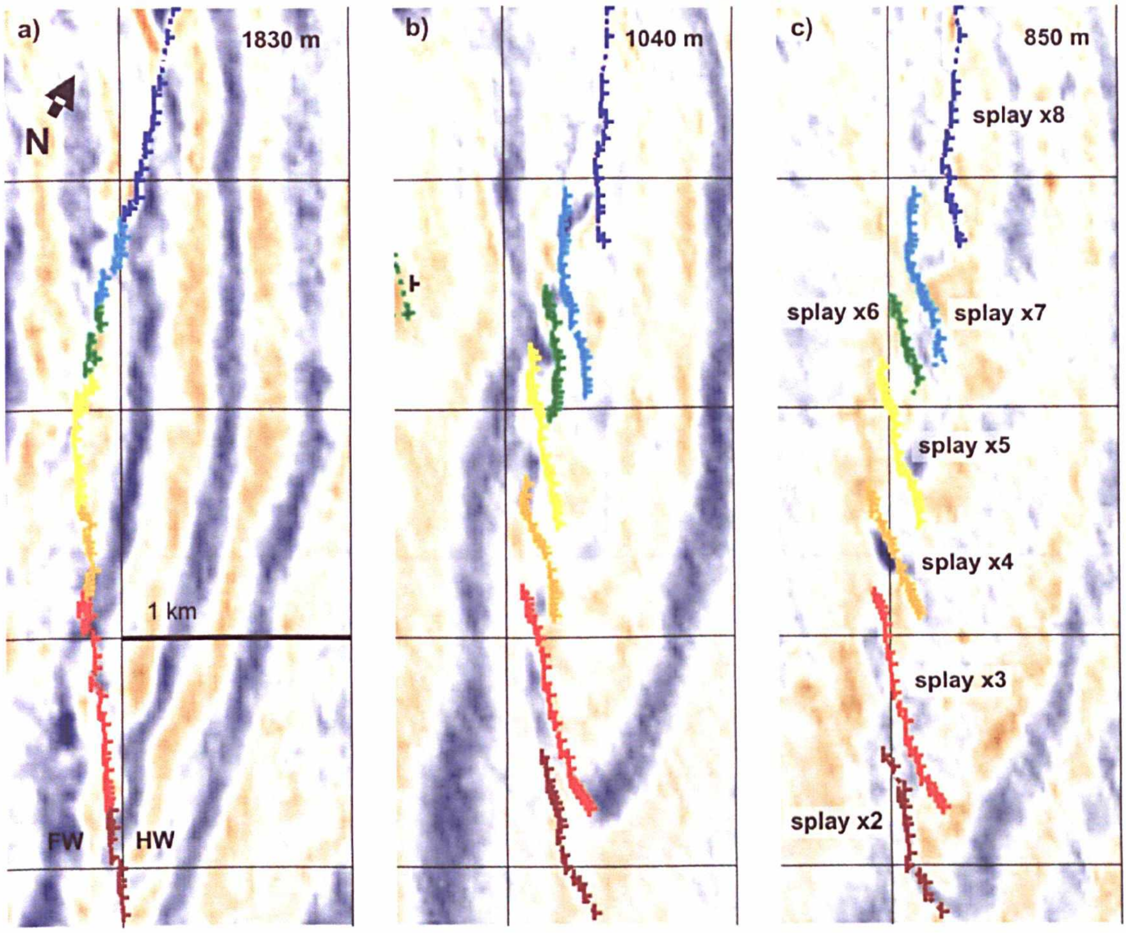

Fig. 5.26: Depth slices at three different levels showing in **a)** the through-going fault trace at depth and in **b)** the beginning counter-clockwise rotation of the segments that leads to formation of an en echelon array of the splays in **c)**. Note the lateral propagation of the segments at shallow levels (b and c) beyond their lengths in a), which causes the en echelon array to overlap at all segments tips.

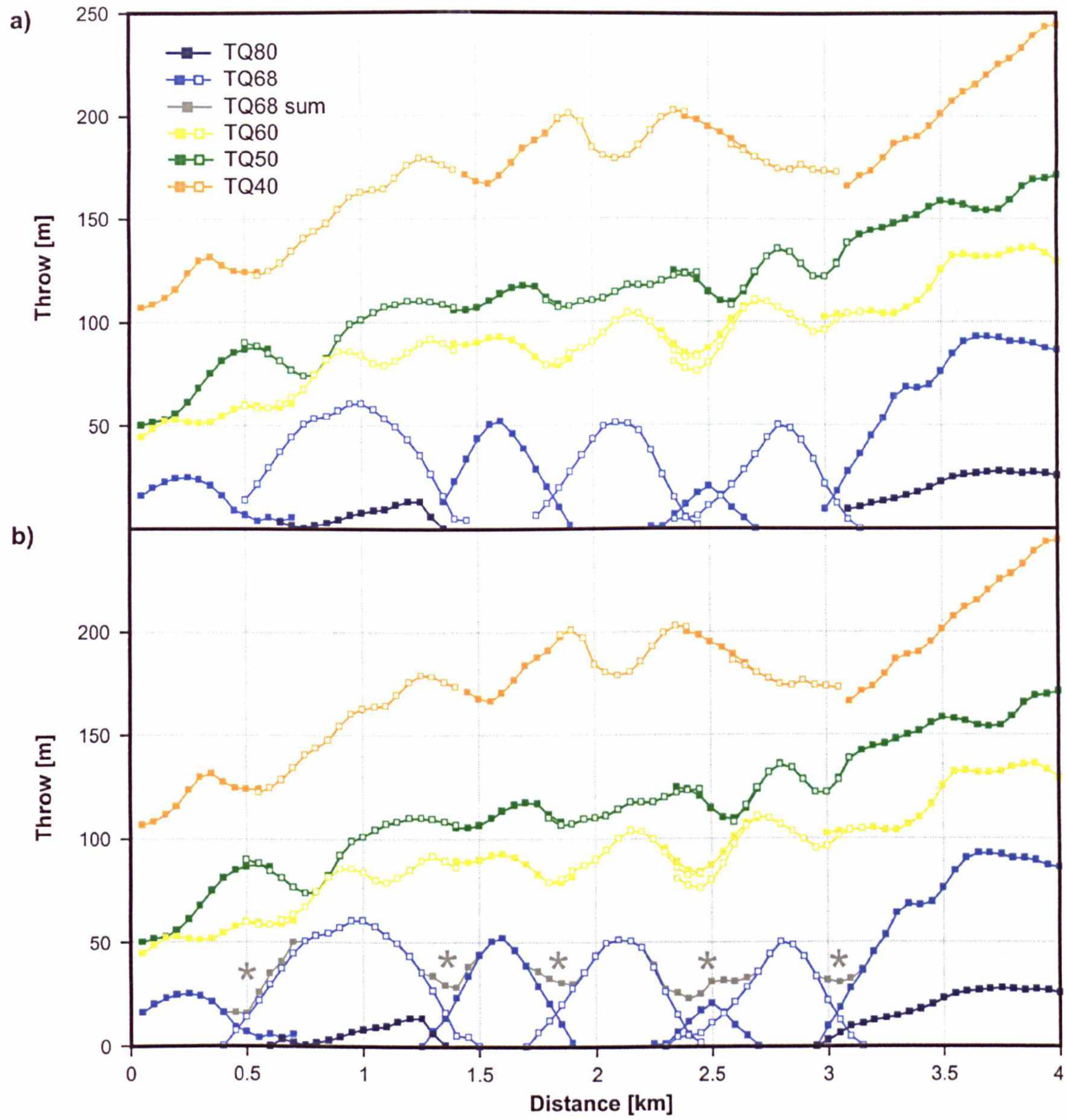

Fig. 5.27: **a)** Fault throw profile of fault system **x** showing continuous throw graphs for the older horizons TQ40-TQ60 and individual throw profiles for each fault splay at the level of horizon TQ68, and where present, horizon TQ80. In **b)**, the fault tips of the graphs for the splays have been manually extended to zero where necessary (TQ68 and TQ80) and the cumulative throw on horizon TQ68 along the fault is shown. Note the significant throw minima where splays overlap (*).

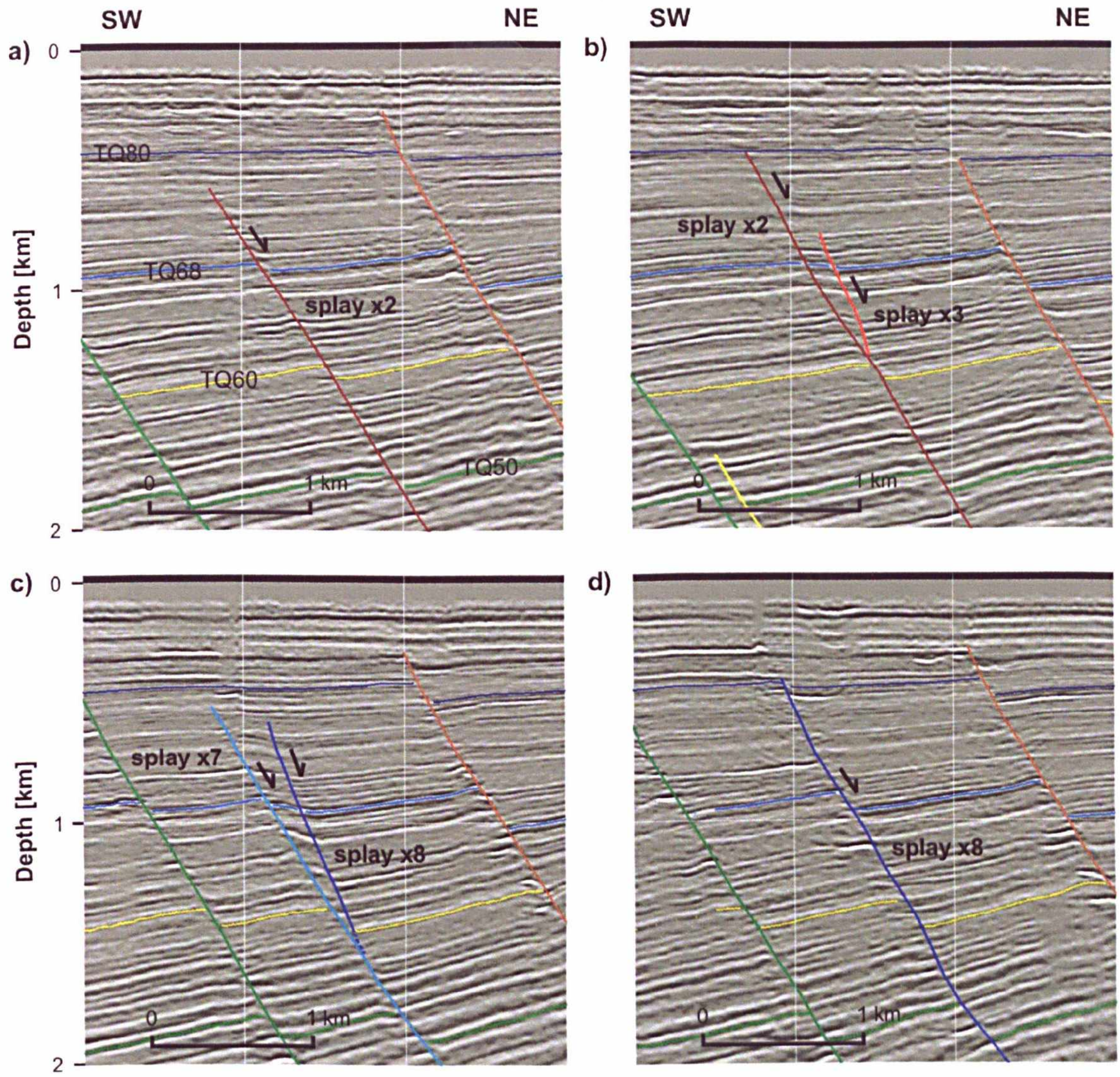

Fig. 5.28: Seismic cross-sections across fault system **x** at different positions along strike (compare to Fig. 5.29), illustrating the gentle, uniform regional land-ward dip of the horizon surface between the fault overlap zones (a and d) and the significant rotation and basin-ward dip of the strata within the relay ramps (b and c).

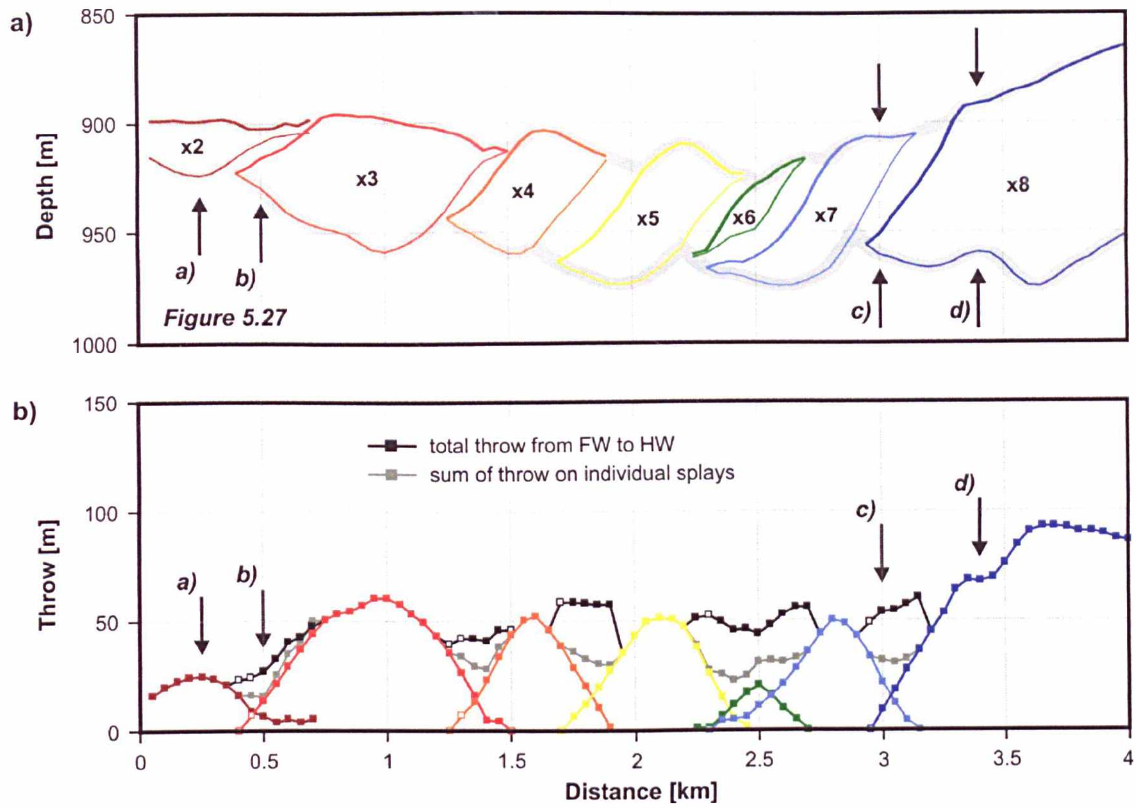

Fig. 5.29: **a)** Footwall (thick line, shallower) and hanging wall (thin line, deeper) cut-off graphs (with extended tips) for the splays of fault system **x** at horizon TQ68, and **b)** the respective throw data. Additionally to the throw data for the splays (coloured), the summed throw between overlapping splays (gray) and the total throw between the footwall and hanging wall across the relay ramps (black) are shown. Empty squares in b) indicate extrapolated data (compare to Fig. 5.27a). Arrows show the position of the cross-sections of Fig. 5.28. Note the general trend of the FW and HW cut-off lines for the entire fault system marked in gray in a) illustrating the through-going nature of the fault despite segmentation into seven splays.

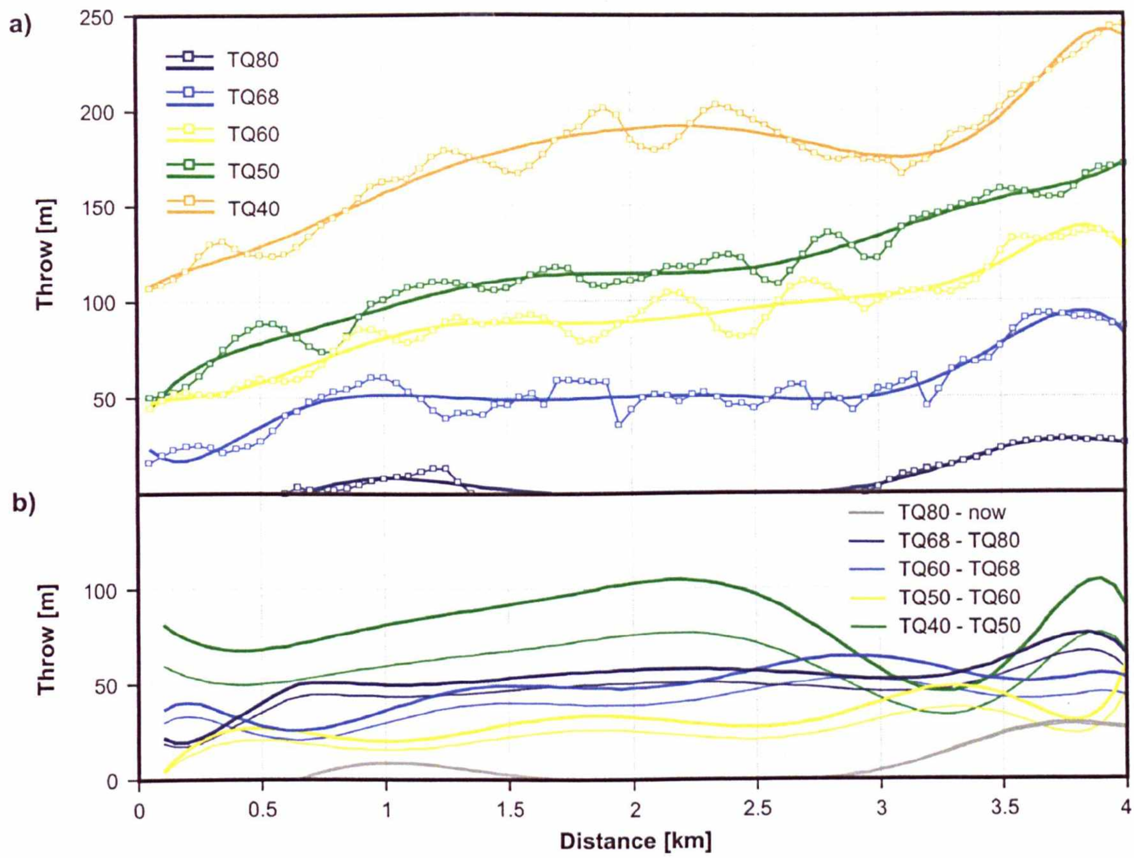

Fig. 5.30: **a)** The throw data for all horizons were smoothed in order to determine the interval-throws between successive horizons. The smoothed throw trends are overlain onto the measured, and for TQ68, calculated (see Fig. 5.29) throw data. In **b)**, the interval-throws for each interval between the mapped horizons are shown as determined for the present-day (thin line) and decompacted (bold line) to initial amounts at the time of deposition of the upper interval boundary. Note the more significant increase of the interval-throw for older time intervals due to greater compaction there.

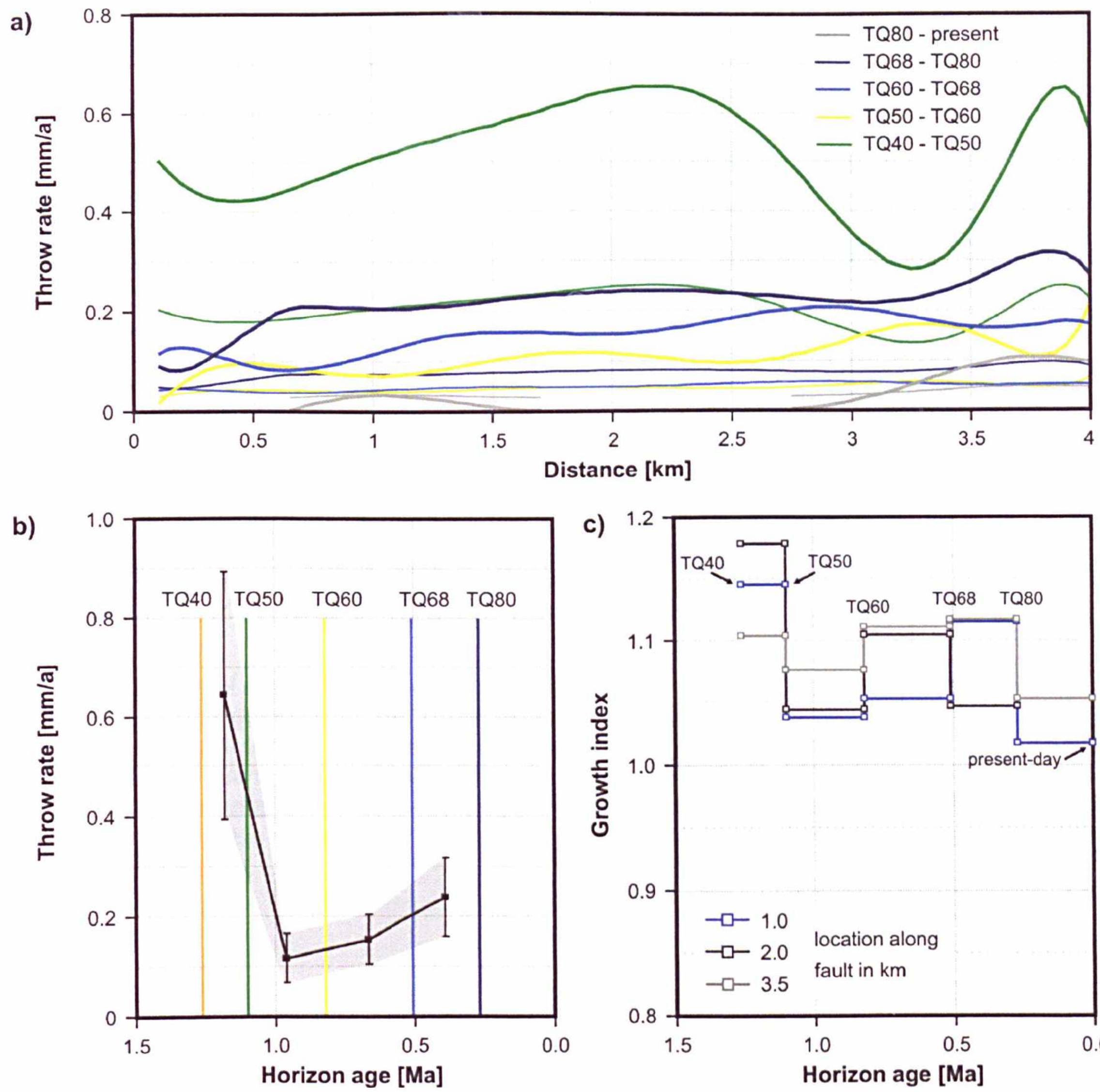

Fig. 5.31: **a)** The throw rates (bold) and their associated errors (thin lines) are shown along strike of fault system **x**. Note that the errors are generally smaller (except for interval TQ80-present) than the actual fault throw rate. **b)** The throw rate at 2 km shows highest values for the oldest interval, a minimum during TQ50-TQ60 and increasing values during the youngest intervals. **c)** Growth indices for three locations along fault system **x**, which are consistently greater that 1.0, indicating syn-sedimentary fault movement. High indices for the oldest interval support the determined high throw rates during this period irrespective of the large errors. Furthermore, good correlation is also observed for the throw rates minimum during interval TQ50-TQ60.

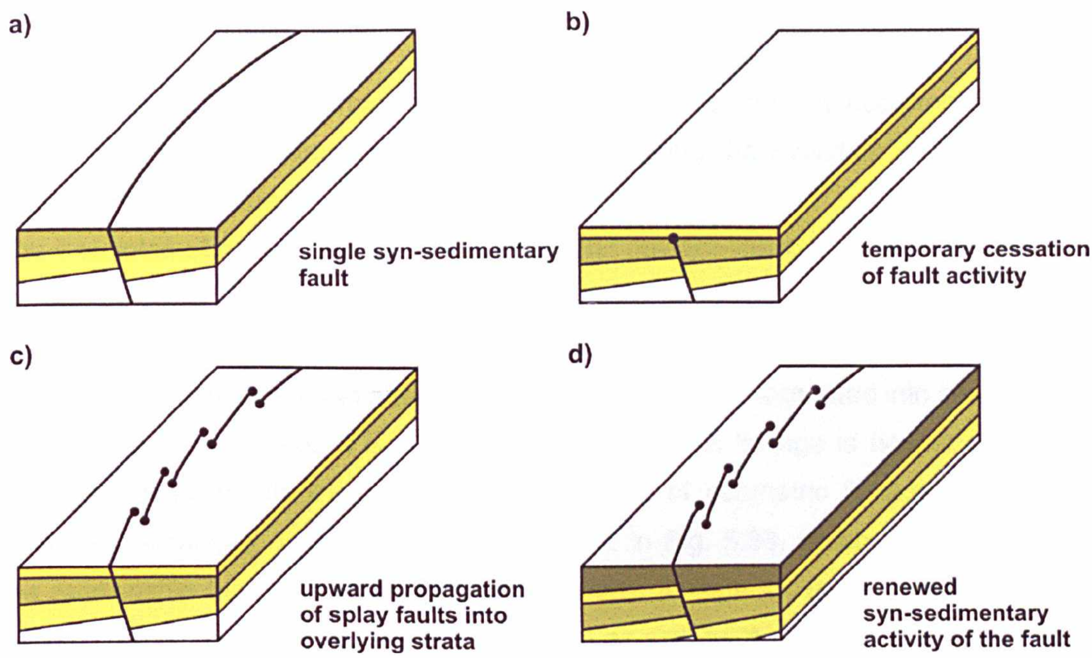

Fig. 5.32: Series of illustrations showing the possible formation of the en-echelon array from a through-going fault due to splaying and rotation during upward propagation. **a)** The syn-sedimentary fault became temporarily inactive and was buried (**b**). **c)** During subsequent propagation into the overlying strata, the fault surface splayes into several strands that rotate out-of-plane to form an en-echelon array. **d)** The individual splays also show some lateral propagation that leads of along-strike overlap of the segments.

5.9 Conclusions

The faults and fault systems described above demonstrate the occurrence of different geometries, throw patterns and fault interaction during the evolution of syn-sedimentary faults of different sizes.

The examples of case studies **d** and **x** show that upward-linkage as well as upward-splaying can be observed during the growth of faults. For fault system **d**, kinematic linkage was reached some time after full geometric linkage, whereas for fault system **x** kinematic linkage was maintained even after the fault surface became separated into seven splays. From these observations, it is suggested that geometric linkage is neither a prerequisite condition for kinematic linkage, nor does the lack of geometric linkage preclude linked kinematic behaviour. These ideas are illustrated in Fig. 5.33, which schematically shows the relationship between geometric and kinematic linkage for case studies **d** and **x** (for different stages during fault evolution for each) as well as the Cassia and Ironhorse faults discussed above (see sections 5.3-5.5, 5.7, and 5.8), and the evolution of relay zones described by PEACOCK & SANDERSON (1991, 1994). For fault system **d**, no geometric linkage exists between the overlapping fault segments prior to the propagation of the breaching fault; however, they will have been soft-linked (location 1 in Fig. 5.33). After hard-linkage of the initial segments was established, full kinematic linkage was initially delayed (location 2) and occurred at a later stage during the faults evolution (location 3). In contrast, the loss of geometric linkage of fault system **x** through up-wards splaying into seven splays does not affect the level of kinematic linkage of the fault system, which remains constant (transition from location 4 to 5).

On the Cassia Fault, persistent throw minima over several horizons suggest that the fault was initially formed through linkage of a number of small faults, although no abandoned fault splays were found in either the HW or FW. The sub-parallel but not physically connected Cassia and Ironhorse faults interact in soft-linked displacement transfer across a distance of ca. 2.5 km (location 6 in Fig. 5.33). The displacement transfer mainly took place during the main phase of initiation of the Ironhorse Fault during interval TP80-TP95. The Ironhorse Fault formed in the hanging wall of the nearby, larger Cassia Fault, after the Cassia Fault had already been uniformly active across the entire study area. While on the Ironhorse Fault a large amount of interval-throw accumulated in the south during interval TP80-TP95, the interval-throw distribution on the Cassia Fault is asymmetric showing a maximum in the north and a minimum in the south. The aggregate interval-throws are, however, almost uniform and show much more systematic patterns than for the individual faults (see section 5.5), and thus demonstrate soft-linked displacement transfer and geometric coherence of the fault system (WALSH & WATTERSON, 1991).

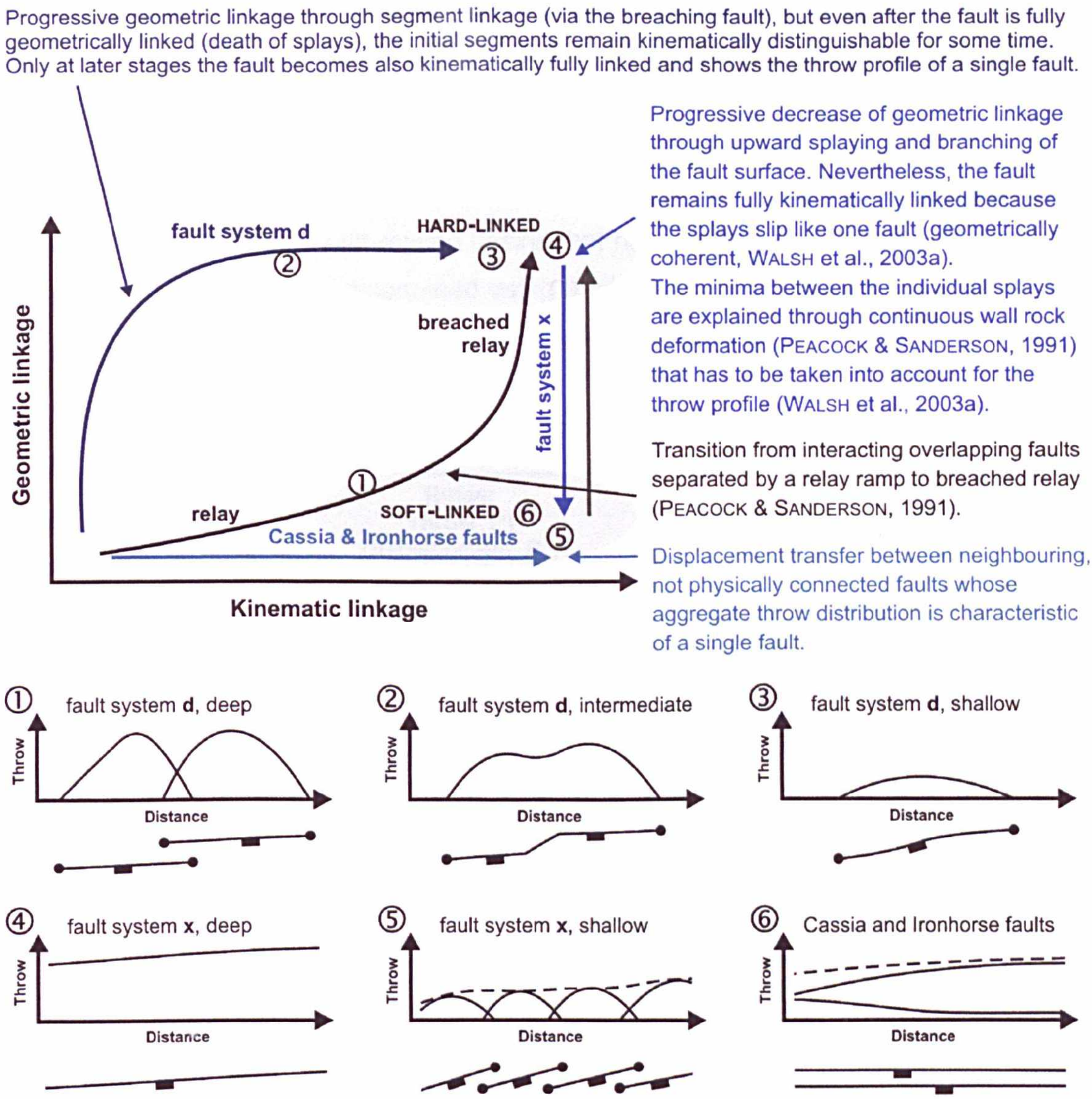

Fig. 5.33: Illustration of the different relationships of geometric and kinematic linkage for fault systems **d** and **x**, the Cassia and Ironhorse faults, and the trend from unbreached to breached relay ramp (PEACOCK & SANDERSON, 1991). The terms hard-linked and soft-linked were defined by WALSH & WATTERSON (1991). The diagrams in the lower part schematically show the fault traces (map view) and the associated throw profiles. Dashed lines indicate total throw on the overlapping segemts and parallel faults, respectively (diagrams 5 and 6).

Most classic models of fault linkage describe the occurrence of kinematic linkage, i.e. overlapping and interacting faults, before geometric linkage is established, through breaching of a relay ramp for example (PEACOCK & SANDERSON, 1991, 1994; CARTWRIGHT et al., 1996; WILLEMSE et al., 1996). Interaction and displacement transfer without geometric linkage is described by WALSH & WATTERSON (1991).The various observed trends between geometric and kinematic linkage for normal faults in the study area, especially the loss of geometric linkage while kinematic linkage remains intact for fault system **x**, indicate that this relationship is very complex. Whilst all fault systems may not converge towards geometric linkage, is appears that high degrees of kinematic linkage are observed in many mature cases of fault interaction observed in this dataset.

Comparison of fault throw rates for the study area and other basins

The throw rates determined for individual gravitational growth faults in the Columbus Basin, ranging from <0.1 mm/a to a maximum ca. 3.5 mm/a, are comparable with fault slip rates reported for extensional faults from several extensional provinces (Table 5.1). The throw rates determined in this study have the same magnitude and cover the same scale range as the slip rates of faults in rift-related basins that have undergone crustal extension. The slip rates listed below were determined using a wide variety of datasets such as seismic data and field data of uplifted terraces, fault scarps, and trenches.

Table 5.1: List of fault slip rates determined for ancient and active extensional faults.

Basin / Area	Type of faulting	Rates: Throw (*) Displacement (**)	Comments	Reference
Columbus Basin (Trinidad)	gravi-tational	small/medium faults (tot. throw <1000 m) <1.0 mm/a * large faults (tot. throw >1000 m) up to 3.5 mm/a *	• high-quality commercial seismic data • time span: 2.78 Ma • interval durations: 0.1-0.6 Ma	this study
Gulf of Mexico	gravi-tational	polycyclic growth history of faults (little correlation between individual faults)	• seismic data • cyclicity probably controlled by sediment loading	CARTWRIGHT et al. (1998)
Bay of Plenty (New Zealand)	back-arc extension	0.52±0.18 mm/a ** (average unlinked) 1.41±0.31 mm/a ** (average linked)	• multi-channel and high-resolution seismic data • time span: 1.34 Ma	TAYLOR et al. (2004)
		max. displ. rate: 3.6±1.1 mm/a, spatial and temporal variability of displacement rates	• high-resolution seismic data	BULL et al. (2006)
Taranaki Graben (New Zealand)	back-arc extension	varying displ. rates: min.: 0.1-0.2 mm/a max.: up to 2.8 mm/a	• seismic data, several time intervals	NICOL et al. (2005)
Apennines (Italy)	continent. extension	large range of throw rates between 0.04-2.00 mm/a	• field data and trench data	MOREWOOD & ROBERTS (2000)
		large range of throw rates between 0.05-1.38 mm/a	• field data and trench data of active faults	ROBERTS & MICHETTI (2004)
Gulf of Corinth (Greece)	back-arc extension	vertical slip rate: 0.7-2.0 mm/a	• paleo-seismological data from trenches for historic times	COLLIER et al. (1998)
		long-term averaged vertical slip rate: 1.2-2.3 mm/a	• seismic and field data for bounding fault	
		max. displacement rate: 2.6-4.7 mm/a	• paleo-seismological data	MOREWOOD & ROBERTS (2002)
		slip rate: 2-5 mm/a	• seismic data	MORETTI et al. (2003)

Basin / Area	Type of faulting	Rates: Throw (*) Displacement (**)	Comments	Reference
Gulf of Corinth (Greece)	back-arc extension	slip rate: 4-7 mm/a	• based on uplifted terraces	McNeill & Collier (2004)
		slip rates for several faults: 0.5 mm/a, 0.8 mm/a, 1.6 mm/a	• seismic data	Lykousis et al. (2007)
North Sea	continent. rift basin	0.055 mm/a ** (max. pre-linkage) ≈ 0.092 mm/a ** (av. post-linkage)	• seismic data • graben-bounding fault	McLeod et al. (2000)
		low rates pre-linkage, higher ones during fault interaction	• seismic data • qualitative rates	Dawers & Underhill (2000)

Chapter 6

Basin-scale throw and throw rate analysis

6.1 Aim and motivation

In the previous chapter, fault throw accumulation and fault evolution of selected individual faults and small fault systems were discussed in considerable detail in order to better understand fault growth. These examples have demonstrated the complex evolution of syn-sedimentary extensional faults including various mechanisms of fault interaction (e.g. linkage, splaying and displacement transfer).

The aim of this chapter is to integrate fault throw information from the major and medium faults in the dataset in order to reconstruct the amount and position of fault activity over time within this part of the Columbus Basin. A 4D model of the spatial and temporal variations of fault activity can be developed.

This investigation allows evaluation of the migration of fault activity, both between neighbouring high-displacement faults and through basin-wide transfer of active extension, during the basin evolution to be visualised and interpreted.

6.2 Methodology

To investigate the distribution and migration of basin-scale fault throw and throw rate, the throw data of all faults that contribute significantly to basin extension were considered (Fig. 6.1). The throw data on each of the faults were, after smoothing, back-stripped to interval-throws between certain horizons. These intervals were chosen to cover groups of horizons instead of using every available interval in order to reduce their number and thus make the data representative and comparable over the study area. From the interval-throw data, throw rates for the respective intervals were determined.

In order to visualise the distribution of the fault activity in the study area, the amounts of interval-throw and fault throw rate for each fault over the respective time intervals were colour-coded and superimposed onto maps of the present day fault heaves of the respective older interval-bounding horizon for each interval. Greater fault heaves denote larger faults. The fault heave data are, however, not back-stripped to interval-heaves and thus do not correlate to the interval-throws or throw rates but represent the present-day heaves mapped on the seismic data. Through a series of such figures (Figs. 6.2 and 6.3), the amount of fault activity and its migration over time are illustrated.

The boundaries for the intervals for which the interval-throw and throw rate were determined are TP70, TP77, TP80, TP95, TQ20, TQ40, TQ60, and TQ80. The horizons TP70 and TP77 were only mapped in the area around the Cassia and Ironhorse faults due to this being the only area in which the horizons could be followed with confidence. Thus, although throw data of both TP70 and TP77 are limited, they give vital information about the timing of fault activity in the western part of the study area.

The investigation of the timing and position of fault activity is limited by the number of horizons available to this study. Due to a lack of older horizons mapped across the Cassia and H faults, their time of initiation could not be determined. Another limiting factor is the extent of the dataset in the NE, where the H and H* faults are only imaged for younger time intervals due to their dip to the northeast.

Due to the size of the seismic survey, which covers ca. 15 km along-strike distance for the NW-SE-trending fault orientation, and the reduced data quality at the edges of the dataset, the maximum along-strike distance for which data can be investigated is limited to 13 km. All block-bounding faults have greater lengths (Chapter 5) and thus only a section of the total length of the large-scale faults present in the study area has been investigated here.

In the case of small fault systems, the distribution of fault activity between fault segments is known to be complex and detailed investigations were carried out in Chapter 5 for fault systems **d** and **x**. For other fault systems, the fault throw data were summed between parallel segments if the activity on these segments was simultaneous and the total throw along the fault trace was used to determine the contribution of these fault systems to the basin-wide throw (faults **f** and G FW). The interval-throw on the A4 Fault for interval TQ40-TQ60 is so small, horizon TQ40 is displaced by less than 10 m immediately below the upper tip of the fault, that the data has not been included in the calculations and the interval-throw data is instead shown in grey.

6.3 Faults used for the analysis

For the analysis of fault throw and throw rate distribution on a basin-scale, the major block-bounding faults and a number of medium-sized faults were chosen. The medium-sized faults were selected on the basis of their significant maximum throw accumulations that contribute to the basin extension, and their fault length within the study area. Table 6.1 lists all 15 faults and fault systems from SW to NE used for the study, and Fig. 6.1 shows their location in the study area.

Details of the geometry, throw data, and evolution of the Cassia, Ironhorse, and G faults, as well as fault systems **d** and **x** have been discussed in detail in Chapter 5. In addition to these, the following faults have been included in the analysis.

- Fault system **c** consists of five fault segments and has a maximum throw of ca. 230 m. The fault system extends over a distance of about 8 km and its northern fault tip is located outside the study area.
- Fault **e** is a medium fault with a maximum throw of ca. 120 m and a length within the study area of ca. 5 km. The northern fault tip is located outside the study area.
- Fault **f** consists of a medium sized fault and a synthetic splay in its hanging wall. The throw data on the two faults has been summed for the investigation of basin-scale throw accumulations. This was done because the splay is small with a strike length of only 1.5 km and the throw on the splay decreases rapidly from a maximum of ca. 100 m near the branch line towards its tip. The splay was included in order to capture the activity of the whole system. The southern tip of Fault **f** is located outside the study area, within which its length is ca. 11 km and the maximum throw is about 200 m. The fault shows pronounced segmentation at a position that is not influenced by the splay.
- Fault **s** is located in the hanging wall of the Ironhorse Fault and is entirely contained within the investigated seismic survey. Its length is 5 km and the maximum throw is 150 m.
- Fault **p** has a maximum throw of ca. 200 m and a length of ca. 5 km within the study area, its southern tip is located outside of the seismic survey.
- Fault A4 is the largest antithetic fault within the study area and the only one included in this study. The A4 Fault might be part of the counter-regional fault system within the Columbus Basin (Chapter 3) whose respective active faults bound the growth faulted shelf deposits basin-ward (see Figs. 3.4 and 3.5). The fault can be mapped for 9 km within the study area. Its southern tip is located outside the seismic dataset, and it has a maximum throw is ca. 320 m.
- The G FW fault system consists of a number of small and partly overlapping faults in the footwall of the G Fault. The throw data for several, laterally limited neighbouring faults were treated like one through-going fault in order to be incorporated into the basin-scale throw analysis. The oldest horizon considered is TP97 due to difficulties in confidently mapping any older horizons in this area of the dataset due to the fault shadow of the G Fault, which significantly reduces the quality of the seismic data. Between the G FW and the G faults, a relay ramp is developed across which displacement is transferred between the faults.
- In the hanging wall of the regional G Fault, poor data quality in large parts limits the investigated faults to a small group in the NE, mapped over a strike distance of up to 4 km. There, the **y** Fault is situated in the hanging wall of fault system **x**, and has a maximum throw of ca. 320 m.
- The largest fault in the NE is the H Fault with a maximum throw of ca. 1300 m (see also Fig. 4.2a).
- The H* Fault is located in the hanging wall of the H Fault and due to the position at the edge of the dataset, only a very short portion of the fault (3.2 km) and a limited number

of horizons (TQ60, TQ80) could be investigated. It is known however from studies carried out by BP Trinidad & Tobago, that the H and H* faults form a major block-bounding fault system in the Columbus Basin. The maximum throw on the H* Fault is ca. 500 m on horizon TQ60, which is the oldest horizon mapped across the fault in this study.

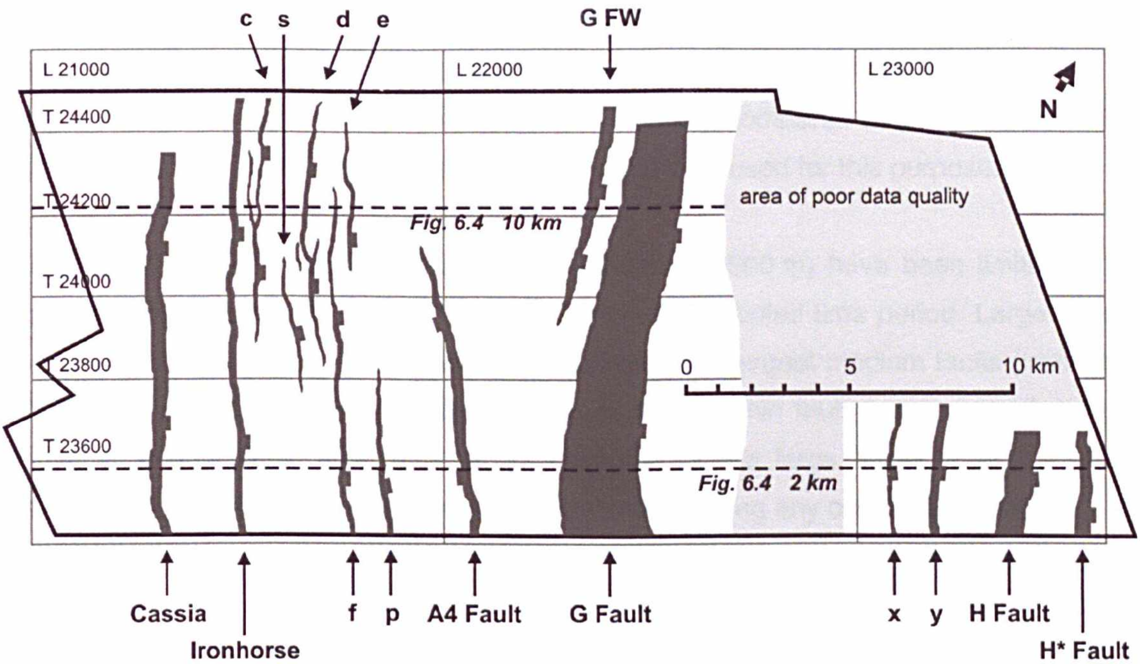

Fig. 6.1: Map of the study area showing the 15 faults used for the basin-scale throw and throw rate analysis. The fault traces are shown for horizon TP95 in the western part of the dataset (Cassia to G Fault) and TQ60 in the eastern part (**x** to H* faults).

Table 6.1: Faults and faults systems for which the accumulation and migration of fault throw and throw rate on a basin-scale were investigated. The major block-bounding faults in the study area are the Cassia, G and H faults.

Fault	Description
Cassia	Major block-bounding fault
Ironhorse	Major fault
c	Fault system (5 segments)
d	Fault system (5 segments)
f	Fault system (2 segments, summed)
e	Medium fault
s	Medium fault
p	Medium fault
A4	Medium fault (antithetic)
G FW	Fault system (summed)
G	Major block-bounding fault (largest fault in study area)
x	Fault system (7 segments)
y	Medium fault
H	Major block-bounding fault
H*	Major fault

6.4 Results

6.4.1 Throw data

In order to assess the amount and location of fault activity in the study area over the investigated time span, the interval-throws accumulated on each fault during successive time intervals were determined from the total throw accrued on the faults. This is illustrated for each time interval in Fig. 6.2. The interval-throws can be compared between different faults during each time interval. However, because the time intervals are of varying durations, the magnitudes of the interval-throws should not be directly compared between different time intervals; the throw rate data (see next section) should be used for this purpose.

The highest interval throw accumulations (in excess of 500 m) have been limited to the block-bounding Cassia, G, and H faults over the entire studied time period. Large interval throws (more than 200 m) have also accumulated on the largest medium faults (Ironhorse, A4, G FW, **y**, and H*). All other single faults or faults within fault systems reach interval throws of (significantly) less than 200 m, demonstrating a large scale-range, up to two orders of magnitude, over which throw is accumulated during any one time interval.
The throw data, although not directly comparable between the successive intervals, reveal a progressive eastward shift of large throw accumulations from the western faults (Cassia and Ironhorse) during the oldest intervals, to the G Fault and eventually to the H Fault in most recent times.

6.4.2 Throw rate data

Throw rates can be compared between successive time intervals because they represent throw values that have been normalised to the interval duration over which they have been accumulated. Fig. 6.3 illustrates the distribution of the fault throw rate in the study area for the investigated time intervals. The throw rates are shown without their respective errors, but these are illustrated for the block-bounding Cassia Fault and G Fault in Figs. 5.4 and 5.12, and for the medium Ironhorse Fault and the fault systems **d** and **x** in Figs. 5.8, 5.21, and 5.30. Because most time intervals for which throw rates were determined in this chapter are well over 0.1 Ma in duration (except interval TP77-TP80), the errors of the throw rates are more dependent on the amount of interval-throw and will be greatest for (very) small interval-throws (less than 20-30 m) (see Section 4.6.1 and Chapter 5).

During the oldest time interval, **TP70-TP77**, data are only available for the Cassia and Ironhorse faults, the westernmost faults considered here. The Cassia Fault is highly active at throw rates of up to 3 mm/a, whereas the Ironhorse Fault had not yet started to move.
During the following interval, **TP77-TP80**, the Cassia Fault continues to accumulate throw at high rates, and the first activity on three isolated segments of the Ironhorse Fault is ob-

served. Activity is also seen on the connected southern and north-eastern segments as well as the isolated north-western segment of fault system **c**. Fault **s** was not yet initiated.

In **TP80-TP95**, the Cassia Fault continues to be highly active, but the throw rate decreases from north to south, as does the amount of interval throw accrued (Fig. 6.2), whereas throw rates and throw accumulation on the now continuously active Ironhorse Fault increase from north to south. This illustrates the presence of a kinematic link with displacement transfer between the faults. For fault system **c**, increased activity compared to the previous interval is evident. Fault **s** becomes active, as well as the two initial segments of fault system **d**. Fault **f** initiates on three isolated segments. The A4 Fault shows low to medium throw rates, but no data is available for the previous interval to constrain the onset of activity.

During interval **TP95-TQ20**, the activity on the Cassia Fault is reduced compared to the previous one, with the highest activity being observed in the group of medium faults within the fault block between the Cassia and G faults (i.e. fault systems **c** and **d** and faults **e, f, p, s**, and A4). Interval TP95-TQ20 is the first for which data for the G-FW Fault, showing increasing activity to the north, and for the G Fault, showing activity limited to the south of the study area, are available. The throw accumulation on the G Fault might represent its initial segment (i.e. the onset of activity).

Interval **TQ20-TQ40** shows similar throw rates for the Cassia Fault as interval TP95-TQ20, but significantly reduced activity for the group of faults from the Ironhorse Fault to the A4 Fault to values below 0.2 mm/a. On the other hand, a dramatic increase of the throw rate is observed on the north-ward propagating G Fault to values up to 3 mm/a. Towards the northern edge of the study area, the G Fault and the G FW Fault form a relay ramp with throws and throw rates increasing in opposite directions, indicating soft-linked displacement transfer between the two faults. Due to reduced quality of the seismic data in the northeast of the survey area at deep levels, no interval-throw and throw rate data are available for interval TQ20-TQ40 for the faults there (faults x, y, H, and H*).

During interval **TQ40-TQ60** the activity of the group of faults between the Cassia and G faults decreases further, as indicated by very low throw rates and tip retreat. Fault system **c**, as well as faults **s**, **f**, **e**, and A4 cease to be active before deposition of horizon TQ60. The G Fault also shows significantly reduced throw rates compared to the previous interval, whereas the oldest data available for the northeast demonstrates low to medium throw rates on the **x**, **y**, and H faults.

During interval **TQ60-TQ80**, activity is further reduced on the faults in the western part of the study area, with only the Cassia, Ironhorse and parts of faults **d** and **p** remaining active. Compared to the previous interval, the throw rates on the G Fault are, however, increased, they remain similar on fault system **x** and fault **y**, and they are reduced on the H Fault.

During the most recent interval, **TQ80-present day**, throw rates on all faults still active in the west and centre of the study area are reduced to very low values of mostly below 0.2 mm/a, and the highest values of up to 1.5 mm/a are limited to the H Fault in the north-east.

Page 125 has been cut down the centre, and a small portion of text is missing.

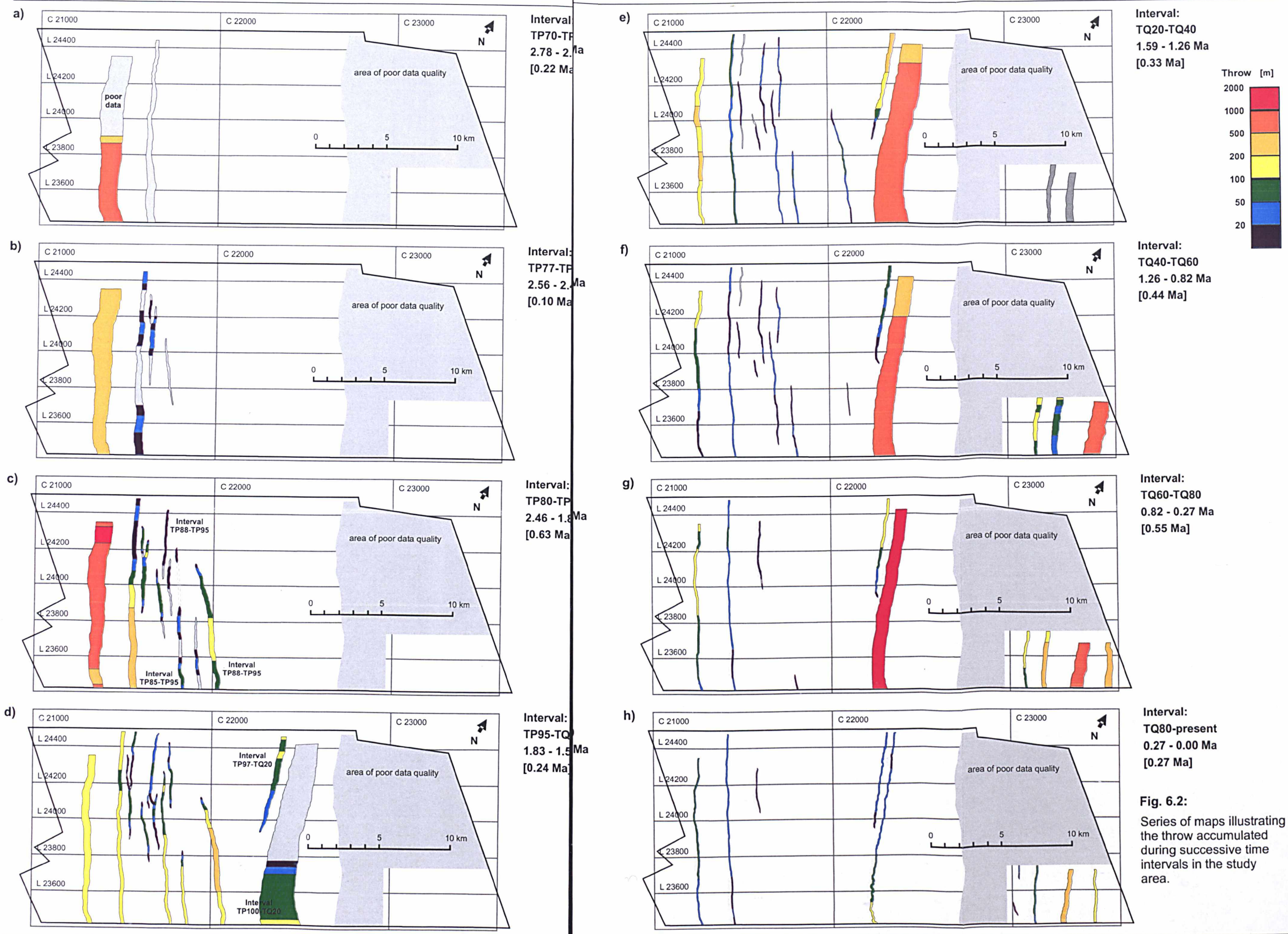

Fig. 6.2:
Series of maps illustrating the throw accumulated during successive time intervals in the study area.

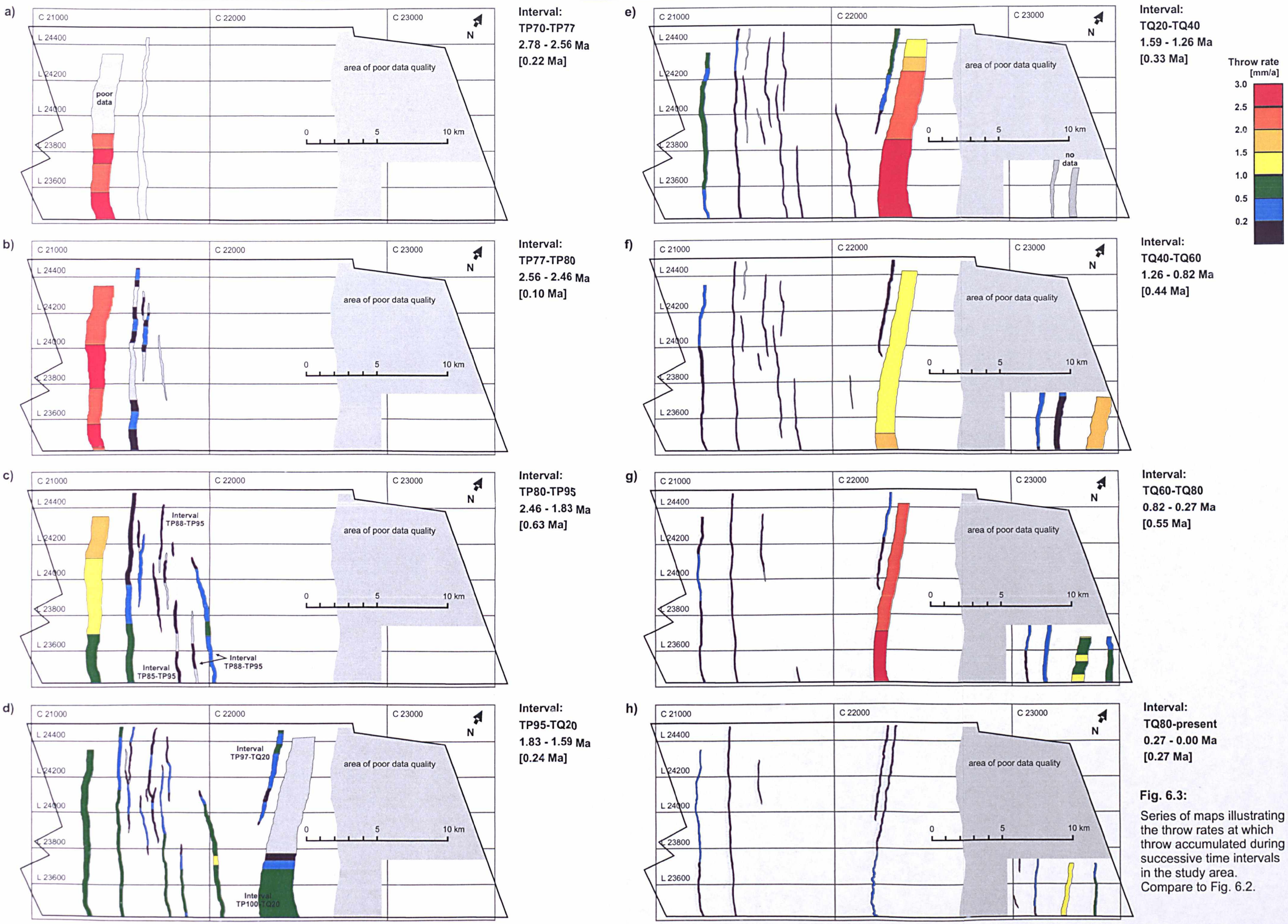

Fig. 6.3: Series of maps illustrating the throw rates at which throw accumulated during successive time intervals in the study area. Compare to Fig. 6.2.

The analysis of fault throw and throw rate data on the major and medium faults in the study area for a series of successive time intervals, spanning in total 2.78 Ma, reveals a pronounced eastward migration of major fault activity since the oldest investigated time interval in the Late Pliocene. In order to assess the total fault activity across the study area and variations thereof, the (decompacted) interval-throws on all faults considered were summed on two cross-sections (at 2 km and 10 km along strike measured from the SE edge of the dataset) for each interval and the resulting aggregate throw rates determined (Fig. 6.4).

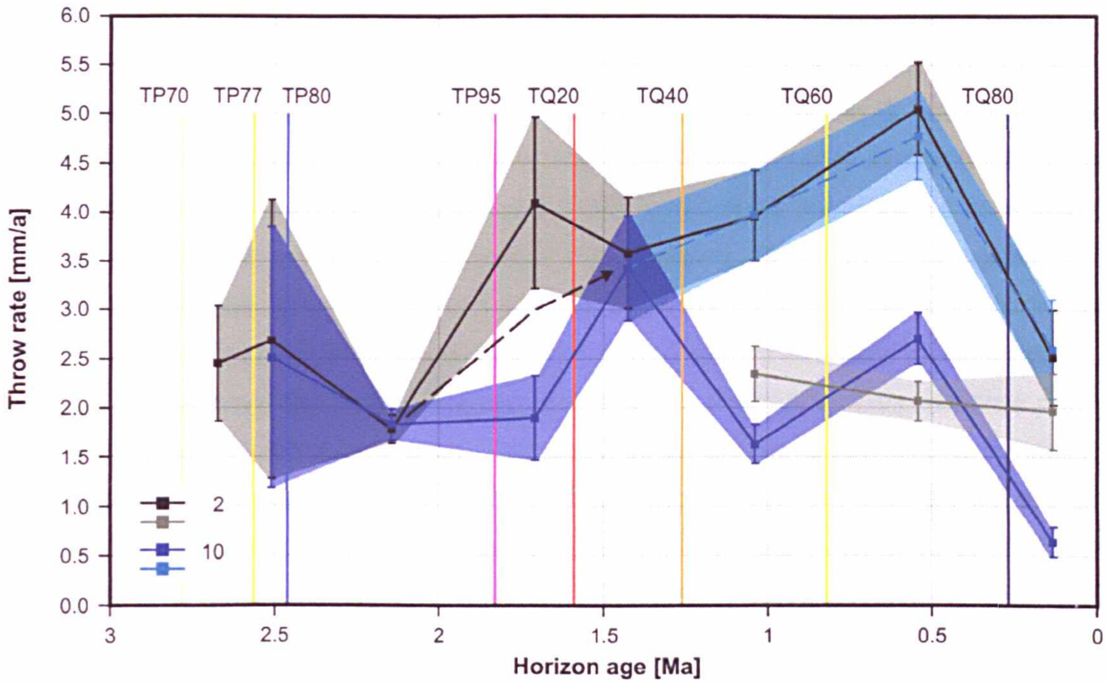

Fig. 6.4: Aggregate throw rates and their associated errors for two sections across the study area (black and blue). The grey throw rates and errors represent the values for the four faults (**x**, **y**, H, H*) in the north-eastern part of the study area at position 2 km. The light blue throw rates and errors are the combined trend of the data at 10 km and for the **x**, **y**, H, and H* faults for the three youngest time intervals. The dashed arrow indicates the throw rate trend from interval TP80-TP95 to TQ20-TQ40 for an average value for interval TP95-TQ20, determined between the two original data points.

For all intervals younger than horizon TP95, the values for the south (2 km) and north (10 km) of the study area deviate considerably. This can be explained by (1) the size of the active faults in each part of the study area contributing to the total throw accumulation, which particularly applies to the results for interval TP95-TQ20, and (2) the more complete dataset for the south than for the north in the hanging wall of the G Fault, which influences the data for the three youngest intervals. During interval TP95-TQ20 (Fig. 6.3d), six faults with very similar interval-throw rates contribute to the total extension in the south (Cassia, Ironhorse, **f**, **p**, A4, and G), whereas in the north, seven faults of varying and generally lower throw rates are active (Cassia, Ironhorse, **c**, **d**, **f**, **e**, and G FW), accumulating together only about half as much interval-throw as the faults in the south. In the north-eastern part of the study area (2 km), the dataset incorporates interval throw data for a number of faults that displace horizons TQ40-TQ80 (**x**, **y**, H, H*, plotted in grey in Fig. 6.4). Equivalent data are missing further along-strike due to reduced quality of the seismic data and result in the significant decrease in aggregate throw rates at the 10 km cross-section. Adding the interval-throw data for faults **x**, **y**, H, and H* to the residual data in the north (plotted in light blue in Fig. 6.4), assuming laterally constant summed throw rates in the hanging wall of the G Fault, results in very similar throw rate values between horizon TQ20 and the present for both sections across the study area. The individual throw rates determined for each interval for the southern (dark grey) and the corrected northern section (dark and light blue), are very similar with differences of less than 7%, except for the values for interval TP95-TQ20. Separating the total throw rates on the faults in the northeast (**x**, **y**, H, and H*), which shows an almost horizontal trend, reveals the large influence that the G Fault has on the younger intervals. Comparison of Fig. 6.4 to Fig. 5.12b shows a very similar trend of high throw rates during intervals TQ60-TQ65 and TQ65-TQ80 (here combined to one) and an abrupt decrease by about 2 mm/a to interval TQ80-present. The pronounced decrease of aggregate throw rates during the youngest time interval may be the result of incomplete data since throw data of faults to the east of the H* Fault are not available to this study.

The throw rates across the study area are not constant over the investigated time period, but vary between 1.5-5.0 mm/a, even excluding the incomplete dataset at 10 km for the youngest intervals. Throw rates of about 2.5 mm/a for the oldest two intervals are followed by a minimum of ca. 1.8 mm/a for interval TP80-TP95. During interval TP95-TQ20, the throw rates increase in the southern half of the study area, whereas they remain nearly constant in the northern part. A steady increase is observed from interval TQ20-TQ40 to TQ60-TQ80, where a maximum of 5 mm/a is reached. The youngest interval sees a significant drop to about half the throw rate of the previous interval (2.5 mm/a).

These temporal variations of the throw rate may, in part, be attributed to the quality and comprehensiveness of the available data, but also reflect the geological evolution of the basin. The distinct along-strike variation in total throw rate seen in Fig. 6.4 for interval TP95-TQ20 is considered unlikely to represent a regional trend of increasing fault activity to the south. A possible along-strike averaged trend of the throw rates during this interval is indicated by the dashed arrow in Fig. 6.4. However, to establish a more complete database, inclusion of more, also smaller faults for this investigation, particularly in the northern half of the available dataset and extension of the study area parallel to the strike direction of the faults is necessary.

Part of the observed throw rate minimum during interval TP80-TP95 might be due to the fact that for some faults (e.g. faults **p** and A4), the hanging wall cut-off of horizon TP80 is missing due to the antithetic relationship between the faults. Therefore, the growth history could not be determined for the full interval TP80-TP95, but only for the shorter interval TP88-TP95. The aggregate throw rates for additionally considered 300 m interval-throw (which is based on the minimal throw estimate for the A4 Fault for horizon TP80) would increase to about 2.25 mm/a but would still leave an overall minimum.

The total throw rates for the oldest and youngest time intervals will be most affected by a lack of data from adjacent faults that are located outside of the study area. Therefore, these are considered incomplete with respect to results for medium aged intervals and less reliability is given to then during the following considerations.

The trend of the residual throw rate with time, after taking local effects into account, is still characterised by a minimum during interval TP80-TP95 and a steady increase from then to a maximum of about 5 mm/a during interval TQ60-TQ80. This suggests increasing strain rates during the Pleistocene, which might have been caused by increasing influx of sediment. This would have increased the load of deposits onto the gravitationally failing shelf or it might have promoted movement on the basal detachment due to confined fluids and resulting high pore-fluid overpressures at great depth.

6.5 Conclusions

This study constrains the throw rates of faults in the Columbus Basin over a time span of 2.78 Ma. The investigated time span was divided into eight individual time intervals based on high-resolution biostratigraphic dating of marker horizons and thus enabled the evolution and migration of fault activity in the study area to be constrained in considerable detail for the first time. The analysis is used to investigate variations in the throw rates on individual faults, the migration of fault activity across the basin, and variations in the aggregate throw rate over time.

Individual throw rates and migration of activity

- The major faults initiated sequentially from west to east over the last 2.7 Ma. This confirms the results of earlier studies based on isopach maps (SYDOW et al., 2003; BEVAN, 2007; GIBSON et al., in press).
- The highest throw rates usually occur soon after initiation of each fault and on the largest faults reach values of up to 3 mm/a (Cassia Fault and G Fault).
- Smaller faults initiate in the hanging wall after the major fault is active, as can be seen in the case of the Cassia Fault and the Ironhorse, c, d, e, f, s, and p faults.
- The highest activity on the small faults in the fault block between the Cassia and G faults is observed during interval TP95-TQ20 – prior to and just after the G Fault becomes active.
- Once the G Fault is fully active (interval TQ20-TQ40), decreasing throw rates and tip line retreat of the faults in its footwall are observed, except for the G FW Fault with which it forms a relay ramp.
- The decreasing fault activity on medium faults, and eventually the Cassia and Ironhorse faults, seems to accompany initiation of the next large-scale fault to the east.

Aggregate throw rates across the study area

- The total throw rates (summed data of all faults considered) are not constant over the investigated time span.
- The total throw rate displays an overall minimum during interval TP80-TP95 (ca. 2 mm/a), and after that a continuous increase of total throw rates to a (possible) overall maximum during interval TQ60-TQ80 (5 mm/a).
- Local uncertainties where interval-throw data could not be determined for the total interval duration due to the cross-cutting relationship of conjugate faults can not explain the scale of variations observed (throw rates for the oldest two and the youngest time interval were not considered due to an incomplete database).
- The observations suggest a steadily increasing strain rate between deposition of horizons TP95 and TQ80 (1.83-0.27 Ma).
- The driving force of the fault movement is gravitational (i.e. sediment loading), but the reason for changes of throw rates on individual faults (especially the G Fault) is unknown. Possible causes include:
  - sea level changes, which govern the location of delta formation and sediment deposition (i.e. shelf-edge deltas during low-stands),
  - lateral migration of the main delta feeders along the shelf-edge and therefore relocation of areas of major deposition and hence gravitational driving forces of faulting,
  - variations of the overall sediment supply to the basin, which could cause long-term variations in loading and thus gravitational forces (failure of faults), and
  - variations of the pore-fluid pressure at greater depths through variations in loading, which could influence fault movement through changes in slip tendency on the basal detachment (CARTWRIGHT et al., 1998).

Chapter 7

Hanging wall anticlines

7.1 Introduction and motivation

Small-scale transverse anticlines are found in the hanging wall of several normal faults within the extensional Columbus Basin (Fig. 7.1). The anticlines have amplitudes of a few 10's m and their fold axes are oriented perpendicular to the fault plane. The fold patterns have been identified on high-displacement faults with maximum throws of at least 500 m (Ironhorse Fault), and are better developed on faults with maximum throws in excess of 1300 m (Cassia, G and H faults). The crests of the anticlines are not aligned vertically but are inclined sub-parallel with the fault dip. The folds occur over a considerable stratigraphic range (Figs. 7.2 and 7.3), and the amplitude of the anticlines decreases rapidly away from the faults (Fig. 7.2). Wider synclines are situated adjacent to upwards-narrowing anticlines. In map view, the anticlines are superimposed onto the km-scale hanging wall synclines (Fig. 7.4) that are the result of general displacement distribution (higher at the centre of the fault) on normal faults (Chapter 2).

Folding in the hanging wall of normal faults in extensional settings has been described previously (ANDERS & SCHLISCHE, 1994; SCHLISCHE, 1995; MCLEOD et al., 2000; YOUNG et al., 2001; GAWTHORPE et al., 2003; FOSSEN et al., 2003). ANDERS & SCHLISCHE (1994) describe km-scale transverse folding in the hanging wall of active normal faults as the result of segmentation. SCHLISCHE (1995) has distinguished between folds with axes parallel to fault strike (longitudinal folds, e.g. normal and reverse drag, rollover in the hanging wall of listric faults) and folds with axes perpendicular to the fault (transverse folds). In the latter case, synclines in the hanging wall of isolated normal faults are associated with the maximum displacement, approximately at the centre of the fault trace and in segmented fault systems with multiple displacement maxima and minima, synclines are located at the segment centres and anticlines are present at the relay ramps between overlapping segments (i.e. displacement minima). According to SCHLISCHE (1995), transverse folding in the hanging wall of normal faults can also be caused by undulations in the fault surface, where synclines form at recesses and anticlines form due to the transfer of the hanging wall block past salients.

The folding described by ANDERS & SCHLISCHE (1994) and SCHLISCHE (1995) occurs at scales of several km to several 10's km, but little other work has been published on small-scale examples to date. This might partly be due to high-resolution 3D seismic datasets that enable mapping and thus investigation of those structures becoming available only recently. Similar anticlines of metre-scale can be seen in surface exposures at Kilve, Somerset. There, the fold axes are also aligned perpendicular to the fault trace in the hanging wall of an extensional fault.

The aim of this study is to investigate the geometry and origin of small-scale transverse anticlines in the hanging walls of normal faults, mapped in seismic data and onshore field outcrops. Furthermore, the significance of these structures for identifying the location of paleo-fault linkage will be assessed. The objectives are detailed mapping of faults and horizons to describe the structures and possible relationships, investigation of throw data and cut-off geometries at and near the anticlines, and to present an evolutionary model for the development of the observed folds.

7.2 Methodology

The investigation of the hanging wall anticlines was carried out by seismic mapping and subsequent integration of the resulting horizon maps, horizon cut-off diagrams and fault throw data analysis. The anticlines were mapped on numerous horizons to build a database of closely spaced maps to investigate the varying geometries of the anticlines at different depths and their relation to the fault geometry.

The generated horizon maps at different stratigraphic levels, the fault system geometry and the fault throw characteristics were compared to fault linkage models and published field data (PEACOCK & SANDERSON, 1991, 1994; TRUDGILL & CARTWRIGHT, 1994; CHILDS et al., 1995; WALSH et al., 1999, 2003a; MANSFIELD & CARTWRIGHT, 2001) in order to analyse similarities and differences (see Chapter 2).

Six horizons (H1-7, H5 corresponds to TQ68) were mapped and correlated across the H Fault, in addition to the basin-wide horizons TQ80, TQ68, TQ60 and TQ50 (Fig. 7.5), in order to create a comprehensive database for throw measurements. The seismic expression of the HW anticlines and the deformed horizons is very clear and the horizons are laterally persistent. There is no disruption of the structures through weak amplitudes or lateral discontinuities other than small faults. The additional horizons (H1-7) were chosen to follow strong, laterally continuous reflections in order to obtain continuous, well defined surfaces.

The throw data (see Section 7.5) were determined from smoothed horizon data of the basin-wide horizons (TQ80, TQ68, TQ60 and TQ50). Horizons H1-7 were not smoothed in SeisWorks® in order to preserve their unaltered geometries, especially of the anticlines.

For all horizons, fault throw data and horizon cut-off depth data were extracted with Trap-Tester® at a spacing of 50 m, with a trim distance of 50 m, and a patch width of 200 m. The basin-wide marker beds have been dated using biostratigraphy, whereas horizons H1-7 were locally introduced to map the anticlinal structures and are only dated relative to the marker horizons.

7.3 Characteristics of the anticlines in the Columbus Basin, Trinidad (seismic dataset)

Hanging wall anticlines occur in the Columbus Basin adjacent to the fault surfaces of high-displacement faults. The anticlines investigated here in detail are associated with the H Fault in the NE of the dataset. Three anticlines can be observed (Figs. 7.3 and 7.6), of which the third to the NW is smaller, much less developed and less distinct than the other two anticlines.

7.3.1 Geometry of the anticlines attached to the H Fault

Anticline 1 shows widths of 90-280 m and heights of ca. 40 m, and anticline 2 is generally smaller with widths of 50-210 m and heights of 20-30 m. The geometry of the structures varies systematically from deep to shallow levels: At deeper levels the anticlines are generally broader, gently inclined, elongated towards the SE, compared to shallower levels, where they are more localised close to the fault surface with steep margins. Simultaneously, the position of the anticlines migrates from ca. 200 m in front of the present-day fault surface at depth to closely attached to it at shallower levels (Figs. 7.3 and 7.7).
The topography that is created on the horizon surfaces by the small hanging wall anticlines and intervening synclines extends less than 1 km away from the hanging wall cut-off into the hanging wall (Figs. 7.6 and 7.7). The horizon surfaces in the hanging wall of the H Fault that are undisturbed by the anticlines show no systematic relief and generally dip towards the fault (S to SW), at angles of less than 10°. These folds are clearly not drag folds because their axes are oriented perpendicular to the fault trace.

7.3.2 3D geometry of the H Fault and associated splays

The H Fault was mapped in detail on closely spaced lines (50-125 m) from the 3D seismic survey to describe the fault trace geometry and to identify possible fault-related deformation in the footwall and hanging wall (e.g. fault splays). The fault trace shows several pronounced kinks at depth (below ca. 1100 m), which enclose two local strands trending ca. 180-190°, significantly oblique to the general fault strike of ca. 140-155° (Figs. 7.6 and 7.7). The H Fault dips at 40-45° in its lower part and 45-50° in the upper part. Only at its upper tip does the fault steepen to a dip of 60°.

Close to the position of one of the kinks, two synthetic splays (S1 and S2) of the H Fault were mapped in its hanging wall. A third splay, S3, was mapped in the footwall of splay S1. Splays S1 and S2 converge towards the H Fault to the NW and join it near the kink at vertical branch lines (Fig. 7.6e&f). The biggest of the splays, S1, covers a depth range of ca. 900 m, has a maximum throw of less than 50 m on horizon H3, and has itself a synthetic splay in its footwall (S3). The splays are each up to 1 km long and intersect the hanging wall anticlines H1-4. Splay S1 reaches highest in the succession and terminates upwards above horizon H4, which is only intersected by a short portion of the fault close to its tip. The splays are at present located in the depth interval between 1.5-2.5 km in the hanging wall block, but have been transferred there during subsequent fault movement of the H Fault, causing the rock volume containing them to subside.

The depth interval where S1 is present in the hanging wall corresponds to 1.1-1.6 km depth in the footwall. This is based on the stratigraphy and considerations that fault activity of the splay faults, especially S1, was syn-sedimentary, similar to the other faults in the dataset. Throw data for S1 are, however, too scattered and the seismic resolution too low to establish a syn-sedimentary pattern in the throw data or distinguish a growth sequence.

Above the level of the synthetic splays and the estimated equivalent depth of ca. 1.1 km in the footwall block, the fault trace of the H Fault becomes progressively smoother upwards (Fig. 7.6a&b) with bends or irregularities disappearing.

Splay S1 is always located to the NE of the crest of the anticline and thus displaces the north-eastern limb of the anticlines on horizons H2, H3, and H4 (Fig. 7.3), preserving the fold crests in its footwall.

The location of the hanging wall anticlines with respect to distinct changes in the fault geometry (i.e. fault splays and kinks in the fault trace) is essential to establishing a model of their relation to each other and the evolution of the observed features. A key observation that can be made in Figs. 7.6 and 7.7 is that the anticlines are consistently located either adjacent to or at the kinks in fault strike.

7.3.3 Horizon cut-off and fault throw diagrams

The two larger anticlines are clearly expressed in the horizon cut-off data for the H Fault at all horizons (Fig. 7.8a), except for the youngest one, TQ80. The anticlines are imaged as local deviations of the hanging wall cut-offs towards shallower depths and correlate in shape and amplitude very well between neighbouring horizons. In contrast to the hanging wall cut-off data, the footwall cut-off geometries are linear and near-horizontal, slightly dipping to the NW for the older horizons, and with only minor undulations for the marker horizons and selected local horizons (H 1, 3, 6, 7) (Fig. 7.8b). A small but noticeable shift of the crest of the anticlines towards the NW (ca. 300 m) is observed for both anticlines.

The throw data along the H Fault show pronounced minima for both anticlines on all mapped horizons except TQ80, with anticline 1 located at around 0.9-1.2 km and anticline 2 at about 1.9-2.1 km along strike (Fig. 7.9). Thus, the fault throw data, which is determined as vertical difference between the cut-off depths at any location, varies systematically along these horizons as a result of the irregularities in the hanging wall geometry, which are caused by the anticlines. The throw minima correlate very well from one horizon to the next and are of the order of up to 100 m less throw than in adjacent areas. The shift in location of the throw minima of about 300 m to the NW up-section within both groups coincides with a subtle shift of the anticlines seen in map view (Fig. 7.7). The uppermost mapped horizon, TQ80, shows only very subtle folding in the hanging wall, and a near-linear, horizontal footwall cut-off graph. This results in a fault throw graph that is slightly undulating but with much smaller amplitudes than for the underlying horizons.

7.4 Other examples of hanging wall anticlines

7.4.1 Kilve, Somerset, UK (field example)

Similar anticlines to those in the seismic data can be seen in outcrop at Kilve, Somerset, UK. They occur in the hanging wall of a S-dipping normal fault that displaces the well-studied succession of inter-bedded shales and limestones of the Lower Jurassic of the Bristol Channel Basin on the tidal platform of the southern Bristol Channel coast (Fig. 7.10). At low tide, the tidal platform is excellently exposed and the structures have been mapped both in outcrop and on aerial photographs.

The field-example of small-scale hanging wall anticlines is located ca. 300 m northwest from Kilve Pill along the shore (Fig. 7.10b). The stratigraphic units in the study area show no thickening of single beds or multi-layer units laterally or across faults. Therefore, the faulting occurred after deposition of the Lower Jurassic, and the extensional faults related to basin formation in the study are interpreted as blind normal faults that did not reach the seabed whilst active. This also applies to the strike-slip faults that originate from a later basin inversion event. There are no signs of reverse fault reactivation due to inversion in the immediate study area.

The Bristol Channel Basin forms a half-graben whose major bounding fault dips to the south (Brooks et al., 1988) and is part of the larger Wessex Basin, which underwent N-S extension in the Mesozoic (Chadwick, 1986). The Bristol Channel Basin contains strata of Permian to Oligocene age (van Hoorn, 1987; Brooks et al., 1988; Glen et al., 2005), with the main basin fill formed by Triassic and Jurassic rocks (Brooks et al., 1988). Along the southern Bristol Channel coast between Watchet and Lilstock, Lower Jurassic rocks (Lias) are exposed. They are composed of bituminous shales, shales and inter-bedded limestones and marls (Whittaker & Green, 1983), and individual beds within the Lower Jurassic succession can be identified and correlated on km-scale along these coastal outcrops

(WHITTAKER & GREEN, 1983). This allows detailed identification and mapping of stratigraphic separation across faults.

Four anticlines are exposed on the foreshore at Kilve and are located in the hanging wall of a large fault, which is referred to as Kilve Fault in the text and figures. All four anticlines are truncated against the fault surface. The fold structures extend between 20-40 m along the strike of the fault and 5-15 m perpendicular to it. The relief of each fold is formed by competent limestone beds, but the fold crests have been eroded.

The Kilve Fault is easily identified due to its mineralised fault core with dip-slip slickensides and dips to the south with 65-75° (strike ca. 100°). It is offset by a younger strike-slip fault between anticline 1 (E) and anticlines 2, 3 and 4 (W) (Fig. 7.11). There is a small but pronounced bend in the trace of the Kilve Fault in the western part between anticlines 3 and 4, where the fault surface steps about 2 m to the south. The fault trace immediately at the bend is covered with boulders and thus not visible. Several small-scale (5-80 cm displacement) synthetic and antithetic faults intersect the anticlines. These subsidiary faults are oriented at low angles (up to 20°) to the Kilve Fault and converge towards it (Fig. 7.12).
The dip of the strata in the footwall and hanging wall of the Kilve Fault varies considerably. In the footwall, the bedding planes are inclined to the E-SE with dip angles of 3-17° and the strata become younger towards the E. In the hanging wall, the alternating anticlines and synclines immediately next to the fault are formed by four successive limestone beds ([187], [189], [192], and [194], Fig. 7.11). The total thickness of this interval with interbedded shales is about 5 m, and the prominent limestone bed [192] shows very little or no dip a few meters away from the fault (Fig. 7.11). The very detailed knowledge of the stratigraphy in the study area and the mapping of individual beds in the footwall and hanging wall of the Kilve Fault enables determination of the stratigraphic offset across the fault: the stratigraphic off-set decreases from W to E by 12.5 m (from 81 m at anticline 4 to 68.5 m at anticline 2) over a strike distance of 134 m.

7.4.2 Basin and Range province, USA (literature example)

ANDERS & SCHLISCHE (1994) and SCHLISCHE & ANDERS (1996) describe the occurrence of km-scale intra-basin highs (up to 10 km wide) in the hanging walls of active extensional faults in the Basin and Range province in North America. There, basins and intra-basin highs alternate in the hanging wall of large-scale (>120 km length) active normal faults. The intra-basin highs (anticlines) have fold axes perpendicular to the fault trace and usually coincide with overlapping major fault segments.
The Star Valley Fault is an example for an unbreached fault overlap zone. Two fault segments overlap for a distance of ca. 10 km, creating an inclined ramp between them and a high adjacent to and in continuation of the frontal (basin-ward) fault tip (Fig. 7.13a). The tip

of the FW-ward fault bends towards the HW-ward fault, indicating possible footwall linkage in the future. Studies of the fault displacement distribution along the Star Valley fault show that displacement is highest near the centres of the fault segments and decreases to zero at the segment tips. This suggests that intra-basin highs form at fault overlap and linkage zones (SCHLISCHE & ANDERS, 1996).

In some cases, displacement is distributed across the intra-basin highs on several normal faults. For the Beaverhead Fault, where highs occur at linkage zones, comparison of the total displacement across an intra-basin high (Blue Dome high, ca. 2.5 km) to that on the major fault in the adjacent basins (Upper and Lower Birch Creek Valley, ca. 3 km), indicates a displacement minimum at the position of the intra-basin high (Fig. 7.13b).

In order to identify the origin and geometric properties of the intra-basin highs, ANDERS & SCHLISCHE (1994) investigated the hanging wall and footwall elevations and compared them to gravity data. The hanging wall elevation graph for the Beaverhead Fault shows distinct elevation highs at the positions of the intra-basin highs (Fig. 7.13c). Good correlation was demonstrated between intra-basin highs and gravity highs for several faults (for example Fig. 7.13d), which is attributed to the presence of shallow basement rocks (WHEELER, 1987) in the intra-basin highs. On the contrary, the footwall elevation profile shows no correlations with fault segment boundaries or the gravity highs.

7.5 Interpretation

An interpretation of the evolution of the hanging wall anticlines requires the following observations to be explained: The folded horizon surfaces, the migration of the anticlines with respect to the fault surface, and the varying fault geometry. Integrating these features, the hanging wall anticlines are interpreted to represent the remnants of fault segment linkage, by which several initially separate overlapping faults evolved into one through-going fault. A series of sketches representing different time steps during the evolution of this fault system are illustrated in Fig. 7.14, concentrating on anticline 1 at the H Fault.

During the early stage of development, two geometrically independent fault segments (subsequently referred to as segments X and Y) overlap over a distance of nearly 1 km parallel and 0.5 km perpendicular to fault strike, respectively. A relay ramp inclined to the SE develops between the overlapping fault tips. Additionally, a monoclinal fault propagation fold exists at the south-eastern (basin-ward) tip of fault segment X, indicated in Fig. 7.14a. This geometry is very similar to that of the Star Valley Fault in Fig. 7.13a. Splays S1 and S2 are interpreted to be the remnants of the fault tip of segment X (horsetail), which were at later stages abandoned (compare to Fig. 7.6f). Both these structures, the relay ramp and the fault propagation fold, interfere to create the broad anticlines at horizon levels H1 and H2, where the fold crest is located up to 300 m in front of the fault surface in the hanging wall block.

Continued propagation of segment Y led to footwall breaching (TRUDGILL & CARTWRIGHT, 1994) of the relay ramp and the development of an oblique breaching fault that causes the pronounced kinks in the fault trace at depth (Figs. 7.6c-f and 7.14b). Once the geometric linkage of segments X and Y is established, and the fault accrues displacement on the newly established fault plane via the breaching fault and propagates upwards, splays S1 and S2 become gradually abandoned (Fig. 7.6d) and the fault trace becomes progressively smoother (Fig. 7.6a&b).

Locally reduced slip tendency (MORRIS et al., 1996), impeding fault slip during continued fault displacement at the positions of the breaching fault, is considered to cause the rocks at the locations of the hanging wall anticlines to be displaced less than at the positions of the adjacent synclines (former fault segment centres) in the subsiding hanging wall block. This creates a pattern of alternating synclines and anticlines along strike dependent on the positions of breaching faults connecting a series of initial fault segments along strike and maintains the relief of the anticlines over a considerable depth range even after fault linkage took place. The anticlines at shallower levels form immediately next to the fault surface up-dip of the positions of the reduced slip tendency.

Linkage of the two segments X and Y was achieved at about the time of deposition of horizon H4, which is the shallowest horizon to be intersected by splay S1. The fact that not only the horizons present during fault linkage (H1-H4), but also younger horizons (H5-H7) show HW anticlines and throw anomalies indicates that a local, deep hindrance to fault slip, resulting from fault linkage, governs the fault throw patterns far above the level of linkage and is independent of fault trace geometry at those shallow levels.

The observed shift of the crest of the anticlines attached to the H Fault towards the NW might be caused by the change in anticline geometry from broad at depth to localised at shallow levels. The early relay ramp is broad and extends between the overlapping initial faults, whereas the anticline on younger horizons is narrow and localised immediately next to the breaching fault. The breaching fault is located near the NW end of the relay ramp (footwall breaching). The shift of the crest of the anticline can therefore be explained as migration of the highest elevation on the hanging wall from the centre of the relay ramp and fault propagation fold further to the NW next to the breaching fault.

ANDERS & SCHLISCHE (1994) and SCHLISCHE & ANDERS (1996) interpret the intra-basin highs in the Basin and Range province as the result of fault segmentation, overlap, and eventual linkage between neighbouring normal fault segments. Basins develop near the centre of initial fault segments and upon linkage of those segments, intra-basin highs form at the positions of overlapping faults and breached relay ramps.

A second process which might also partly contribute to formation of anticlines in the hanging wall block is compressive deformation of the wall rock while sliding down past a salient in the fault plane (SCHLISCHE, 1995).

The geometric linkage of fault segments X and Y and subsequent movement causes the fault trace to become smoother above the actual level of footwall breaching (above ca. 1.1 km). The prominent kink, remnant of the breaching fault connecting the initial fault segments, is preserved at depth in the FW block, loosing amplitude upwards where the fault traces becomes progressively smoother. Younger growth strata that were deposited in the presence of a significantly smoothed fault trace are therefore deformed whilst being transferred down the fault and over the kink that acts as a salient as described in SCHLISCHE (1995).

The kink is still present at 1460 m depth, roughly the level of the hanging wall cut-off of horizon H5, but much less defined above 1280 m depth. Therefore, horizons H1-H7 might have been deformed during displacement of the hanging wall block past the indenter. On the other hand, horizons H1, H2 and H3 are located at depths where the kink was either present during deposition or was established through linkage of the initial fault segments. This only leaves horizons H4-H7 to be deformed.

The deformation caused by slip over a salient is assumed to be of broader width and probably lower amplitude than the folds created by fault slip minima and is likely to decrease with a reduction of the salient through upwards-smoothing of the fault trace following fault linkage and decreasing distance of displacement of the hanging wall strata past the salient. Deformation due to a salient in the fault surface could be superimposed onto the deformation due to reduced slip tendency at the positions of fault linkage but assessment of the contribution of the former process is difficult.

7.6 Significance

These anticlinal features are not unique to the Columbus Basin. Similar structures have been found over a large scale range for instance in seismic data in the North Sea (MCLEOD et al., 2000; YOUNG et al., 2001; FOSSEN et al., 2003) and in field examples in the Basin and Range province, the Gulf of Suez (GAWTHORPE et al., 2003), and in Kilve, Somerset.

The knowledge of fault and horizon geometries and resulting throw profiles of a fully developed fault linkage zone can be used to aid interpretation of data where fault splays are not present or high-frequency anomalies are superimposed onto the general throw trend. In the latter case, the unidentified throw anomalies can be compared to the linkage-related patterns, and a similar origin might be concluded based on wavelength, amplitude, and degree of vertical correlation.

Fault splays, which are the abandoned remnants of former fault tips, might not be present if the seismic resolution is too low to resolve the displacement on the splay or the fault segments did not overlap before linkage. However, the throw minima typical for linkage zones will be developed and seismic attribute extraction (e.g. horizon dip maps) can additionally help to identify faults at the resolution limit.

7.7 Conclusion

Hanging wall anticlines are found on a number of extensional faults in the Columbus Basin. Similar examples of hanging wall anticlines have been found in field examples in Kilve (UK), the Basin and Range province (USA), and Gulf of Suez (GAWTHORPE et al., 2003), and in seismic examples in the North Sea (MCLEOD et al., 2000; YOUNG et al., 2001; FOSSEN et al., 2003). These different examples occur over a large scale range from meters (Kilve) to 100's m (Columbus Basin) to km (Basin and Range). The hanging wall anticlines observed in the Columbus Basin are attached to the fault planes of high-displacement faults in regions of bends in the fault plane, where locally the fault strike direction varies significantly from the regional strike of the fault. Hanging wall anticlines are characterised by a series of properties: 1) they are persistent through a considerable stratigraphic sequence (ca. 1500 m on the H Fault), 2) they arise through variations in the HW geometry, irrespective of FW geometry (Figs. 7.8 and 7.13d), and 3) they lead to formation of persistent throw minima on successive horizons (Fig. 7.9).

Hanging wall anticlines seen in the seismic dataset are interpreted to be remnants of topography that is created during interaction and eventual linkage of initially separate, overlapping faults into a through-going fault. The initial geometry of the hanging wall anticlines consists of the inclined relay ramp, which formed between the overlapping fault segments and the fault-propagation fold, which formed at the basin-ward tip of the hanging wall (frontal) segment (see Fig. 7.14a). Footwall breaching of the relay ramp establishes a through-going fault surface and leads to formation of a fault splay from part of the initial basin-ward fault segment and its gradual abandonment; the newly established fault trace becomes progressively smoother above the level of fault linkage. The breaching fault is likely to remain a region of reduced slip tendency for a considerable part of the fault history, which causes the anticlines (former relay ramp) as well as the synclines (former fault segment centres) to persist above the level of fault linkage. Thus, hanging wall anticlines are considered to relate to former and eventually breached relay ramps and are, therefore, an indicator of fault interaction.

7.8 Figures

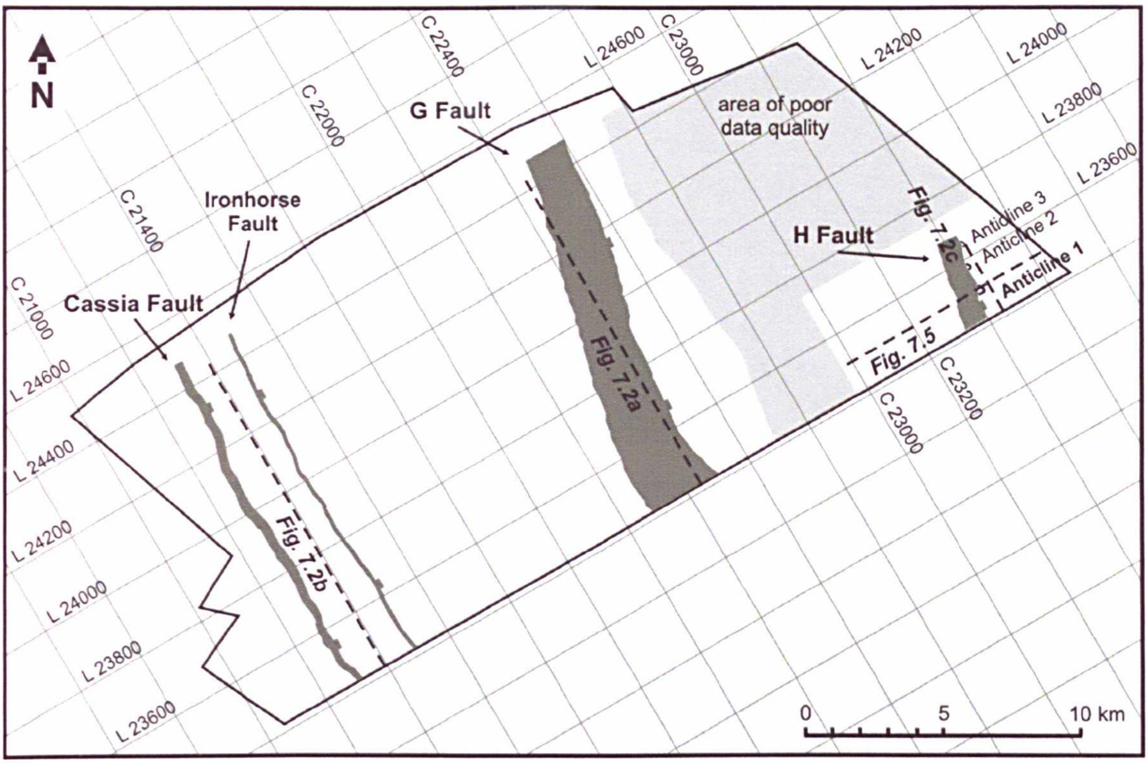

Fig. 7.1: Basemap of the survey area with the positions of the major faults with which hanging wall anticlines are associated. Fault heave geometries of the Cassia, Ironhorse and G faults are based on horizon TP100, and for the H Fault on TQ60, respectively.

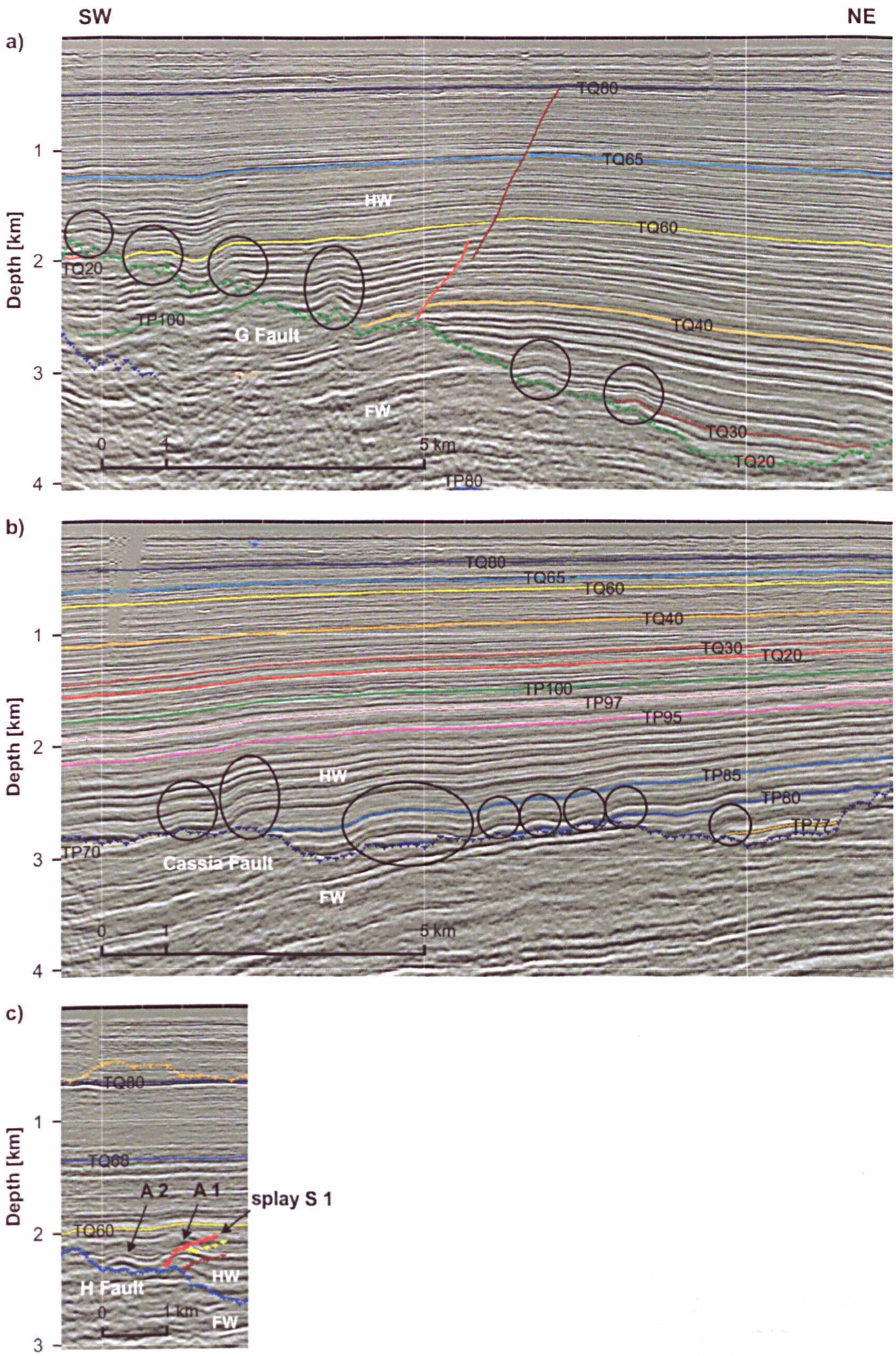

Fig. 7.2: Vertical strike-sections sub-parallel to the trend of **a)** the G Fault, **b)** the Cassia Fault, and **c)** the H Fault showing multiple strands of vertically aligned hanging wall anticlines (A1: anticline 1, A2: anticline 2). Note that because the sections are vertical and the faults dip, the anticlines disappear upwards in the section.

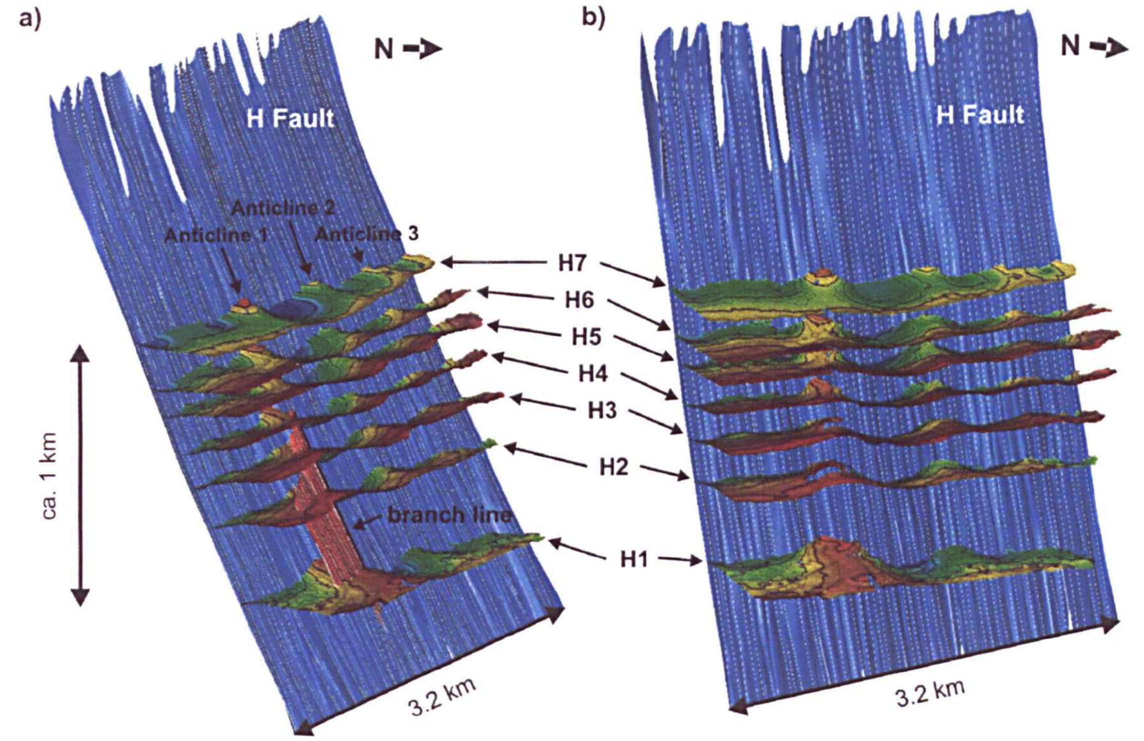

Fig. 7.3: 3D views of the hanging wall anticlines adjacent to the H Fault. Looking from the HW onto the fault surface, **a)** shows the synthetic splay S1 intersecting the deeper anticlines, **b)** only shows the H Fault. Note the broad nature of the anticlines at depth (horizons H1 and H2) and the progressively narrowing and localising geometry upwards (see also Fig. 7.7). Horizon depth-contours are at every 10 m.

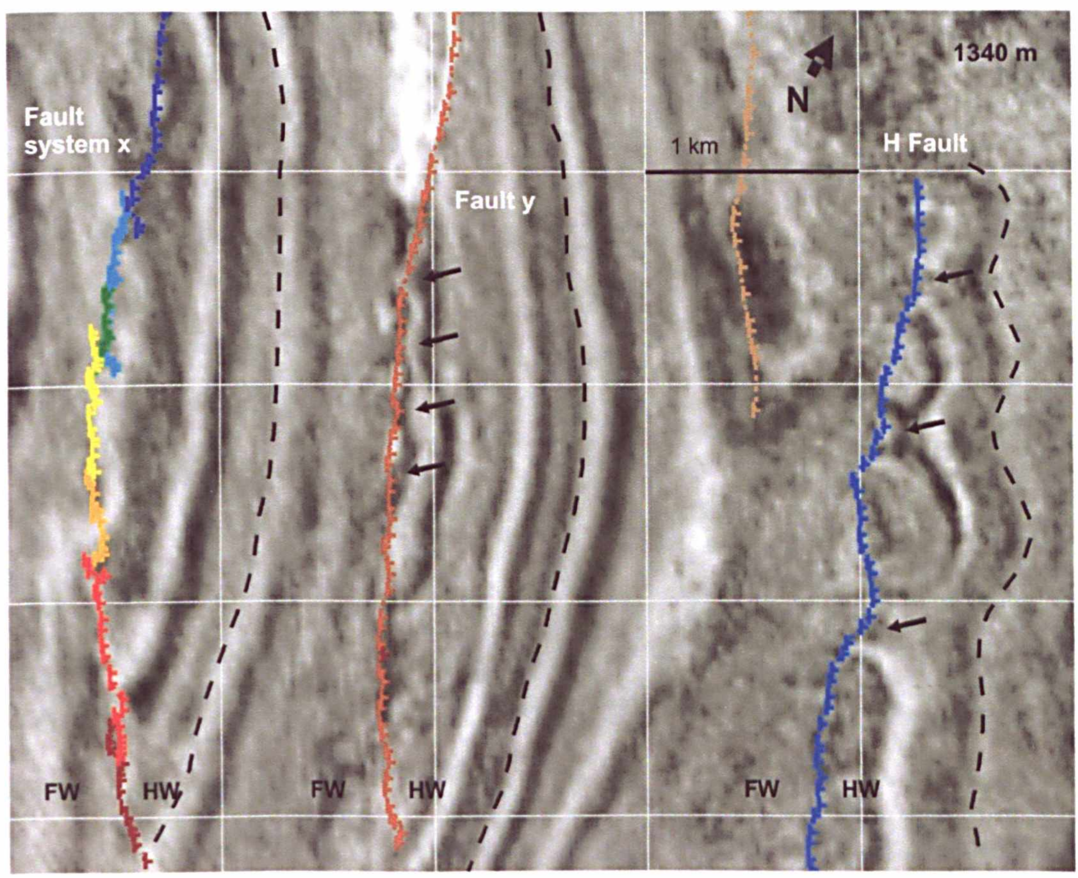

Fig. 7.4: Depth slice at 1340 m of the north-eastern part of the dataset, illustrating the broad hanging wall synclines (dashed black lines) associated with the fault system **x**, and the **y** and H faults and the smaller scale hanging wall anticlines (arrows).

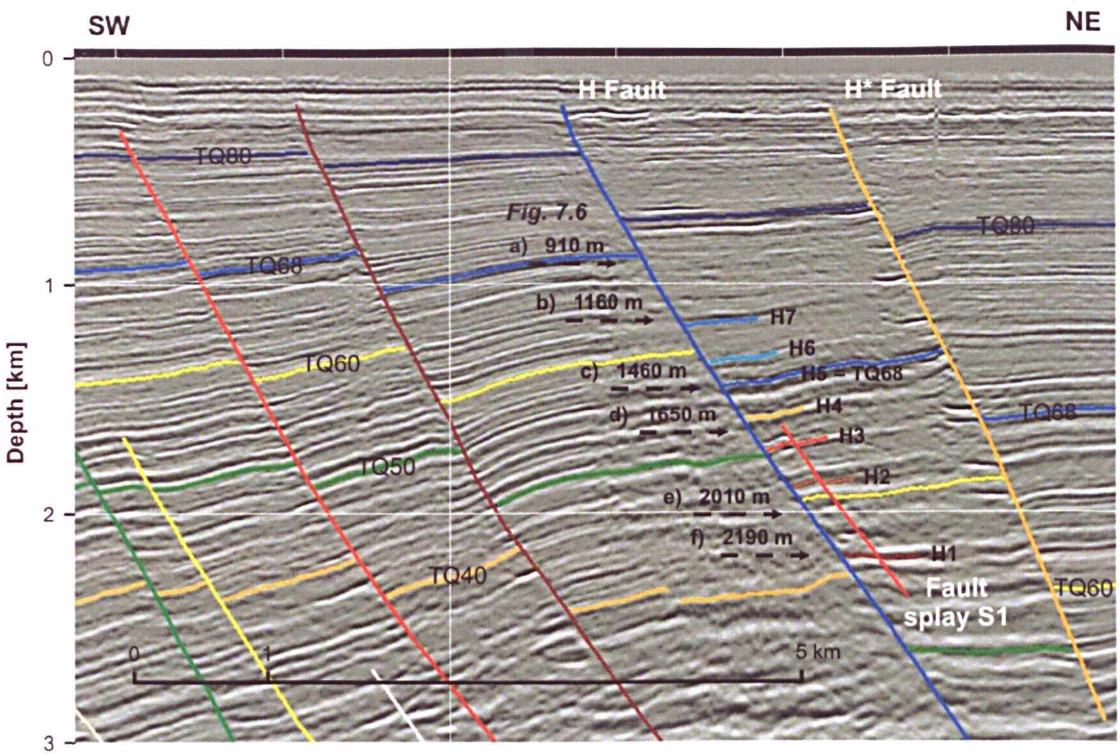

Fig. 7.5: Seismic cross-section through the bigger HW anticline (anticline 1) associated with the H Fault with indication of regional and local horizon surfaces and the position of the depth slices shown in Fig. 7.6. The additionally mapped horizons are only shown in the hanging wall but were all correlated across the H Fault.

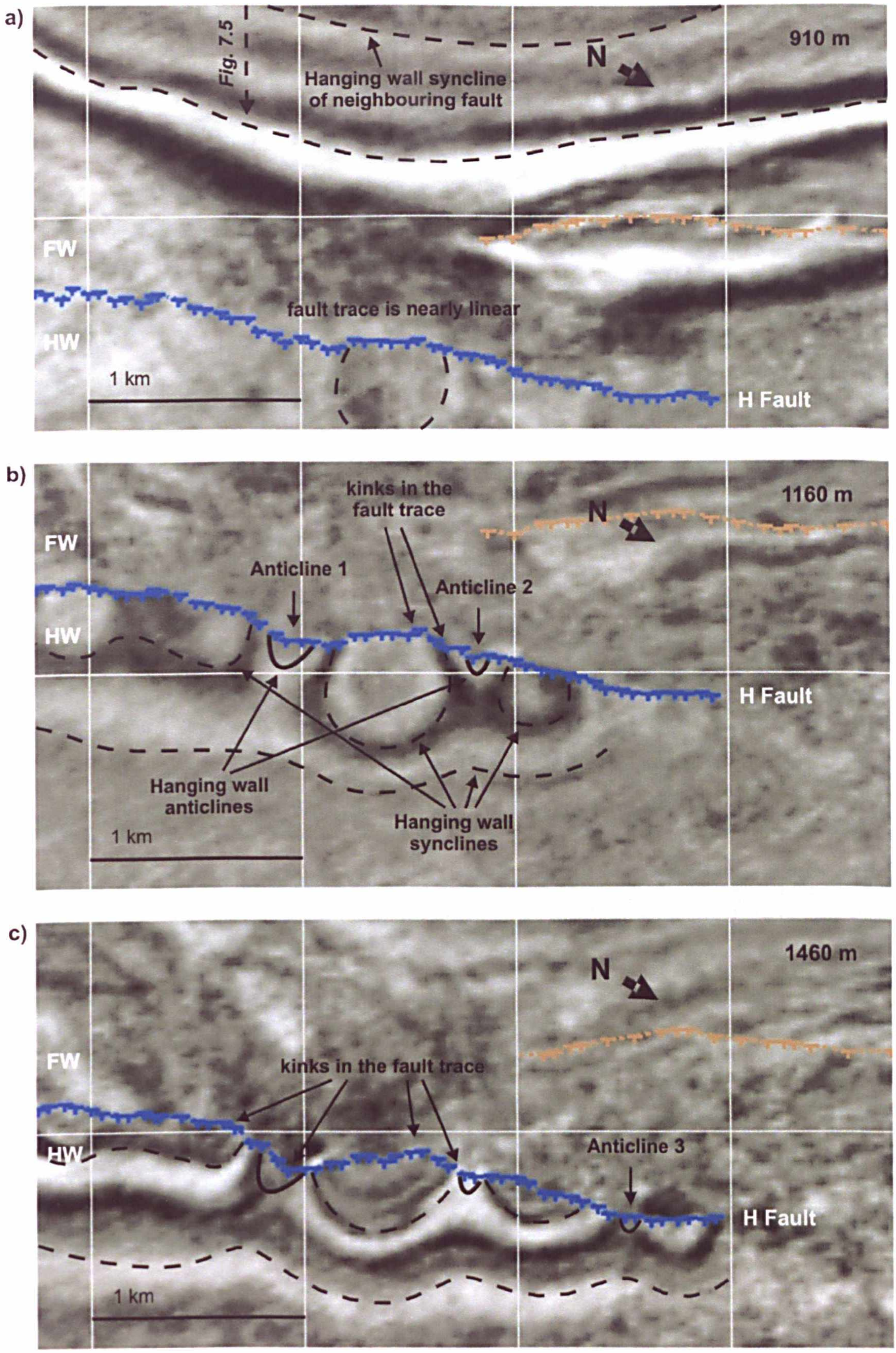

Fig. 7.6: Series of depth-slices illustrating the geometry of the H Fault and the synthetic splays S1, S2 and S3 at various depths. Note the three synthetic splays converging towards the H Fault at depth (d, e, and f) and the progressively smoother, more linear fault trace of the H Fault at shallow levels (a and b).

d)

e)

f)

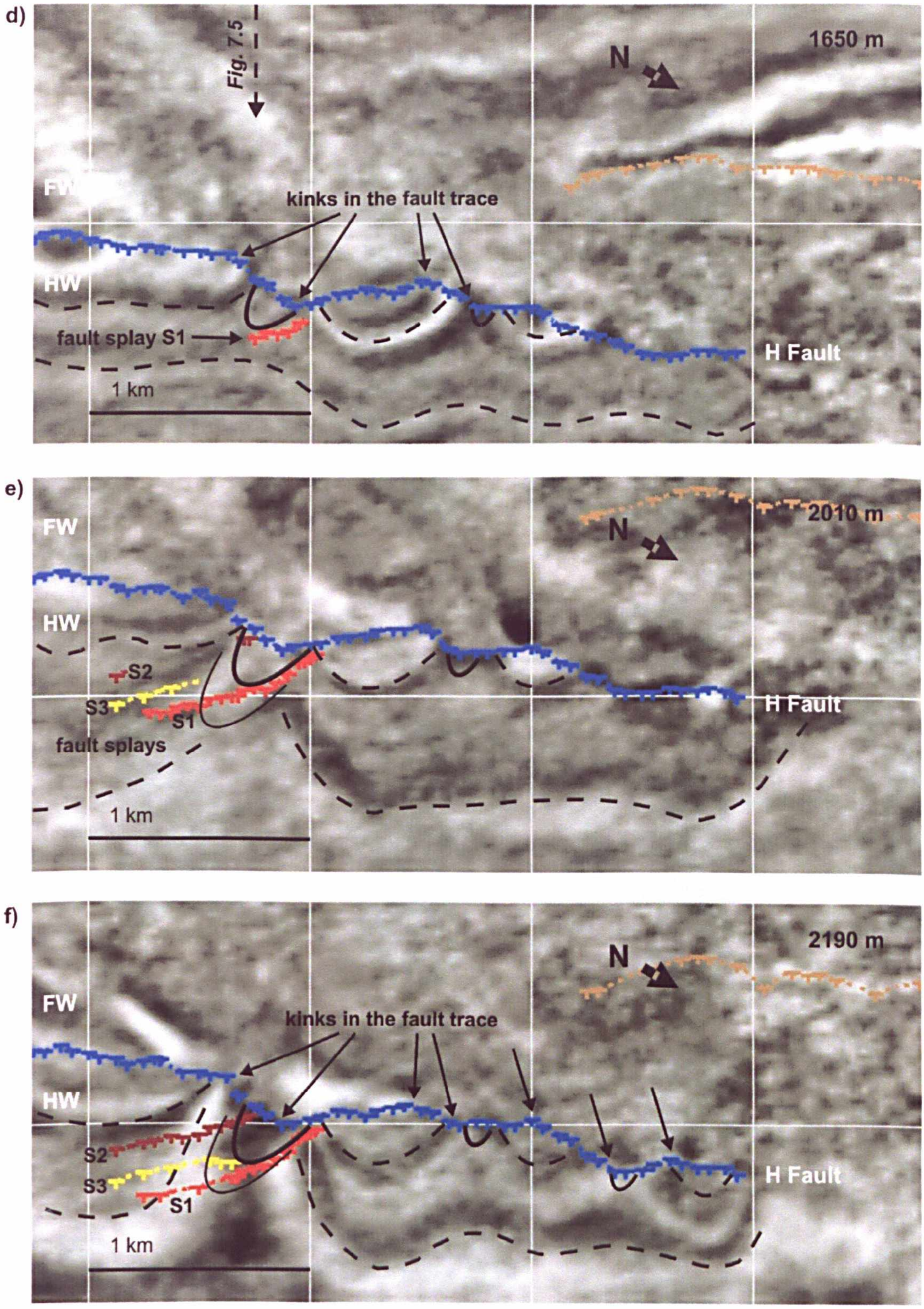

Fig. 7.6: continued.

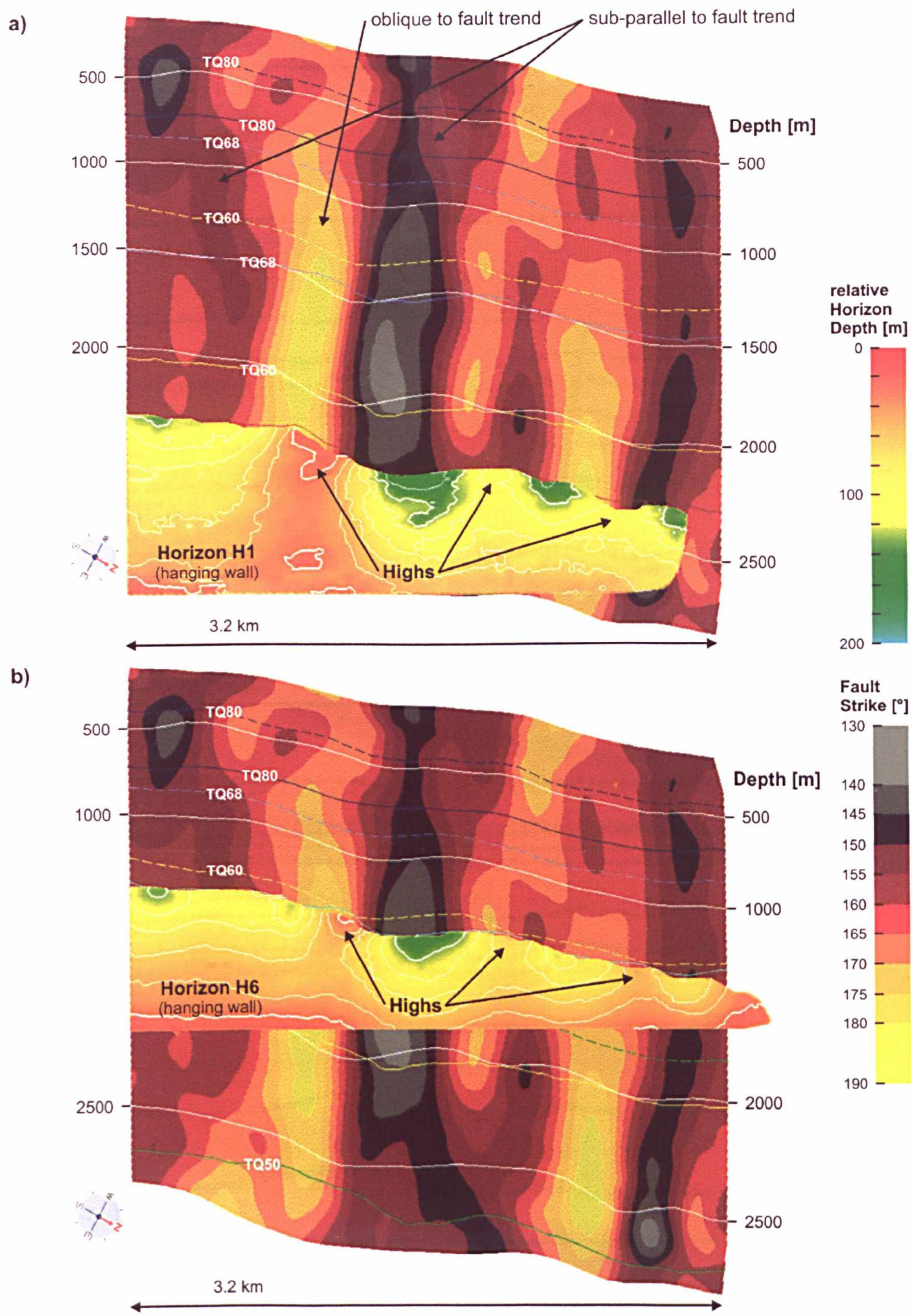

Fig. 7.7: Map views of depth-contoured horizon surfaces, **a)** H1 and **b)** H6, in relation to the strike-direction-contoured fault surface. Note the pronounced kinks in the fault surface near the position of the hanging wall anticlines (trending 170-190°) compared to the general fault strike (trending 130-160°) (compare to Fig. 7.6). Depth contours are at every 20 m on the horizon surfaces, and at every 500°m on the fault surface.
Note the migration of the anticlinal crest from a position in front to the fault surface at depth (horizon H1) to immediately bordering the fault surface at shallower levels (horizon H6).

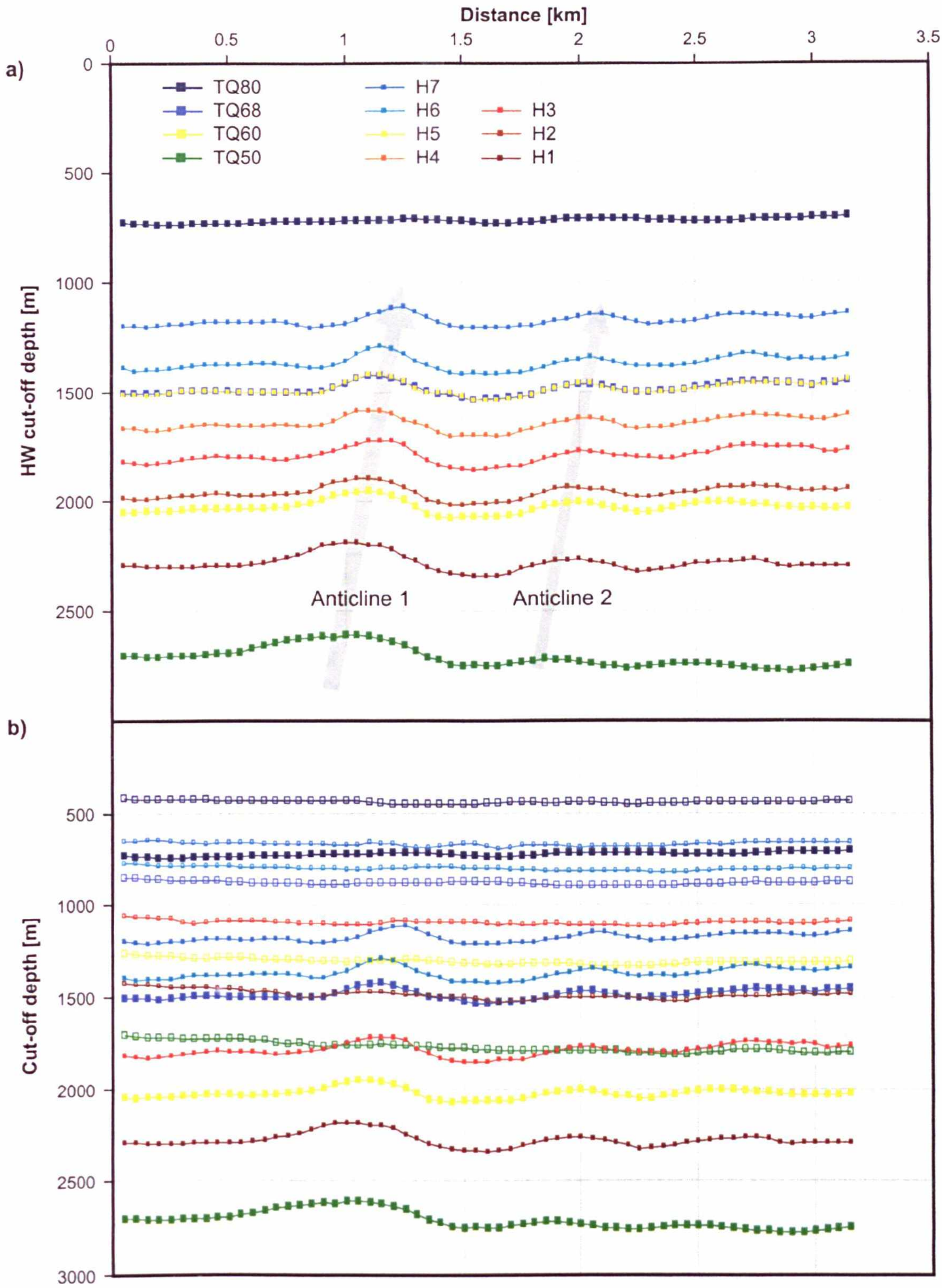

Fig. 7.8: Horizon cut-off depths on the H Fault as determined by TrapTester®. The hanging wall cut-offs in **a)** for the basin-wide (big squares) and local horizons (small squares) show pronounced deviation towards shallower values at the positions of the two hanging wall anticlines (arrows). In contrast, the FW cut-off geometries in **b)** for selected horizons (filled squares: HW cut-off, open squares: FW cut-off) are gently inclined but linear for all horizons.

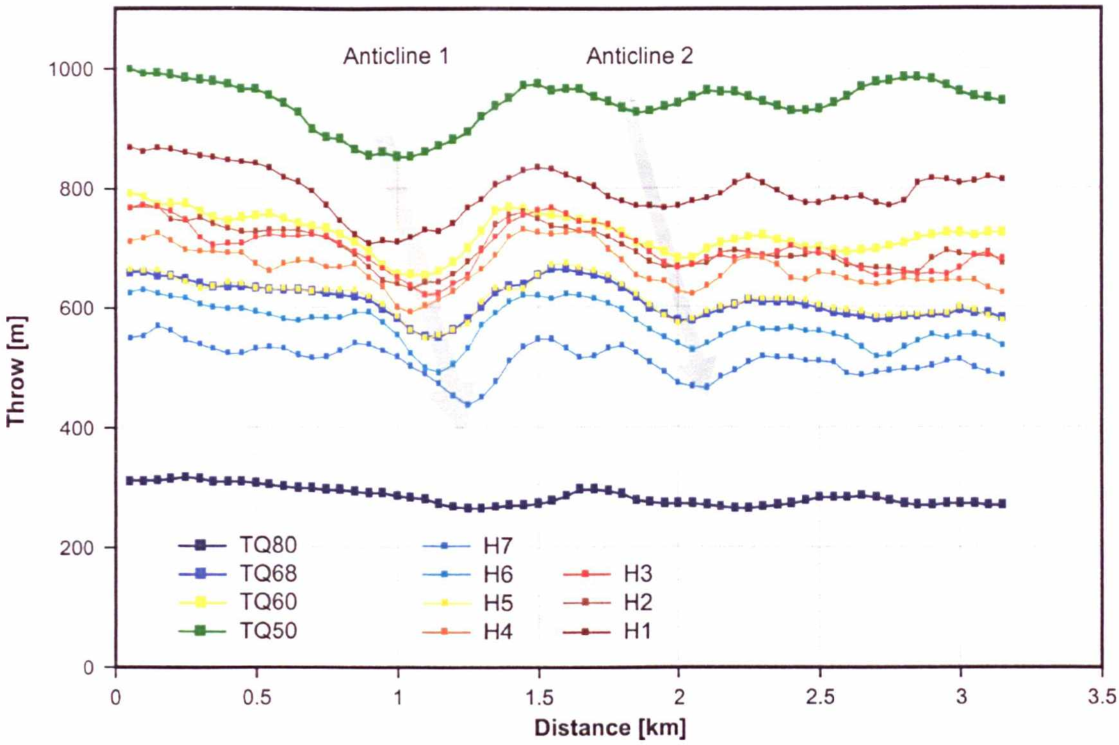

Fig. 7.9: Fault throw diagram of the horizons displaced by the H Fault revealing pronounced throw minima at the position of the HW anticlines, which indicates fault interaction and linkage.

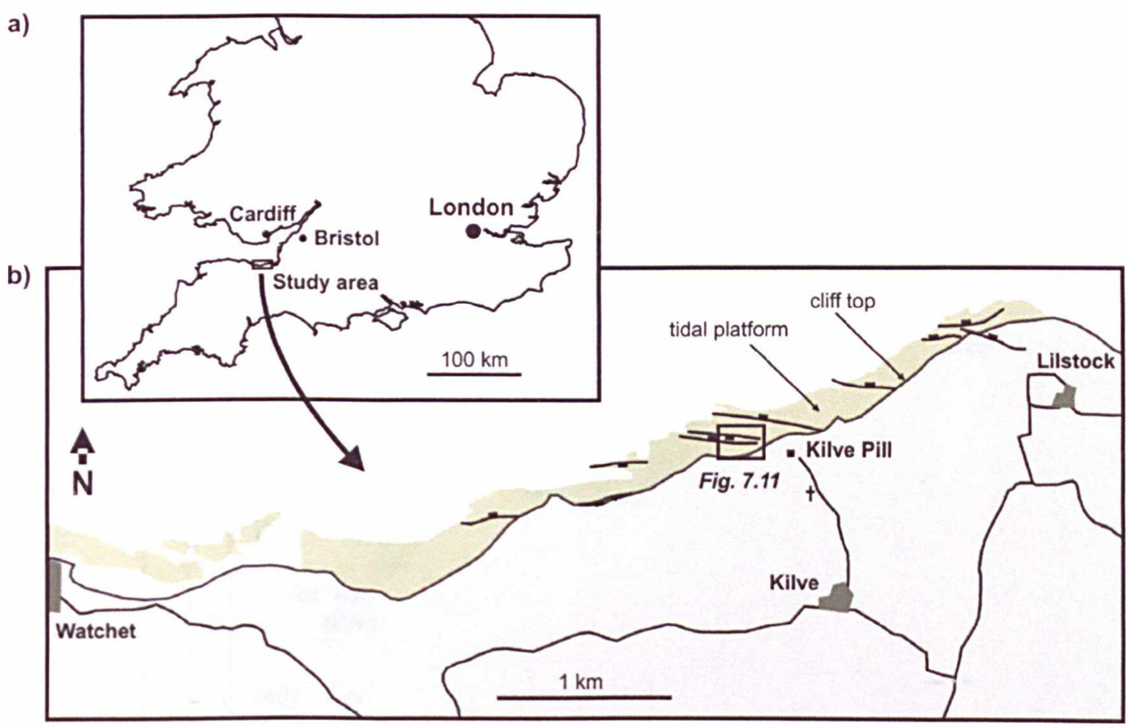

Fig. 7.10: Location map of the study area, **a)** on the Bristol Channel coast, and **b)** the position of the Kilve Fault on the tidal platform near Kilve Pill between Watchet and Lilstock. The position of major faults is indicated on the tidal platform.

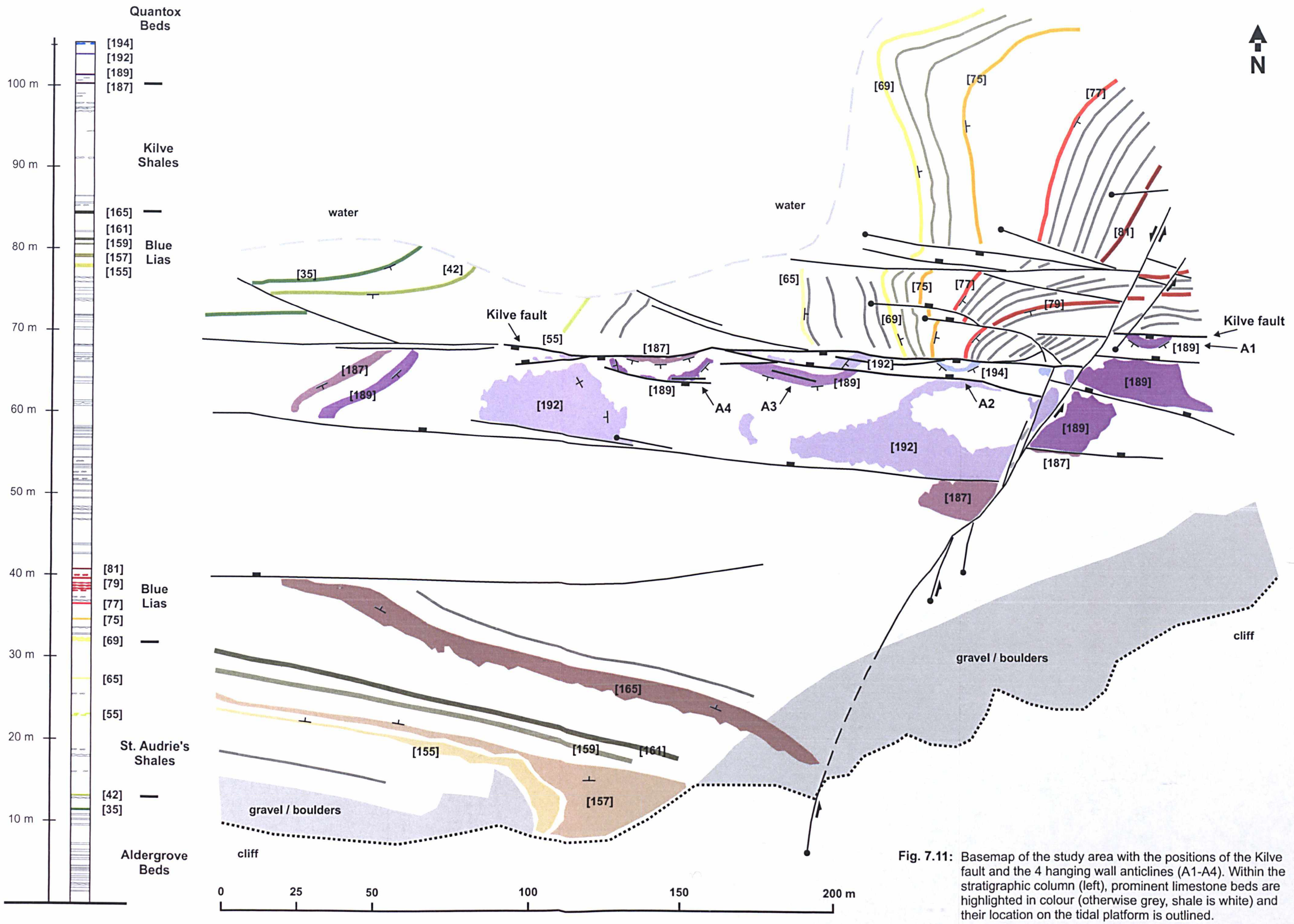

Fig. 7.11: Basemap of the study area with the positions of the Kilve fault and the 4 hanging wall anticlines (A1-A4). Within the stratigraphic column (left), prominent limestone beds are highlighted in colour (otherwise grey, shale is white) and their location on the tidal platform is outlined.

a)
b)

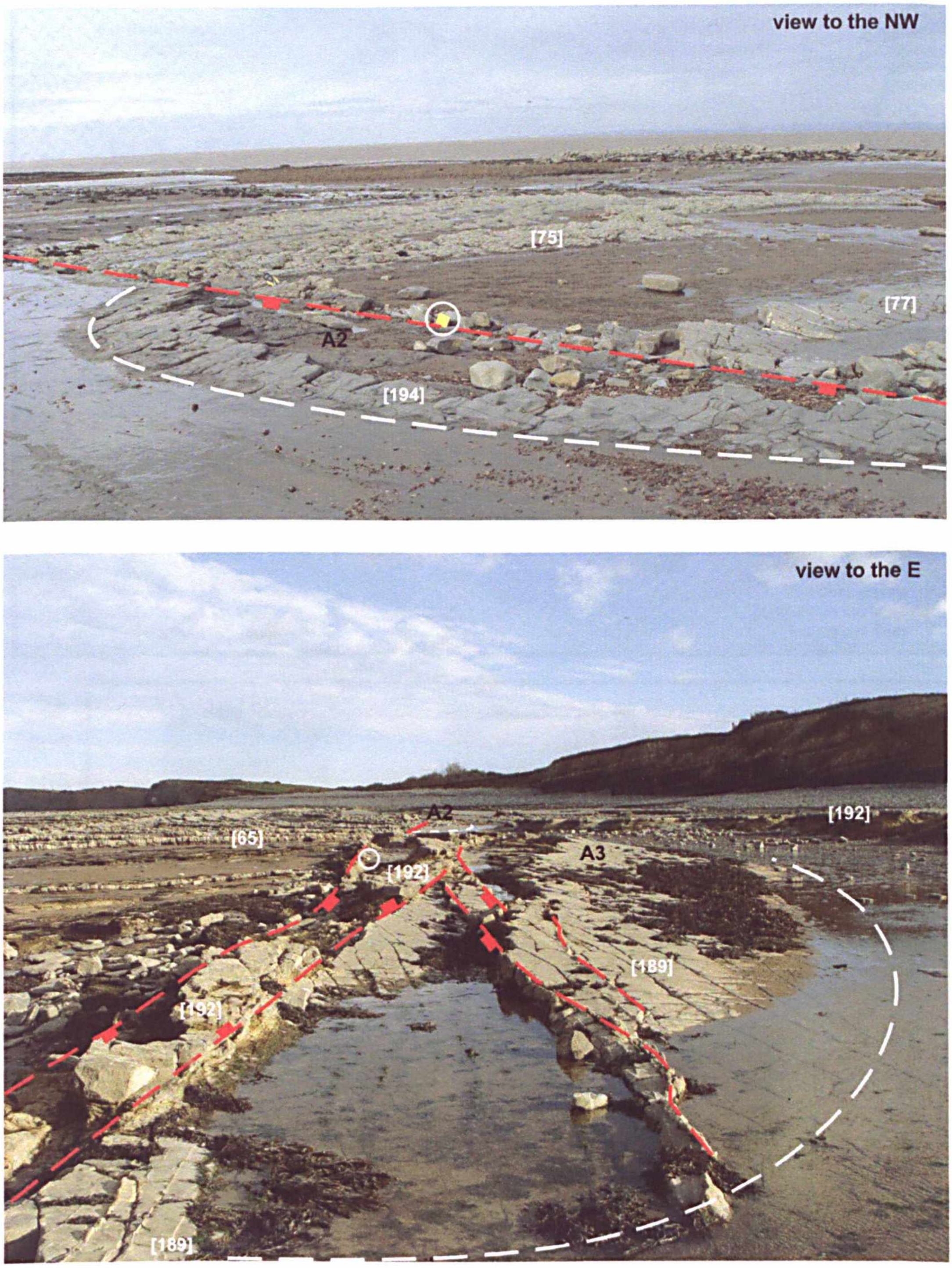

Fig. 7.12: Photographs of **a)** anticline 2 and **b)** anticline 3. The relief of the respective anticlines is outlined in white and the fault traces are indicated in red. Note the circled scales (notebook), the numbered limestone beds (compare to Fig. 7.11), and the subsidiary faults cross-cutting anticline 3.

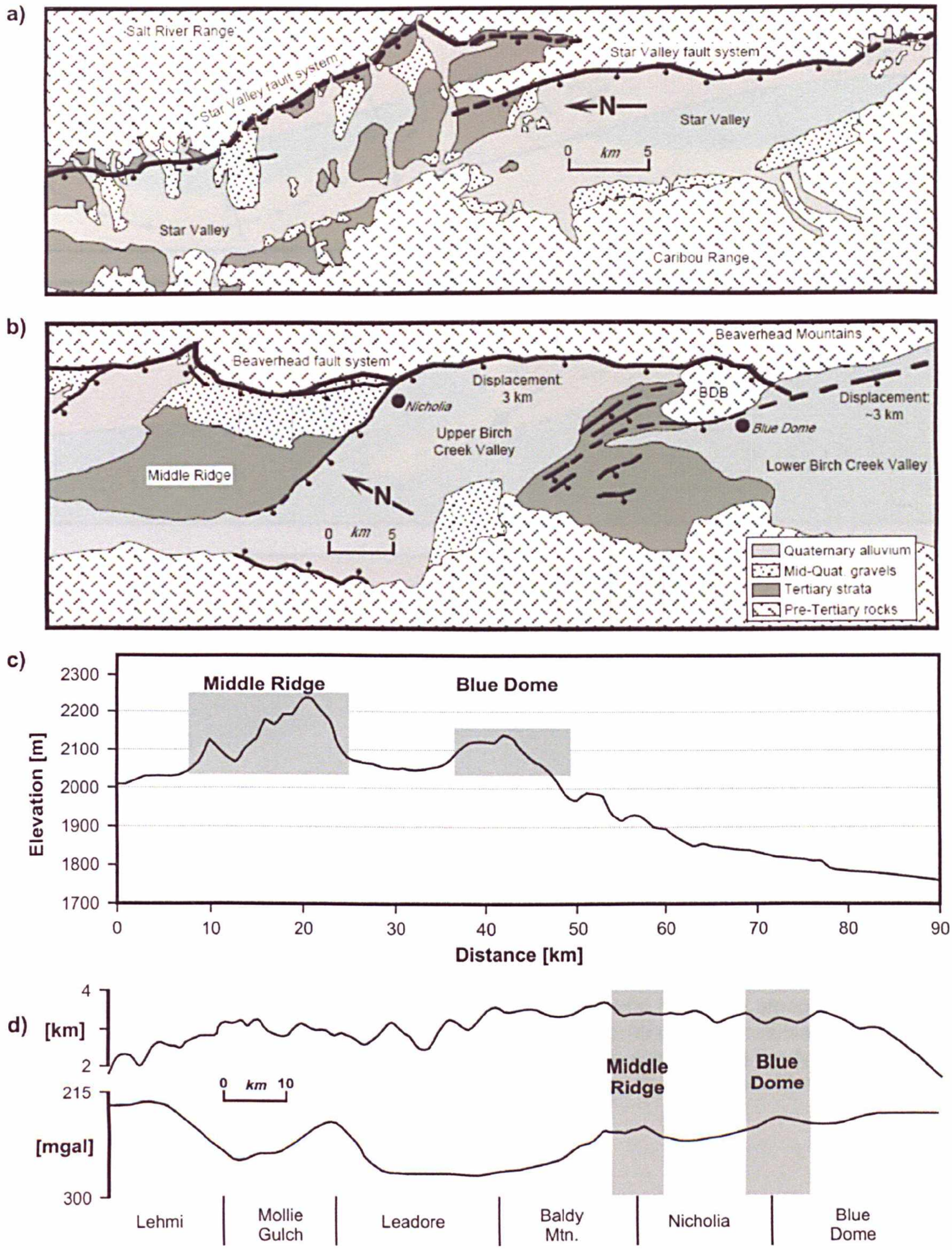

Fig. 7.13: **a)** Geological map of the Star Valley fault system with two overlapping fault segments. Note the intra-basin high, formed by pre-Tertiary and Tertiary rocks (legend in b), between the overlapping tips and in continuation of the basin-ward fault tip. **b)** Geological map of the Beaverhead fault system, illustrating two intra-basin highs (Middle Ridge and Blue Dome high) in between basins. The Blue Dome high is displaced by a number of synthetic normal faults and the summed displacement across it is ca. 2.5 km, less than the 3 km displacement measured on the bounding fault in the Upper and Lower Birch Creek Valley. Both maps are from SCHLISCHE & ANDERS (1996). **c)** Elevation profile of the HW of the Beaverhead Fault, the position of the intra-basin highs is indicated by grey bars. **d)** Elevation and gravity profile (Bouguer gravity anomaly profile) for the Beaverhead fault system, regions of multiple fault overlap are shaded grey and vertical lines indicate fault segment boundaries. Both diagrams are redrawn from ANDERS & SCHLISCHE (1994).

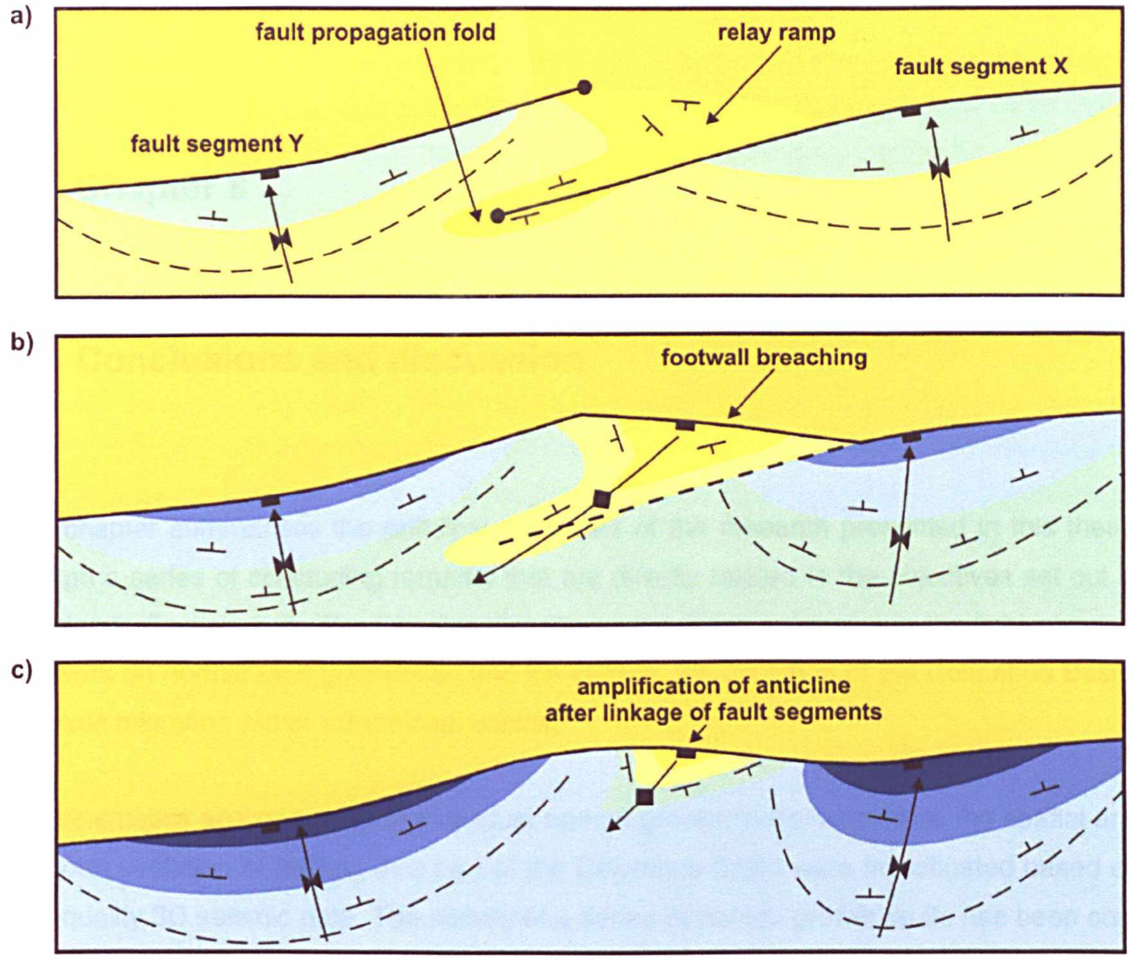

Fig. 7.14: A series of schematic sketches illustrating the most likely evolution of the H Fault and the development of the HW anticlines. **a)** Two overlapping faults (segment X and Y) separated by a relay ramp. At the tip of the basin-ward fault a fault propagation fold is developed, at the centres of the fault segments synclines are present. **b)** Linkage of the fault segments through footwall propagation, the frontal fault tip is gradually abandoned and the relief created by the fault propagation fold decreases. **c)** Fault linkage is fully established and the fault trace becomes smoother. The anticline migrates towards the fault plane and becomes more localised during fault movement after linkage had been established. The synclines at the former segment centres form distinct lows, which are broader than the anticline. The dashed lines indicate the extent of the hanging wall synclines

Chapter 8

Conclusions and discussion

This chapter summarises the principal outcomes of the research presented in this thesis through a series of concluding remarks that are directly related to the objectives set out in Chapter 1 (Section 1.2). The Chapter also discusses these outcomes in the light of previous work on normal fault geometries and kinematics, the evolution of the Columbus Basin, and fault migration within extensional basins.

The kinematics and geometry of individual normal growth faults, as well as the spatial and temporal evolution of faulting in a part of the Columbus Basin were investigated based on high-quality 3D seismic data. The activity of a series of normal growth faults has been constrained using fault throw measurements as opposed to other methods such as isopach data and growth indices. From the present-day fault throw distribution the amount of throw accumulated during successive time intervals bound by marker horizons was determined. This process is referred to as fault displacement back-stripping. From the interval-throw data, throw rates were calculated using biostratigraphic horizon ages. The described techniques were used to investigate a number of individual faults and fault systems, which were then integrated alongside other faults across the study area to obtain a more basin-wide view of the fault evolution. The approach to use throw data and throw rates enables the fault activity to be constrained quantitatively.

8.1 Conclusions

Geometry and kinematics of extensional growth faulting

The data presented in this thesis reveal a variety of complex fault geometries, evolutions, and interactions.

- The large-scale Cassia Fault and the neighbouring medium-scale Ironhorse Fault both show highest throw rates during early stages of their activity, and tapering throw rates almost until the present-day. This confirms the results of earlier studies (SYDOW et al., 2003; GIBSON et al., in press).

- The displacement distribution on both faults is characterised by soft-linked displacement transfer during early stages that is evident from the throw distribution on each fault. However, the aggregate throw data across both faults shows a much more uniform throw distribution along strike and thus demonstrates geometric coherence between the faults (WALSH & WATTERSON, 1991).
- The large-scale G Fault, the biggest fault in the study area, shows a very different throw rate trend to the Cassia and Ironhorse faults. Very high throw rates occur during early and later stages (1.46-1.26, and 0.82-0.27), with a minimum at around 1.26-0.82 Ma and very rapidly decreasing throw rates towards the present-day. The reason for the late throw rate high is unknown, but activity of the fault may have been influenced by a lateral shift of deposition within the Columbus Basin or a general increase in sediment supply.
- Fault system **d** exhibits linkage of two initially independent, overlapping faults via an oblique breaching fault. This may have initiated as a blind splay of one of the initial segments and then intersected the seabed and propagated towards the overlapping fault and established hard-linkage between the faults.
- Fault system **x** is characterised by a through-going fault surface at depth that evolved into an en echelon array of seven individual splays at shallow levels. The splays have formed through counter-clockwise rotation around a sub-vertical axis and local lateral propagation.
- The opposing relationship of geometric linkage and kinematic linkage during the evolution of both these fault systems – the initial segments remained kinematically distinguishable for some time even after full geometric linkage of fault system **d** was reached along the newly established fault surface and the fault only moved as one entity during its last stages, whereas fault system **x** remained fully kinematically linked at the level of the splays although geometric linkage had ceased – suggests that no simple correlation between geometric linkage and kinematic linkage exists. Geometric linkage is neither a prerequisite for nor induces kinematic linkage.
- Interval throw rates are highest for the largest faults, reaching up to 3.6±0.9 mm/a on the G Fault and 2.5±0.6 mm/a on the Cassia Fault. Throw rates on the smaller faults are generally below 1.0 mm/a.
- A series of small-scale transverse anticlines in the hanging walls of major faults are remnants of fault linkage. The anticlines are located immediately next to the fault surface, often adjacent to kinks in the fault, and coincide with vertically persistent displacement minima at these positions.

Spatial and temporal distribution of fault activity

- Extension of the Columbus Basin through NE-dipping regional normal faults has experienced a progressive eastward migration of the initiation of faulting and the location of major fault activity over the last 2.8 Ma in the study area, which is in agreement with findings by SYDOW et al. (2003) and BEVAN (2007).

- Subsidiary faulting in the hanging wall of major block-bounding faults initiates after the major fault has become active.
- Initiation of the next major fault basinward of an existing one leads to reduction and eventual cessation of activity on the earlier fault.
- The aggregate throw rate for all major and medium faults across the study area is not constant over the investigated time span. From a minimum of 1.8±0.2 mm/a between 2.46-1.83 Ma, a continuous increase to a maximum of 5.1±1.0 mm/a between 0.82-0.27 Ma is observed.
- The reasons for this increase in aggregate throw rates are uncertain. The trend might partly be explained by an incomplete dataset along the trend of fault migration, as a result of lateral migration of fault activity along-strike of the major faults, or might be due to increasing regional strain rates with time.
- Vertically persistent throw minima that are the result of relief in the hanging wall compared to a planar footwall cut-off can be used as an indicator of paleo-fault linkage at these locations. The presence of inactive fault splays linked to the active fault in either its hanging wall or footwall, which are most likely the remnants of abandoned fault tips, can underline this interpretation but is not essential since the resolution or quality of the seismic data might not allow to resolve low-displacement splay faults.

8.2 Discussion

Novel aspects of this study

This analysis of fault throw data was carried out on a depth-converted seismic survey which allows determination of fault throws in meters. The velocity model used for the depth-conversion is three dimensional and based on numerous well data from in and around the study area in order to apply the most accurate velocity distribution with depth and was provided by BP Trinidad & Tobago. A number of previous studies of fault growth and evolution are based on time data (e.g. DAWERS & UNDERHILL, 2000; MCLEOD et al., 2000) or on seismic data that has been depth-converted using a constant velocity over the investigated interval (e.g. MEYER et al., 2002). Fault throw data based on three dimensionally depth-converted seismic allow much more accurate investigation of throw accumulation and fault growth because the depths and distances measured best reflect the actual geometries in the subsurface. In particularly if the throw data occur over a significant depth range, three dimensional depth-conversion accounts for the non-linear increase of the acoustic velocities within the sedimentary sequence with depth and possible lateral variations due to facies changes. For throw data in time, the amount of throw accrued on deep horizons might be significantly underestimated compared to that on shallow horizons. With a uniform velocity model, deep throws might be underestimated or shallow throws overestimated depending on the velocity applied. Hence, it is more reliable to compare depth-converted throw data of horizons at various depths directly, whereas throw data in time or depth-converted using a uniform velocity with depth should be viewed more cautiously.

Decompaction of the throw data is also essential in order to correct for modifications of the initial amount of throw on each horizon during subsequent burial of the strata. In the case of syn-sedimentary faults as observed in the Columbus Basin, the initial increment of throw for any horizon interval accumulated close to the seabed. The accommodation created on the down-thrown hanging wall side is very quickly filled with unconsolidated sediments. The difference in throw between successive horizons can be represented by a column of sediments that is, during continued activity of the fault and ongoing sedimentation, subject to burial and hence compaction. Compaction is a complex process (GILES, 1997) leading to thickness reduction of sedimentary units with increasing burial depth. The systematic relationship between porosity loss and burial depth (decreasing porosity with increasing depth, MAGARA, 1980) was used in this study to quantify the amount of compaction at various depths and to determine a decompaction factor to correct for the reduction of layer thickness (interval-throws) since deposition. It is recommended (GILES, 1997) to use locally derived porosity-depth data for decompaction because they will reflect the porosity-depth trend of the strata of interest best. The porosity-depth trend applied in this study was provided by BP Trinidad & Tobago and is derived from a basin model integrating well and log data. If the throw data are not corrected for sediment compaction, the throw on older and deeper intervals will be systematically underestimated, the more so the deeper the interval is buried present-day. In this study, the greatest decompaction factor that was applied to the present-day interval-throw is 1.45. This is in contrast to TAYLOR et al. (2007), who argue that the loss of displacement due to compaction is generally less than 20% and that general displacement patterns and fault growth histories can be identified without decompaction. If the present-day interval-throw data are not decompacted, this would also influence the subsequently determined throw rates, which would be systematically underestimated for older and deeper buried intervals.

A novel aspect introduced to fault displacement back-stripping of faults with upwards-retreating tip lines was the comparison of throw graphs for successive horizons. If the tip line of a fault retreats and younger horizons are progressively shorter, the trace length and throw of the respective younger horizon were normalised to the trace length of the next older horizon. This method maintains a constant throw to length ratio and compares the amount of throw on successive horizons with the assumption that the fault trace length remained constant. It was applied in order to determine the actual throw difference between any pair of horizons, and hence the throw accumulated during each interval.

This approach makes it possible to compare the amount of throw on successive horizons of equal (normalised) length. Should the last stage of faulting be blind, the normalised throw graph would be expected to coincide with the one it was normalised to, and would thus be recognised. The normalisation of the younger throw graph increases the maximum throw on this horizon and results after subtraction from the throw on the older horizon in a lower maximum interval throw. The normalisation of the throw data is an attempt to account for retreating tip lines between successive horizons towards the upper tips of a fault as an alternative to simple subtraction of throw values between the horizons at each sample location.

Tectonic setting of the basin compared to others

The Columbus Basin is a detached basin characterised by gravitational faulting of prograding delta successions on a shelf and continental slope. Other basins at passive continental margins show similar large-scale gravitational faulting of thick, prograding deltas (Gulf of Mexico, Congo Basin and Niger Delta on the West African margin). They differ however, through the substrate lithology, evaporite and mobile shale successions, which can significantly influence the deformation style in the basin (mini-basins, diapirs, and rafts). These basins have a different geological setting compared to well-studied, rift-related extensional basins, for example the North Sea, the Gulf of Corinth (Aegean), the Apennines (Italy), the Bay of Plenty, Taranaki Graben, and Taupo Rift (New Zealand) (back-arc basins), and the Basin and Range province (USA) (continental extension).

Throw rates on individual faults

The majority of individual normal faults in the study area show similar trends of throw rates with time: Maxima during early stages are followed by tapering values until the death of the respective faults. This is in contrast to findings by NICOL et al. (1997), suggesting near-constant fault displacement rates with time for faults from the North Sea and the Timor Sea, but in agreement with results by NICOL et al. (2005) who find varying displacement rates for a large-scale fault in the Taranaki Basin, New Zealand. NICOL et al. (2005) attribute their results to either displacement transfer between faults or regional fluctuation of strain rates with time. In the Columbus Basin, the decreasing throw rates towards the death of the faults can be explained independently of regional variations of strain rate by the basinward migration of active faulting and the resulting gradual abandonment of the respective landward faults.

The magnitude and scale range of the throw rates at which individual gravitational faults in the Columbus Basin are moving are very similar to throw and displacement rates observed in a number of rift-related extensional settings (see Section 5.9, Table 5.1 and Fig. 6.3). This large degree of consistency between the results for the Columbus Basin and rift-related basins is somewhat surprising since the geological settings are very different (i.e. possibly aseismic (GIBBS, 1989), gravitational faulting above a basal detachment as opposed to basement-involved faulting, respectively). The rate of extension, and hence the rate of (vertical) fault movement, in a detached gravitational (thin-skinned) system is dependent on the rate of movement on the basal detachment (which is a function of its shear strength (commonly formed by salt or shale), shear strength might be reduced in shale due to pore fluid overpressure) and the rate of accumulation of the gravitationally failing strata (which are displaced by normal faults). In rift-related or back-arc settings, faulting is driven by (upper) crustal extension.

Comparison to other studies of fault migration

Fault displacement rates in the Columbus Basin correlate with fault size (either maximum displacement or trace length) (see Fig. 6.3). The larger faults generally have higher displacement rates than smaller ones throughout the evolution of the fault system. The block-bounding faults have consistently higher throw rates than the medium faults and only show a decrease to very low values towards their deaths. This relationship was also observed for normal fault systems of the Inner Moray Firth (North Sea) and the Timor Sea (Australia) (WALSH et al., 2001; MEYER et al., 2002; WALSH et al., 2003b).

In the Columbus Basin, subsidiary faults initiate in the hanging wall of each of the largest faults with the progressive migration of active faulting. Thus, the total number of active faults does not decrease with time but their location shifts. This is in contrast to observations made by GUPTA et al. (1998), COWIE et al. (2000), WALSH et al. (2001), MEYER et al. (2002), and WALSH et al. (2003b) for numerically modelled fault populations in rift basins as well as examples based on seismic data: displacement and strain progressively localise onto fewer large faults as the fault population evolves, which is accompanied by the death of smaller faults and leads to the reduction of the total number of active faults.
The basinward migration of the large-scale regional (down-to-the-basin) growth faults and the associated subsidiary faults is attributed to the progressive progradation of the shelf-edge since Middle Miocene times (SYDOW et al., 2003). The prograding Orinoco Delta deposited large amounts of poorly consolidated, gravitationally unstable siliciclastic sediments on the outermost shelf and slope. This, together with the basinward dipping near-Top Cretaceous shale detachment horizon and possible pore fluid overpressure, is considered to have led to the formation of large-scale gravitational failure in the form of normal faults. The progradation of the delta and hence the progressive shift of the main depocentre of unstable strata with time caused the associated faulting to also migrate in a basinward direction.

Listric extensional growth faults and associated depocentres migrate down-slope and therefore young in a basinward direction in the Columbus Basin (LEONARD, 1983; WOOD, 2000; SYDOW et al., 2003; BEVAN, 2007; GIBSON et al., in press; this study). This is similar to other basins with gravitational faulting of prograding delta successions, such as the northern Gulf of Mexico (DIEGEL et al., 1995; ROWAN et al., 1999), the Niger Delta (EVAMY et al., 1978), and the Nile Delta (BEACH & TRAYNER, 1991). These faults are very similar in geometry, detach into shale units (Columbus Basin) or onto the top of salt units or into salt welds (Gulf of Mexico) and form due to gravitational mass movement (LOPEZ, 1990; WOOD, 2000; ROWAN et al., 1999; BEVAN, 2007).

The observed down-slope migration is in contrast to migration patterns of gravitational listric growth faults of Upper Carboniferous age in western Ireland (County Clare) (RIDER, 1978). The majority of these faults detach into a thin shale horizon and only one fault was largely active at any one time (WIGNALL & BEST, 2004). Faulting initiated and migrated in a dominantly paleo-landward direction (WIGNALL & BEST, 2004). BRUCE (1973) attributes the sequence of initiation of extensional gravitational growth faults to the relative ratio of sedimentation rate to created accommodation space. The strata on the shelf off-shore Congo are affected by extensional faults detaching onto evaporites and raft tectonics (DUVAL et al., 1992; ROUBY et al., 2003). The migration of salt (inflation and deflation of salt pillows and diapirs) is considered to significantly influence the style of deformation and might mask any systematic sequence of fault initiation and migration there.

Comparison of aggregate throw rates across the basin/study area

The aggregate fault throw rates across the study area have been found not to be constant over the investigated time span but increase steadily from 1.8±0.2 mm/a to 5.1±1.0 mm/a. For the Taupo Rift, New Zealand, VILLAMOR & BERRYMAN (2001) determined aggregate time-averaged vertical displacement rates to 7.2±0.4 mm/a, and NICOL et al. (2006) found near-constant aggregate displacement rates of ca. 7.5 mm/a across all faults in the rift. The magnitude of these results is very similar, especially considering the angular relationship between throw and displacement, and the very different geological setting.

The near-constant aggregate displacement rates of the Taupo Rift over the past 60 ka are according to NICOL et al. (2006) due to the constant rate of plate motion driving the rift extension. The nature of the Columbus Basin, i.e. a detached basin with gravitational faulting, makes assessment of the contribution of different driving forces of the basin extension very difficult. Within the scope of this study, it is not possible to determine the magnitude and influence of the displacement transfer from the plate boundary towards the south, possible variations of the slip rate of the detachment layer on which the strata glide basinward, e.g. due to fluid overpressure, and the sediment input causing the gravitational collapse on the regional extension rate.

8.3 Further work

In order to understand the growth of individual syn-sedimentary faults and especially the spatial and temporal evolution of faulting in the Columbus Basin better, further work is necessary that builds on the results presented here and takes more data of an enlarged study area into account.

Within the current study area, older horizons need to be considered to constrain the onset of faulting for a number of important faults (Cassia, A4, and G faults). The detailed documentation and interpretation of more fault systems characterised by dip-linkage, fault-splay interaction and up-ward splaying would also contribute to our knowledge of these processes. Inclusion of more data from smaller faults into the investigation of basin-scale throw and throw rate distribution and migration would result in more comprehensive results. It could also help to address possible strain localisation within a fault block that might be masked by the overall migration of activity.

The study area should be extended across fault strike both in the SW and NE. In the SW, the next block-bounding fault, the Claro Fault, is located just a few km outside of the present study area (Fig. 3.4). Throw data for the Claro Fault would help to constrain the magnitude and migration of faulting during older times and thus complement the dataset significantly, regarding both the growth of large-scale gravitational growth faults and the total strain rate across the basin. In the NE, the horizons mapped across the large-scale H and H* faults should be extended to older horizons in order to determine the onset of faulting and its migration more precisely. Additionally, more faults in the hanging wall of the H* Fault and possibly the next block-bounding fault should be taken into account.
If the study area is extended to cover the large-scale counter-regional faults (near present-day shelf edge), their growth history could be determined and compared to that of the regional faults, and a much more complete picture of the strain rate evolution across the Columbus Basin could be obtained (Fig. 3.5).

Extension of the dataset along fault strike would offer the opportunity to investigate the evolution of the large-scale block-bounding faults more comprehensively, since the current study area only covers a portion of the total length of each of these faults present. Additionally, along-strike extension of the study area could be used to investigate lateral variations in the number of active faults and their contribution to extension (throw or strain rate) within each fault block. These data should be integrated with information about the temporal and spatial migration of the Orinoco Delta from sedimentological investigations.

Similar studies into the evolution and characteristics of individual extensional growth faults and/or the total throw or strain rate across other gravitationally faulted basins would contribute substantially to our knowledge about these systems. It would also create a database for comparisons of the results from the respective basins in order to evaluate the impact of varying sedimentation rates, detachment lithologies, and deformation styles (diapis, rafts) on fault evolution.

References

ALGAR ST & PINDELL JL (1993) *Structure and deformation of the Northern Range of Trinidad and adjacent areas.* – Tectonics, **12**: 814-829

ALLAN US (1989) *Model for hydrocarbon migration and entrapment within faulted structures.* – AAPG Bulletin, **73**: 803-811

ANDERS MH & SCHLISCHE RW (1994) *Overlapping faults, intrabasin highs, and the growth of normal faults.* – Journal of Geology, **102**: 165-180

AXEN GJ (1988) *The geometry of planar domino-style normal faults above a dipping basal detachment.* – Journal of Structural Geology, **10**: 405-411

BADLEY GEOSCIENCE LIMITED (2007) *TrapTester® Reference Manual.* – Available from: http://www.badleys.co.uk/index.html

BARNETT JAM, MORTIMER J, RIPPON JH, WALSH JJ & WATTERSON J (1987) *Displacement geometry in the volume containing a single normal fault.* – AAPG Bulletin, **71**: 925-937

BEACH A & TRAYNER P (1991) The geometry of normal faults in a sector of the offshore Nile Delta, Egypt. – In: ROBERTS AM, YIELDING AM & FREEMAN B (eds.) *The geometry of normal faults.* – Geological Society, London, Special Publications, **56**: 173-182

BEVAN TG (2007) *Structural cross-sections of the Columbus Basin: An integrated geological model based on a comprehensive 3D seismic database.* – GSTT 4th Geological Conference & Exhibition, Port of Spain, Trinidad 17-22 June

BHATTACHARYA JP & DAVIES RK (2001) *Growth faults at the prodelta to delta-front transition, Cretaceous Ferron sandstone, Utah.* – Marine and Petroleum Geology, **18**: 525-534

BHATTACHARYA JP & DAVIES RK (2004) *Sedimentology and structure of growth faults at the base of the Ferron Sandstone Member along Muddy Creek, Utah.* – In: CHIDSEY TC, ADAMS JR RD & MORRIS TH (eds.) *Analog for fluvial-deltaic reservoir modelling: Ferron Sandstone of Utah.* – AAPG Studies in Geology, **50**: 279-304

BROOKS M, TRAYNER PM & TRIMBLE TJ (1988) *Mesozoic reactivation of Variscan thrusting in the Bristol Channel area, UK.* – Journal of the Geological Society, London, **145**: 439-444

BROWN AR (2003) *Interpretation of Three Dimensional Seismic Data.* – 6th edition, AAPG Memoir, **42**, 541pp.

BRUCE CH (1973) *Pressured shale and related sediment deformation: Mechanism for development of regional contemporaneous faults.* – AAPG Bulletin, **57**: 878-886

BULL JM, BARNES PM, LAMARCHE G, SANDERSON DJ, COWIE PA, TAYLOR SK, DIX JK (2006) *High-resolution record of displacement accumulation on an active normal fault: implications for models of slip accumulation during repeated earthquakes.* – Journal of Structural Geology, **28**: 1146-1166

BUSCH DA (1975) *Influence of growth faulting on sedimentation and prospect evaluation.* – AAPG Bulletin, **59**: 217-230

CARTWRIGHT JA, MANSFIELD CS & TRUDGILL BD (1996) *The growth of normal faults by segment linkage.* – In: BUCHANAN PG & NIEUWLAND AD (eds.) *Modern developments in structural interpretation, validation and modelling.* – Geological Society, London, Special Publications, **99**: 163-177

CARTWRIGHT JA, BOUROULLEC R, JAMES D & JOHNSON H (1998) *Polycyclic motion history of some Gulf Coast growth faults from high-resolution displacement analysis.* – Geology, **26**: 819-822

CARTWRIGHT JA & HUUSE M (2005) *3D seismic technology: the geological Hubble.* – Basin Research, **17**: 1-20

CHADWICK RA (1986) *Extension tectonics in the Wessex Basin, southern England.* – Journal of the Geological Society, London, **143**: 465-488

CHAPMAN GR, LIPPARD SJ & MARTYN JE (1978) *The stratigraphy and structure of the Kamasia Range, Kenya Rift Valley.* – Journal of the Geological Society, London, **135**: 265-281

CHAPMAN TJ & MENEILLY AW (1991) *The displacement patterns associated with a reverse-reactivated, normal growth fault.* – In: ROBERTS AM, YIELDING AM & FREEMAN B (eds.) *The geometry of normal faults.* – Geological Society, London, Special Publications, **56**: 183-191

CHILDS C, EASTON SJ, VENDEVILLE BC, JACKSON MPA, LIN ST, WALSH JJ & WATTERSON J (1993) *Kinematic analysis of faults in a physical model of growth faulting above a viscous salt analogue.* – Tectonophysics, **228**: 313-329

CHILDS C, WATTERSON J & WALSH JJ (1995) *Fault overlap zones within developing normal fault systems.* – Journal of the Geological Society, London, **152**: 535-549

CHILDS C, NICOL A, WALSH JJ & WATTERSON J (2003) *The growth and propagation of synsedimentary faults.* – Journal of Structural Geology, **25**: 633-648

COLLIER REL, PANTOSTI D, D'ADDEZIO G, DE MARTINI PM, MASANA E & SAKELLARIOU D (1998) *Paleoseismicity of the 1981 Corinth earthquake fault: Seismic contribution to extensional strain in central Greece and implications for seismic hazard.* – Journal of Geophysical Research, **103** B: 30001-30019

COWIE P & SCHOLZ CH (1992) *Displacement-length scaling relationship for faults: data synthesis and discussion.* – Journal of Structural Geology, **14**: 1149-1156

COWIE PA, Gupta S & Dawers NH (2000) *Implications of fault array evolution fro syn-rift depocentre development: insights from a numerical fault growth model.* – Basin Research, **12**: 241-261

COSGROVE JW & AMEEN MS (1999) *A comparison of the geometry, spatial organization and fracture pattern associated with forced folds and buckle folds.* – In: COSGROVE JW & AMEEN MS (eds): *Forced folds and fractures.* – Geological Society, London, Special Publications, **169**: 7-21

DAMUTH JE (1994) *Neogene gravity tectonics and depositional processes on the deep Niger Delta continental margin.* – Marine and Petroleum Geology, **11**: 320-346

DAVIES SJ, DAWERS NH, MCLEOD AE & UNDERHILL JR (2000) *The structural and sedimentological evolution of early synrift successions: the Middle Jurassic Tarbert Formation, North Sea.* – Basin Research, **12**: 343-365

DAWERS NH & UNDERHILL JR (2000) *The role of fault interaction and linkage in controlling synrift stratigraphic sequences: Late Jurassic, Statfjord East area, Northern North Sea.* – AAPG Bulletin, **84**: 45-64

DIEGEL FA, KARLO JF, SCHUSTER DC, SHOUP RC & TAUVERS PR (1995) *Cenozoic structural evolution and tectono-stratigraphic framework of the northern Gulf Coast continental margin.* – In: JACKSON MPA, ROBERTS DG & SNELSON S (eds.) *Salt tectonics: a global perspective.* – AAPG Memoir, **65**: 109-151

DUERTO L & MCCLAY KR (2002) *Three-dimensional geometry and evolution of shale diapirs in the Eastern Venezuela Basin.* – AAPG Bulletin, **86**: supplement

DULA WF (1991) *Geometric models of listric normal faults and rollover folds.* – AAPG Bulletin, **75**: 1609-1625

DUVAL B, CRAMEZ C & JACKSON MPA (1992) *Raft tectonics in the Kwanza Basin, Angola.* – Marine and Petroleum Geology, **9**: 389-404

EDWARDS MB (1976) *Growth faults in Upper Triassic deltaic sediments, Svalbard.* – AAPG Bulletin, **60**: 341-355

EVAMY BD, HAREMBOURE J, KAMERLING P, KNAAP WA, MOLLOY FA & ROWLANDS PH (1978) *Hydrocarbon habitat of Tertiary Niger Delta.* – AAPG Bulletin, **62**: 1-39

FOSSEN H, HESTHAMMER J, JOHANSEN TES & SYGNABERE TO (2003) *Structural geology of the Huldra Field, northern North Sea – a major tilted fault block at the eastern edge of the Horda Platform.* – Marine and Petroleum Geology, **20**: 1105-1118

GALLOWAY WE (1986) *Growth faults and fault-related structures of prograding terrigenous clastic continental margins.* – Transactions, Gulf Coast Association of Geological Societies, **36**: 121-128

GALLOWAY WE (1987) *Depositional and structural architecture of prograding clastic continental margins: tectonic influence on patterns of basin filling.* – Norsk Geologisk Tidsskrift, **76**: 237-251

GAWTHORPE RL, JACKSON CAL, YOUNG MJ, SHARP IR, MOUSTAFA AR & LEPPARD CW (2003) *Normal fault growth, displacement localisation and the evolution of normal fault populations: the Hammam Faraun fault block, Suez rift, Egypt.* – Journal of Structural Geology, **25**: 883-895

GERTHSEN C & VOGEL H (1997) *Physik.* – 19th ed., Springer-Lehrbuch, 1262 pp.

GIBBS AD (1984) *Structural evolution of extensional basin margins.* – Journal of the Geological Society, London, **141**: 609-620

GIBBS AD (1987) *Development of extension and mixed-mode sedimentary basins.* – In: COWARD MP, DEWEY JF & HANCOCK PL (eds.) *Continental extensional tectonics.* – Geological Society, London, Special Publications, **28**: 19-33

GIBBS AD (1989) *Structural styles in basin formation.* – In: TANKARD AJ & BALKWILL HR (eds.) *Extensional tectonics and stratigraphy of the North Atlantic Margins.* – AAPG Memoir, **46**: 81-93

GIBSON JR, WALSH JJ & WATTERSON J (1989) *Modelling of bed contours and cross-sections adjacent to planar normal faults.* – Journal of Structural Geology, **11**: 317-328

GIBSON RG & DZOU LIP (2004) *Shelf petroleum system of the Columbus basin, offshore Trinidad, West Indies. II. Field geochemistry and petroleum migration model.* – Marine and Petroleum Geology, **21**: 109-129

GIBSON RG, DZOU LIP & GREELEY DF (2004) *Shelf petroleum system of the Columbus basin, offshore Trinidad, West Indies. I. Source rock, thermal history, and controls on product distribution.* – Marine and Petroleum Geology, **21**: 97-108

GIBSON RG, MEISLING KE & SYDOW JC (in press) *Columbus Basin, offshore Trinidad: A detached pull-apart basin in a transpressional foreland setting.* – In: BALLY AW & ROBERTS DG (eds): *Phanerozoic Regional Geology of the World*

GILES MR (1997) *Diagenesis: a quantitative perspective, implications for basin modelling and rock property prediction.* – Kluwer Academic, 526p.

GLEN RA, HANCOCK PL & WHITTAKER A (2005) *Basin inversion by distributed deformation: the southern margin of the Bristol Channel Basin, England.* – Journal of Structural Geology, **27**: 2113-2134

GOLDSWORTHY M & JACKSON J (2000) *Active normal fault evolution in Greece revealed by geomorphology and drainage patterns.* – Journal of the Geological Society, London, **157**: 967-981

GUPTA S, COWIE PA, DAWERS NH & UNDERHILL JR (1998) *A mechanism to explain rift-basin subsidence and stratigraphic patterns through fault-array evolution.* – Geology, **26**: 595-598

HAMBLIN WK (1965) *Origins of "reverse drag" on the down-thrown side of normal faults.* – Geological Society of America Bulletin, **16**: 1154-1164

JACKSON JA & MCKENZIE DP (1983) *The geometrical evolution of normal fault systems.* – Journal of Structural Geology, **5**: 417-482

JACKSON JA, WHITE NJ, GARFUNKEL Z & ANDERSON H (1988) *Relations between normal fault geometry, tilting and vertical motions in extensional terrains: an example from the southern Gulf of Suez.* – Journal of Structural Geology, **10**: 155-170

JACKSON JA & WHITE NJ (1989) *Normal faulting in the upper continental crust: observations from regions of active extension.* – Journal of Structural Geology, **11**: 15-36

KERR AC & TARNEY J (2005) *Tectonic evolution of the Caribbean and north-western South America: The case for accretion of two Late Cretaceous oceanic plateaus.* – Geology, **33**: 269-272

LARSEN P-H (1988) *Relay structure in a Lower Permian basement-involved extension system, East Greenland.* – Journal of Structural Geology, **10**: 3-8

LEONARD R (1983) *Geology and hydrocarbon accumulations, Columbus Basin, offshore Trinidad.* – AAPG Bulletin, **67**: 1081-1093

LOPEZ JA (1990) *Structural styles of growth faults in the U.S. Gulf Coast Basin.* – In: BROOKS J (ed.) *Classic petroleum provinces.* – Geological Society, London, Special Publications, **50**: 203-219

LUNDIN ER (1992) *Thin-skinned extensional tectonics on a salt detachment, northern Kwanza Basin, Angola.* – Marine and Petroleum Geology, **9**: 405-411

LYKOUSIS V, SAKELLARIOU D, MORETTI I & KABERI H (2007) *Late Quaternary basin evolution of the Gulf of Corinth: Sequence stratigraphy, sedimentation, fault-slip and subsidence rates.* – Tectonophysics, **440**: 29-51

MAGARA K (1980) *Comparison of porosity–depth relationships of shale and sandstone.* – Journal of Petroleum Geology, **3**, 175-185

MANSFIELD CS & CARTWRIGHT JA (1996) *High resolution fault displacement mapping from three-dimensional seismic data: evidence for dip linkage during fault growth.* – Journal of Structural Geology, **18**: 249-263

MANSFIELD CS & CARTWRIGHT JA (2001) *Fault growth by linkage: observations and implications from analogue models.* – Journal of Structural Geology, **23**: 745-763

MCCLAY KR (1990) *Extensional fault systems in sedimentary basins: a review of analogue model studies.* – Marine and Petroleum Geology, **7**: 206-233

MCKENZIE D (1978) *Some remarks on the development of sedimentary basins.* – Earth and Planetary Science Letters, **40**: 25-32

MCLEOD AE, DAWERS NH & UNDERHILL JR (2000) *The propagation and linkage of normal faults: insights from the Strathspey-Brent-Statfjord fault array, northern North Sea.* – Basin Research, **12**: 263-284

MCNEILL LC & COLLIER RELL (2004) *Uplift and slip rates of the eastern Eliki fault segment, Gulf of Corinth, Greece, inferred from Holocene and Pleistocene terraces.* – Journal of the Geological Society, London, **161**: 81-92

MEYER V, NICOL A, CHILDS C, WALSH JJ & WATTERSON J (2002) *Progressive localisation of strain during the evolution of a normal fault population.* – Journal of Structural Geology, **24**: 1215-1231

MORETTI I, SAKELLARIOU D, LYKOUSIS V & MICARELLI L (2003) *The Gulf of Corinth: an active half graben?.* – Journal of Geodynamics, **36**: 323-340

MOREWOOD NC & ROBERTS GP (2000) *The geometry, kinematics and rates of deformation within an en echelon normal fault segment boundary, central Italy.* – Journal of Structural Geology, **22**: 1027-1047

MOREWOOD NC & ROBERTS GP (2002) *Surface observations of active normal fault propagation: implications for growth.* – Journal of the Geological Society, London, **159**: 263-272

MORRIS A, FERRILL DA & HENDERSON DB (1996) *Slip-tendency analysis and fault reactivation.* – Geology, **24**: 275-278

MOURGUES & COBBOLD (2006) *Sandbox experiments on gravitational spreading and gliding in the presence of fluid overpressures.* – Journal of Structural Geology, **28**: 887-901

NICOL A, WALSH JJ, WATTERSON J & UNDERHILL JR (1997) *Displacement rates of normal faults.* – Nature, **3**, 175-185

NICOL A, WALSH JJ, BERRYMAN K & NODDER S (2005) *Growth of a normal fault by accumulation of slip over millions of years.* – Journal of Structural Geology, **27**: 327-342

NICOL A, WALSH JJ, BERRYMAN K & VILLAMOR P (2006) *Interdependence of fault displacement rates and paleo-earthquakes in an active rift.* – Geology, **34**: 865-868

NOLL CA & HALL M (2006) *Normal fault growth and its function on the control of sedimentation during basin formation: A case study from the Upper Cambrian Owen Conglomerate, West Coast Range, western Tasmania, Australia.* – AAPG Bulletin, **90**: 1609-1630

NORTON MG (1986) *Late Caledonide extension in Western Norway: a response to extreme crustal thickening.* – Tectonics, **5**: 195-204

NUNN JA (1985) *State of stress in the northern Gulf Coast.* – Geology, **13**: 429-432

PEACOCK DCP & SANDERSON DJ (1991) *Displacements, segment linkage and relay ramps in normal fault zones.* – Journal of Structural Geology, **13**: 721-733

PEACOCK DCP & SANDERSON DJ (1994) *Geometry and development of relay ramps in normal fault systems.* – AAPG Bulletin, **78**: 147-165

PEACOCK DCP & SANDERSON DJ (1996) *Effects of propagation rate on displacement variations along faults.* – Journal of Structural Geology, **18**: 311-320

PEACOCK DCP, KNIPE RJ & SANDERSON DJ (2000) *Glossary of normal faults.* – Journal of Structural Geology, **22**: 291-305

PETERSEN K, CLAUSEN OR & KORSTGÅRD JA (1992) *Evolution of a salt-related listric growth fault near the D-1 well, block 5605, Danish North Sea: displacement history and salt kinematics.* – Journal of Structural Geology, **14**: 565-577

PLATT JP (1986) *Dynamics of orogenic wedges and the uplift of high-pressure metamorphic rocks.* – Geological Society of America Bulletin, **97**: 1037-1053

PRICE NJ & COSGROVE JW (1990) *Analysis of geological structures.* – Cambridge University Press, 502pp.

RIDER MH (1978) *Growth faults in Carboniferous in Western Ireland.* – AAPG Bulletin, **62**: 2191-2213

ROBERTS GP & MICHETTI AM (2004) *Spatial and temporal variations in growth rates along active normal fault systems: an example from The Lazio–Abruzzo Apennines, central Italy.* – Journal of Structural Geology, **26**: 339-376

ROUBY D & COBBOLD PR (1996) *Kinematic analysis of a growth fault system in the Niger Delta from restoration in map view.* – Marine and Petroleum Geology, **13**: 565-580

ROUBY D, FOSSEN H & COBBOLD PR (1996) *Extension, displacement, and block rotation in the larger Gullfaks area, Northern North Sea: Determined from map view restoration.* – AAPG Bulletin, **80**: 875-890

ROUBY D, RAILLARD S, GUILLOCHEAU F, BOUROULLEC R & NALPAS T (2002) *Kinematics of a growth fault/raft system on the West African margin using 3-D restoration.* – Journal of Structural Geology, **24**: 783-796

ROUBY D, GUILLOCHEAU F, ROBIN C, BOUROULLEC R, RAILLARD S, CASTELLTORT S & NALPAS T (2003) *Rates of deformation of an extensional growth fault/raft system (offshore Congo, West African margin) from combined accommodation measurements and 3-D restoration.* – Basin Research, **15**: 183-200

ROWAN MG, JACKSON MPA & TRUDGILL BD (1999) *Salt-related fault families and fault welds in the northern Gulf of Mexico.* – AAPG Bulletin, **83**: 1454-1484

RYKKELID E & FOSSEN H (2002) *Layer rotation around vertical fault overlap zones: observations from seismic data, field examples, and physical experiments.* – Marine and Petroleum Geology, **19**: 181-192

SAVAGE JC & HASTIE LM (1966) *Surface deformation associated with dip-slip faulting.* – Journal of Geophysical Research, **71**: 4897-4904

SCHETTINO A & SCOTESE CR (2000) *A synthetic APWP for Africa (Jurassic–present) and global plate tectonic reconstructions.* – EOS (Transactions, American Geophysical Union), **81**: S180

SCHLISCHE RW (1995) *Geometry and origin of fault-related folds in extensional settings.* – AAPG Bulletin, **79**: 1661-1678

SCHLISCHE RW & ANDERS MH (1996) *Stratigraphic effects and tectonic implications of the growth of normal faults and extensional basins.* – In: BERATAN KK (ed.) *Reconstructing the history of Basin and Range extension using sedimentology and stratigraphy.* – Geological Society of America, Special Publications, **303**: 183-203

SCHLUMBERGER OILFIELD GLOSSARY (2007) *Gamma ray log.* – http://www.glossary.oilfield.slb.com/Display.cfm?Term=gamma%20ray%20log

SCLATER JG & CHRISTIE PAF (1980) *Continental stretching: An explanation of the post-mid-Cretaceous subsidence of the central North Sea Basin.* – Journal of Geophysical Research, **85**, B7: 3711-3739

SEGALL P & POLLARD DD (1980) *Mechanics of discontinuous faults.* – Journal of Geophysical Research, **85**: 4337-4350

SHELTON JW (1984) *Listric normal faults: an illustrated summary.* – AAPG Bulletin, **68**: 801-815

STEIN RS, KING GCP & RUNDLE JB (1988) *The growth of geological structures by repeated earthquakes: 2. Field examples of continental dip-slip faults.* – Journal of Geophysical Research, **93**: 13319-13331

STEWART SA & ARGENT JD (2000) *Relationship between polarity of extensional fault arrays and presence of detachments.* – Journal of Structural Geology, **22**: 693-711

SUPPE J (1985) *Principles of structural geology.* – Prentice-Hall, 560p.

SYDOW JC, FINNERAN J & BOWMAN AP (2003) *Stacked shelf-edge delta reservoirs of the Columbus Basin, Trinidad, West Indies.* – In: ROBERTS HH, ROSEN NC, FILLON RH & ANDERSON JB (eds.): *Shelf margin deltas and linked down-slope petroleum systems: global significance and future exploration potential.* – Proceedings of the 23rd Annual GCSSEPM Foundation Bob F. Perkins Research Conference, 441-465.

SYKES LR, MCCANN WR & KAFKA AL (1982) *Motion of Caribbean plate during last 7 million years and implications for earlier Cenozoic movements.* – Journal of Geophysical Research, **87**, B13: 10656-10676

TAYLOR SK, BULL JM, LAMARCHE G & BARNES PM (2004) *Normal fault growth and linkage in the Whakatane Graben, New Zealand, during the last 1.3 Myr.* – Journal of Geophysical Research, **109**: B02408

TAYLOR SK, NICOL A & WALSH JJ (2007) Displacement loss on growth faults due to sediment compaction. – Journal of Structural Geology, doi: 10.1016/j.jsg.2007.11.006

THORE P, SHTUKA A, LECOUR M, AIT-ETTAJER T & COGNOT R (2002) *Structural uncertainties: Determination, management, and applications.* – Geophysics, **67**: 840-852

TRUDGILL BD & CARTWRIGHT JA (1994) *Relay-ramp forms and normal-fault linkages – Canyonlands National Park, Utah.* – Geological Society of America Bulletin, **106**: 1143-1157

TWISS RJ & MOORES EM (1992) *Structural Geology.* – WH Freeman and Company, New York, 532pp.

VAN HOORN B (1987) *The South Celtic Sea/Bristol Channel Basin: origin, deformation and inversion history.* – Tectonophysics, **137**: 309-334

VALLE PJ, GJELBERG JG & HELLAND-HANSEN W (2001) *Tectonostratigraphic development in the eastern Lower Congo Basin, offshore Angola, West Africa.* – Marine and Petroleum Geology, **18**: 909-927

VILLAMOR P & BERRYMAN K (2001) *A late Quaternary extension rate in the Taupo Volcanic Zone, New Zealand, derived from fault slip data.* – New Zealand Journal of Geology and Geophysics, **44**: 243-269

WALSH JJ & WATTERSON J (1987) *Distribution of cumulative displacement and seismic slip on a single normal fault surface.* – Journal of Structural Geology, **9**: 1039-1046

WALSH JJ & WATTERSON J (1988) *Analysis of the relationship between displacements and dimensions of faults.* – Journal of Structural Geology, **10**: 239-247

WALSH JJ & WATTERSON J (1989) *Displacement gradients on fault surfaces.* – Journal of Structural Geology, **11**: 307-316

WALSH JJ & WATTERSON J (1991) *Geometric and kinematic coherence and scale effects in normal fault systems.* – In: ROBERTS AM, YIELDING G & FREEMAN B (eds.) *The geometry of normal faults.* – Geological Society, London, Special Publications, **56**: 193-203

WALSH JJ, WATTERSON J, BAILEY WR & CHILDS C (1999) *Fault relays, bends and branch-lines.* – Journal of Structural Geology, **21**: 1019-1026

WALSH JJ, CHILDS C, MEYER V, MANZOCCHI T, IMBER J, NICOL A, TUCKWELL G, BAILEY WR, BONSON CG, WATTERSON J, NELL PAR & STRAND J (2001) *Geometric controls on the evolution of normal fault systems.* – In: HOLDSWORTH RE, STRACHAN RA, MAGLOUGHLIN JF & KNIPE RJ (eds.) *The nature and tectonic significance of fault zone weakening.* – Geological Society, London, Special Publications, **186**: 157-170

WALSH JJ, NICOL A & CHILDS C (2002) *An alternative model for the growth of faults.* – Journal of Structural Geology, **24**: 1669-1675

WALSH JJ, BAILEY WR, CHILDS C, NICOL A & BONSON CG (2003a) *Formation of segmented normal faults: a 3-D perspective.* – Journal of Structural Geology, **25**: 1251-1262

WALSH JJ, CHILDS C, IMBER J, MANZOCCHI T, WATTERSON J & NELL PAR (2003b) *Strain localisation and population changes during fault system growth within the Inner Moray Firth, North Sea.* – Journal of Structural Geology, **25**: 307-315

WATTERSON J (1986) *Fault dimensions, displacements and growth.* – Pure and Applied Geophysics, **124**: 365-373

WERNICKE B & BURCHFIEL BC (1982) *Modes of extensional tectonics.* – Journal of Structural Geology, **4**: 105-115

WHEELER RL (1987) *Boundaries between segments of normal faults – criteria for recognition and interpretation.* – In: CRONE AJ & OMDAHL EM (eds.) *Proceeding of Conference XXXIX, Directions in paleoseismology.* – US Geol. Survey Open-File Rept., **87-673**: 385-398

WHITE NJ, JACKSON JA & MCKENZIE DP (1986) *The relationship between the geometry of normal faults and that of the sedimentary layers in their hanging walls.* – Journal of Structural Geology, **8**: 897-909

WHITTAKER A & GREEN GW (1983) *Geology of the country around Weston-super-Mare.* – Memoir Geological Survey GB, Sheet 279 with parts of 263 and 295

WIGNALL PB & BEST JL (2004) *Sedimentology and kinematics of a large, retrogressive growth-fault system in Upper Carboniferous deltaic sediments, western Ireland.* – Sedimentology, **51**: 1343-1358

WILLEMSE EJM, POLLARD DD & AYDIN A (1996) *Three-dimensional analyses of slip distributions on normal fault arrays with consequences for fault scaling.* – Journal of Structural Geology, **18**: 295-309

WILLEMSE EJM (1997) *Segmented normal faults: Correspondence between three-dimensional mechanical models and field data.* – Journal of Geophysical Research, **102**, B1: 675-692

WILLIAMS G & VANN I (1987) *The geometry of listric normal faults and deformation in their hanging walls.* – Journal of Structural Geology, **9**: 789-795

WOOD LJ (2000) *Chronostratigraphy and tectonostratigraphy of the Columbus basin, eastern offshore Trinidad.* – AAPG Bulletin, **84**: 1905-1928

WU S, BALLY AW & CRAMEZ C (1990) *Allochthonous salt, structure and stratigraphy of the north-eastern Gulf of Mexico. Part II: Structure.* – Marine and Petroleum Geology, **7**: 334-370

XIAO H & SUPPE J (1992) *Origin of rollover.* – AAPG Bulletin, **76**: 509-529

YIELDING G (1990) *Footwall uplift associated with Late Jurassic normal faulting in the northern North Sea.* – Journal of the Geological Society, London, **147**: 219-222

YILMAZ Ö & DOHERTY SM (1987) *Seismic data processing.* – Society of Exploration Geophysicists, 526pp.

YOUNG J (unpublished) – with updated ages from: STANT SA, LARA J, MCGONIGAL KL & LADNER BC (2004) *Quaternary nannofossil biostratigraphy from Ocean Drilling Program Leg 189, Tasmanian Gateway.* – Proceedings of the Ocean Drilling Program, Scientific Results, **189**: 1-26

YOUNG MJ, GAWTHORPE RL & HARDY S (2001) *Growth and linkage of a segmented normal fault zone; the Late Jurassic Murchison-Statfjord North Fault, northern North Sea.* – Journal of Structural Geology, **23**: 1933-1952